NASA Contractor Report 3683

Analysis and Test for Space Shuttle Propellant Dynamics

Robert L. Berry, Leonard J. Demchak, and James R. Tegart

CONTRACT NAS9-15302
JUNE 1983

25th Anniversary
1958-1983

NASA

NASA Contractor Report 3683

Analysis and Test for Space Shuttle Propellant Dynamics

Robert L. Berry, Leonard J. Demchak,
and James R. Tegart
Martin Marietta Aerospace
Denver, Colorado

Prepared for
Lyndon B. Johnson Space Center
under Contract NAS9-15302

National Aeronautics
and Space Administration

**Scientific and Technical
Information Branch**

1983

CONTENTS

Figure

Table

ABSTRACT

This report, prepared by Martin Marietta Denver Aerospace, under Contract NAS9-15302, presents the results of an analytical and experimental study of Space Shuttle propellant dynamics during External Tank/Orbiter separation in a return-to-launch-site (RTLS) abort situation. The study was performed from April 1977 to January 1981 and was administered by the National Aeronautics and Space Administration, Lyndon B. Johnson Space Center, Houston, Texas, under the direction of Mr. Mark Craig, Technical Monitor.

1.0 INTRODUCTION

The Space Shuttle has been designated as Amc.ica's prime space launch vehicle for the 1980s and beyond. The Shuttle system is a manned flight system requiring extensive mission planning, including intact operations. One such abort mode requires the mated orbiter/external tank (ET) to "fly" back to the launch site at an altitude of over 61 km (200,000 ft) using the main orbiter engines. This return to launch site (RTLS) mission abort sequence requires the orbiter and ET to separate under aerodynamic loading when a significant amount of propellant remains in the ET. The typical separation sequence is as follows:

1) Begin powered pitchdown, from angle-of-attack $\bar{>}$40 deg, at MECO -20 s;

2) Achieve an angle-of-attack of -4 deg, using main engine thrust vector control and the reaction control system;

3) MECO, main orbiter engine cutoff;

4) Coast for approximately 13 s using the reaction control system (RCS) to maintain attitude;

5) Separation of the orbiter and ET using all downfiring orbiter RCS thrusters to move the orbiter away from the ET.

During the separation sequence, the ET nominally contains a 1% residual volume of liquid oxygen (LOX)*; approximately 5.52 m^3 (195 ft^3), 6,067 kg (13,376 lb). Additionally, the LOX line is full. The ET liquid hydrogen (LH_2) tank also contains a residual volume, but its impact due to liquid motion is small in comparison to the LOX tank, due to the low density of LH_2.

Aerodynamic forces decelerate the orbiter/ET during the 13-s coast after MECO. During this coast, the residual propellant "sloshes" forward developing a velocity relative to the ET at separation. Clearance between the ET and orbiter is provided, somewhat, by orbiter RCS jets moving the orbiter away, but more significantly, by aerodynamics acting on the ET to move it away. During separation, the motion of the propellant in the ET significantly influences the ET motion, which could cause the ET to recontact the orbiter. It is not possible to lower the dynamic pressure at separation sufficiently to avoid this phenomenon, nor can initial conditions be obtained to avoid it.

---

*One percent is the current OFT 1 baseline volume. Future missions may baseline much higher separation volumes (e.g., 25%).

NASA simulations of orbiter/ET RTLS separation indicate a potential collision problem. However, these simulations have been performed using a propellant slosh model, which has not been verified by test. To validate these simulations, a need to obtain empirical data was identified. The objectives of this study were: (1) to obtain test data in a low-g environment on scale model tanks for use in validating a slosh simulation approach; and (2) to develop a simulation approach and computer code for use by NASA in RTLS simulations. To achieve these objectives, a three-phase study was initiated in April 1977.

Phase I of this study was a drop tower test program designed to simulate the ET LOX motion during RTLS separation. Thirty-two tests were conducted in Martin Marietta's Drop Tower Test Facility using two 1/60th-scale models of the ET LOX tank; one with internal baffles, and one without. A scaling approach developed in a previous NASA study [Refs 1, 2] was used to relate drop tower test time to full scale ET time, and to insure liquid motion representative of the full-scale ET.

During the Phase I tests, small biaxial accelerations were applied to the model tanks, simulating aerodynamic deceleration of the ET during the RTLS separation sequence. The resulting propellant reorientation forces exerted on the tank were measured by crystal load cells, and liquid motion was photographed at 200 frames/s. The tests were conducted both with and without LOX tank baffles to facilitate analytical model development and to assess the effect of baffles on reorientation. In addition, a limited number of tests were performed simulating inflow to the tank from the LOX feedline. Subsequent analyses led to the conclusion that inflow would be negligible during separation. Based on scaling considerations, three test liquids were chosen for use in the test program: FC114B2, FC43, and HEXANE. The Phase I study is detailed in Reference [3].

The Phase I study indicated the importance that Bond and Reynolds number scaling had on the character of propellant reorientation. Tests demonstrated that the motion of the bulk liquid did not change, even though the Reynolds number was varied an order of magnitude by changing test liquids. However, both the Bond and Reynolds numbers for the model tanks, were much smaller than the values for the full-scale ET LOX tank. Closer approximation of full scale Bond and Reynolds numbers was not possible due to restrictions in model size imposed by the drop tower geometry.

To further investigate the effects of Bond and Reynolds number and to validate the scaling concepts used, it was desirable to conduct a test program with a larger LOX tank model. Hence, Phase II of the study was initiated. In this phase, an available 1/10th-scale LOX tank model was modified for use in NASA's KC-135 "zero-g" test aircraft. Aircraft testing allowed larger accelerations to be applied to the model tank. This resulted in a closer simulation of full scale Bond and Reynolds numbers, as indicated in Table 1-1.

TABLE 1-1.
COMPARISON OF TEST AND FULL-SCALE PARAMETERS FOR PROPELLANT REORIENTATION TESTS

Parameter	Full-Scale LOX	1/10th Scale Freon 113	1/60th Scale Freon 114B2
Bond Number	2.19×10^5	2.70×10^4	4.49×10^2
Reynolds Number	5.16×10^7	2.39×10^6	1.35×10^5

The Phase II test program consisted of four KC-135 flights involving 89 low-g parabolas with an average test time of 20 s. Tests were conducted both with and without the slosh baffles included in the 1/10th-scale tank. Two test liquids were used to evaluate viscosity effects: FC113, and a water-methocel solution. The tank was mounted in an instrumented fixture that measured the reorientation forces. In addition, liquid motion was photographed at 60 frames per second (fps) Adjustment of the aircraft flight path allowed application of biaxial accelerations to the tank, similar to those used in the Phase I drop tower study. Detailed documentation on the Phase II study is contained in Reference [4].

After evaluating the Phase I and Phase II test data, it was concluded that the scaling approach employed is valid, and that the liquid motion observed in the drop tower and KC-135 tests is representative of that expected in the full-scale ET [Ref 4]. The character of the liquid motion observed in the two test programs was the same even though there was a factor of six difference in geometric scaling. The differences observed were primarily due to the reduced influence of surface tension forces (i.e., higher Bond number) in the KC-135 tests, which led to more breakup of the liquid surface.

Test data from both test programs (Phase I and Phase II) were correlated to analytical simulations of the test conditions, using a "slosh" model similar to NASA's Space Vehicle Dynamic Simulation (SVDS) model. The analytical model employed in these correlation studies, LAMPS [Refs 1, 2], portrays the propellant as a point mass moving on an ellipsoidal constraint surface. The constraint surface is a distorted ellipse that best fits the center-of-mass envelope obtained by analytically rotating the tank in a 1-g field. Results of this correlation study indicated that the point mass model is inadequate to represent the propellant interaction forces during reorientation. The model was found to be conservative in predicting the reorientation forces. Both the magnitude and impulse (integrated effect) of the liquid forces predicted by the analysis exceed those measured in test.

It was therefore concluded that the NASA SVDS slosh model will over predict the slosh forces acting on the ET during RTLS separation. Phase III of the study was initiated based on these results.

Phase III consisted of the development of two and three dimensional, multiple mass models for simulating low g propellant slosh. The modeling concept developed, employs a finite element representation of the liquid. This formulation results in a realistic distribution of liquid mass within the tank. Finite elements are used to express liquid incompressibility by maintaining a constant elemental volume. The elements are also used in the formulation of internal viscous shear forces. The tank is represented by a ellipsoidal surface, and liquid "nodes" are constrained from penetrating this boundary. The formulation of this modeling approach and the associated computer codes are documented in this report. The models developed in Phase III have been used to simulate Phase I and Phase II test conditions and the results correlate very well to the measured data.

This report summarizes the entire 3-year study. Chapter 2.0 presents a discussion of both test programs. More detailed discussion of the test programs can be found in References [3 and 4]. Chapter 3.0 details the two dimensional finite element model formulation [LAMPS2] and correlation. Chapter 4.0 details the three dimensional model formulation [LAMPS3] and correlation. Conclusions of the study and recommendations for further development are presented in Chapter 5.0.

2.0 SCALE MODEL TESTING

The primary objective of the scale model testing was to acquire empirical data, on the character of propellant reorientation during the RTLS orbiter/ET separation sequence, for use in validating an analytical simulation approach. The full-scale conditions were scaled so that representative liquid (LOX) motion could be produced in subscale tanks. Phase I testing used a 1/60th scale ET LOX tank and Martin Marietta's Drop Tower Test Facility. Phase II testing used a 1/10th-scale ET LOX tank and NASA's KC-135 "zero g" test aircraft [Refs 5, 6].

During both test programs, liquid reorientation was photographed at high speed and the dynamic interaction forces applied to the tank by the moving propellant were measured. Comparison of data from the two test programs permitted validation of the scaling approach. This chapter summarizes both phases of the test program. More detail on the experimental aspects of this study can be found in References [3 and 4].

2.1 SCALING ANALYSIS

During the RTLS separation sequence, the external tank (ET) experiences axial ($\ddot{X}_o$) and lateral ($\ddot{Z}_o$) accelerations due to aerodynamic drag. These accelerations are shown in Figure 2-1, with respect to the orbiter coordinate system. The initial position of the residual LOX is established by the direction of the main engine thrust vector just before MECO. The initial position of the LOX free surface is perpendicular to the thrust vector, which is oriented at an angle γ to the orbiter X axis. The following values for each of these variables defined the full-scale conditions that were considered in the test program:

$\ddot{X}_o$ = 0.015 to 0.030 g

$\ddot{Z}_o$ = -0.005 to -0.030 g

γ = 0°, 13°, 30°

Residual LOX volume = 1%, 2%, 5%, 10%, 15%, 25% at separation.

A dimensional analysis of variables related to liquid reorientation in a container yields the following dimensionless parameters that characterize motion:

$$Fr = \frac{V}{\sqrt{Ar}} \text{ (Froude number); ratio of inertia to gravity forces} \qquad (2\text{-}1)$$

Figure 2-1. Definition of External Tank State Just after Separation

$$Bo = \frac{\rho A r^2}{\sigma}$$ (Bond number); ratio of gravity to surface tension forces (2-2)

$$Re = \frac{\rho V r}{\mu}$$ (Reynolds number); ratio of inertia to viscous forces. (2-3)

where

A = Liquid acceleration (cm/s^2)

V = Liquid velocity (cm/s)

r = Characteristic dimension, tank radius (cm)

ρ = Liquid density (gm/cm^3)

σ = Liquid surface tension (dynes/cm)

μ = Liquid viscosity (cp)

With respect to large amplitude liquid motion, it has been shown [Ref 7] that the Froude number can be related to the Bond and Reynolds numbers. Based on numerous liquid reorientation tests, an empirical expression has been established to describe this relationship [Ref 7]:

$$Fr = K_{Re} \left\{ 0.48 \left[1 - \left(\frac{0.84}{Bo} \right)^{\frac{Bo}{4.7}} \right] \right\}$$ (2-4)

Experimental data showing the relationship between Froude number and Bond number is shown in Figure 2-2a. These data indicate that the Froude number is independent of Bond number when the Bond Number is > 10. However, adjustments for viscosity must be made at low Reynolds numbers (Fig. 2-2b). If the Reynolds number is greater than 50, viscous effects are negligible. Therefore, these relationships indicate that for any propellant reorientation that has a Bond number greater than 10 and a Reynolds number greater than 50, scaling can be based on Froude number alone. As will be shown later, the requirements for Froude number scaling are satisfied for both the full-scale RTLS separation event and the scale model tests.

Equating Froude numbers for the full-scale ET LOX tank and the scale model tanks allows calculation of the full-scale time simulated by the test.

$$Fr_p = Fr_m$$ (2-5)

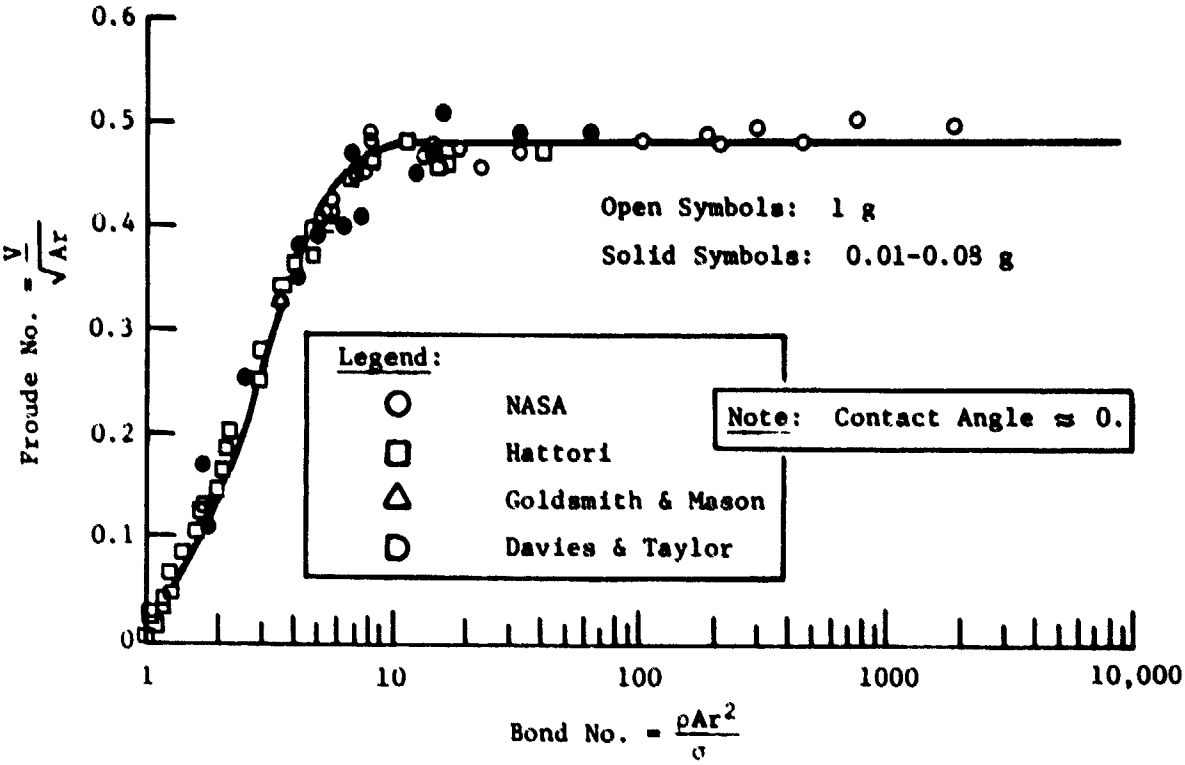

2-2a. *Froude-Bond Number Relationship (from Ref 7)*

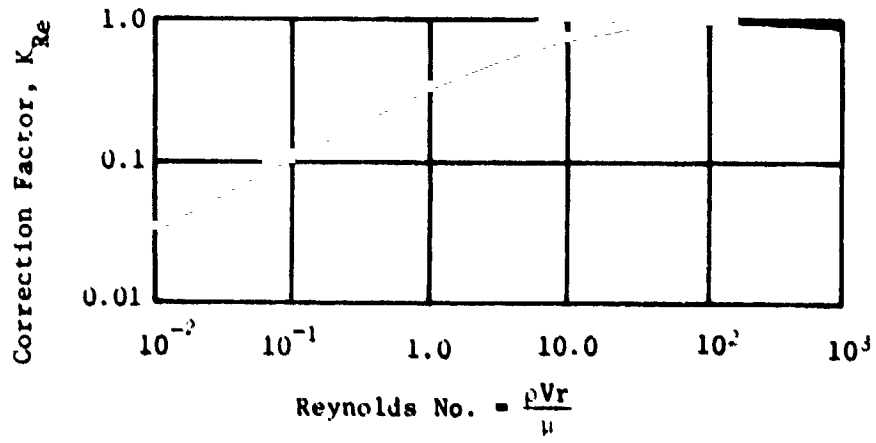

2-2b. *Effect of Reynolds Number (from Ref 7)*

Figure 2-2. Scaling Relationships

The subscript "p" refers to the full-scale tank, and the subscript "m" refers to the model. Therefore, equating Froude numbers:

$$\frac{V_p}{\sqrt{A_p r_p}} = \frac{V_m}{\sqrt{A_m r_m}} \tag{2-6}$$

Since velocity is proportional to the product of acceleration and time ($V = At$):

$$t_p = t_m \sqrt{\frac{A_m}{A_p}\frac{r_p}{r_m}} \quad , \text{seconds} \tag{2-7}$$

Equation (2-7) defines the time scaling for a selected geometrical scaling and the ratio of prototype (full scale) to model accelerations. It is independent of the liquid properties.

2.1.1 Geometric Scaling

Selection of model scaling was based on being able to simulate enough full-scale time to encompass the critical period during the RTLS separation sequence. This critical period was defined by NASA to be the time during which the propellant moves from its initial position to the front of the ET LOX tank. The required simulation time is approximately equal to the time required for an object to free fall the tank length (≈15 m). Based on the expected RTLS accelerations, the desired full scale simulation time varies from ≈10 s (for 0.03 g) to ≈14 s (for 0.015 g).

The scaling analyses for both the Phase I (drop tower) and Phase II (KC-135) test programs had to consider facility-imposed limits on the values of r_m, A_m, and t_m. A primary consideration was to maximize the reorientation forces (to facilitate measurement) while maintaining adequate full scale simulation time, t_p. To maximize forces, a large model size was desirable. For both test programs, the maximum model size permitted by the facility was selected as optimum. For drop tower, a 1/60th-scale (r_m/r_p) model was chosen, and for the KC-135 a 1/10th-scale model was chosen. An additional consideration was that a 1/10th-scale model was already in existence that could be modified for the test program.

To maximize the time scaling and reorientation forces, a large value of A_m is desirable; however, some practical limits exist. In the drop tower, large values of A_m reduce the test time, t_m, because the drop capsule is accelerated with respect to a drag shield and the travel distance is fixed. A value of $A_m = 0.09$ g is a practical upper limit that will still provide adequate test time (≈1.6 s). In the KC-135, A_m is limited to ≈0.2 g by operational considerations (A_m is actually a negative acceleration resulting in adverse wing loading on the KC-135).

Based on model sizes chosen and test acceleration limits, the full-scale time can be calculated. Table 2-1 tabulates the full-scale time simulated for each second of test time in the drop tower and KC-135 test programs. The tabulated values indicate that scaling is adequate to simulate the critical RTLS period ($t_p \approx 10$ to 14 s).

Table 2-1. TIME SCALING FOR THE DROP TOWER AND KC-135 TEST PROGRAMS

Test Program	r_p/r_m	A_m (g)	t_p/t_m*	
			A_p = 0.015 g	A_p = 0.030 g
Drop Tower	60	0.09	18.97	13.42
KC-135	10	0.1	8.16	5.77
KC-135	10	0.2	11.55	8.16

*Approximate values of t_m are as follows:

Drop Tower: $t_m \approx 1.6$ s

KC-135: $t_m \approx 20.0$ s

2.1.2 Test Liquid Selection

The properties of the test liquids enter into the scaling by assuring that Bond and Reynolds numbers are sufficiently large to meet the requirements for Froude number scaling. A very dense liquid helps make both the Reynolds and Bond numbers large, and also assures that the forces due to a given volume of liquid will be maximized. Low surface tension and viscosity are also desirable. Safety and compatibility with the plastic tank models were other considerations in choosing the test liquids.

For both test programs, several test liquids were chosen to evaluate the effects of viscosity. In the Phase I drop tower testing, three liquids were used: FC*-43, FC-114B2, and HEXANE. Due to its ideal properties, the primary test liquid for this phase was FC-114B2. The other two liquids were used in a limited number of tests to evaluate viscous effects.

Freon 113 (also known as Freon TF) was the primary liquid used in the Phase II KC-135 testing. Freon 113 has a high density, low surface tension and viscosity, and does not pose any hazards. Freon 113 has a vapor pressure of 3.7 N/cm^2 (5.3 psia) at 20°C, which is usually not a problem at normal temperatures. However, problems of rapid vaporization were encountered when the Freon and model tank were at temperatures around 30°C.

---

*FC = Fluorocarbon

To evaluate the influence of viscous effects, a second Phase II test liquid with a higher viscosity was desired. This was achieved by using water to which a thickening agent had been added. Methocel, a methyl cellulose thickener made by Dow Chemical, was used to increase the water viscosity. Type F4M Methocel was used in the proportion of 2.1 grams per liter of water to increase the viscosity from its normal 1.0 to 5.1 cp. This gave a factor of 10 increase in the kinematic viscosity over the Freon. An antifoam emulsion (SWS-211 made by SWS Silicones Corp.) was added to the mixture to reduce foaming.

The final criterion for test liquid selection was that the Bond number and Reynolds number be sufficiently large to permit Froude numbers scaling. Table 2-2 delineates the liquid parameters for the full-scale ET and the Phase I and Phase II test programs.

TABLE 2-2. FULL SCALE AND TEST LIQUID PARAMETERS

System	Density (gm/cm^3)	Surface Tension (dynes/cm)	Viscosity (cp)	Acceleration (g)	Bo $\left(\frac{\rho Ar^2}{\sigma}\right)$	Re $\left(\frac{\rho Vr}{\mu}\right)^*$
LOX (-183°C) Full-Scale ET [8,9]	1.14	13.5	0.195	0.015 0.030	2.19×10^5 4.39×10^5	5.17×10^7 7.31×10^7
Phase I: 1/60th Scale Drop Tower Tests						
- FC-114B2 (20°C) [10]	2.18	18.8	0.75	0.09	4.49×10^4	1.35×10^5
- FC-43 (20°C) [11]	1.91	16.7	6.50	0.09	4.91×10^3	1.36×10^4
- HEXANE (20°C) [8,9]	0.66	18.4	0.33	0.09	1.54×10^4	9.30×10^4
Phase II: 1/10th Scale KC-135 Tests						
- FC-113 (25°C)†	1.57	20.1	0.67	0.1 0.2	1.35×10^4 2.70×10^4	1.69×10^5 2.39×10^5
- water/ Methocel†	0.998	47.9	5.05	0.1 0.2	3.60×10^3 7.20×10^3	1.42×10^5 2.01×10^5

*To calculate Re, the value to be used for velocity, V, must be defined. A representative velocity is the free-fall velocity based on tank length, which approximates the maximum velocity achieved by the liquid as it first moves the length of the tank.

†Properties were measured using actual samples of the test liquids.

As shown by the values in Table 2-2, the basic requirements for Froude number scaling were met for both test programs. In addition, the magnitudes of Bond and Reynolds numbers for FC-113 in the KC-135 test program were within an order of magnitude of the values for the full-scale ET.

The primary objective of the Phase II test program was to allow closer approximation of full-scale conditions, to validate the scaling approach. The dimensionless parameters for the aircraft tests were significantly greater (closer to full scale) than those for the drop tower tests. Phase II testing increased Bond number by approximately two orders of magnitude and Reynolds number by one order of magnitude. As Bond number increases, the effects of surface tension decrease, resulting in more surface breakup.

In the drop tower tests, the Bond number was low enough to produce some surface cohesiveness, which was far less evident in the KC-135 tests. When reorientation occurs at large Bond numbers ($>10^3$), the liquid motion may take the form of "rain" (primarily during axisymmetric reorientation). However, with off axis acceleration components, such as those present during RTLS separation, the lateral acceleration component acts to hold the liquid mass together as it traverses the tank wall. This type of motion has been demonstrated at the Bond number up to 6×10^3 under both axisymmetric and off axis reorientation conditions [Ref 12].

In summary, scaling considerations and subsequent comparisons of drop tower and KC-135 test results, indicate that the test results should be representative of liquid reorientation during full scale RTLS separation.

2.2 TEST SYSTEM DESCRIPTION

2.2.1 Phase I Test Program

The Phase I test program employed Martin Marietta's Drop Tower Test Facility. This facility was developed under numerous prior test programs in order to simulate low-g environments. Only minor modifications were required to perform Phase I testing.

Test Hardware - The Martin Marietta drop tower test system consists of a drag shield that contains a drop capsule on which a test module is mounted. Figure 2-3 is a schematic showing the major components of the drop test system. Figure 2-4 is a photograph of the drop test facility. The system provides a maximum of $\simeq 2$ s of test time. The drag shield is released from a height of 23 m ($\simeq 75$ ft), and is decelerated by landing in a bin of wheat at the end of the free fall period.

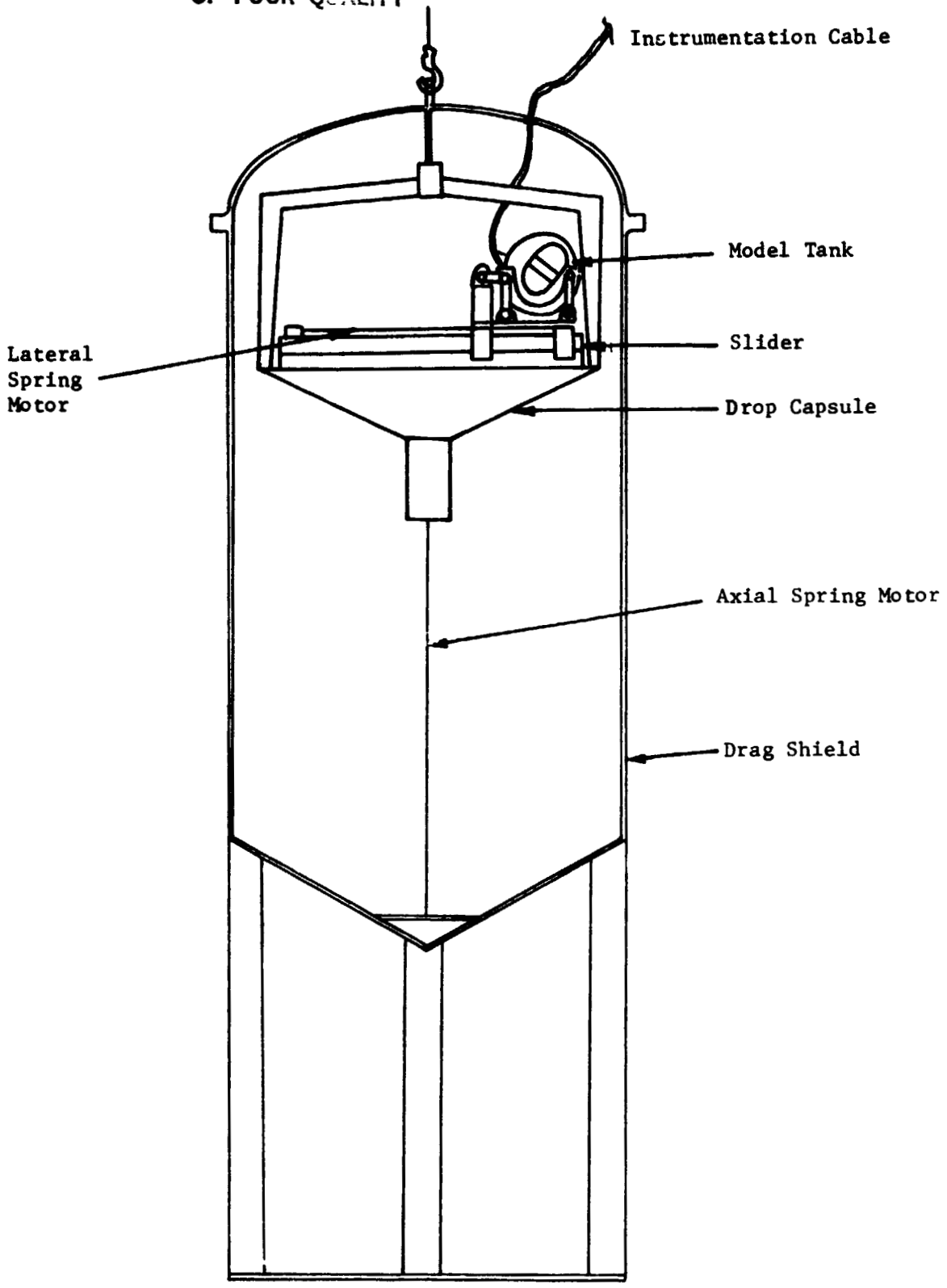

Figure 2-3. Drop Capsule Schematic

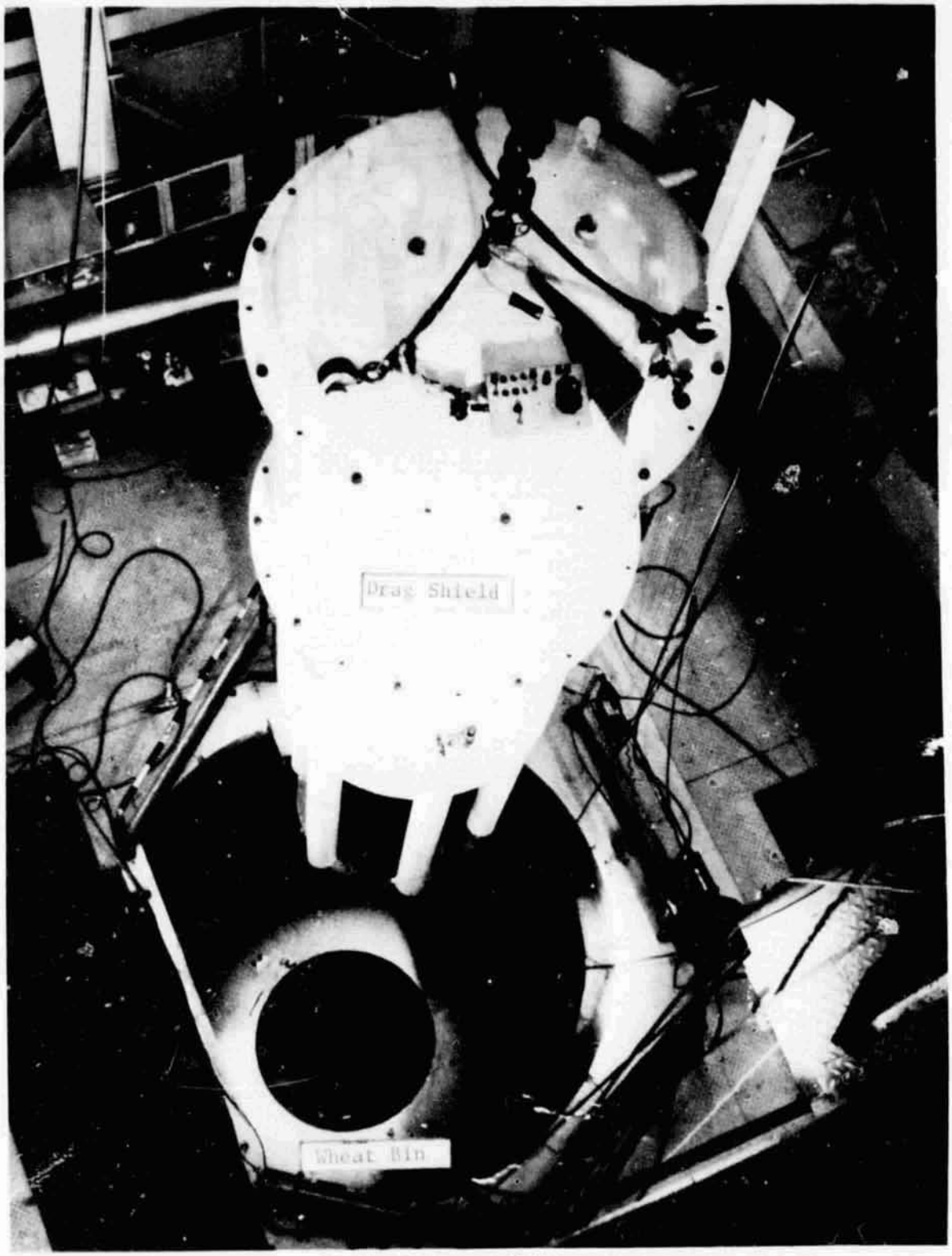

Figure 2-4. Drop Tower Test Facility

Figure 2-5 is a photograph of the test module that was used in the Phase I test program. The test module is shown mounted on the drop capsule. It consisted of a model tank, force measurement module, and a slider mechanism. Figure 2-6 is a closer view of the measurement module in which the model tanks were supported. The measurement module supported the tanks on three crystal load cells, and allowed for tank rotation to achieve various initial liquid orientations. The calibration fixture (Fig. 2-6) was used to calibrate the load cell system. The load cells (Kistler model 912) were fully capable of measuring small reorientation forces (on the order of 0.4 N, 0.1 lb) and surviving impact decelerations at the end of the test.

Two 1/60th-scale replicas of the full scale ET LOX tank were constructed; one with no internal baffles (Fig. 2-7), the other with both slosh and antivortex baffles (Figs. 2-8 and 2-9). Although the baffles were simplified somewhat, compared to the full-scale LOX tank, the overall geometry was accurate. Spacing between the baffles and tank wall was generally representative of the actual LOX tank. However, the model did not reflect the "zero gap" between the wall and baffles that occurs at two of the baffle stations in the full-scale tank. This had some effect on reorientation for very small fill volumes, allowing the liquid to flow primarily behind the baffles.

Biaxial accelerations were applied to the model tanks by using linear spring motors that: (1) accelerated the measurement module laterally on the slider, and (2) accelerated the drop capsule axially with respect to the drag shield (Fig. 2-3). The drop capsule was automatically released from the drag shield at drop initiation. Three force links (containing the load cells) allowed forces within the plane of the applied accelerations to be measured. Bearings at each end of the links permitted only forces along the link axis to be measured. Three flexures, perpendicular to the plane of the force links, prevented any out-of-plane tank motion. These flexures were sized (by stiffness) such that they would not significantly alter the forces measured by the load cells. The design of the test system resulted in essentially planar reorientation. Out-of-plane motion and forces were insignificant.

As mentioned in Chapter 1.0, some tests included the simulation of inflow into the tank from the LOX line. This was achieved by using a spring-operated piston/reservoir controlled by a solenoid valv . Flow rate was controlled by a metering valve. The tests inflowed a volume of liquid approximately equivalent to totally draining the LOX feedline. However, an analysis [Ref 3] has indicated that, conservatively, only about 5% of the liquid in the line will drain into the tank during RTLS. This volume (≈0.05% of the LOX tank volume) should have a negligible effect on propellant reorientation.

The liquid motion was filmed using a 16 mm Milliken DBM-3a camera, mounted on the slider, at a frame rate of 200 frames per second (fps). Test accelerations were varied by changing the magnitude of

Figure 2-5. Drop Tower Test Module

Figure 2-6. Force Measurement Module with Calibration Fixture Installed

Figure 2-6

Figure 2-7. Unbaffled Drop Tower Tank (1/60th Scale)

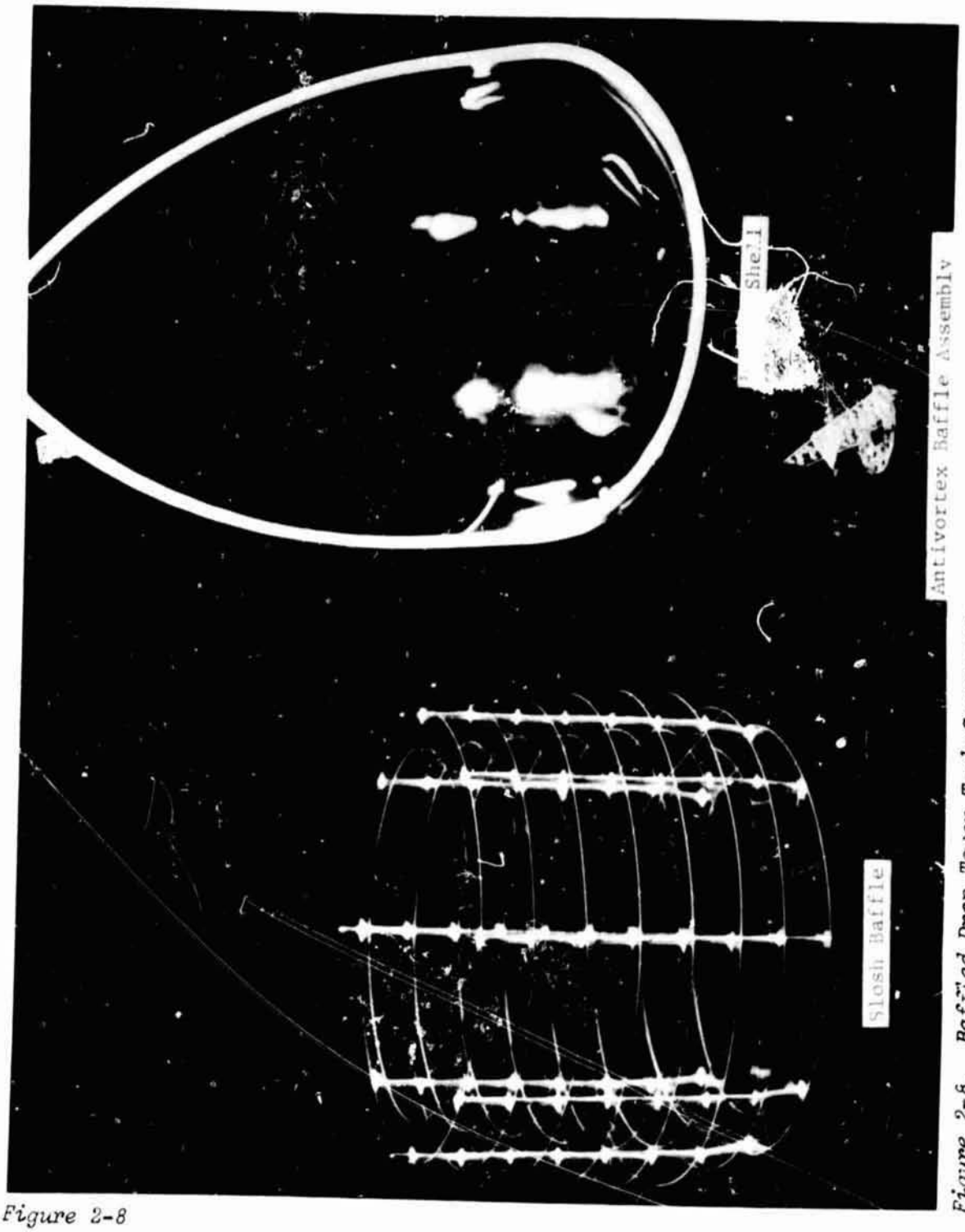

Figure 2-8. Baffled Drop Tower Tank Components

Figure 2-8

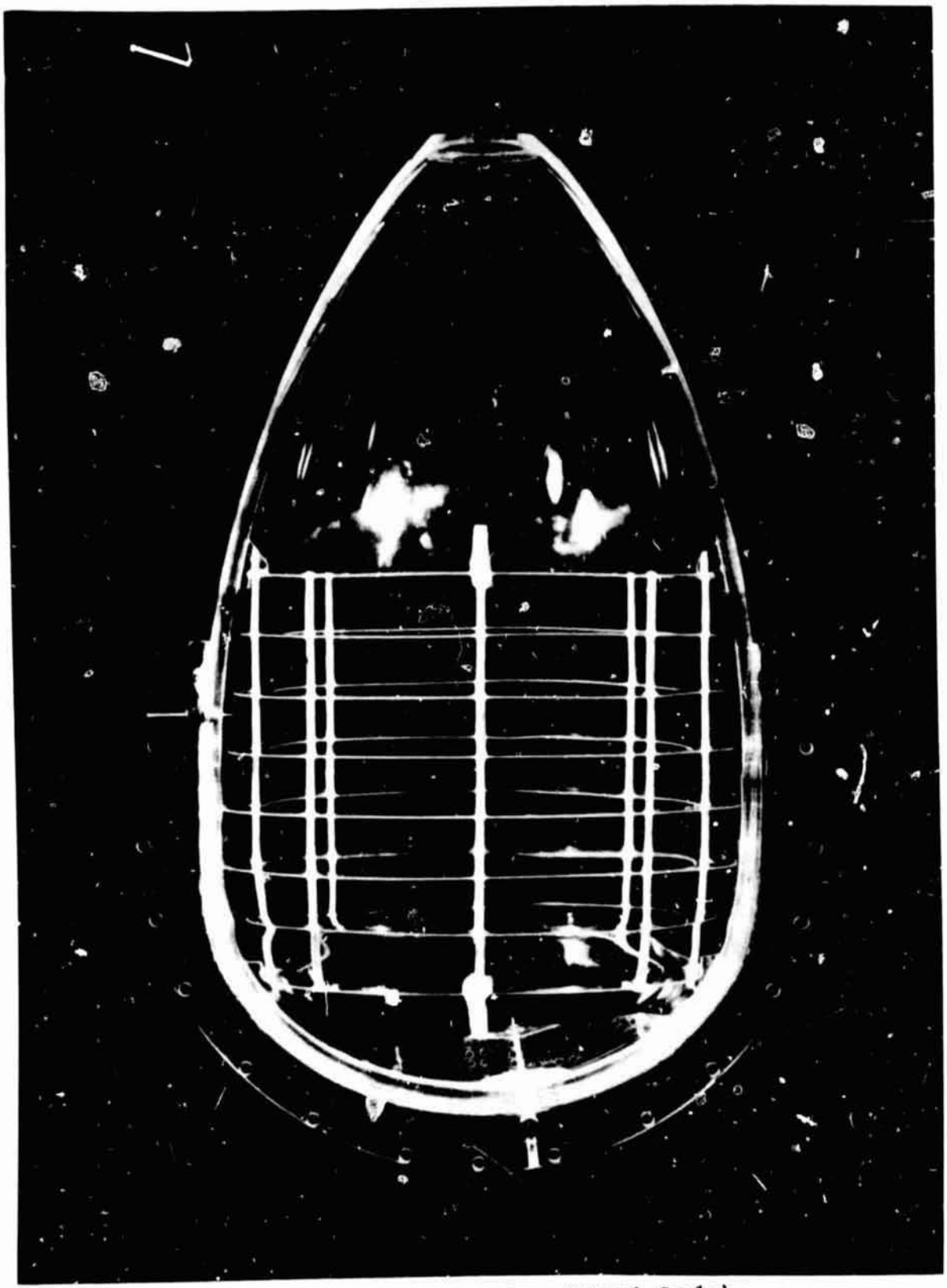

Figure 2-9. Baffled Drop Tower Tank (1/60th Scale)

the spring motors. The lateral acceleration applied to the tank was calculated based on lateral travel as a function of time. Lateral travel was determined by a scale mounted in view of the camera and time was based on camera frame rate. Average axial acceleration was calculated by kinematic equations for the two bodies (drag shield, drop capsule); given body masses, applied forces, and travel distance of the drop capsule relative to the drag shield. The travel time of the drop capsule relative to the drag shield was based on the load cell time histories.

Test Conditions - Test conditions were chosen to provide reorientation representative of that expected during RTLS separation. Table 2-3 presents the expected ET accelerations due to aerodynamics during RTLS: (1) during mated coast, and (2) after orbiter/ET separation.

Table 2-3. EXPECTED ET RTLS ACCELERATIONS

RTLS Phase	ET Acceleration (Orbiter Coordinates*)	
	$\ddot{X}_o$ (g)	$\ddot{Z}_o$ (g)
Mated Coast	0.045	-0.005
After Separation	0.03	-0.03
*See Figure 2-1		

In the drop tower, lateral and axial accelerations were applied to the tanks. Figure 2-10 shows the relationship between orbiter coordinates and the test-applied accelerations. These accelerations are related to orbiter coordinates as follows.

$$A_{axial} = \ddot{X}_o \cos\gamma + \ddot{Z}_o \sin\gamma \qquad (2\text{-}8)$$

$$A_{lat} = -\ddot{Z}_o \cos\gamma + \ddot{X}_o \sin\gamma \qquad (2\text{-}9)$$

The desired ratio of A_{axial} to A_{lat} can be calculated for the RTLS accelerations of Table 2-3 (γ assumed 13 deg) using equations (2-8) and (2-9).

Mated coast: $A_{axial}/A_{lat} = 1.64$

After Separation: $A_{axial}/A_{lat} = 0.62$

Due to drop tower limitations and the desire to maximize test times and force levels, use of these actual ratios was not feasible. A value of $A_{axial} = 0.09$ g has been found optimal from test time and force level considerations in previous test programs. Choice of a value for A_{lat} was based on the desire for a test time (t_m) of about 1.6 s (Table 2-1). Because of the available lateral slider

travel, lateral accelerations greater than ≈0.03 g will reduce the test time below 1.6 s. Consequently, the majority of the tests used the ratio:

$$A_{axial}/A_{lat} = \frac{0.09}{0.03} = 3.0$$

Although this approach did not duplicate actual expected ratios of acceleration components, it did produce liquid motion representative of full-scale conditions, which was the primary objective. As long as there is a lateral component of acceleration, the liquid will move along the tank walls rather than through the tank center. Changing the ratio of accelerations primarily changes the final equilibrium position for the liquid and the rate of motion. The basic character of the motion will remain the same. The test results supported this approach.

The test matrix was structured such that the effect of various parameters could be evaluated. Table 2-4 presents the actual test matrix, including calculated acceleration values.

Data Reduction - To facilitate correlation with analytical results, load cell data were recorded and later transformed to a tank centered coordinate system (Fig. 2-10). Digitized data were smoothed to remove test fixture and camera-induced noise with a moving average digital low pass filter set at 10 Hz. An investigation was conducted to insure that filtering did not reduce peak force levels.

Data interpretation and correlation had to consider the fact that forces due to the tank and support structure mass were imbedded in the load cell data along with liquid reorientation forces. Another consideration was the large transient encountered at drop initiation when the tank transitioned from normal gravity to low g test accelerations. To overcome these problems during analytical correlation, the analytical simulations account for actual test conditions (including loads due to structural mass). Reference [3] details the actual data reduction process.

2.2.2 Phase II Test Program

NASA's KC-135 "zero-g" test aircraft was used in the Phase II test program to produce low-g environments representative of RTLS separation. The test fixture and associated hardware were fabricated and assembled by Martin Marietta and NASA JSC personnel. Both organizations participated in test conduct and data reduction. The objective of the Phase II test program was to more closely simulate the Bond and Reynolds numbers expected during full-scale RTLS separation to validate the scaling approach of Section 2.1.

Test Hardware - The test fixture was a scaled up version of the Phase I drop tower measurement module. The fixture consisted of a box frame that was supported from a base structure by three strain gage

TABLE 2-4. DROP TOWER TEST MATRIX

Test	Test # Liquid	Acceleration (g)		γ^o	LOX Outflow	Baffled Tank	% Fill	Parameter of Interest
		A_{axial}	A_{lat}					
1	1	0.090	0.029	13	Yes	No	2	LOX Outflow
2	2	0.093	0.031	13	Yes	No	2	
3	1	0.093	0.031	13	Yes	Yes	2	
4	2	0.092	0.032	13	Yes	Yes	2	
5	1	0.091	0.030	13	No	No	10	Liquid Viscosity
6	2	0.091	0.029	13	No	No	10	
7	1	0.092	0.032	13	No	Yes	10	
8	2	0.092	0.032	13	No	Yes	10	
9	1	0.090	0.031	13	No	No	2	
10	2	0.092	0.032	13	No	No	2	
11	1	0.092	0.034	13	No	Yes	2	
12	2	0.092	0.033	13	No	Yes	2	
13	1	0.088	0.014	13	No	Yes	2	A_{lat}
14	2	0.088	0.013	13	No	Yes	2	
15	1	0.089	0-0.055*	13	No	No	2	Change in A_{lat}
16	1	0.091	0-0.053	13	No	No	10	
17	1	0.090	0-0.055	13	No	Yes	2	
18	1	0.091	0-0.052	13	No	Yes	10	
19	1	0.093	0.033	13	No	Yes	5	% Fill
20	1	0.088	0.032	13	No	Yes	15	
21	1	0.091	0.032	13	No	No	5	
22	1	0.093	0.032	13	No	No	15	
23	1	0.091	0.034	30	No	Yes	2	$\gamma=30^o$
24	1	0.092	0.033	30	No	No	2	
25	1	0.091	0.031	30	No	No	10	
26	1	0.088	0.031	30	No	Yes	10	
27	1	0.043	0.033	0	No	Yes	2	$\gamma=0^o$ A_{axial}
28	1	0.043	0.032	0	No	No	2	
29	1	0.050	0.038	0	No	Yes	10	
30	1	0.042	0.032	0	No	No	10	
31	1	0.090	0.032	13	Yes$^\Delta$	Yes	2	Special Tests
32	3	0.090	0.032	13	No	No	10	

# Liquid 1 = FC114B2
2 = FC43
3 = HEXANE

* Lateral slider delayed = 0.5 s

Δ Tank outlet increased by factor of 2, flow rate reduced

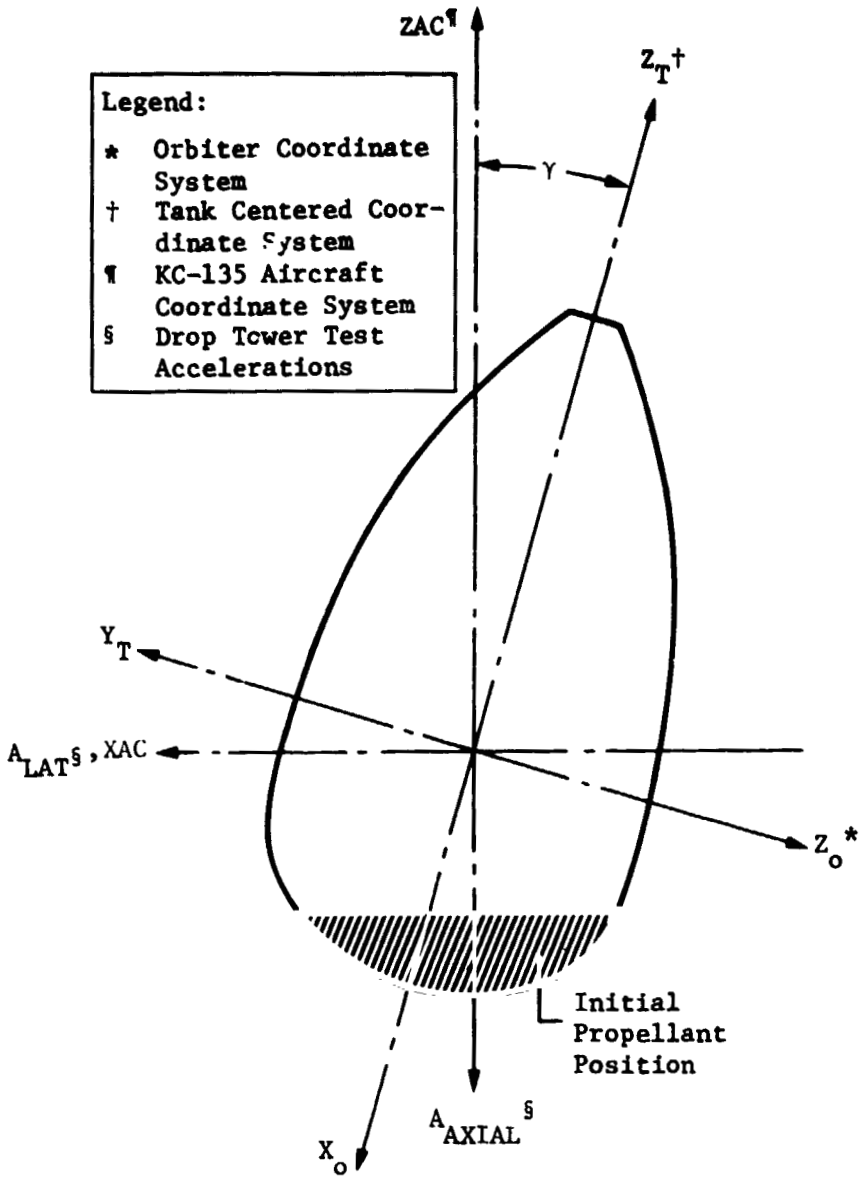

Figure 2-10. Orientation of Tank Coordinate Systems

load cells (Interface, Inc.). The tank was mounted to the box frame at two pivots, allowing the tank to be tilted at 0, 13, and 30° (Y).

The load cells measured forces in the plane of the tank parallel with the aircraft longitudinal axis. Rod end bearings were used to connect the load cells to the base and box frame. Four flexures prevented out-of-plane movement of the tank and box frame. These were sized, by stiffness, such that they would not significantly affect load cell measurements.The tank was a 1/10th scale model of the ET LOX tank. It's overall length was 151 cm (4.95 ft) and the barrel section diameter was 84 cm (2.76 ft). The tank, which was fabricated of transparent acrylic plastic, was made in two sections joined with bolted flanges at the junction of the lower dome.

The tank contained removable baffles. The antivortex baffle was made of transparent acrylic plastic. The slosh baffles were fabricated as an integral unit from aluminum. Both the slosh and antivortex baffles were geometric scale replicas of the full-scale tank. However, the slosh baffles lacked details of the supports between baffles (unimportant in the test program). Installation of the slosh baffles accurately represented the baffle-to-wall spacing of the full-scale LOX tank.

Figures 2-11 and 2-12 show the tank mounted in the fixture at the 13- and 30-deg orientations respectively. Figure 2-13 is a photograph of the test system including the instrumentation rack.

During a flight, the volume of test liquid in the tank was varied numerous times. Transfer of the test liquid between the model tank and a supply tank was performed with an electrical pump. Figure 2-14 is

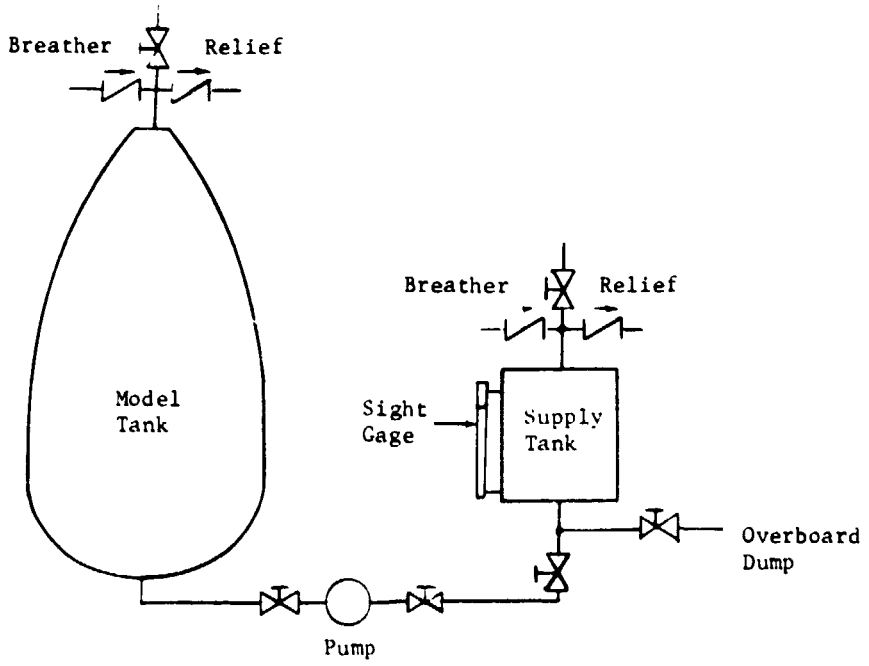

Figure 2-14. Plumbing Schematic

a plumbing schematic of the test system. Interchanging lines at the valves adjacent to the pump permitted the direction of flow to be reversed for tank draining. A calibrated sight gage on the supply tank was used to determine the volume of liquid transferred to the tank.

The plumbing system employed check valves [0.7 N/cm^2 (1 psi) cracking pressure] as breather and relief valves. These valves were intended to prevent the pressure differential between the tank and cabin from exceeding +0.7 N/cm^2, as aircraft altitude varied. However, on the second flight (with the baffles installed) when Freon 113 (1% volume) was used as the test liquid, rapid vaporization occurred when the cooler Freon contacted the warm tank walls and baffles. Due to the relatively long test time (≈20 s), the Freon collected over the relief valve inlet (top of tank) and sufficient tank venting was not possible. This resulted in tank failure (Fig. 2-15).

The tank was repaired and a large vent port was added in the side of the tank. A flexible rubber disk closed the port, but any increase in tank pressure caused it to open. This permitted essentially unrestricted release of vapor, since the liquid was not usually oriented near the port. This design functioned satisfactorily, preventing any further problems with tank pressure.

As part of the repair, the flange on the upper part of the tank was replaced with an aluminum ring that was glued and bolted to the original plastic tank section. Figure 2-16 is a photograph of the repaired tank.

The motion of the liquid was recorded with 16 mm Milliken motion picture cameras operating at 60 fps. Three camera positions were used for complete coverage. A three-axis accelerometer measured applied accelerations. Load cell data were output on a chart recorder for quicklook data evaluation and were also recorded on magnetic tape for subsequent data reduction. The acceleration time histories were also recorded. Synchronization between the film and recorded data was provided by a bilevel signal. When a push button was depressed, lamps were illuminated in the camera field of view, and the change in level of a dc electrical signal was tape recorded. Figure 2-17 details the test configuration in the KC-135.

Test Conditions - Low-g accelerations were applied to the tank by slightly modifying the normal KC-135 parabolic flight path. During a typical test, the following flight profile was followed. The parabola was initiated by diving the KC-135 and then pulling up to achieve the desired airspeed and angle of attack for the parabola. During the pull up, the vertical acceleration, which was perpendicular to the aircraft floor (ZAC, Fig. 2-11), reached levels of +1.8 to +2.0 g.

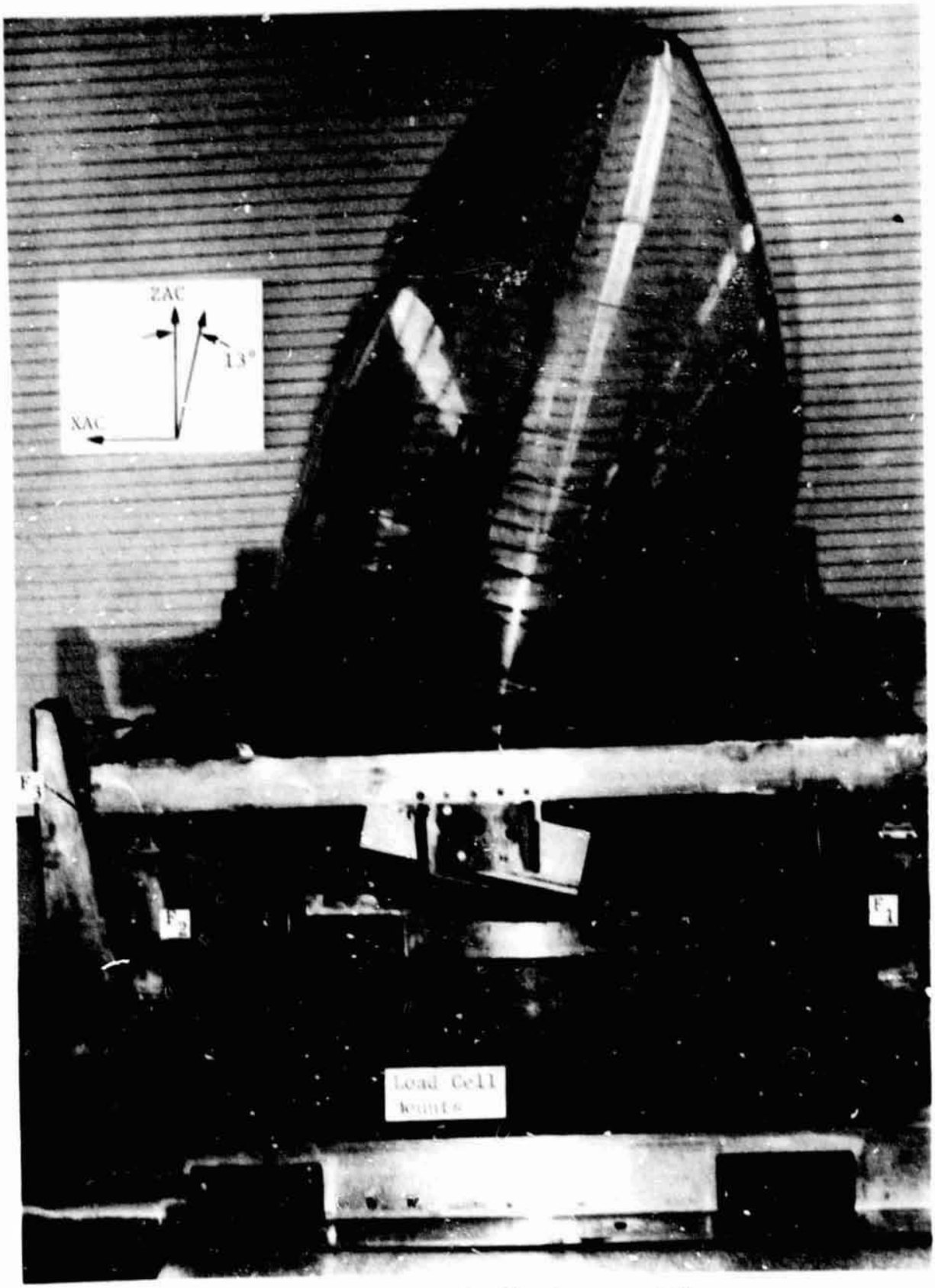

Figure 2-11. 1/10th-Scale Tank Tilted to γ = 15°

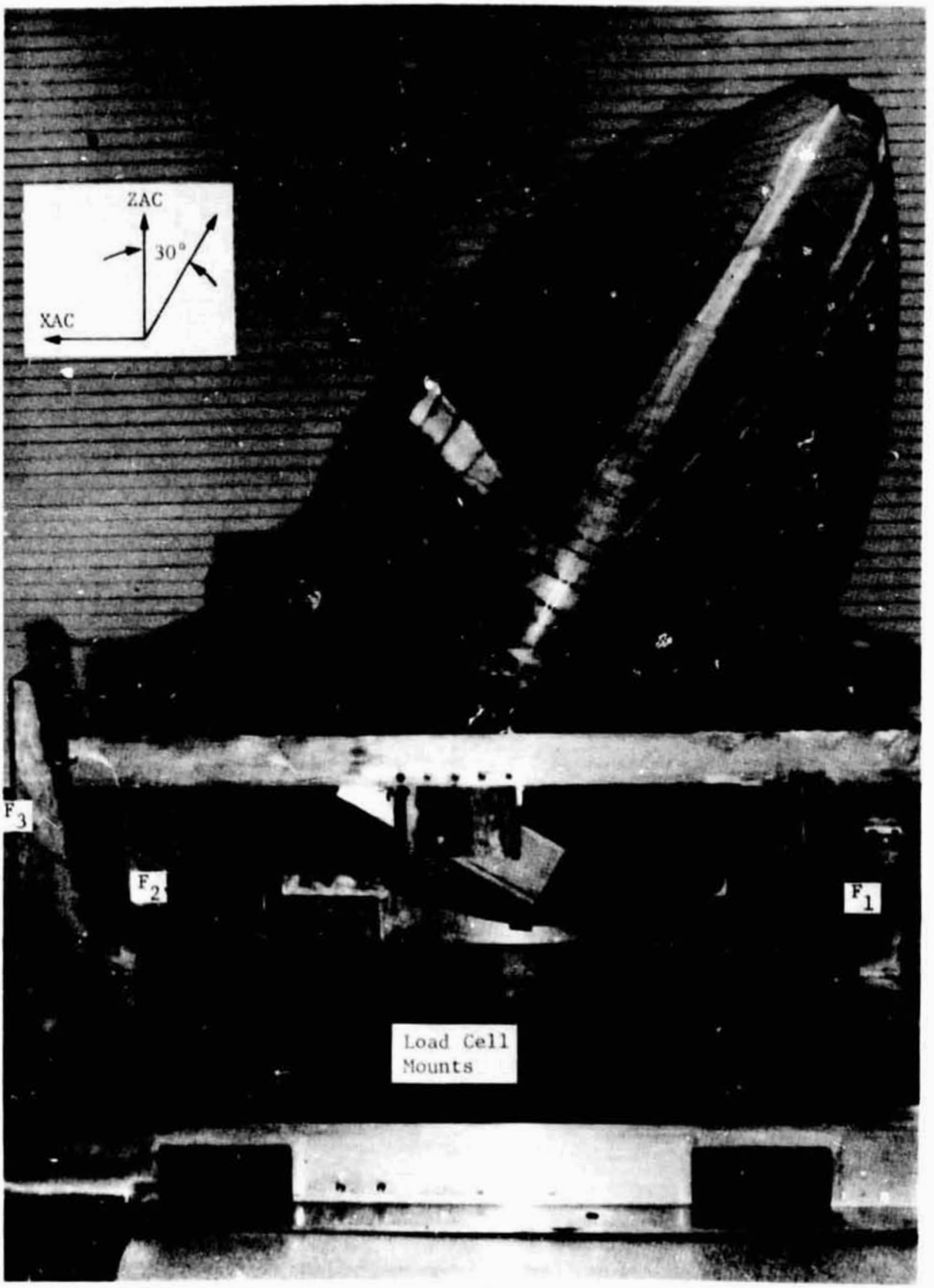

Figure 2-12. 1/10th-Scale Tank Tilted to γ = 30°

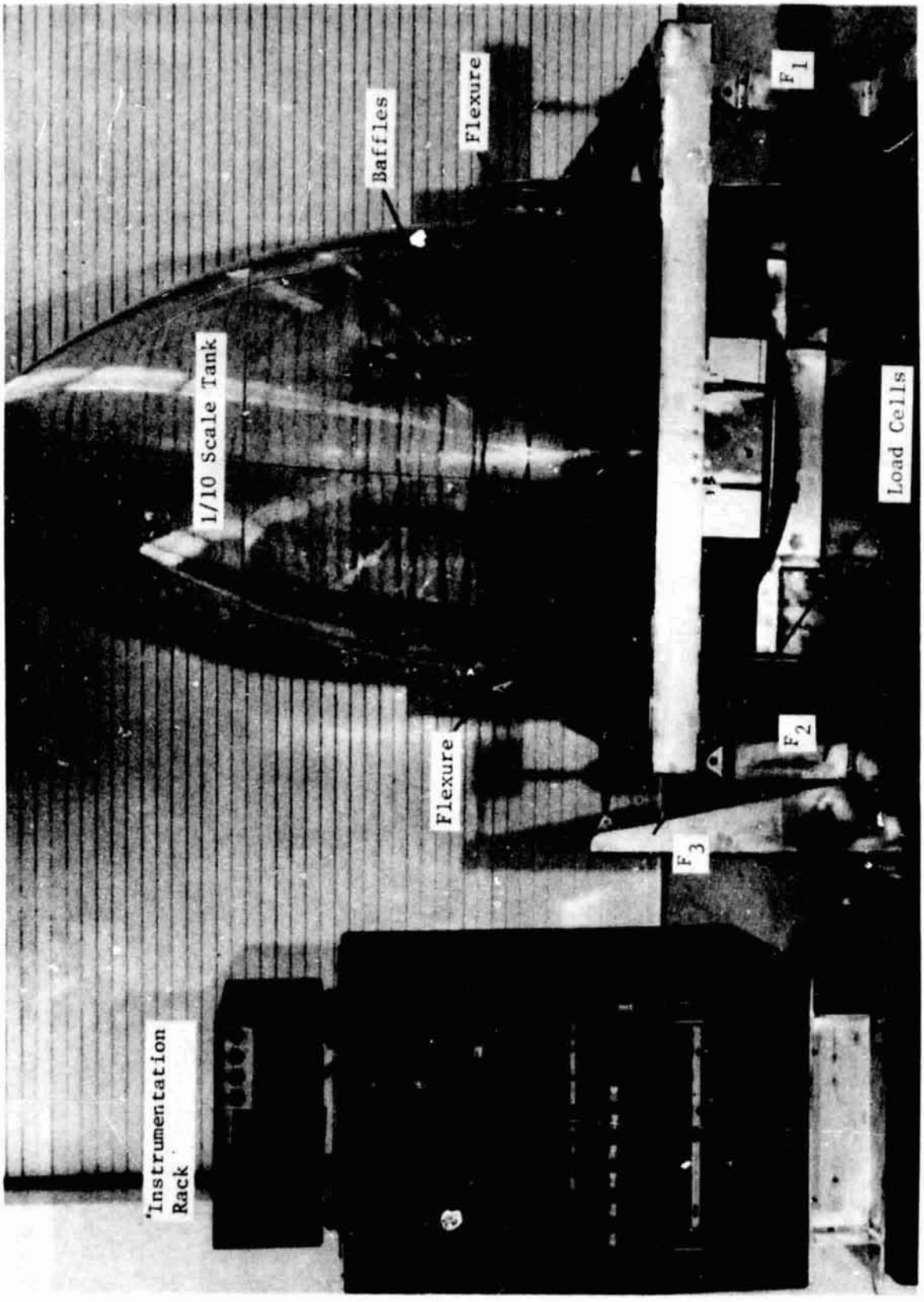

Figure 2-13. 1/10th-Scale LOX Tank Model, Test Fixture and Instrumentation Rack

Figure 2-13.

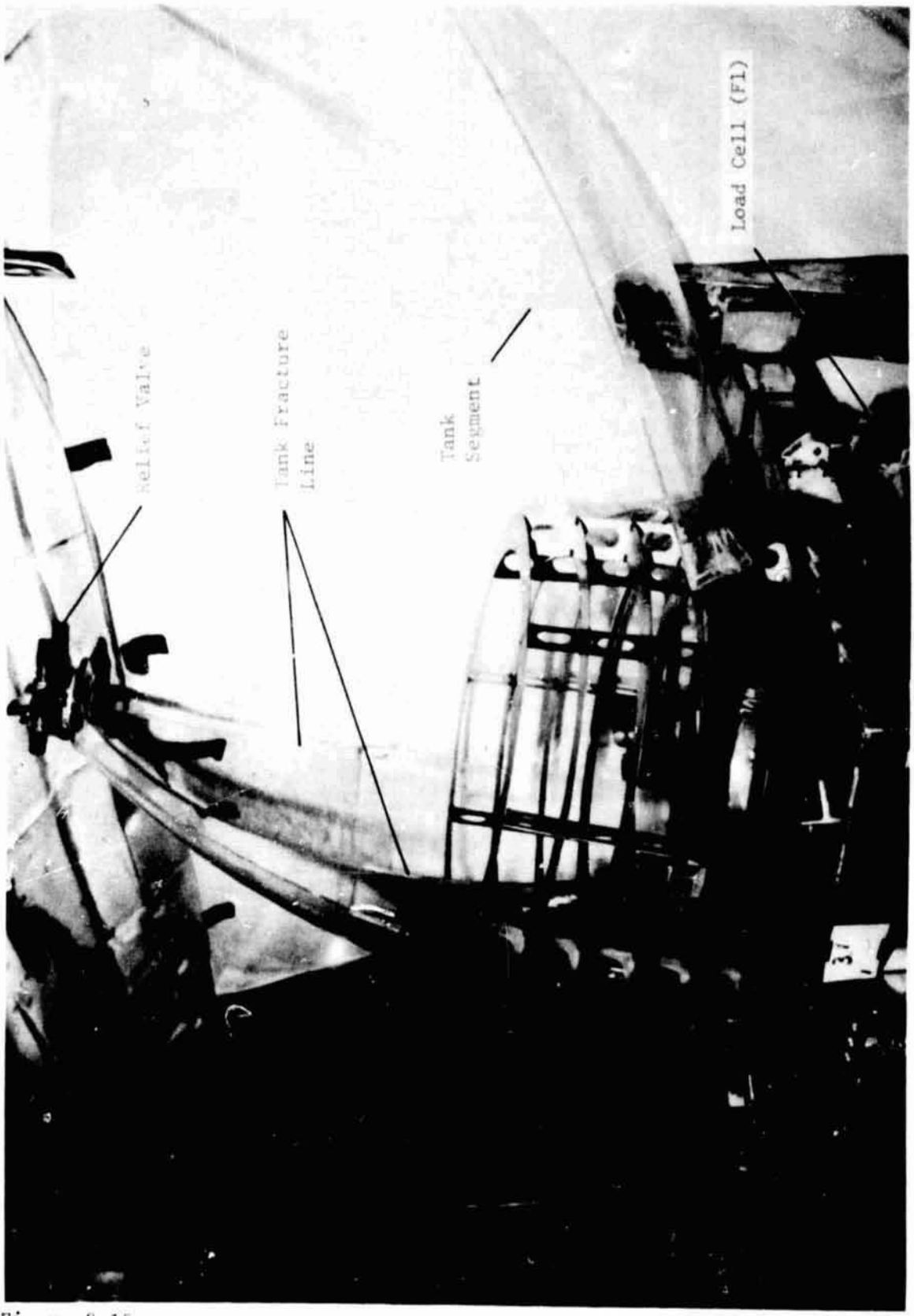

Figure 2-15. 1/10th -Scale Tank after Failure due to Over Pressurization

Figure 2-16. Repaired 1/10th-Scale Tank

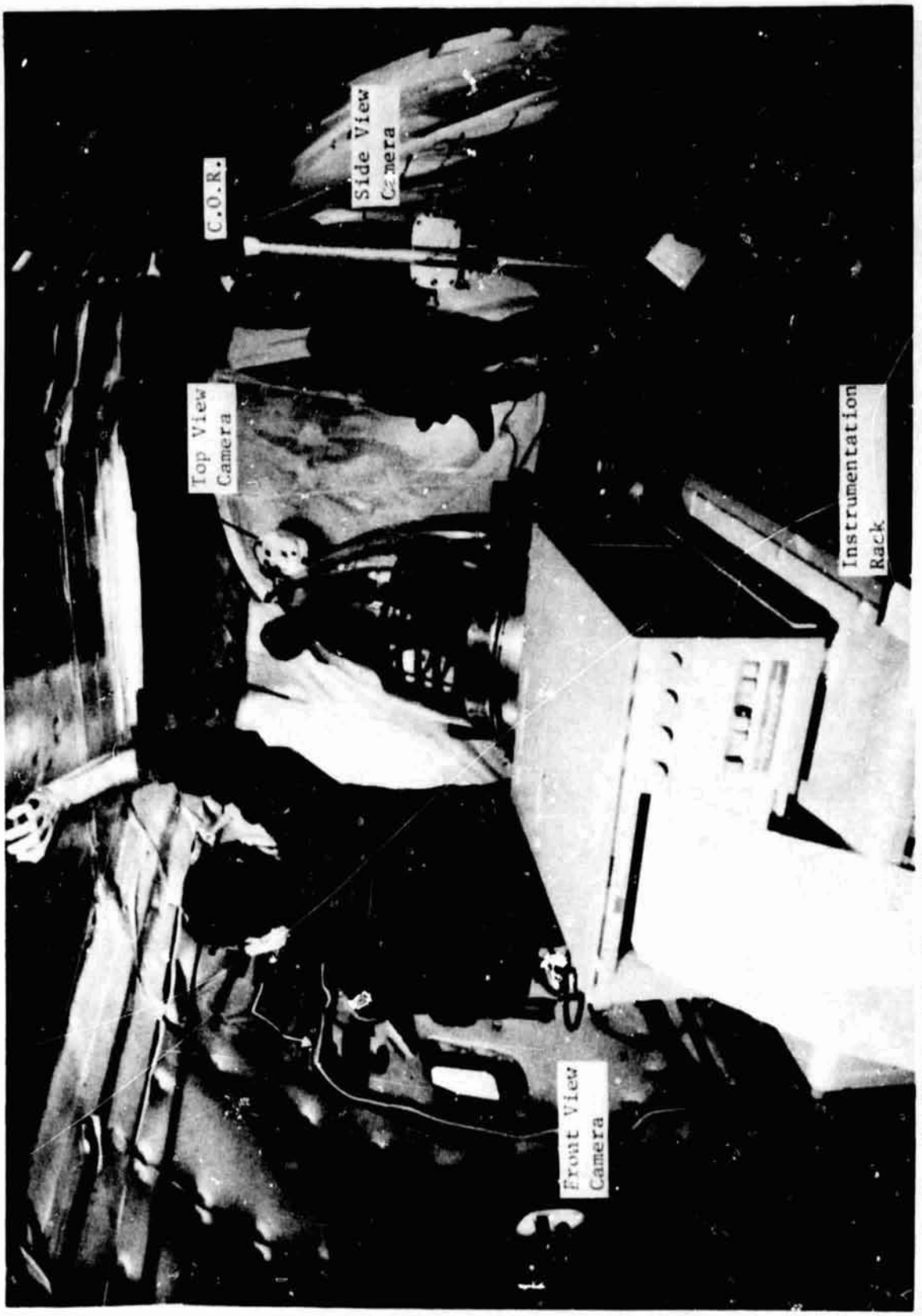

Figure 2-17. KC-135 Test Configuration

This acceleration acted to settle the liquid at the bottom of the tank, duplicating the propellant location in the ET before MECO. As the aircraft entered the parabolic arc, there was a rapid transition (≈2 s) from the high positive acceleration to the negative low-g test acceleration. During the test program, accelerations of ≈-0.1 g and ≈-0.2 g (ZAC) were used. The lateral component (XAC) was obtained by adjusting the throttles so that the aircraft continued to accelerate as it entered the parabola.

During some tests, out-of-plane (YAC) accelerations occurred. Because of the variability of the accelerations, approximately three tests were performed for each test condition and tests with out of plane (YAC) liquid motion or similar defects were discarded.

Test conditions, similar to those in Phase I, were selected to facilitate comparison of results. Table 2-5 delineates the Phase II test matrix. The test program included 30 test conditions (a total of 89 low-g parabolas). Four KC-135 flights were flown to accommodate configuration changes: baffle installation and removal, and test liquid.

Data Reduction - The data reduction process for Phase II was similar to that of Phase I. The analog flight tapes, including force and acceleration measurements, were digitized and converted to engineering units. Approximately 25 s of time encompassing each test were digitized. The load cell data were then resolved to the tank centered coordinate system (Fig. 2-10) for correlation with analyses. Reference [4] details the Phase II data reduction process.

2.3 SUMMARY OF TEST RESULTS

This section is a summary of the test results from both Phase I and Phase II. Observations on the character of the liquid motion, as well as comparisons of measured force data are presented. More detail on the test results can be found in References [3] and [4].

In general, it was found that the drop tower provides a more controlled test environment. Test conditions are repeatable and acceleration environments can be accurately specified. Although liquid reorientation forces in the drop tower are small, they are measurable, and photographic coverage is excellent.

TABLE 2-5. KC-135 TEST MATRIX

Test Number	Test Liquid	Baffles	Acceleration ΣAC, g	Orientation, γ, deg	Fill Volume, %*
1.0	Empty	No	-0.1	13	0
1.1	Freon 113	↓	-0.2	↓	5
1.2	↓	↓	↓	↓	10
1.3	↓	↓	↓	↓	15
1.4	↓	↓	-0.1	↓	5
1.5	↓	↓	↓	↓	10
1.6	↓	↓	↓	↓	15
2.1	↓	Yes	-0.1	↓	1
2.2	↓	↓	↓	↓	5
2.3	↓	↓	↓	↓	10
2.4	↓	↓	↓	↓	15
2.5	↓	↓	-0.2	↓	1
2.6	↓	↓	↓	↓	3
2.7	↓	↓	↓	↓	10
2.8	↓	↓	↓	↓	15
3.1	↓	↓	↓	30	1
3.2	↓	↓	↓	↓	5
3.3	↓	↓	↓	↓	10
3.4	↓	↓	↓	↓	15
3.5	↓	↓	↓	0	10
3.6	↓	↓	↓	0	5
4.1	Water	↓	-0.1	13	2
4.2	↓	↓	↓	↓	5.5
4.3	↓	↓	↓	↓	10
4.4	↓	↓	↓	↓	16
4.5	↓	↓	↓	↓	25
4.6	↓	↓	-0.2	↓	2
4.7	↓	↓	↓	↓	5.5
4.8	↓	↓	↓	↓	10
4.9	↓	↓	↓	↓	16

*Actual Flight Values.

Testing in the KC-135, on the other hand, provides some special problems. Acceleration environments are quite variable and depend substantially on pilot technique. Because of the large transients at the beginning and end of a parabola, force resolution is still a problem. Instrumentation must accommodate the large transients yet still be sensitive enough to measure the reorientation forces. The large transient accelerations (on the order of 2 g) dictate a "beefy" test fixture that partially obscures photographic coverage. However, the KC-135 does provide for substantially longer full-scale simulation time than the drop tower. In addition, Bond and Reynolds numbers are much closer to those expected in the full-scale ET.

A comparison of the KC-135 and drop tower test data [Ref 4] resulted in the conclusion that the general character of the liquid reorientation was the same in the two test programs. Although some minor differences were evident (e.g., more surface breakup in the KC-135 due to higher Bond number), the bulk motion of the liquid was similar. Reference [4] also presented a comparative analysis between the drop tower and KC-135 data, which demonstrated the validity of the time scaling analysis of Section 2.1.

Analytical correlations (Chap. 3.0) to both the KC-135 and drop tower test data, also validate the scaling approach. The analytical model is based on the premise that Froude number scaling is valid.

The following paragraphs present some observations on the influence of selected parameters varied during the two test programs. Only drop tower force time histories are presented for comparison. The variability of KC-135 accelerations makes it difficult to directly compare force time histories.

2.3.1 Unbaffled Tank

Liquid reorientation in the unbaffled tank was well behaved. In all cases, the biaxial acceleration caused the liquid to reorient along the tank wall. Previous test programs [Ref 14] have demonstrated that the liquid will reorient along the tank wall, even for purely axial accelerations, if the tank is tilted as little as 1 deg with respect to the axial acceleration vector. During drop tower testing, a wave formed in the liquid center early in the test, indicating a tendency for the liquid to traverse the tank center. This wave, generally called a Taylor instability, forms because the motion of the liquid along the tank wall lags the bulk liquid motion produced by acceleration forces. These instabilities, which were generally short lived, rapidly joined the flow along the wall. This instability was not as evident in the KC-135 tests due to the larger Bond number and the generally larger lateral acceleration components.

Figures 2-18 through 2-25 contain single frame photographs from the high speed drop tower and KC-135 movies. The discrete time of each frame, from test initiation, is noted. These figures will be discussed in the following paragraphs.

Effect of Fill Volume - Fill volume did not influence the general character of the liquid motion. Figures 2-18 through 2-20 contain single frame photographs from the high speed drop tower movies for fill volumes of 2, 15, and 10%, respectively (FC-114B2). In general, a liquid film led the bulk liquid motion around the tank. In the case of the 2% fill volume, the majority of the liquid was distributed in the film. The leading edge of the liquid, for some fill volumes, completely circulated the tank. However, the majority of the liquid began to decelerate and collect after passing through the tank's ogive dome. With a longer test time, the liquid would have collected and eventually reached an equilibrium position as determined by the acceleration vector.

The ogive dome of the ET LOX tank trapped the liquid as it passed through, especially for larger fill volumes. The general reorientation character was one of filling and then emptying the dome. However, at the smaller 2% volume, the liquid flowed smoothly through the dome. This reorientation character is different than that observed for tanks having hemispherical domes [Refs 1, 2]. Hemispherical domes allow the liquid to flow through smoothly. The entrapment tends to dissipate energy through turbulence. This observation is consistent with the results of other drop tower tests on cylindrical tank compartments performed at Martin Marietta. The sharp corners of these tanks significantly damped the liquid motion.

Figures 2-26 and 2-27 are plots of the measured force time histories (F_{YT}, F_{ZT} tank coordinate system) for fill volumes ranging from 2 to 15% (identical test conditions). Larger fill volumes exhibit larger forces that peak sooner than smaller volumes. Smaller volumes must traverse a longer distance to reach the same relative point in the tank, which results in a peak force time delay. However, fill volume does not have an effect on the overall character of the measured forces.

Effect of Liquid Viscosity - The scaling analysis indicated that the influence of viscosity during reorientation should be negligible if the Reynolds number is greater than 50. To investigate viscous effects, the 10% fill volume case was run with three different test liquids in the drop tower test program. Figures 2-20 through 2-22 show the reorientation time histories for FC-114B2 (μ = 0.75 cp), FC-43 (μ = 6.50 cp), and HEXANE (μ = 0.33 cp). Figure 2-23 shows a similar KC-135 test condition using FC-113 (μ = 0.67 cp). The general character of the bulk liquid motion was the same in all four tests. The primary observable difference was in the motion of the liquid film that leads the bulk liquid motion. A comparison of the 0.4-s frames in Figures 2-20 through 2-22, shows that the lower the viscosity, the higher the film velocity. HEXANE leads, closely followed by the FC-114B2; the FC-43 film lags both.

Viscosity also influenced how much liquid circulated completely around the tank during the test. However, the bulk motion was not significantly altered even though viscosity varied by a factor of 19.7 and the Reynolds number varied by a factor of 25.7 over the four tests. This supports the scaling premise that viscous forces have a negligible effect on bulk liquid reorientation in the RTLS Reynolds number regime.

Figure 2-28 shows a force comparison for drop tower tests 5, 6, and 32 (Figs. 2-20 to 2-22). Absolute magnitude comparisons cannot be made due to the different liquid densities. However, any viscosity effects would probably appear in the phasing of force peaks. FC-43 is over eight times as viscous as FC-114B2, and almost 20 times as viscous as HEXANE. The results, however, are inconclusive. No clear trend is present in Figure 2-28. The F_{YT} plot supplies the most information. For FC-114B2, the negative F_{YT} peak occurs slightly ahead (in time) of the peak for FC-43. This may indicate that the less viscous FC-114B2 is moving a little faster than the FC-43. In general, however, viscosity does not seem to have an appreciable effect on the force time histories.

Effect of Tank Orientation - Several tests were run at tank orientations of 0 and 30 deg. In addition, the axial acceleration component was halved in some tests. These changes did not significantly alter the overall liquid motion characteristics. Figures 2-24 and 2-25 show drop tower tests 30 ($\gamma = 0°$) and 25 ($\gamma = 30°$), respectively.

The KC-135 test program also included tests at $\gamma = 0$, 13, and 30 deg. No appreciable difference in the liquid motion was observed in those tests either.

γ = 13°

Fill Volume = 2%

Test Liquid = FC-114B2

0.031 g

0.090 g

T = 0.0 s

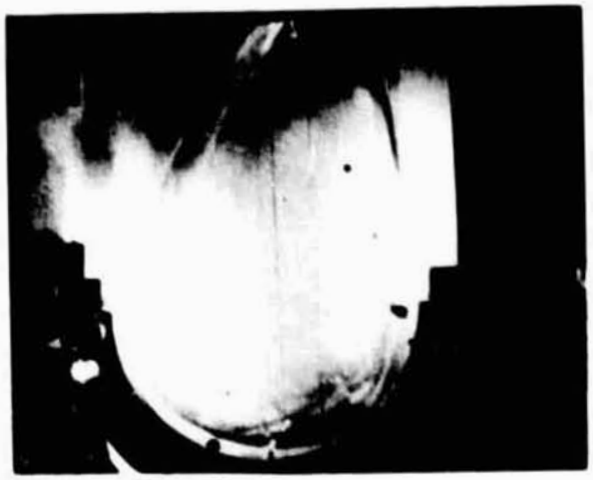

T = 0.4 s

T = 0.8 s

T = 1.2 s

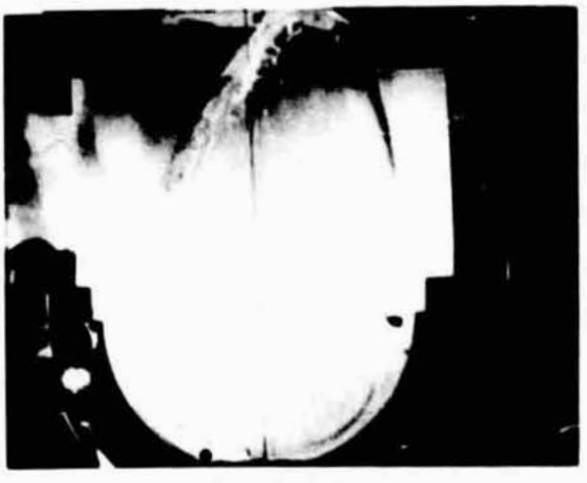

T = 1.6 s

Figure 2-18. Drop Tower Test 9, Unbaffled Tank

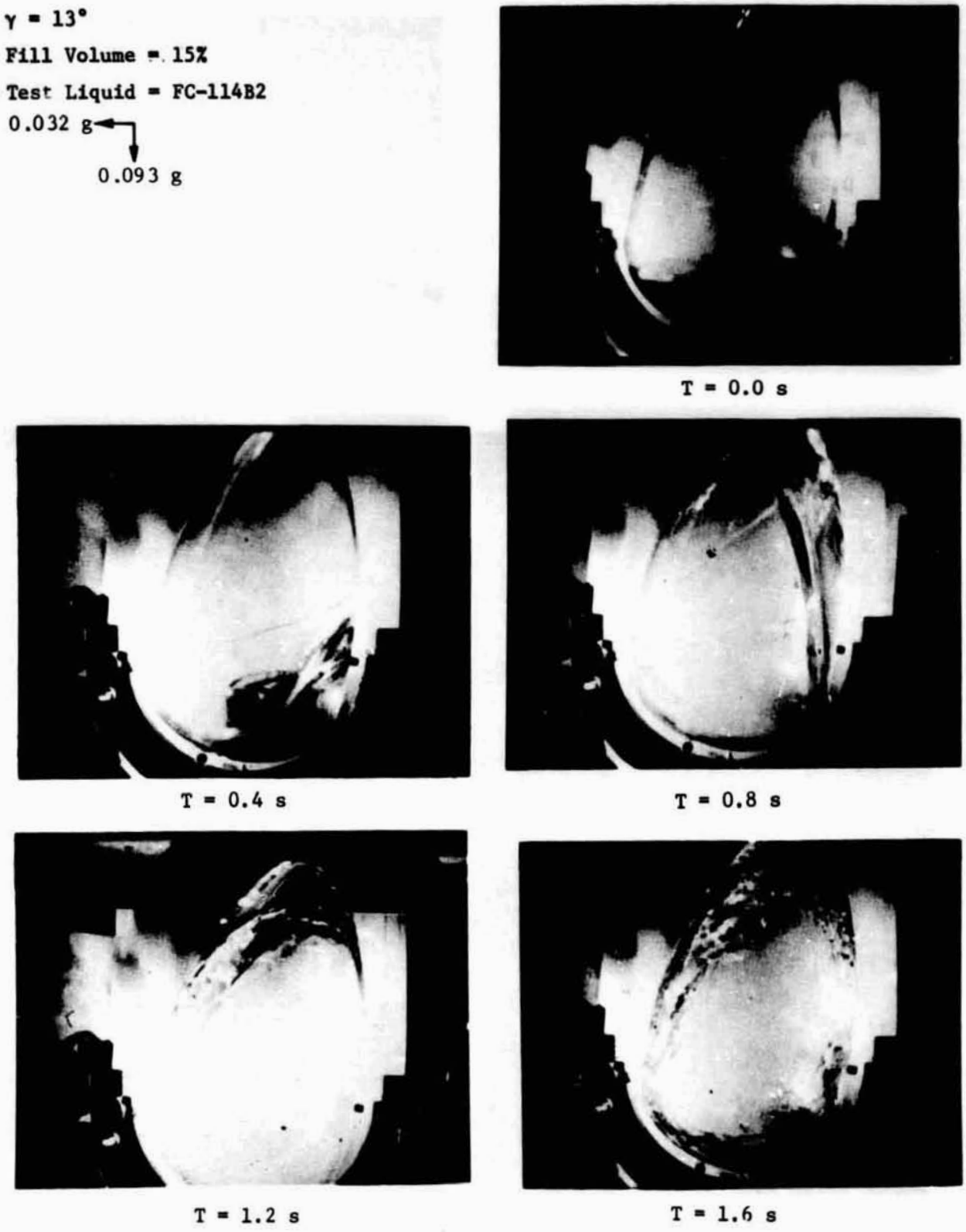

Figure 2-19. Drop Tower Test 22, Unbaffled Tank

γ = 13°

Fill Volume = 10%

Test Liquid = FC-114B2

0.030 g ← ↓ 0.091 g

T = 0.0 s

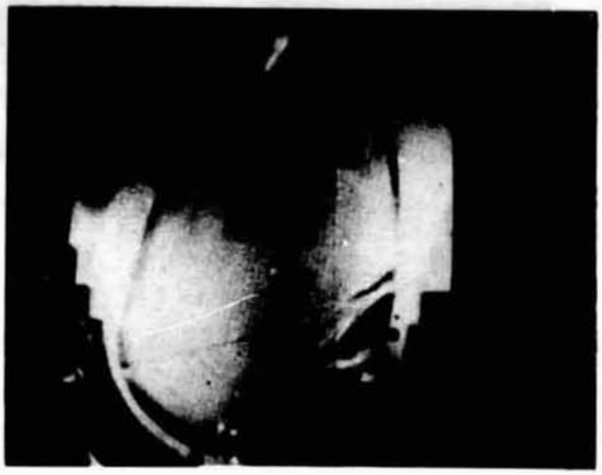

T = 0.4 s

T = 0.8 s

T = 1.2 s

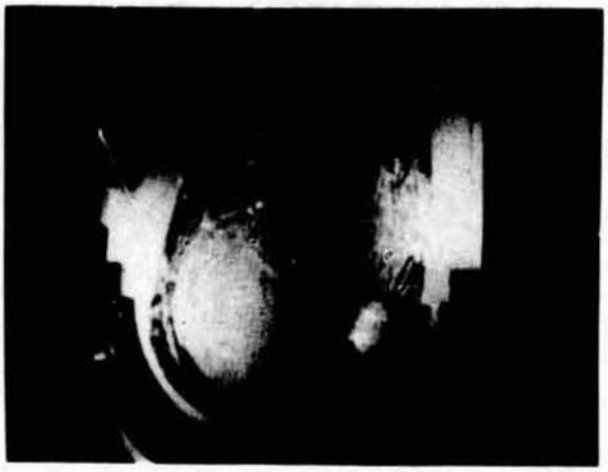

T = 1.6 s

Figure 2-20. Drop Tower Test 5, Unbaffled Tank

γ = 13°
Fill Volume = 10%
Test Liquid = FC-43
0.029 g
0.091 g

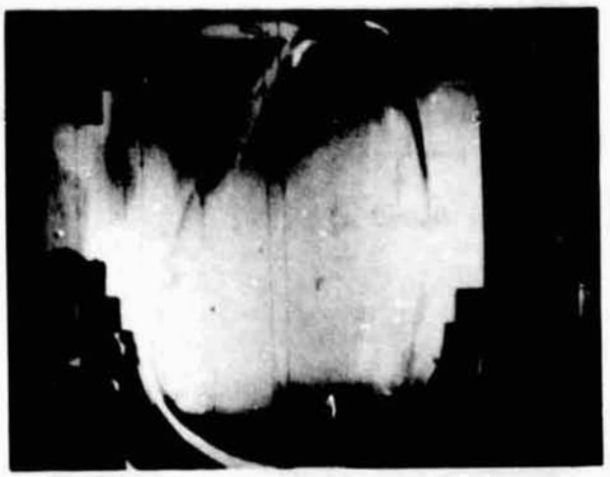

T = 0.0 s

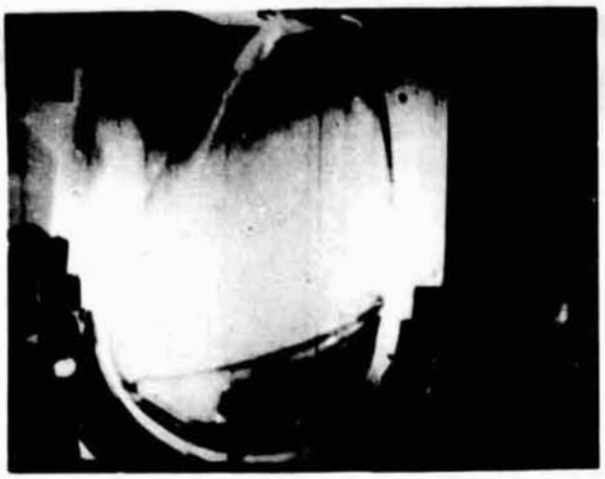

T = 0.4 s

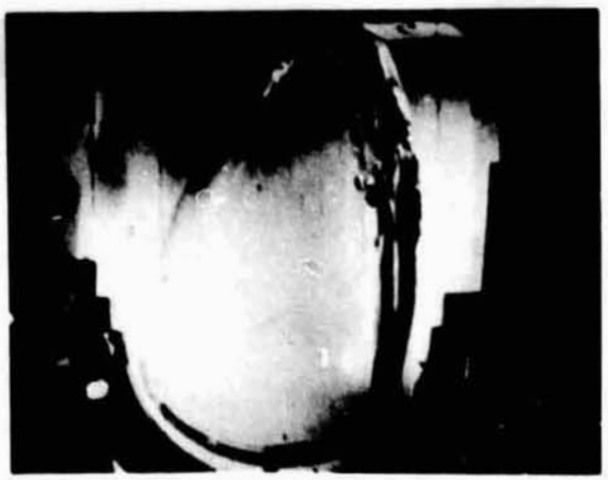

T = 0.8 s

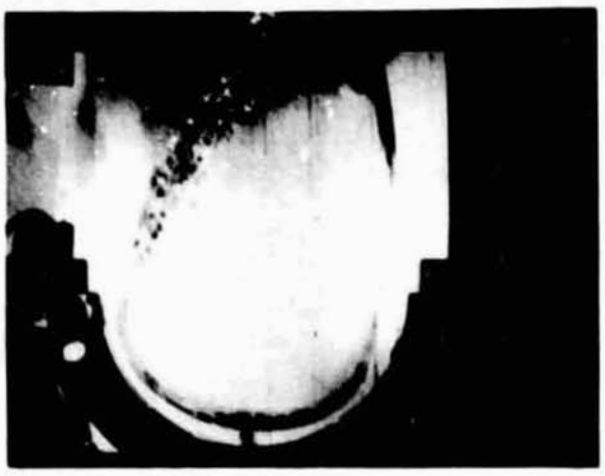

T = 1.2 s

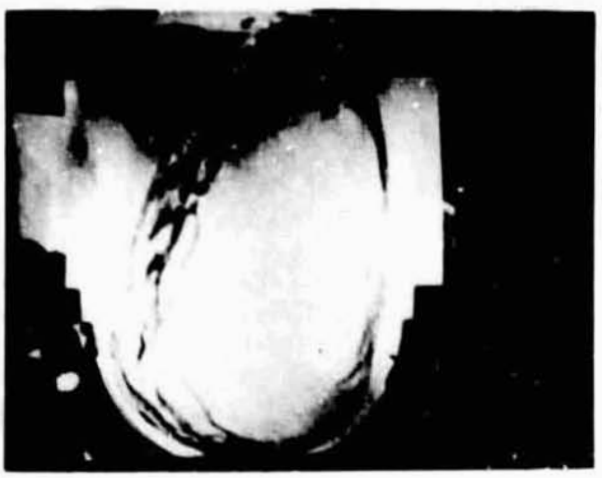

T = 1.6 s

Figure 2-21. Drop Tower Test 6, Unbaffled Tank

γ = 13°

Fill Volume = 10%

Test Liquid = HEXANE

0.032 g ←

↓ 0.090 g

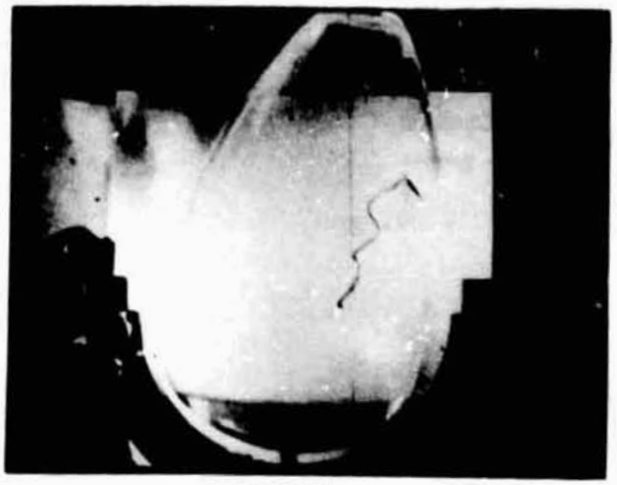

T = 0.0 s

T = 0.4 s

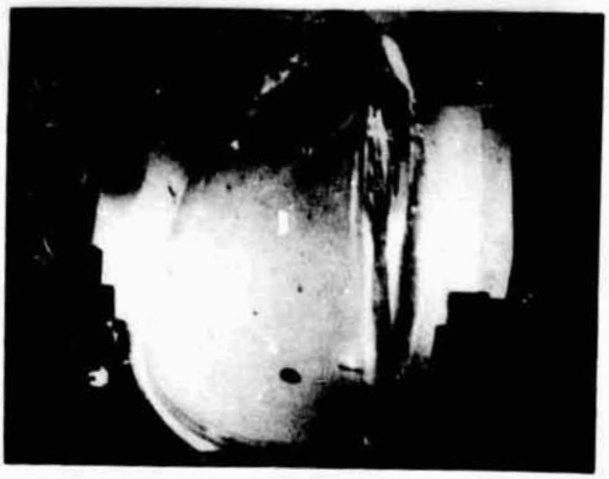

T = 0.8 s

T = 1.2 s

T = 1.6 s

Figure 2-22. Drop Tower Test 32, Unbaffled Tank

γ = 13°

Fill Volume = 10%

Test Liquid = FC-113

≈0.02 g

≈0.2 g

T = 2.7 s

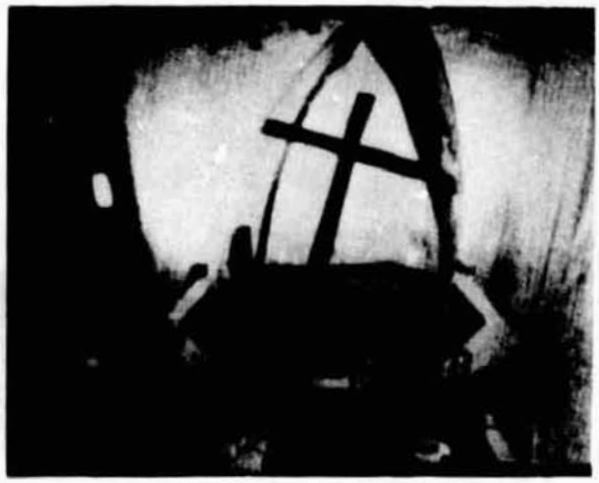

T = 3.8 s

T = 4.4 s

T = 5.1 s

Figure 2-23. KC-135 Test 1.2.2, Unbaffled Tank

γ = 0°

Fill Volume = 10%

Test Liquid = FC-114B2

0.032 g ← ↓ 0.042 g

T = 0.0 s

T = 0.4 s

T = 0.8 s

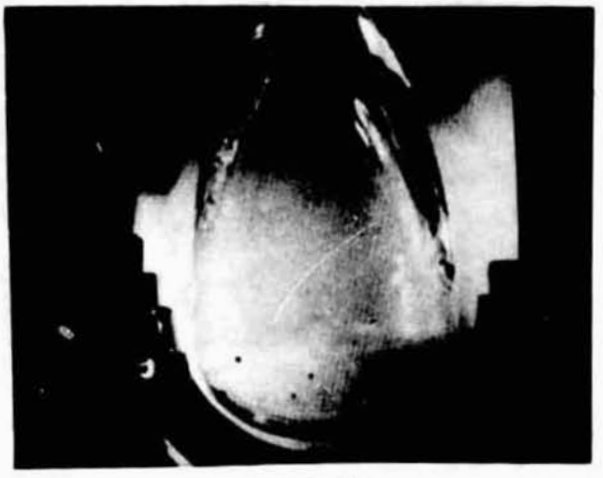

T = 1.2 s

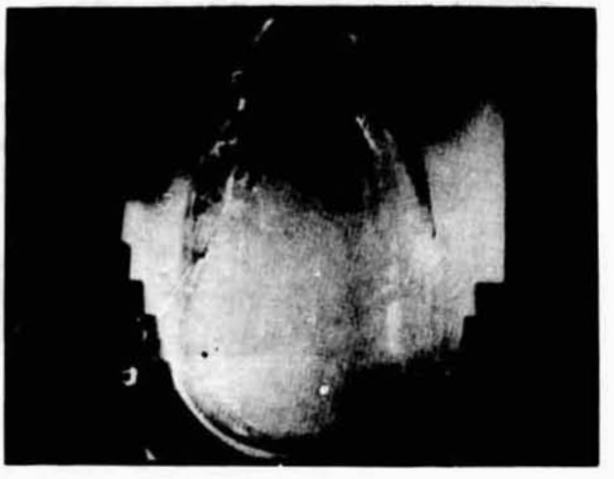

T = 1.6 s

Figure 2-24. Drop Tower Test 30, Unbaffled Tank

γ = 30°

Fill Volume = 10%

Test Liquid = FC-114B2

0.031 g ←┐

↓

0.091 g

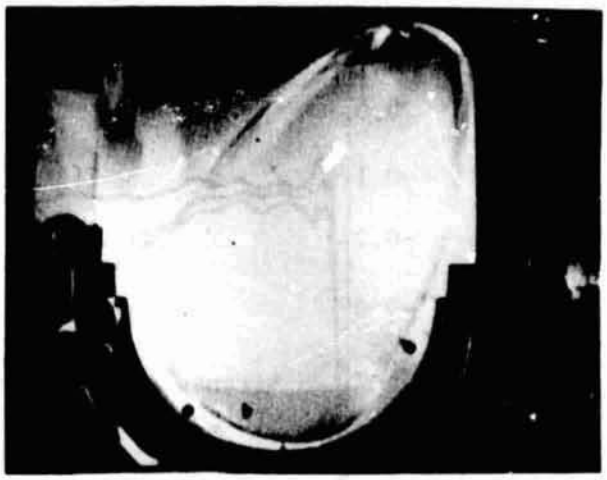

T = 0.0 s

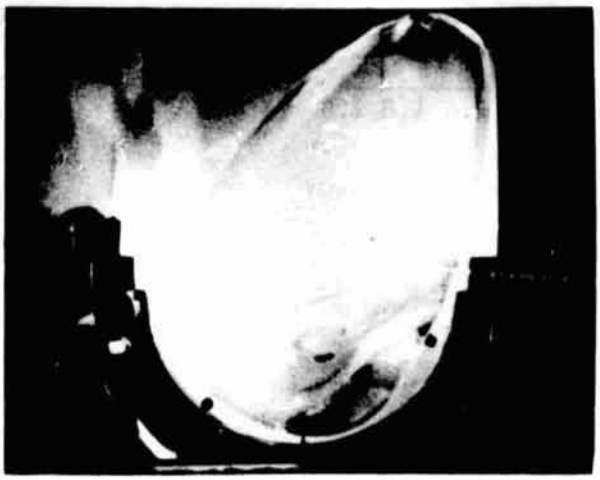

T = 0.4 s

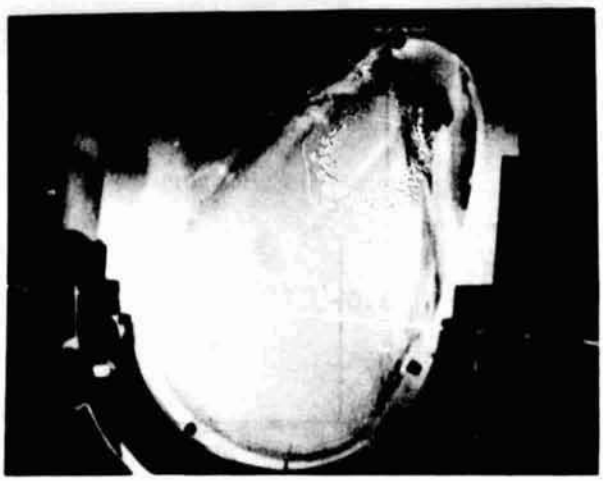

T = 0.8 s

T = 1.2 s

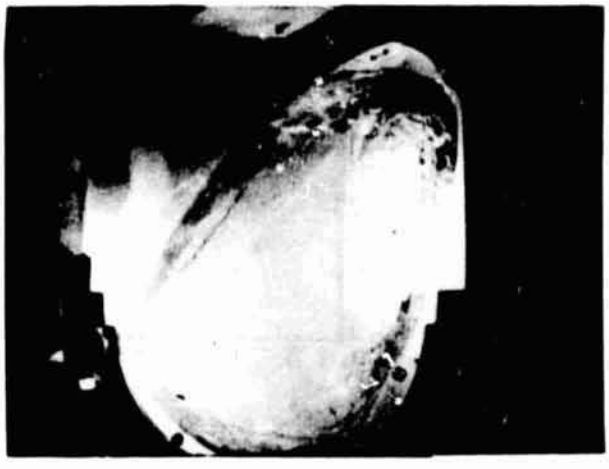

T = 1.6 s

Figure 2-25. Drop Tower Test 25, Unbaffled Tank

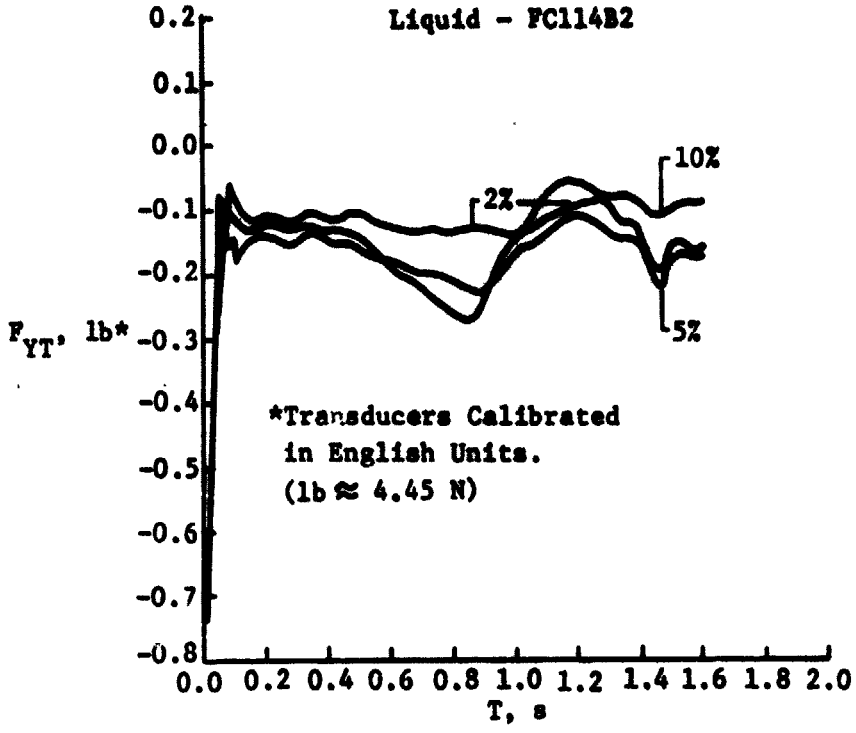

a) Y_T Force Time History

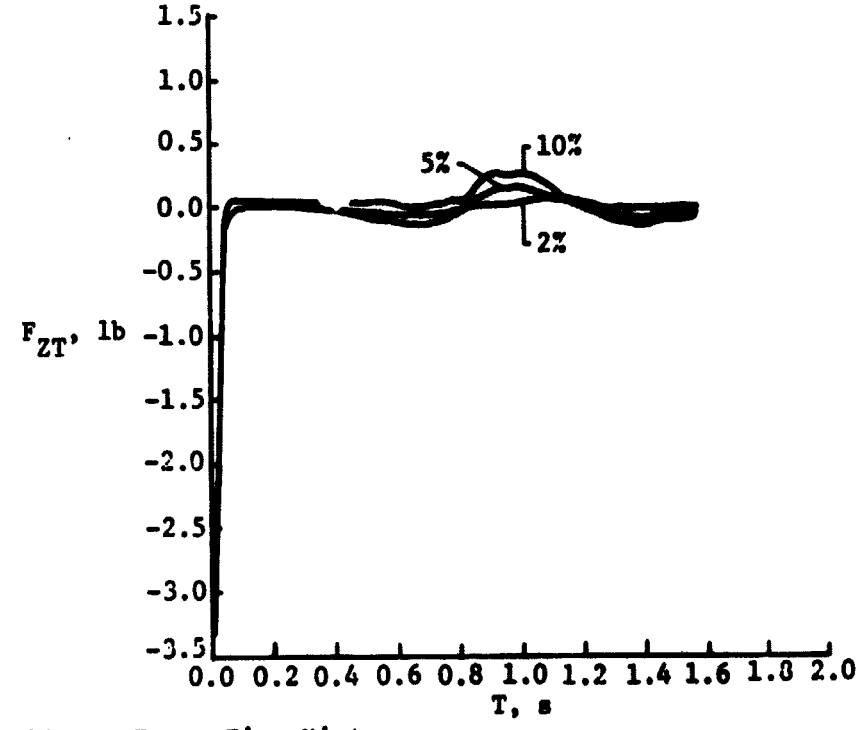

b) Z_T Force Time History

Figure 2-26.
Unbaffled Tank, Drop Tower Liquid Reorientation Force Time Histories: Fill Volume Comparison (Tests 5, 9, and 21)

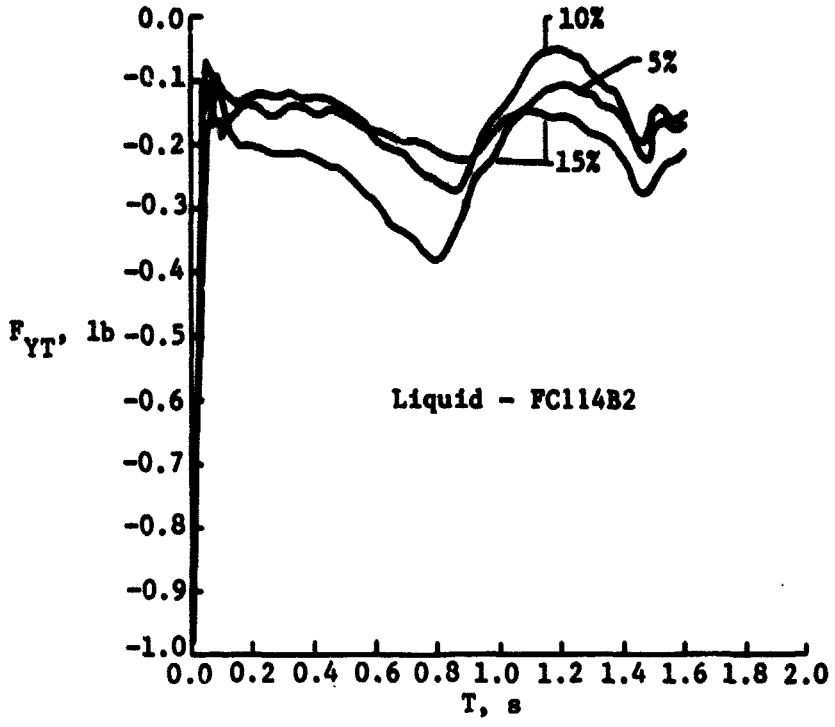

a) Y_T Force Time History

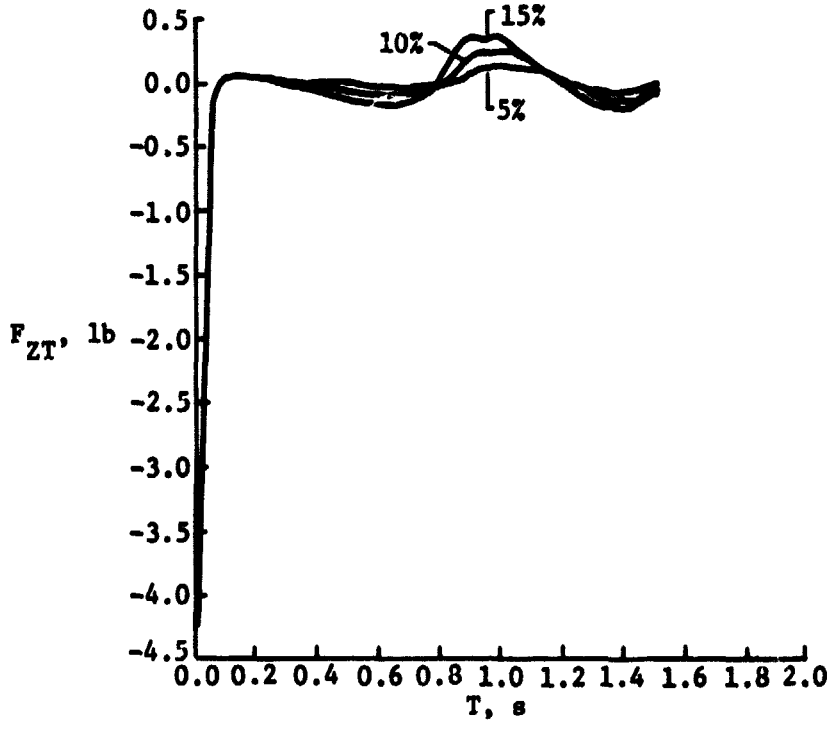

b) Z_T Force Time History

Figure 2-27.
Unbaffled Tank, Drop Tower Liquid Reorientation Force Time Histories: Fill Volume Comparison (Tests 5, 21, and 22)

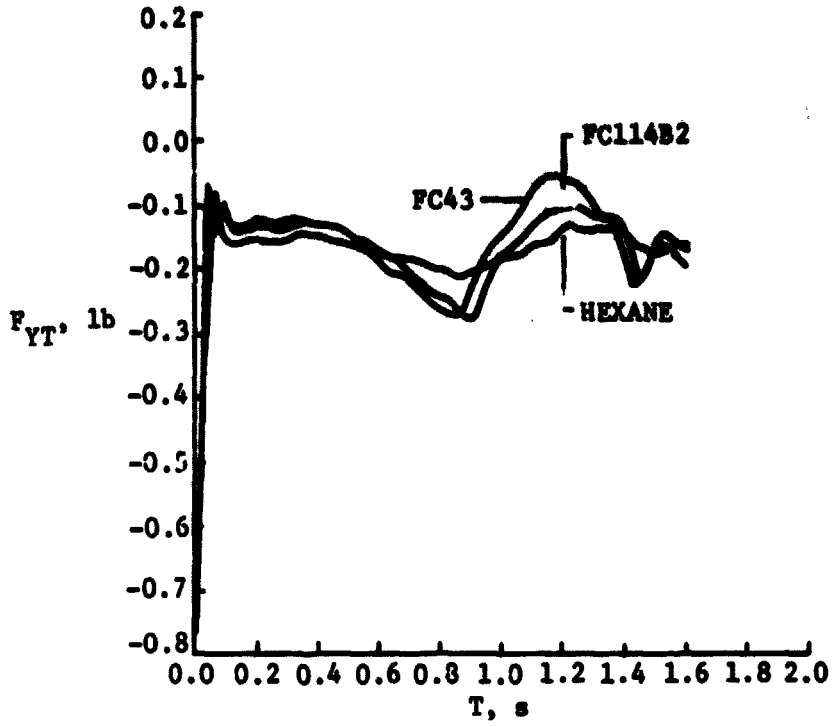

a) Y_T Force Time History

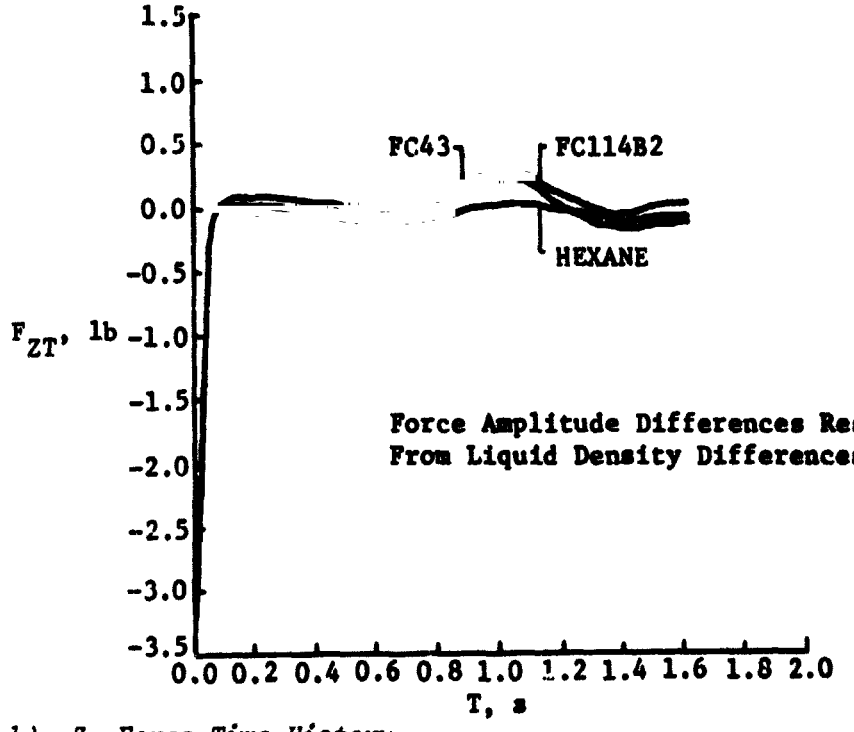

b) Z_T Force Time History

Figure 2-28.
Unbaffled Tank, Drop Tower Liquid Reorientation Force Time Histories: Liquid Viscosity Comparison (Tests 5, 6, and 32)

2.3.2 Baffled Tank

Incorporation of baffles into the tanks resulted in extremely turbulent flow. Figures 2-29 through 2-34 contain single frame photos from the high speed KC-135 and drop tower movies for selected baffled tank tests. Although the general reorientation character was similar to the unbaffled tank, the baffles significantly altered the reorientation forces.

For small fill volumes (2%), the antivortex baffle caused a portion of the liquid to traverse the tank interior and impact the wall near the ogive dome. This did not occur in the KC-135 tests because the XAC acceleration began to act while the ZAC acceleration component was still positive. This tended to position the liquid away from the antivortex baffle. Construction of the 1/60th-scale (drop tower) tank baffles allowed the liquid to flow between the baffles and the tank wall. The 1/10th-scale (KC-135) tank baffles were more representative of the full scale ET LOX tank and prevented this wall flow.

Figures 2-29 and 2-30 show reorientation for similar test conditions in the drop tower and KC-135. Although the higher Bond number in the KC-135 test resulted in more surface breakup, the general reorientation character was similar. The baffles in the KC-135 tank did a better job of containing the liquid in the upper part of the ogive dome (see Fig. 2-30, T = 5.6 to 6.4 s). This was due to the smaller baffle/wall gap in the 1/10th-scale tank and would be the expected behavior in the full-scale ET.

Figures 2-31 and 2-32 show the influence of fill volume. The effect of the antivortex baffle on small fill volume (as discussed above) can be seen in Figure 2-31. Figures 2-33 and 2-34 show tests performed at $\gamma = 0$ and 30°, respectively. As in the unbaffled tank tests, no appreciable difference in reorientation character was evident.

Turbulence caused by the baffles generally reduced the liquid reorientation forces. Figures 2-35 and 2-36 present a comparison of drop tower reorientation force time histories for similar baffled and unbaffled tank test conditions. Similar results were noted for all test conditions. Figures 2-37 and 2-38 show drop tower test 16 and 18, in which the lateral (A_{LAT}) acceleration component was delayed for ≈ 0.5 s after test initiation. Figure 2-39 presents a comparison of the force time histories for these two tests. Note that the baffles also reduced the force levels for this case.

γ = 13°

Fill Volume = 10%

Test Liquid = FC-114B2

0.032 g ←┐

0.092 g ↓

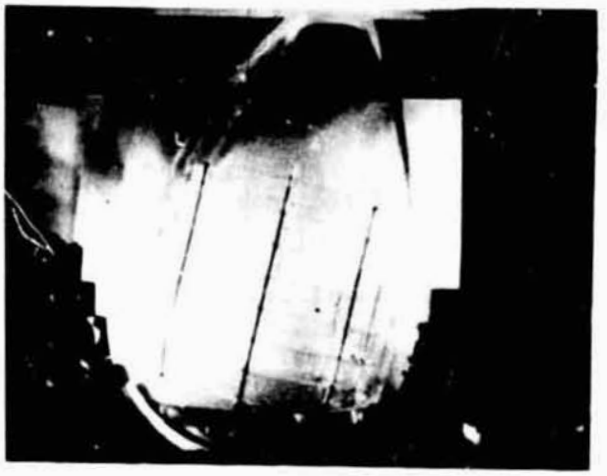

T = 0.0 s

T = 0.4 s

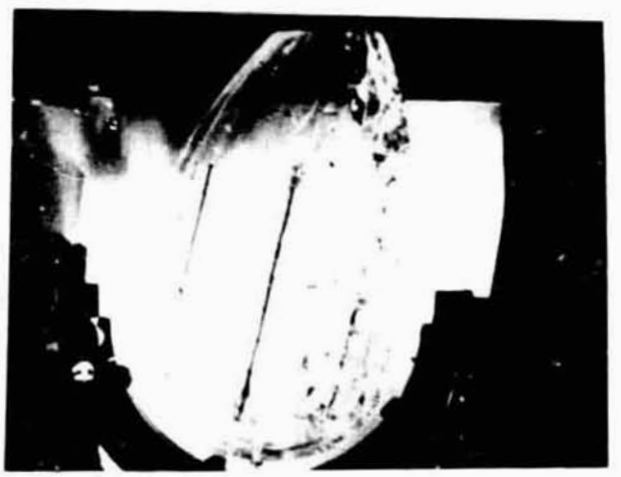

T = 0.8 s

T = 1.2 s

T = 1.6 s

Figure 2-29. Drop Tower Test 7, Baffled Tank

γ = 13°

Fill Volume = 10%

Test Liquid = FC-113

≈0.015 g

≈0.2 g

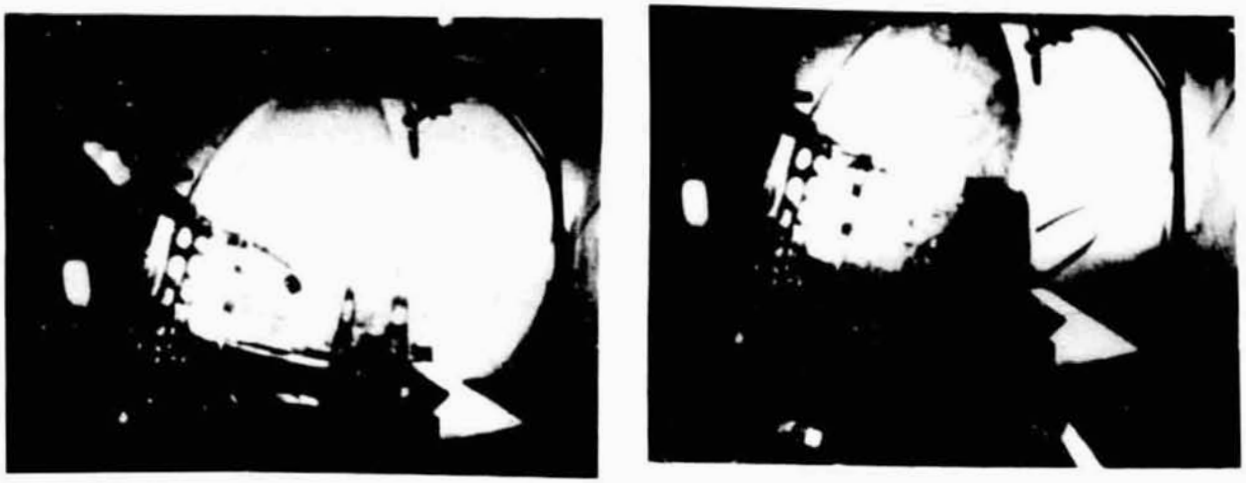

T = 3.9 s

T = 4.8 s

T = 5.6 s

T = 6.4 s

Figure 2-30. KC-135 Test 2.7.2, Baffled Tank

γ = 13°

Fill Volume = 2%

Test Liquid = FC-114B2

0.034 g ←↓

0.092 g

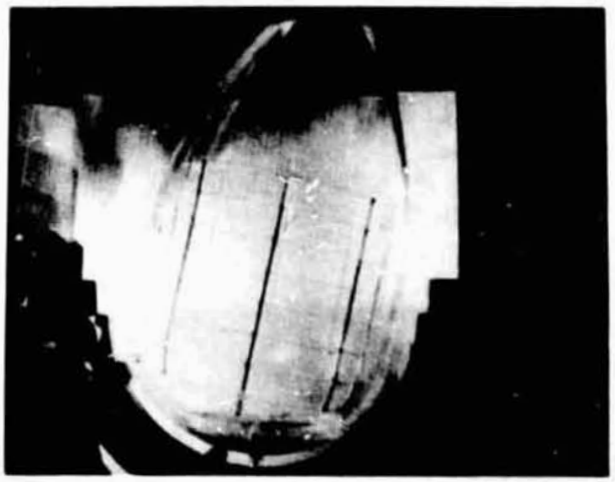

T = 0.0 s

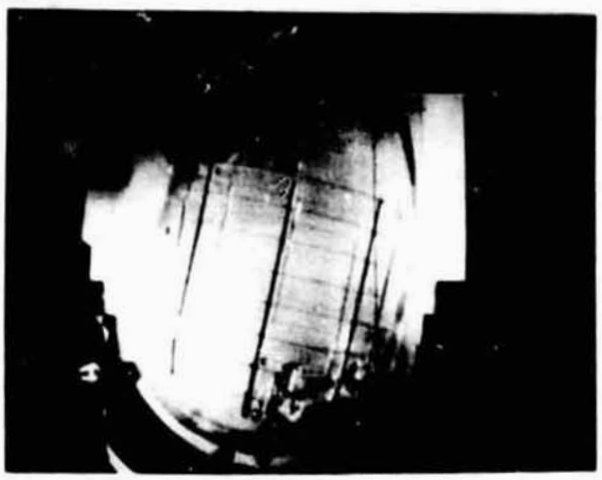

T = 0.4 s

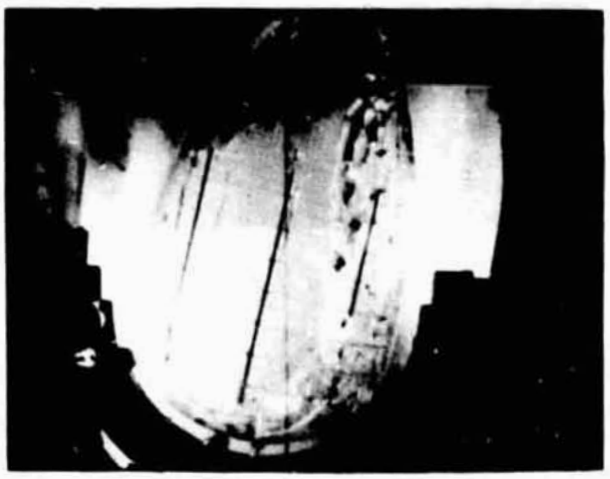

T = 0.8 s

T = 1.2 s

T = 1.6 s

Figure 2-31. Drop Tower Test 11, Baffled Tank

γ = 13°

Fill Volume = 15%

Test Liquid = FC-114B2

0.032 g

0.088 g

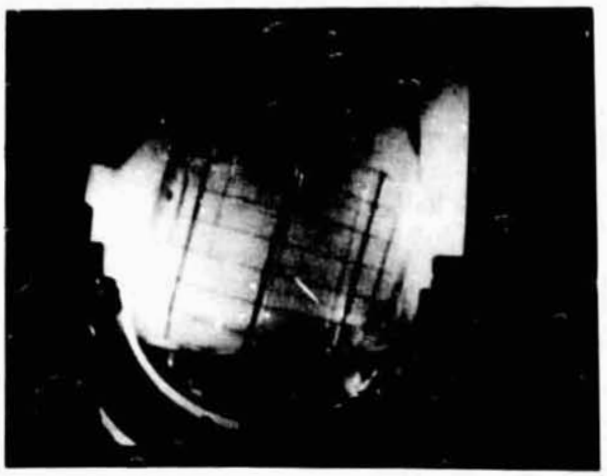

T = 0.0 s

T = 0.4 s

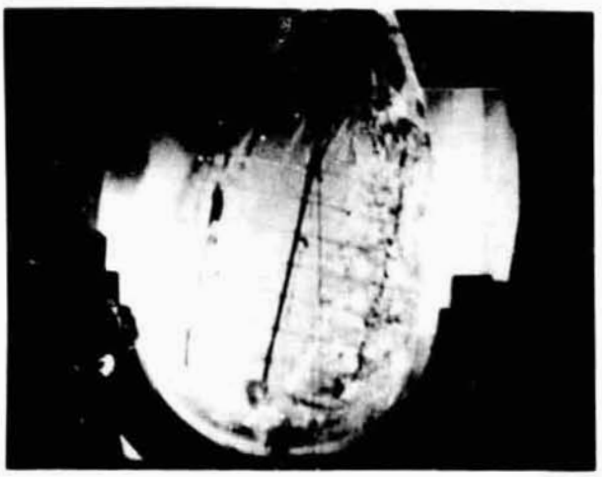

T = 0.8 s

T = 1.2 s

T = 1.6 s

Figure 2-52. Drop Tower Test 20, Baffled Tank

γ = 0°

Fill Volume = 10%

Test Liquid = FC-114B2

0.038 g ←┐

↓

0.050 g

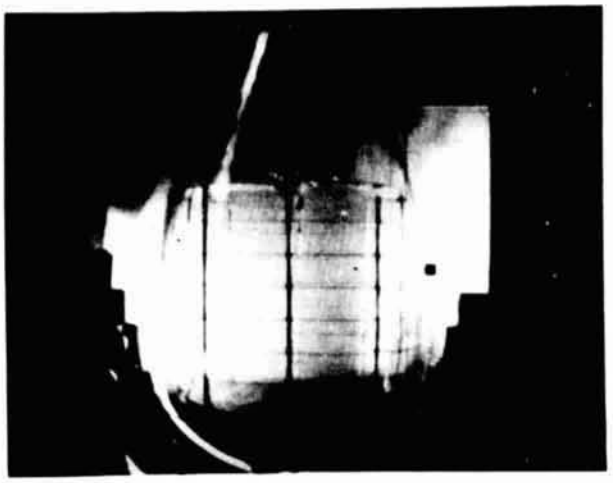

T = 0.0 s

T = 0.4 s

T = 0.8 s

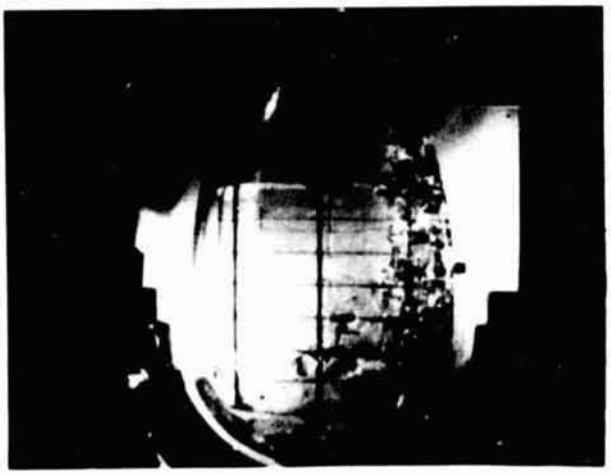

T = 1.2 s

T = 1.6 s

Figure 2-33. Drop Tower Test 29, Baffled Tank

γ = 30°

Fill Volume = 10%

Test Liquid = FC-114B2

0.031 g

0.088 g

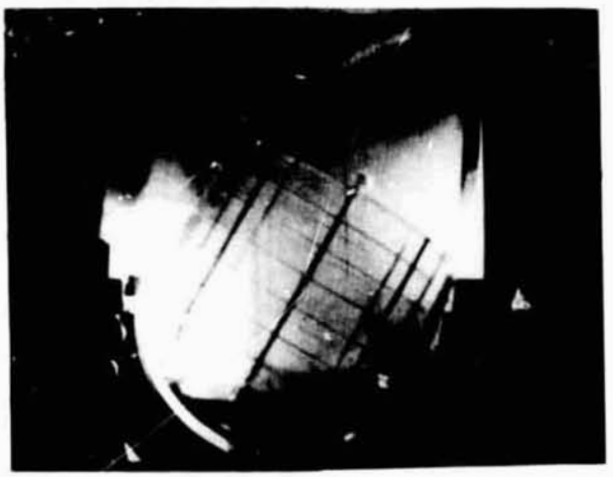

T = 0.0 s

T = 0.4 s

T = 0.8 s

T = 1.2 s

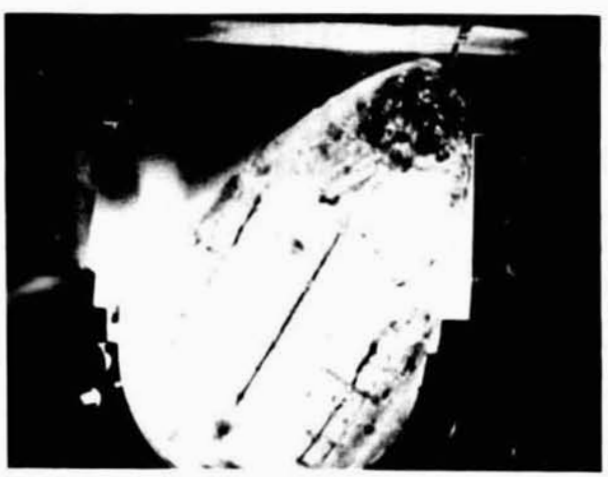

T = 1.6 s

Figure 2-34. Drop Tower Test 26, Baffled Tank

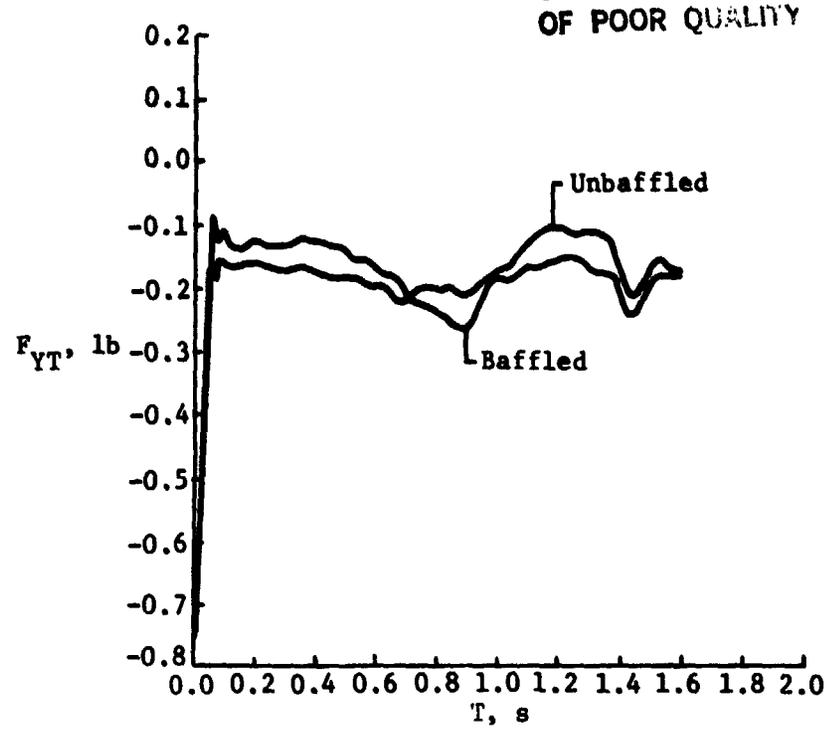

a) Y_T Force Time History

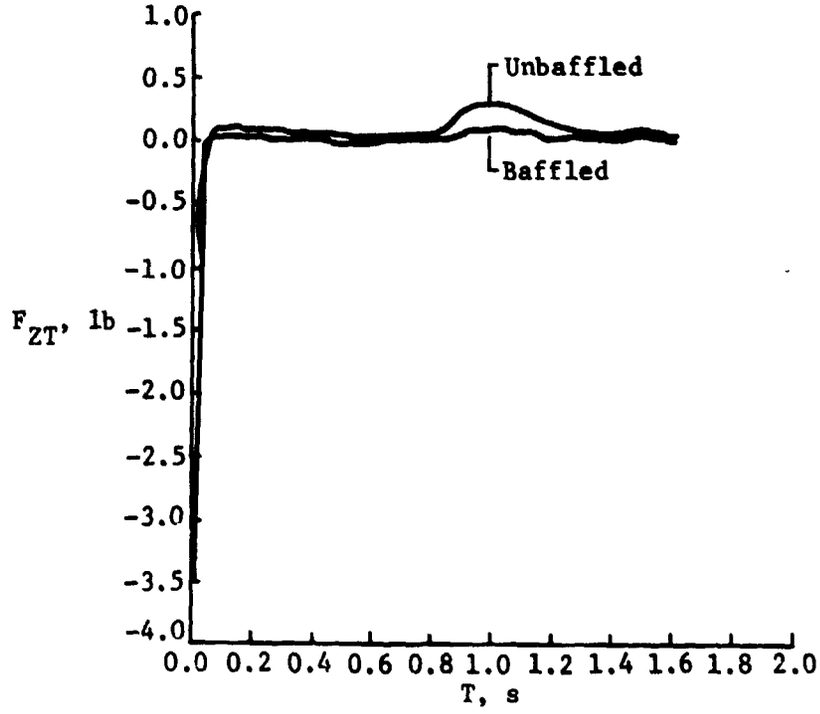

b) Z_T Force Time History

Figure 2-35.
Drop Tower Liquid Reorientation Force Time Histories: Baffled/ Unbaffled Comparison (Tests 6 and 8)

a) Y_T Force Time History

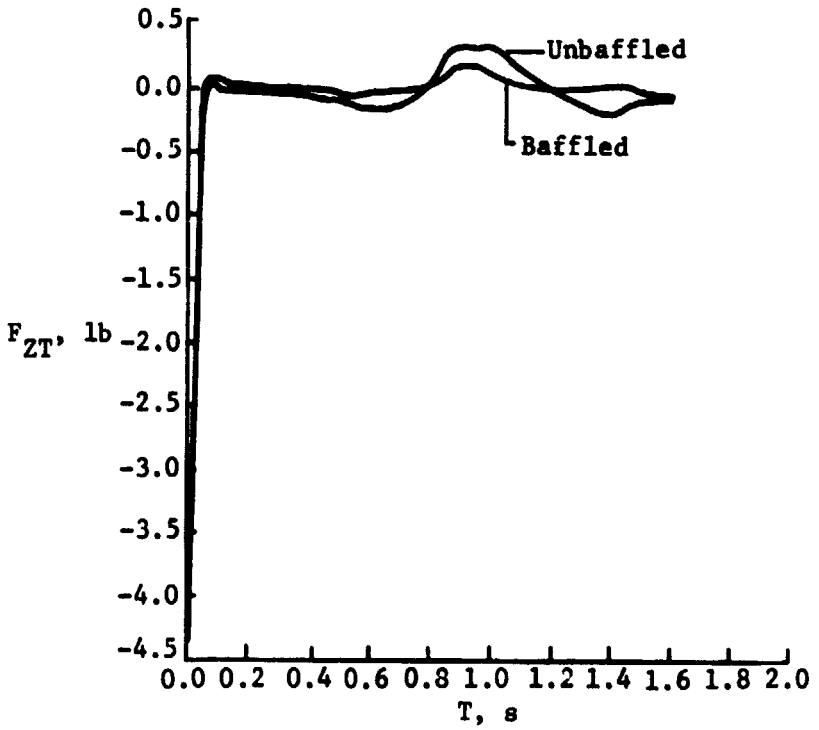

b) Z_T Force Time History

Figure 2-36.
Drop Tower Liquid Reorientation Force Time Histories: Baffled/Unbaffled Comparison (Tests 20 and 22)

γ = 13°

Fill Volume = 10%

Test Liquid = FC-114B2

0.0 to 0.053 g* ← ↓ 0.091 g

*Lateral Acceleration
Delayed ≈0.5 s

T = 0.0 s

T = 0.4 s

T = 0.8 s

T = 1.2 s

T = 1.6 s

Figure 2-37. Drop Tower Test 16, Unbaffled Tank

γ = 13°

Fill Volume = 10%

Test Liquid = FC-114B2

0.0 to 0.052 g* ← ↓ 0.091 g

*Lateral Acceleration
Delayed ≈0.5 s

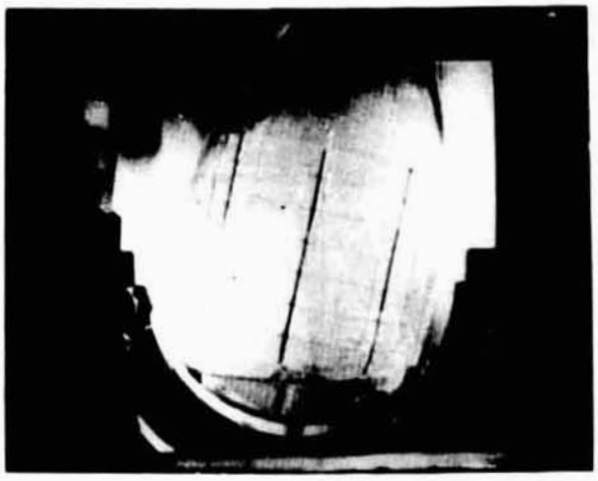

T = 0.0 s

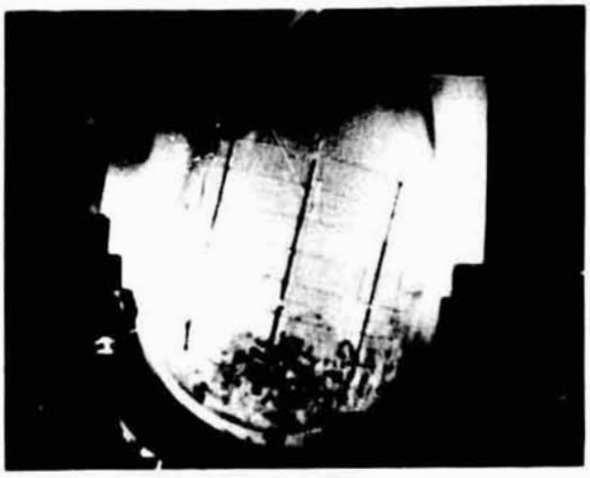

T = 0.4 s

T = 0.8 s

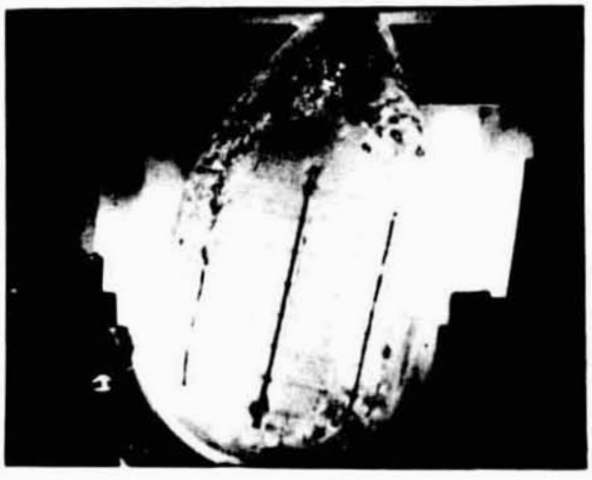

T = 1.2 s

T = 1.6 s

Figure 2-38. Drop Tower Test 18, Baffled Tank

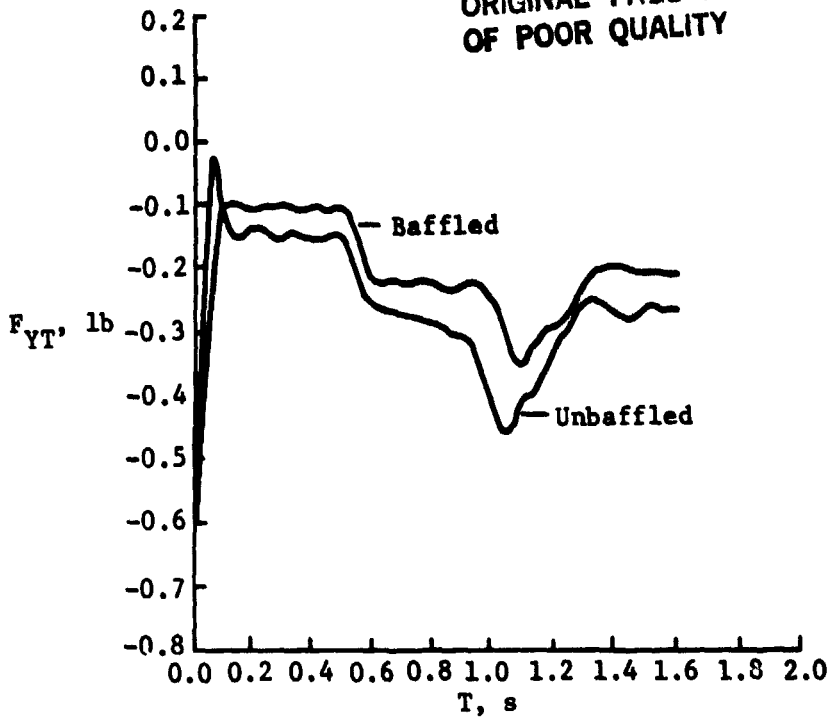

a) Y_T Force Time History

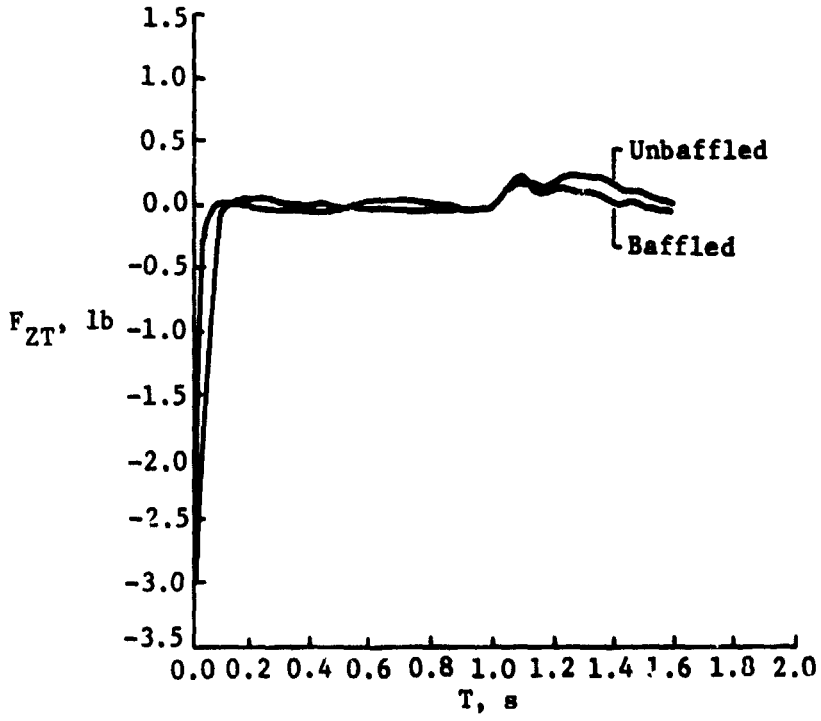

b) Z_T Force Time History

Figure 2-39.
Drop Tower Liquid Reorientation Force Time Histories: Baffled/Unbaffled Comparison (Tests 16 and 18)

3.0 TWO DIMENSIONAL FINITE ELEMENT MODEL (LAMPS2)

3.1 INTRODUCTION

The liquid motion during the RTLS maneuver has previously been analyzed by a single point mass mechanical analog developed for NASA's Space Vehicle Dynamics Simulation Program (SVDS). This analog portrays the liquid as a point mass moving on an ellipsoidal constraint surface $\left(\left(\frac{y}{b_0}\right)^2 + \left(\frac{z}{a_0 - a_1 z}\right)^2\right) = 1$. This constraint surface is defined as the ellipsoid that best fits the locus of center of mass locations prescribed by analytically rotating the tank in a 1-g field. Therefore, the constraint surface is a function of tank geometry and fill volume. The forces that constrain the CM to the ellipsoidal surface are representative of the forces the liquid exerts on the ET tank. A similar model, called LAMPS, was developed at Martin Marietta. The LAMPS model portrays the liquid as a point mass moving on an ellipsoid constraint surface. Conceptually, the LAMPS model expresses the forces of the moving propellant as,

$$F = M\left(f_m\right)\frac{V^2}{\rho} + MA \qquad (3\text{-}1)$$

where

MA = D'Alembert component of force;

$M\left(f_m\right)\frac{V^2}{\rho}$ = modified centriptal component of force;

f_m = effective mass factor.

The effective mass factor concept was developed in a previous NASA study [Ref 2]. This study concluded that as the liquid reorients and accelerates, the free surface begins to assume a curved interface. Analytically breaking the liquid into finite sections, (Fig. 3-1) reveals that each segment exerts a centriptal acceleration force on the tank perpendicular to its velocity vector. Figure 3-1 shows that the net centriptal acceleration force exerted on the tank is less than that obtained by lumping the total liquid mass at its center of mass. The graph in Figure 3-1 presents the mass factor versus percent fill volume relationship derived in the referenced study.

The LAMPS model was used to simulate the Phase I drop tower test data. Figure 3-2 shows a comparison of the this model and drop tower test data for the z-axis force. This comparison is for drop tower test 22, a 15% fill volume case. The model produces a large force spike as the center of mass moves through the large change in curvature at the top of the ET LOX tank. The integrated effect or impulse applied to the tank is shown in Figure 3-3. Again, this result is conservative with respect to the test data.

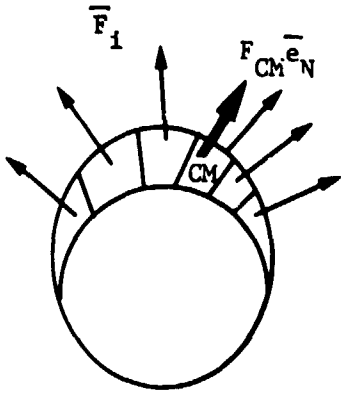

$\Sigma \bar{F}_i \cdot \bar{e}_N < F_{CM}\,\bar{e}_N$

Where:

$\bar{e}_N$ = Unit Normal Vector to the Constraint Surface at the Liquid CM

$\bar{F}_i$ = Segment Centripetal Acceleration Forces

F_{CM} = Centripetal Acceleration Force Resulting from Lumping Total Mass at Liquid CM

Liquid Effective Mass Justification

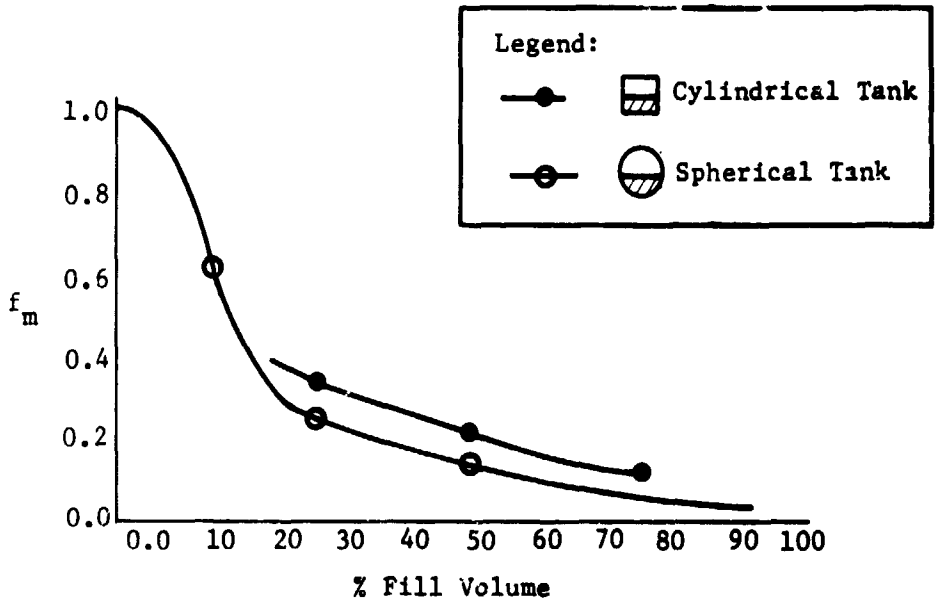

Liquid Effective Mass Comparison

Figure 3-1. Liquid Effective Mass Development

Application of a reduced mass factor produces a reduction in the level of forces but results in a nonconservative simulation of the impulse applied to the tank. These results are shown in Figures 3-4 and 3-5. From these observations, it was concluded that a distributed or multiple mass representation of the liquid motion was required to more closely simulate the propellant dynamics.

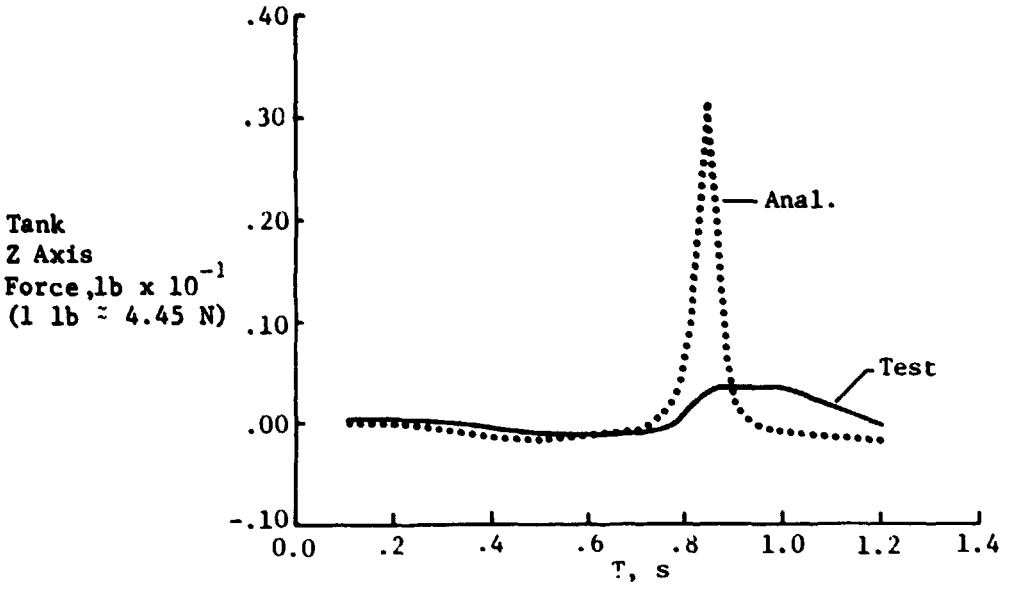

Figure 3-2.
LAMPS Model Comparison to Drop Tower Test 22 Data, Tank Z Axis Force

3.2 LAMPS2 MODEL CONCEPTUALIZATION

The drop tower and KC-135 tests were performed with biaxial accelerations applied to the tank, which resulted in planar reorientation. Evaluation of a multiple mass approach could therefore be performed using a two-dimensional representation of the liquid. This representation was obtained by passing a plane (Y-Z) through the axis of symmetry of the tank. This produced a two-dimensional slice of liquid that was divided into triangular regions (finite elements). The thickness, normal to the paper, varies from element to element but was assumed constant within the boundaries of a given element. The total liquid volume was the sum of the volumes of the triangular regions. The mass within each element was collocated to the vertices or node points of each triangle. This resulted in a distribution of the liquid mass throughout the liquid volume (Fig. 3-6).

Dividing the liquid in this fashion results in two generalized coordinates for each liquid node: the y and z position coordinates of each node point. The element node points were categorized according to location in the liquid volume. Type I node points occur on the free surface, type II node points lie on the tank boundary, and type III points are those points interior to the liquid. Under normal circumstances, the liquid cannot penetrate the tank wall boundary. At the tank boundary, the velocity of the liquid normal to the wall must be zero. Therefore, node points in the vicinity of the wall may only have velocities tangent to the wall. This constrains the type II node points to follow the tank wall.

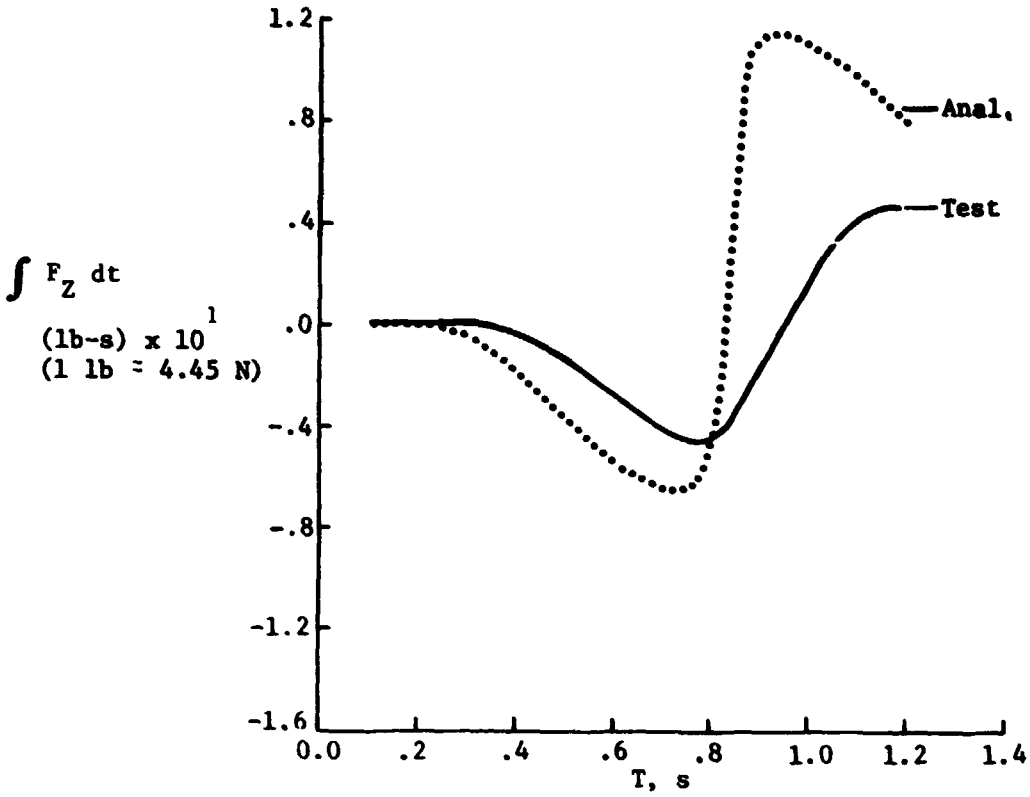

Figure 3-3.
LAMPS Model Comparison to Drop Tower Test 22 Data, Impulse of Tank Z Axis Force

This constraint is similar to that employed in the LAMPS formulation [Ref 1]. The difference being that the actual tank boundary is used as the constraint surface. whereas the LAMPS constraint surface represents the locus of center of mass points, assuming the liquid has a flat surface. Test observations have shown that, in fact, the surface becomes curved as the liquid circulates the tank. Therefore, the true center of mass locations would be different from those assumed in the LAMPS model. The distributed mass approach circumvents this problem by using the tank boundary as the constraint surface.

The forces interconnecting the node points result from the liquid being incompressible and capable of developing internal viscous shear forces. The liquid incompressibility manifests itself as a set of nonholonomic onstraint conditions applied to the generalized coordinates. The incompressibility forces, along with the boundary constraint forces, are included in the equations of motion by using the Lagrange undetermined multiplier method. The viscous shear forces appear as a set of dissipative generalized forces applied to the right side of the equations of motion.

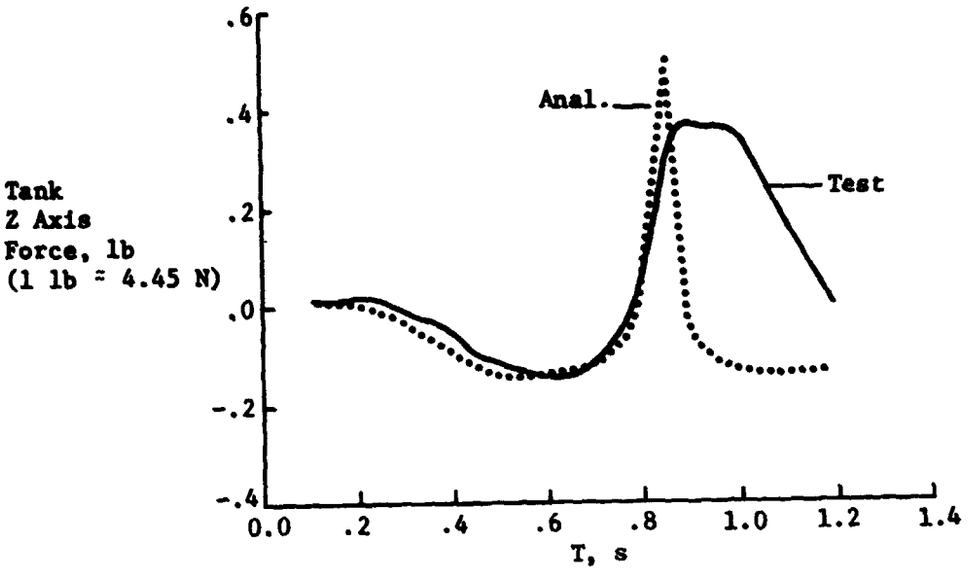

Figure 3-4.
LAMPS Model Comparison to Drop Tower Test 22 Data, Tank Z Axis Force, Mass Factor = .15

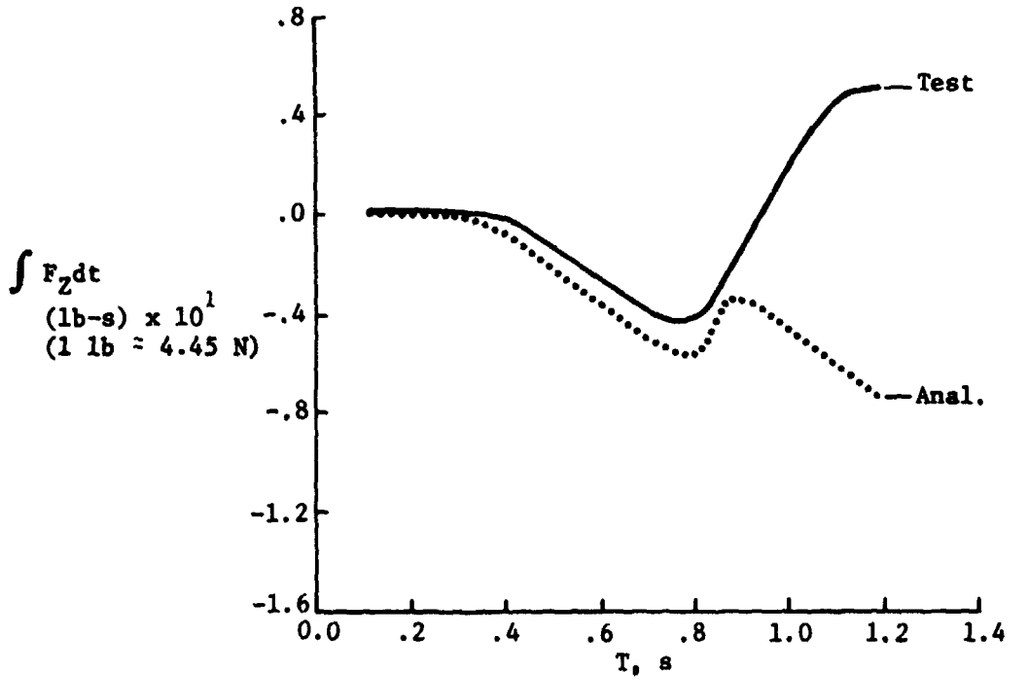

Figure 3-5.
LAMPS Model Comparison to Drop Tower Test 22 Data, Impulse of Tank Z Axis Force, Mass Factor = .15

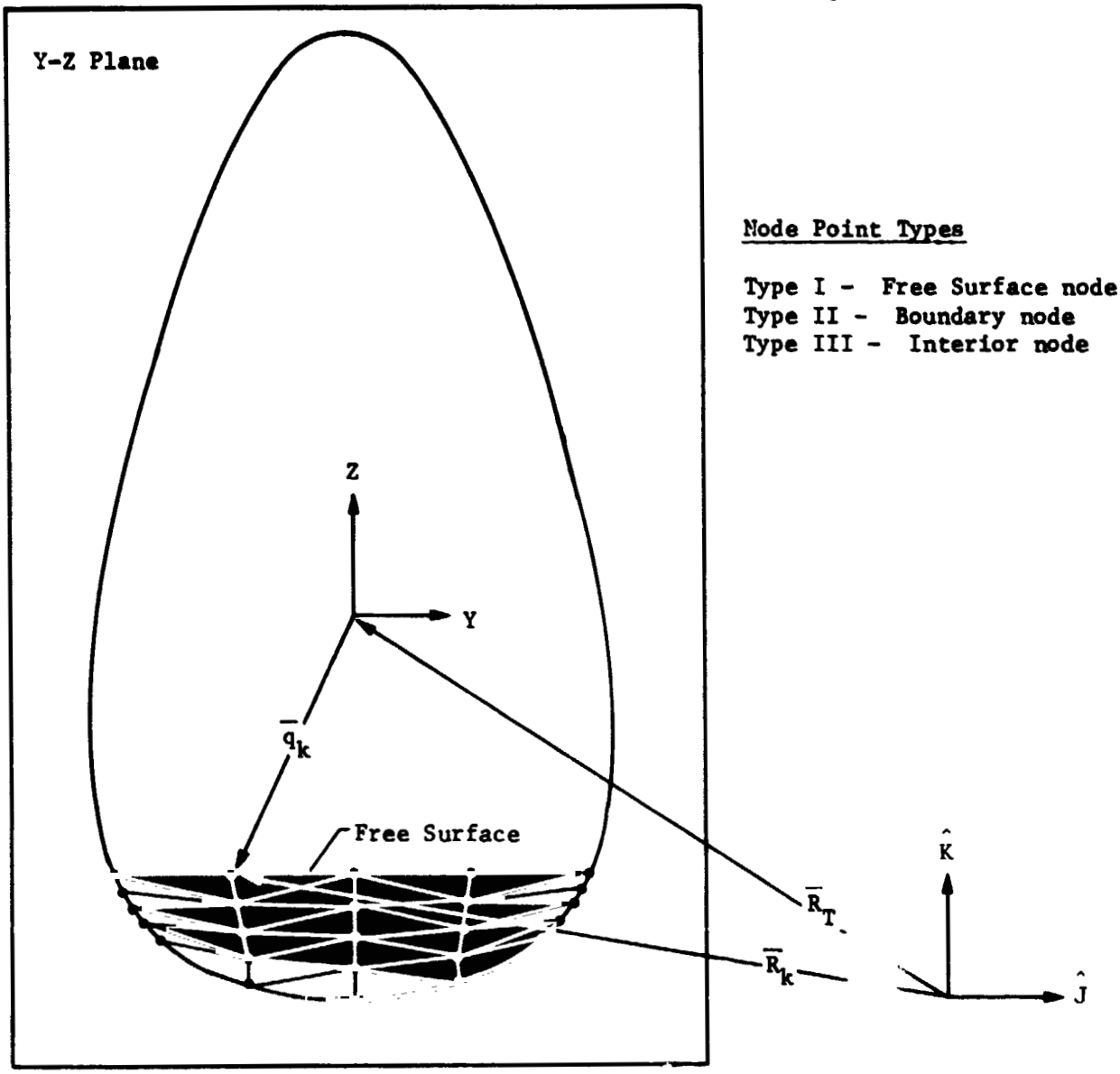

Figure 3-6. Two Dimensional Finite Element Model of Liquid

The equations of motion are numerically integrated with respect to time to obtain the new position coordinates of the liquid. These new coordinates are used to update the finite element geometry. The new geometry is employed to update the liquid incompressibility and viscous forces. The equations of motion are again evaluated and the procedure repeated. This approach produces a time history of the liquid motion which may be directly compared to the photographs of the test data. Furthermore, the forces the liquid exerts on the tank can be correlated with those measured in the drop tower and KC-135 tests.

3.3 DEVELOPMENT OF THE EQUATIONS OF MOTION

The primary objective of developing the two-dimensional model was to demonstrate the applicability of the finite element formulation in solving the liquid motion problems. This model was designed to be correlated with the drop tower and KC-135 test data. In both these data the liquid motion was planar and occurred in a nonrotating frame of reference. With these considerations in mind the equations of motion for the liquid were developed from Lagrange's equations. These equations consider generalized forces and employ nonholonomic constraints. This classic form can be expressed as,

$$\frac{d}{dt}\left(\frac{\partial L}{\partial \dot{\bar{q}}_k}\right) - \frac{\partial L}{\partial \bar{q}_k} = \bar{Q}_k + b_{k\ell}\,\lambda_\ell \qquad (3\text{-}2)$$

with the auxiliary equations,

$$b_{\ell k}\,\dot{\bar{q}}_k = 0 \qquad (3\text{-}3)$$

where

$\bar{q}_k$ = kth generalized coordinate (k=1, 2, ...n coordinates);

L = Lagrangian (kinetic - potential energy);

$b_{k\ell}$ = coefficients of the Lagrange multipliers;

λ_ℓ = Lagrange multipliers (ℓ = 1, 2, ...m constraints);

$\bar{Q}_k$ = the generalized force for the kth coordinate.

The Lagrangian (L) for the liquid was assumed to consist only of kinetic energy terms. The velocity, and hence the kinetic energy for the kth liquid mass point, can be written with the use of Figure 3-6.

$$\vec{R}_k = \vec{q}_k + \vec{R}_T \text{ (nonrotating frame)} \tag{3-4}$$

$$KE = \tfrac{1}{2} M_k \left(\dot{\vec{R}}_k \cdot \dot{\vec{R}}_k \right) = \tfrac{1}{2} M_k \left(\dot{\vec{q}}_k^{\,2} + \dot{\vec{R}}_T^{\,2} + 2\dot{\vec{q}}_k \cdot \dot{\vec{R}}_T \right) \tag{3-5}$$

where

$\dot{\vec{q}}_k$ = velocity of the liquid relative to the tank frame;

$\dot{\vec{R}}_T$ = velocity of the tank frame;

M_k = kth mass point.

The positions of the liquid relative to the tank frame were selected as the generalized coordinates (all test liquid motion was observed relative to the moving tank frame). Therefore, evaluating the partial derivatives of Lagrange's Equation,

$$\frac{\partial KE}{\partial \vec{q}_k} = 0; \quad \frac{\partial KE}{\partial \dot{\vec{q}}_k} = M_k \left(\dot{\vec{q}}_k + \dot{\vec{R}}_T \right) \tag{3-6}$$

Hence, Lagrange's equations for the liquid can be written as,

$$M_k \ddot{\vec{q}}_k = -M_k \ddot{\vec{R}}_T + \bar{Q}_k + b_{k\ell} \lambda_\ell \tag{3-7}$$

This expression, along with equation (3-3) can be recast into a convenient matrix format,

$$\underset{(nxn)}{[M]} \underset{(nx1)}{\{\ddot{q}\}} = -\underset{(nxn)}{[M]} \underset{(nx1)}{\{\ddot{R}_T\}} + \underset{(nx1)}{\{Q\}} + \underset{(nxm)}{[b]^T} \underset{(mxm)}{[\varepsilon]} \underset{(mx1)}{\{\lambda\}} \tag{3-8}$$

$$[\varepsilon][b]\{\dot{q}\} = (0) \tag{3-9}$$

where

$[\varepsilon]$ = diagonal matrix of 1's and 0's;

ε_{ii} = 1, turns i th constraint on;

ε_{ii} = 0, turns i th constraint off.

Combining the [ε] matrix and the [b] matrix, a short hand notation can be employed,

$$[b_\varepsilon] = [\varepsilon]\ [b] \tag{3-10}$$

Before proceeding with the detailed development of the generalized forces and constraint conditions, the techniques used to solve this set of equations will be discussed.

Multiplying equation (3-8) by $[M]^{-1}$ and employing the short hand notation,

$$\{\ddot{q}\} = -\{\ddot{R}_T\} + [M]^{-1}\ [b_\varepsilon]^T\ \{\lambda\} + [M]^{-1}\ \{Q\} \tag{3-11}$$

Differentiating (3-9),

$$[b_\varepsilon]\ \{\ddot{q}\} + [\dot{b}_\varepsilon]\ \{\dot{q}\} = \{0\} \tag{3-12}$$

Substituting equation (3-11) into equation (3-12), $\{\lambda\}$ can be solved for,

$$\{\lambda\} = \left[[b_\varepsilon]\ [M]^{-1}\ [b_\varepsilon]^T\right]^{-1}\left[[b_\varepsilon]\ \{\ddot{R}_T\} - [\dot{b}_\varepsilon]\ \{\dot{q}\} - [b_\varepsilon]\ [M]^{-1}\ \{Q\}\right] \tag{3-13}$$

The values for $\{\lambda\}$ can be substituted back into equation (3-11) to obtain the solution for the generalized accelerations.

3.3.1 Conservation of Momentum

The boundary nodes are permitted to leave the constraint surface, travel interior to the tank, and recontact the constraint surface at another location. Likewise, free surface points may contact the tank constraint surface. During these impacts, the momentum of the liquid mass normal to the constraint surface is imparted to the tank. Therefore, by conservation of momentum (assuming a coefficient of restitution equal to zero: the liquid does not rebound), the impulse-momentum equations in terms of the constraint conditions can be derived.

$$\int F dt = [b_\varepsilon]^T\ \{f\} = [M]\left[\{\dot{q}\}_+ - \{\dot{q}\}_-\right] \tag{3-14}$$

where

f = the impulsive force;

$\dot{q}_-$ = velocities prior to contact;

$\dot{q}_+$ = velocities after contact.

Hence,

or
$$[M]\ \{\dot{q}\}_+ = [M]\ \{\dot{q}\}_- + [b_\varepsilon]^T\ \{f\} \tag{3-15}$$

$$\{\dot{q}\}_+ = \{\dot{q}\}_- + [M]^{-1}\ [b_\varepsilon]^T\ \{f\} \tag{3-16}$$

Recalling that, after contact, the liquid velocity normal to the wall is zero,

$$[b_\varepsilon]\ \{\dot{q}\}_+ = 0 \tag{3-17}$$

Substituting equation (3-16) into equation (3-17) and solving for the impulsive force,

$$\{f\} = -\left[[b_\varepsilon]\ [M]^{-1}\ [b_\varepsilon]^T\right]^{-1}\ [b_\varepsilon]\ \{\dot{q}\}_- \tag{3-18}$$

Substituting equation (3-18) back into equation (3-16) the final expression for the velocities after contact is,

$$\{\dot{q}\}_+ = \{\dot{q}\}_- - [M]^{-1}\ [b_\varepsilon]^T \left[[b_\varepsilon]\ [M]^{-1}\ [b_\varepsilon]^T\right]^{-1}\ [b_\varepsilon]\ \{\dot{q}\}_- \tag{3-19}$$

3.3.2 The Definition of the Conditions of Constraint

Two constraint conditions are imposed upon the equations of motion for the liquid. The liquid, which is assumed to be incompressible, requires the element volumes to remain constant. This is a time invariant constraint condition. The number of incompressible constraints equals the total number of liquid elements. The second constraint condition requires the liquid to remain within the boundary of the tank (i.e., the tank wall is impermeable). This is a time varying constraint condition, in that, node points may leave and recontact the tank wall. The number of potential impermeable constraints equals the sum of boundary nodes (type II) and free surface nodes (type I). These conditions are expressed in the elements of the [b] matrix. Although the number of actual constraint conditions imposed may vary with time,

the size of the [b] matrix remains constant due to the definition of the [ε] matrix [equation (3-10)]. This approach greatly simplifies the programming of the constraint equations.

Impermeability Constraints - Those node points that lie on the tank wall must satisfy the scalar equation,

$$\bar{n}_j \cdot \dot{\bar{q}}_j = 0 \tag{3-20}$$

where

$\bar{n}_j$ = the outward normal vector to the constraint surface at the jth node point location;

$\dot{\bar{q}}_j$ = velocity vector of the jth boundary node point.

The normal vector is defined as the gradient of the constraint surface, ϕ, evaluated at the jth boundary node point location.

$$\bar{n}_j = \nabla\phi = \left.\frac{\partial\phi}{\partial y}\right|_{y_j,\, z_j} + \left.\frac{\partial\phi}{\partial z}\right|_{y_j,\, z_j} \tag{3-21}$$

where ∇ is the differential operator.

The constraint surface selected to represent the tank wall is a distorted ellipsoid. Referring to the tank sketch (Fig. 3-7), the constraint surface can be defined as,

$$\phi = (y/b_0)^2 + \left(z/(a_0 - a_1 z)\right)^2 - 1 = 0 \tag{3-22}$$

where

$a_0 = a_{fwd}\,(1 + a_1)$;

$a_1 = \left(a_{aft} - a_{fwd}\right)\Big/\left(a_{aft} + a_{fwd}\right)$;

b_0 = semiminor axis of ellipse (tank radius).

Using this definition of the constraint surface, the partial derivatives can be evaluated to obtain an analytical expression for the impermeability constraint of the jth boundary node,

$$\bar{n}_j \cdot \dot{\bar{q}}_j = \frac{2y_j}{b_0^2}\,\dot{y}_j + \frac{2a_0\, z_j}{(a_0 - a_1 z_j)^3}\,\dot{z}_j = 0 \tag{3-23}$$

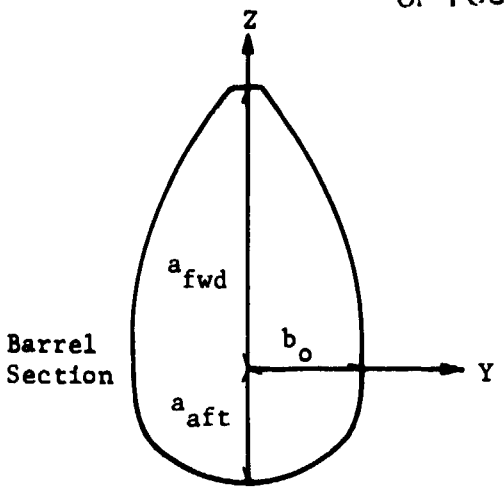

FULL SCALE ET PARAMETERS
a_{fwd} = 176.3 in.
a_{aft} = 424.7 in.
b_o = 165.0 in.

Figure 3-7. Constraint Surface Definition

in matrix form,

$$\left[\frac{2y_j}{b_0^2} \;\middle|\; \frac{2a_0\, z_j}{(a_0 - a_1\, z_j)^3}\right] \begin{Bmatrix} \dot{y}_j \\ \dot{z}_j \end{Bmatrix} = \left[\; b \;\right]_j \{\dot{q}\}_j = \{0\} \tag{3-24}$$

Equation (3-12) requires the time derivatives of the [b] matrix. Hence,

$$[\dot{b}] = \frac{\partial b}{\partial y}\frac{\partial y}{\partial t} + \frac{\partial b}{\partial z}\frac{\partial z}{\partial t} \tag{3-25}$$

Evaluating the partial derivatives,

$$\frac{\partial b}{\partial y} = \frac{2}{b_0^2} \tag{3-26a}$$

$$\frac{\partial b}{\partial z} = \frac{2a_0^2 + 4a_0\, a_1\, z_j}{(a_0 - a_1\, z_j)^4} \tag{3-26b}$$

and writing in matrix form for the j th boundary point,

$$\left[\dot{b}\right]_j = \left[\left(\frac{2}{b_0^2}\right)\dot{y}_j \;\middle|\; \left(\frac{2a_0^2 + 4a_0\, a_1\, z_j}{(a_0 - a_1\, z_j)^4}\right)\dot{z}_j\right] \tag{3-27}$$

Constraint Surface Definition for the Slosh Baffles Region - The ET tank contains slosh baffles that perturb the liquid as it circulates the tank. The concept for incorporating the baffles involves superpositioning the distorted ellipse with a (1 - cos) function to represent the baffles region. The surface equation development begins with the definition of the baffles function. Figure 3-8 shows a schematic of the tank baffles and the definition of the (1 - cos) function, η.

where

$$\eta = \left(1 - \cos \frac{2\pi\xi}{L}\right) h/2 \qquad (3\text{-}28)$$

$$\xi = z - z_l + L/2 \qquad (3\text{-}29)$$

h = Baffle Height
(or Effective Height)

$$L = \frac{z_u - z_L}{N-1}$$

N = Number of Baffles

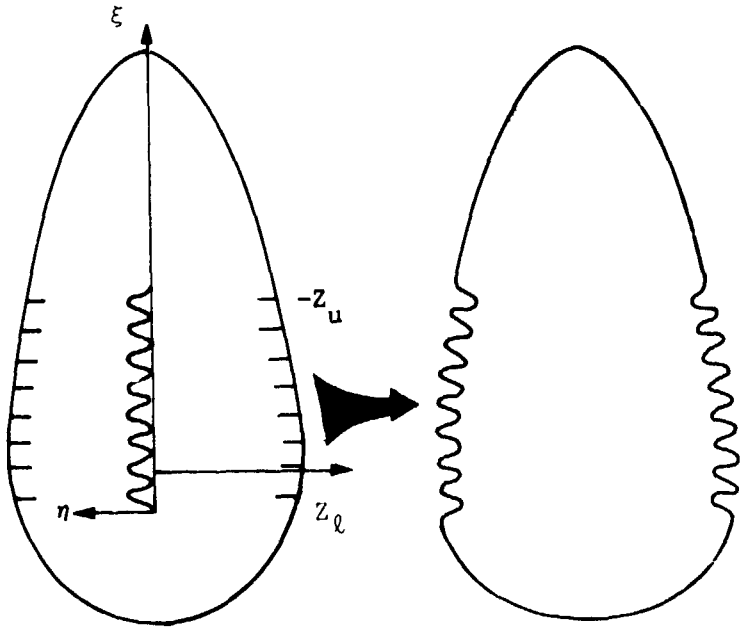

Figure 3-8. Constraint Surface Definition in Baffles Region

Combining equation (3-22) and baffle function in the region of the baffles yields the following surface equation.

$$\phi = \left(\frac{y}{b_0}\right)^2 + \left(\frac{z}{a_0 - a_1 z}\right) - 1 + \frac{2\eta}{b_0}\left[1 - \left(\frac{z}{a_0 - a_1 z}\right)^2\right]^{\frac{1}{2}} - \left(\frac{\eta}{b_0}\right)^2 = 0 \qquad (3\text{-}30)$$

$$\phi = \phi_e + \phi_b$$

$\nabla\phi$ for the baffles region can be written as,

$$\nabla\phi = \left(\frac{\partial\phi_e}{\partial y} + \frac{\partial\phi_b}{\partial y}\right)\hat{j} + \left(\frac{\partial\phi_e}{\partial z} + \frac{\partial\phi_b}{\partial z}\right)\hat{k} \tag{3-31}$$

Defining,

$$\alpha = 1 - \left(\frac{z_j}{a_0 - a_1 z_j}\right)^2 \tag{3-32}$$

and performing the indicated partial differentiations,

$$\frac{\partial\phi_e}{\partial y} = \frac{2y}{b_0{}^2} \tag{3-33a}$$

$$\frac{\partial\phi_e}{\partial z} = -\frac{\partial\alpha}{\partial z} \tag{3-33b}$$

$$\frac{\partial\phi_b}{\partial y} = 0 \ (\phi_b \text{ is a function of z only}) \tag{3-33c}$$

$$\frac{\partial\phi_b}{\partial z} = \frac{\eta}{b_0}\left[\left(\frac{\partial\alpha}{\partial z}\right)\alpha^{-\frac{1}{2}} - \frac{2}{b_0}\frac{\partial\eta}{\partial z}\right] + \frac{2}{b_0}\frac{\partial\eta}{\partial z}\alpha^{\frac{1}{2}} \tag{3-33d}$$

where

$$\frac{\partial\alpha}{\partial z} = \frac{-2a_0 z_j}{(a_0 - a_1 z_j)^3} \quad \text{and} \quad \frac{\partial\eta}{\partial z} = \frac{\pi h}{\ell}\sin\left(\frac{2\pi\xi}{\ell}\right)$$

In matrix form,

$$\left\{\frac{2y_j}{b_0{}^2} \;\middle|\; -\frac{\partial\alpha}{\partial z} + \frac{\eta}{b_0}\left[\frac{\partial\alpha}{\partial z}\alpha^{-\frac{1}{2}} - \frac{2}{b_0}\frac{\partial\eta}{\partial z}\right] + \frac{2}{b_0}\frac{\partial\eta}{\partial z}\alpha^{\frac{1}{2}}\right\}\begin{Bmatrix}\dot{y}_j\\ \dot{z}_j\end{Bmatrix} = [b]_j\{\dot{q}\}_j = \{0\} \tag{3-34}$$

In a fashion similar to the development of equation (3-27), the time derivative of the [b] matrix for the baffles region can be written as,

$$\left\{\frac{2\dot{y}_j}{b_0{}^2} \;\middle|\; \left[-\frac{\partial^2\alpha}{\partial z^2} + \frac{\alpha^{-\frac{1}{2}}}{b_0}\left[\frac{\eta\partial^2\alpha}{\partial z^2} + 2\alpha\frac{\partial^2\eta}{\partial z^2} + 2\frac{\partial\eta}{\partial z}\frac{\partial\alpha}{\partial z} - \frac{\eta}{2}\left(\frac{\partial\alpha}{\partial z}\right)^2\alpha^{-1}\right]\right.\right. \tag{3-35}$$

$$\left.\left. - \frac{2}{b_0{}^2}\left[\left(\frac{\partial\eta}{\partial z}\right)^2 + \eta\frac{\partial^2\eta}{\partial z^2}\right]\right]\dot{z}_j\right\}\begin{Bmatrix}\dot{y}_j\\ \dot{z}_j\end{Bmatrix} = [\dot{b}]_j\{\dot{q}\}_j$$

where

$$\frac{\partial^2 \alpha}{\partial z^2} = \frac{-2a_0\left[a_0 - 2a_1 z_j\right]}{\left(a_0 - a_1 z_j\right)^3}$$

$$\frac{\partial^2 \eta}{\partial z^2} = \frac{2h\pi^2}{\ell^2} \cos\left(\frac{2\pi\xi}{\ell}\right)$$

Propellant/Tank Interaction Forces - The constraint force, λ, is defined positive (compression) when acting inward toward the liquid and negative (tension) when acting outward. Therefore, when the constraint force is acting to prevent wall penetration, λ is positive. The units of [b] in equation (3-9) are (1/cm), and the units of [$\dot{b}$] in equation (3-12) are (1/cm-s). Hence, the units of the impermeability lambda's in equation (3-13) are,

$$\left[\frac{1}{cm}\,\frac{1}{gr}\,\frac{1}{cm}\right]^{-1}\left[\frac{1}{s^2}\right] = \frac{cm^2\ gr}{s^2} = \text{dyne-cm} \tag{3-36}$$

The units should be dynes. The inconsistency occurs because the definition of the impermeability constraint, equation (3-20), used the normal vector, $\bar{n}_j$, instead of the unit normal, $\bar{n}/|\bar{n}|$. Therefore, the impermeability lambdas must be multiplied by the magnitude of the normal to obtain the proper units. These forces are resolved into the tank coordinate system by using components of the normal vector. Therefore, the total liquid forces acting on the tank are,

$$F_y = -\sum_1^j \left(\lambda_j \quad \left(\bar{n}_j \cdot \hat{j}\right)\right) \tag{3-37}$$

$$F_z = -\sum_1^j \left(\lambda_j \quad \left(\bar{n}_j \cdot \hat{k}\right)\right) \tag{3-38}$$

$$M_x = \sum_1^j \left(F_{y_j} z_j - F_{z_j} y_j \right) \tag{3-39}$$

Boundary Constraint Relaxation and Enforcement - Because the impermeability constraint varies in time, criteria for switching the constraint are required. Criteria for enforcement and relaxation of the constraint must satisfy the physics of the problem and account for the limitations of the numerical integration method.

The obvious physical condition for enforcing the constraint is that the node point reaches the boundary. Substituting the node points position coordinates into the surface equation,

$$\left[(y/b_0)^2 + \left(\frac{z}{a_0 - a_1 z}\right)^2\right],$$

will yield a value for ϕ identically equal to one when the node is on the boundary. Coordinates of a point inside the boundary will have a value less than one and points outside the boundary will have a value greater than one. Therefore, by evaluating ϕ, a criteria for enforcement can be established.

Numerical integration is not a continuous solution but rather a solution at some discrete interval of time. Therefore, node points approaching the boundary (possible enforcement) will generally not fall exactly on the boundary. This problem can be solved by defining two parallel surfaces interior to the actual boundary. Referring to Figure 3-9, define ϕ_1, as the most interior surface, and ϕ_2 the surface closest to the actual boundary. These surfaces are located epsilon distances from the tank boundary (ϵ_1 and ϵ_2) such that, $\phi_1 = 0.98$ and $\phi_2 = 0.99999$. A node point (point A, Figure 3-9) entering the region between ϕ_1 and the tank boundary shall be considered a candidate for constraint enforcement. Penetration of the boundary by point A is prevented during the next integration time interval, as follows. If the velocity vector of point A, (V_A), is directed towards the boundary, penetration is likely. Therefore, if the angle, σ, between the velocity vector and the tank surface normal is less then 91°, the constraint is enforced. A node point (point B) entering the region between ϕ_2 and the boundary is considered to be in the proximity of the boundary resulting in constraint enforcement.

Test observations have shown that the liquid will leave the tank wall when encountering the baffles. To account for this phenomenon, the constraint forces are relaxed (removed) if three criteria are met. Referring to Figure 3-10, these criteria can be defined as,

1) $\lambda < 0$, tensile force on liquid;

2) FT > GF * Fa, the tank/liquid interaction force component in the direction of the D'Alembert force, Fa, is greater than a factor, GF, times the D'Alembert force. Note, the force on the tank is opposite the liquid constraint force;

3) The node point to be relaxed is adjacent to a free surface node.

The first criterion indicates the liquid is "pulling" on the tank wall and is no longer trying to penetrate. This force should equal or exceed the projection of the D'Alembert forces onto the surface normal. The coefficient, GF, provides a mechanism to account for adhesive or other empirical forces the liquid might exert on the tank (generally, GF was equal to 1.0 in the correlation analysis). The third criterion prevents a bubble from forming between liquid and the wall.

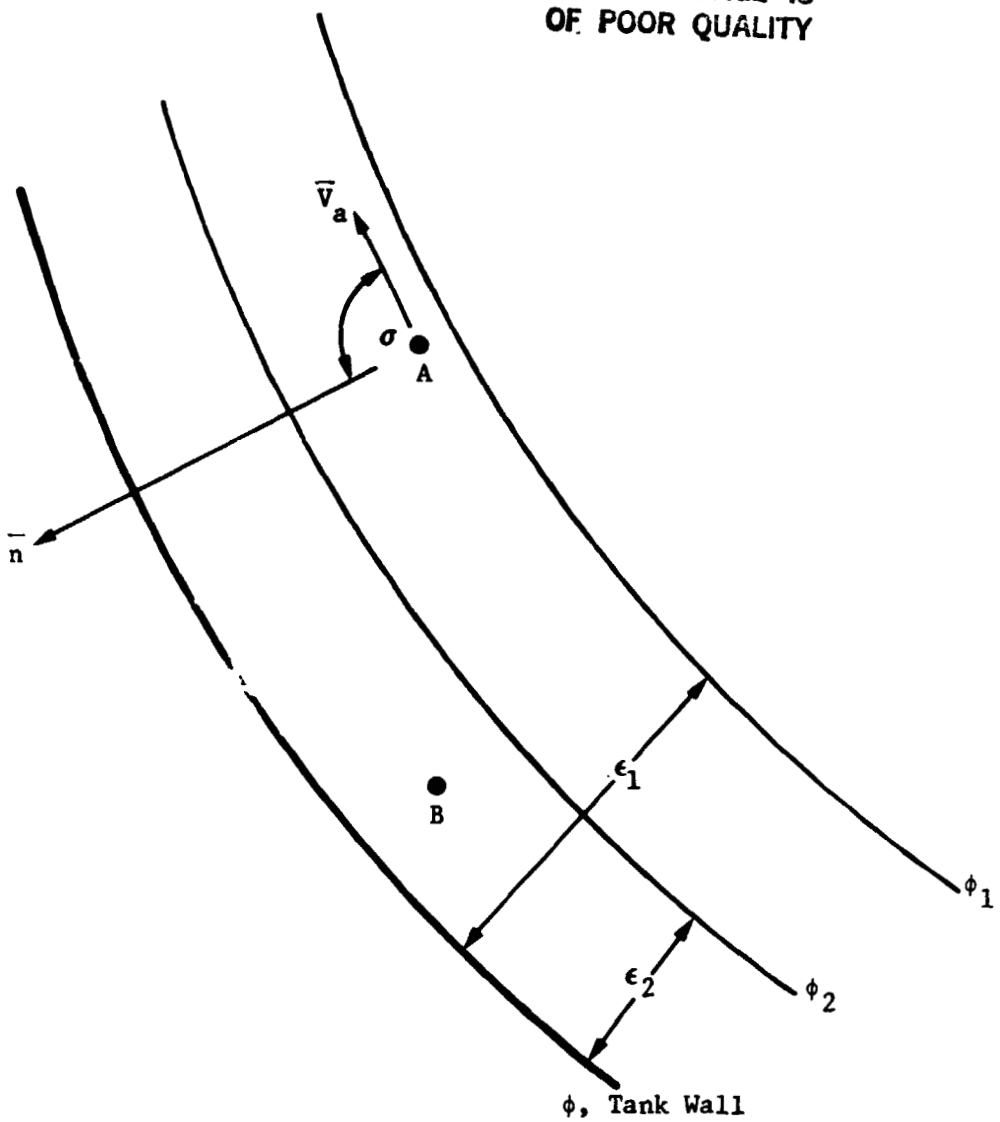

Figure 3-9. Constraint Enforcement Criteria

Incompressibility Constraints - The incompressibility constraint is maintained at all times, therefore it is an invariant constraint condition. This constraint requires the time rate of change of each finite element volume to be zero. The finite element employed in this model is a constant thickness triangular element that has one node point at each vertex. Figure 3-11 depicts a typical element with a vertex numbering of i, j, k. If two vectors, $\bar{a}$ and $\bar{b}$, are defined where $\bar{a}$ is a vector from the vertex i to k and $\bar{b}$ is a vector from vertex i to j, the element volume can be written,

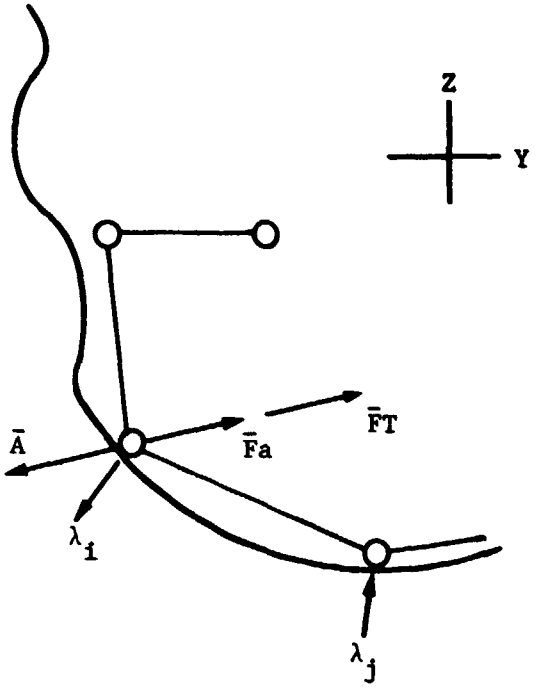

Figure 3-10. Constraint Relaxation Criteria

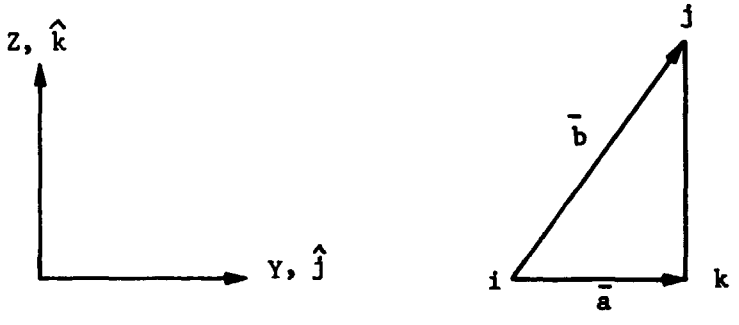

Figure 3-11. Triangular Element Definition

$$\Psi_e = A_e \quad t = \frac{1}{2}(\bar{a} \times \bar{b}) = \text{constant} \tag{3-40}$$

where

Ψ_e = element volume (constant);

A_e = element area;

t = element thickness

$\bar{a} = (y_k - y_i)\hat{j} + (z_k - z_i)\hat{k}$

$\bar{b} = (y_j - y_i)\hat{j} + (z_j - z_i)\hat{k}$

Expanding the vector cross product and dividing through by 1/2 t, equation (3-40) becomes,

$$(y_k - y_j)(z_j - z_i) - (z_k - z_i)(y_j - y_i) = \text{new constant} \tag{3-41}$$

The time derivative of this expression must equal zero. Therefore, differentiating with respect to time,

$$\begin{aligned}(z_k - z_j)\dot{y}_i + (z_i - z_k)\dot{y}_j + (z_j - z_i)\dot{y}_k + (y_j - y_k)\dot{z}_i \\ + (y_k - y_i)\dot{z}_j + (y_i - y_j)\dot{z}_k = 0\end{aligned} \tag{3-42}$$

Casting into the matrix form: $[b]\{\dot{q}\}$,

$$\left[z_k - z_j \;\middle|\; y_j - y_k \;\middle|\; z_i - z_k \;\middle|\; y_k - y_i \;\middle|\; z_j - z_i \;\middle|\; y_i - y_j\right] \begin{Bmatrix} \dot{y}_i \\ \dot{z}_i \\ \dot{y}_j \\ \dot{z}_j \\ \dot{y}_k \\ \dot{z}_k \end{Bmatrix} \tag{3-43}$$

The time derivative of [b] for the incompressibility constraint is,

$$[\dot{b}] = \left[\dot{z}_k - \dot{z}_i \;\middle|\; \dot{y}_j - \dot{y}_k \;\middle|\; \dot{z}_i - \dot{z}_k \;\middle|\; \dot{y}_k - \dot{y}_i \;\middle|\; \dot{z}_j - \dot{z}_i \;\middle|\; \dot{y}_i - \dot{y}_j\right] \quad (3\text{-}44)$$

These constraint conditions (number of elements in size) were combined with the impermeability constraints (number of exterior node points in size) to complete the constraint definition.

3.3.3 Viscous Dissipative Forces

The generalized forces, Q_k, applied to the liquid are composed of viscous dissipative forces. To arrive at an expression for these generalized forces, the viscous shear forces within an element were equated to the forces applied at the element's node points. Consider a differential volume of liquid within the triangular finite element (Fig. 3-12).

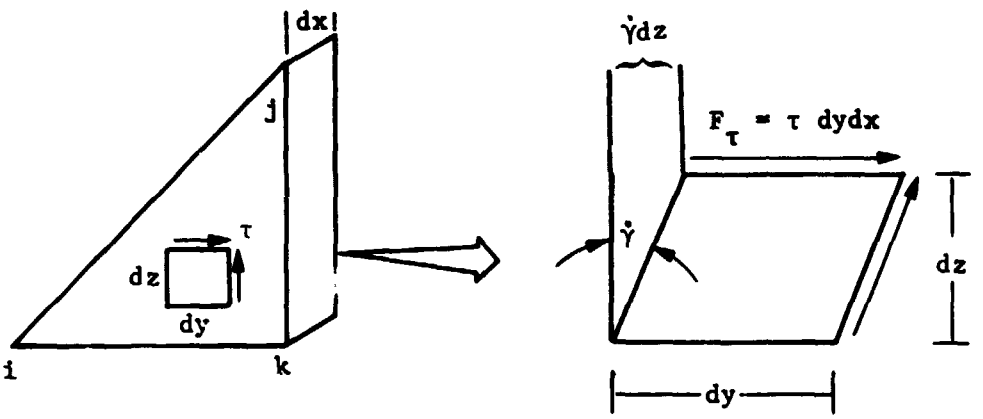

where

$\dot{\gamma}$ = Shear Strain Rate

τ = Shear Stress*

dx = t, the Element Thickness

F_τ = Shear Force

*In a fluid, deviatoric shear stress cannot occur without motion; shear is a function of Velocity instead of displacement.

Figure 3-12. Liquid Shear Stress Definition

The virtual velocities of the liquid can be defined analogous to virtual displacements. Therefore, expressing $\dot{\gamma}dz$ as the shearing velocity, the virtual velocities of the liquid in shear are, $\delta\dot{\gamma}\,dz$. When this was combined with the shear force expression shown in Figure 3-12, the virtual power (time derivative of virtual work, $\delta\dot{W}$) of the dissipative forces was obtained.* Thus,

---

*Refer to Appendix A for a detailed discussion of the virtual power concept.

$$\delta\dot{W} = -\tau\delta\dot{\gamma}\ dxdydz \tag{3-45}$$

The virtual power of the nodal point forces must equal the virtual power of the internal shear forces. Defining $\delta\ \dot{q}_e$ as the virtual velocities of the generalized coordinates, the virtual power of the nodal point forces can be written as,

$$\delta\dot{W} = F_v \cdot \delta\dot{q}_e = -\tau\delta\dot{\gamma}\ dxdydz \tag{3-46}$$

where

F_v = nodal point forces due to viscous shearing.

Solving for the nodal point forces,

$$F_v = -\tau \frac{\delta\dot{\gamma}}{\delta\dot{q}_e}\ dxdydz \tag{3-47}$$

The total nodal point forces for an element are obtained by integrating over the element volume.

$$F_{v_e} = -\int_{\Psi} \tau \frac{\delta\dot{\gamma}}{\delta\dot{q}_e}\ dxdydz = -t \int_{A} \tau \frac{\delta\dot{\gamma}}{\delta\dot{q}_e}\ dydz \tag{3-48}$$

Now, the shear strain rate can be expressed in terms of the liquid velocities. Thus, for two-dimensional flow,

$$\dot{\gamma} = \frac{\partial w}{\partial y} + \frac{\partial v}{\partial z} \tag{3-49}$$

where

v = velocity in y direction;

w = velocity in z direction.

Furthermore, from fluid mechanics, the shear stress can be expressed as,

$$\tau = \mu\dot{\gamma}, \text{ for nonparallel laminar flow} \tag{3-50a}$$

or

$$\tau = (\mu + \rho\varepsilon)\dot{\gamma}, \text{ for turbulent flow} \tag{3-50b}$$

where

μ = liquid dynamic viscosity;

ρ = liquid density;

ε = liquid eddy viscosity (not a fluid property).

By employing the laminar flow definition of the shear stress and using equation (3-49) the nodal point force definition becomes,

$$F_{v_e} = -\mu t \int_A \left(\frac{\partial w}{\partial y} + \frac{\partial v}{\partial z}\right) \frac{\partial}{\partial \dot{q}_e} \left(\frac{\partial w}{\partial y} + \frac{\partial v}{\partial z}\right) dydz \tag{3-51}$$

The expression for the nodal point forces requires definition of the velocity field within the finite element. Displacements and velocities of the element can be approximated by linear shape functions. These shape functions relate displacement and velocities of any point within the element's boundaries to the displacements and velocities of the element's node points. The area coordinates of the triangular elemental region were selected as the approximating shape functions (these are linear shape functions having constant derivatives).* Thus, the displacement field within the element can be written as,

$$y = N_i y_i + N_j y_j + N_k y_k \tag{3-52a}$$

$$z = N_i z_i + N_j z_j + N_k z_k \tag{3-52b}$$

with the condition,

$$N_i + N_j + N_k = 1 \tag{3-52c}$$

The shape functions for each node point are,

---

*An excellent discussion of the use of area coordinates in finite elements is presented in Reference [13].

$$N_i = \frac{1}{2A}\left[y_j z_k - y_k z_j + \left[z_j - z_k\right]y + \left[y_k - y_j\right]z\right] \quad (3\text{-}53a)$$

$$N_j = \frac{1}{2A}\left[y_k z_i - z_k y_i + \left[z_k - z_i\right]y + \left[y_i - y_k\right]z\right] \quad (3\text{-}53b)$$

$$N_k = \frac{1}{2A}\left[y_i z_j - y_j z_i + \left[z_i - z_j\right]y + \left[y_j - y_i\right]z\right] \quad (3\text{-}53c)$$

where

A = area of the element;

y_n, z_n = the coordinates of the element's nth vertex.

The area coordinates are functions of geometry only. Therefore, the velocity field can be written as,

$$v = N_i\dot{y}_i + N_j\dot{y}_j + N_k\dot{y}_k \quad (3\text{-}54a)$$

$$w = N_i\dot{z}_i + N_j\dot{z}_j + N_k\dot{z}_k \quad (3\text{-}54b)$$

The strain rates can now be determined,

$$\frac{\partial w}{\partial y} = \frac{\partial w}{\partial N_i}\frac{\partial N_i}{\partial y}\dot{z}_i + \frac{\partial w}{\partial N_j}\frac{\partial N_j}{\partial y}\dot{z}_j + \frac{\partial w}{\partial N_k}\frac{\partial N_k}{\partial y}\dot{z}_k \quad (3\text{-}55a)$$

$$\frac{\partial v}{\partial z} = \frac{\partial v}{\partial N_i}\frac{\partial N_i}{\partial z}\dot{y}_i + \frac{\partial v}{\partial N_j}\frac{\partial N_j}{\partial z}\dot{y}_j + \frac{\partial v}{\partial N_k}\frac{\partial N_k}{\partial z}\dot{y}_k \quad (3\text{-}55b)$$

or

$$\frac{\partial v}{\partial y} = 1/2A\left[\dot{z}_i(z_j - z_k) + \dot{z}_j(z_k - z_i) + \dot{z}_k(z_i - z_j)\right] \quad (3\text{-}56a)$$

$$\frac{\partial v}{\partial z} = 1/2A\left[\dot{y}_i(y_k - y_j) + \dot{y}_j(y_i - y_k) + \dot{y}_k(y_j - y_i)\right] \quad (3\text{-}56b)$$

For convenience, define a local element coordinate system, that originates at node i. Therefore, the j and k nodal coordinates relative to node i can be expressed,

$$\bar{y} = y - y_i = N_j \bar{y}_j + N_k \bar{y}_k \tag{3-57a}$$

$$\bar{z} = z - z_i = N_j \bar{z}_j + N_k \bar{z}_k \tag{3-57b}$$

By Using this definition of the coordinates, equations (3-56a) and (3-56b) become,

$$\frac{\partial w}{\partial y} = 1/2A \left[\dot{z}_i \left(\bar{z}_j - \bar{z}_k \right) + \dot{z}_j \left(\bar{z}_k \right) - \dot{z}_k \left(\bar{z}_j \right) \right] \tag{3-58a}$$

$$\frac{\partial v}{\partial z} = 1/2A \left[\dot{y}_i \left(\bar{y}_k - \bar{y}_j \right) - \dot{y}_j \left(\bar{y}_k \right) + \dot{y}_k \left(\bar{y}_j \right) \right] \tag{3-58b}$$

In addition to the strain rates we require $\frac{\partial}{\partial \dot{q}_k} \left(\frac{\partial w}{\partial y} + \frac{\partial v}{\partial z} \right)$.

When performing the indicated partial differentiation the rate of change of the shear strain rate is determined with respect to the nodal point generalized velocities.

$$\frac{\partial}{\partial \dot{y}_i} = \left(\bar{y}_k - \bar{y}_j \right) / 2A \tag{3-59a}$$

$$\frac{\partial}{\partial \dot{y}_j} = -\bar{y}_k / 2A \tag{3-59b}$$

$$\frac{\partial}{\partial \dot{y}_k} = \bar{y}_j / 2A \tag{3-59c}$$

$$\frac{\partial}{\partial \dot{z}_i} = \left(\bar{z}_j - \bar{z}_k \right) / 2A \tag{3-59d}$$

$$\frac{\partial}{\partial \dot{z}_j} = \bar{z}_k / 2A \tag{3-59e}$$

$$\frac{\partial}{\partial \dot{z}_k} = -\bar{z}_j / 2A \tag{3-59f}$$

By substituting equations (3-58) and (3-59) to equation (3-51) and integrating over the element volume, the nodal point dissipative forces are obtained,

$$Fvy_i = -t\mu\left(\bar{y}_k - \bar{y}_j\right)\dot{\gamma}/4A \tag{3-60a}$$

$$Fvz_i = -t\mu\left(\bar{z}_j - \bar{z}_k\right)\dot{\gamma}/4A \tag{3-60b}$$

$$Fvy_j = t\mu\ \bar{y}_k\ \dot{\gamma}/4A \tag{3-60c}$$

$$Fyz_j = -t\mu\ \bar{z}_k\ \dot{\gamma}/4A \tag{3-60d}$$

$$Fvy_k = -t\mu\ \bar{y}_j\ \dot{\gamma}/4A \tag{3-60e}$$

$$Fvz_k = t\mu\ \bar{z}_j\ \dot{\gamma}/4A \tag{3-60f}$$

where

$$\dot{\gamma} = \left[\dot{z}_i\left(\bar{z}_j - \bar{z}_k\right) + \dot{z}_j\bar{z}_k - \dot{z}_k\bar{z}_j + \dot{y}_i\left(\bar{y}_k - \bar{y}_j\right) - \dot{y}_j\bar{y}_k + \dot{y}_k\bar{y}_j\right] \tag{3-61}$$

The nodal point forces (Eq. 3-60) are the components of the generalized force vector, $\bar{Q}_k$, in equation (3-7).

3.3.4 Element Mass Matrices

Two techniques were employed to distribute the liquid mass to the element node points. The first technique was a lumped mass approach. The mass of each element was calculated (based on the element volume) and divided equally among the three node points. Element volume was determined from the element area and thickness normal to the Y-Z plane. The thickness was permitted to vary from element to element dependent upon the tank width (X direction) at a given element's centroid. This resulted in elements at the tank boundary having less mass than those at the center of the tank. This method of mass distribution for an element produces a (6x6) diagonal mass matrix. The element mass matrix [equation (3-62)], has 1/3 of the element's mass lumped in the Y and Z direction at each element node point.

$$M_E = \rho t A \begin{bmatrix} 1/3 & & & & & & & & & & & 0 \\ & 1/3 & & & & & & & & & & \\ & & 1/3 & & & & & & & & & \\ & & & 1/3 & & & & & & & & \\ & & & & 1/3 & & & & & & & \\ & & & & & 1/3 & & & & & & \\ & & & & & & 1/3 & & & & & \\ & & & & & & & 1/3 & & & & \\ & & & & & & & & 1/3 & & & \\ & & & & & & & & & 1/3 & & \\ & & & & & & & & & & 1/3 & \\ 0 & & & & & & & & & & & 1/3 \end{bmatrix} \tag{3-62}$$

The second approach developed a consistent mass matrix for each element. This form of mass matrix was derived from the kinetic energy expression for the liquid. Kinetic energy can be expressed by using generalized coordinates, q, and the liquid density, ρ.

$$\text{K.E.} = 1/2 \int_{\forall} \rho \dot{q}^2 \, d\forall \tag{3-63}$$

It is assumed that the displacements of these generalized coordinates can be approximated over a finite element region of the volume by a set of linear approximating functions. Thus, for one element,

$$\{q\} = [N] \{q_e\}: \tag{3-64}$$

where

$[N]$ = The shape functions over an elemental region [see equation (3-53)];

$\{q_e\}$ = The nodal point displacements for the element.

The kinetic energy expression requires the time derivative of the generalized coordinates. Furthermore, this representation of the velocities should be consistent with the representation of the displacements; therefore, recalling equation (3-54) the generalized velocities can be written as,

$$\{\dot{q}\} = [N] \{\dot{q}_e\} \tag{3-65}$$

Substituting the expression for the generalized velocities into the kinetic energy expression and summing over the number of elements used to represent the liquid volume results in,

$$K.E. = 1/2 \sum_{i=1}^{i=numel} \int_{\forall_i} \left\{\dot{q}_{e_i}\right\}^T [N]^T \rho_i [N] \left\{\dot{q}_{e_i}\right\} d\forall_i \qquad (3\text{-}66)$$

The element mass matrix is defined from this expression as,

$$M_e = \int_{\forall_e} [N]^T \rho [N] d\forall_e \qquad (3\text{-}67)$$

If the expressions for the shape functions [equations (3-53)] are substituted into the integral, assuming constant density and constant thickness over the area of the element, the results are:

$$M_e = \rho t \int_A \begin{vmatrix} N_iN_i & N_iN_j & 0 & N_iN_k & 0 & \\ 0 & N_iN_i & 0 & N_iN_j & 0 & N_iN_k \\ N_jN_i & 0 & N_jN_j & 0 & N_jN_k & 0 \\ 0 & N_jN_i & 0 & N_jN_j & 0 & N_jN_k \\ N_kN_i & 0 & N_kN_j & 0 & N_kN_k & 0 \\ 0 & N_kN_i & 0 & N_kN_j & 0 & N_kN_k \end{vmatrix} dA \qquad (3\text{-}68)$$

Now it can be shown that,

$$\iint N_r N_s dydz = \begin{cases} 1/12 \text{ area}, & r \neq s \\ 1/6 \text{ area}, & r = s \end{cases} \qquad (3\text{-}69)$$

Therefore, the consistent mass matrix for an element i,

$$M_e = \rho t A \begin{vmatrix} 1/6 & 0 & 1/12 & 0 & 1/12 & 0 \\ 0 & 1/6 & 0 & 1/12 & 0 & 1/12 \\ 1/12 & 0 & 1/6 & 0 & 1/12 & 0 \\ 0 & 1/12 & 0 & 1/6 & 0 & 1/12 \\ 1/12 & 0 & 1/12 & 0 & 1/6 & 0 \\ 0 & 1/12 & 0 & 1/12 & 0 & 1/6 \end{vmatrix} \quad (3\text{-}70)$$

Note that the consistent element mass matrix produces inertial coupling between the element node points. For example, the first row of equation (3-70) couples the y coordinat s for the element's three node points. Thus, the inertial forces in the y direction at node one reflect the y acceleration at nodes two and three. The total mass at each node is determined by summing the consistent mass matrices over all the elements.

This discussion concludes the development of the two-dimensional equations of motion for the liquid. These equations were incorporated into a FORTRAN IV program called LAMPS2. A user's guide for the program is delineated in Appendix B. The next section of this chapter discusses the implementation of the computer prog am and some special numerical techniques used in solving the equations of motion.

3.4 COMPUTER PROGRAM IMPLEMENTATION AND NUMERICAL TECHNIQUES

Several numerical techniques were required to implement the equations of motion into a workable computer program. These techniques included methods to generate the finite element mesh, initialize the position of the liquid in the tank and integrate the equation of motion with a variable time step. The following paragraphs delineate these techniques.

3.4.1 Finite Element Mesh Generation (MESH2 Program)

A technique to divide the liquid volume into a set of triangular finite elements was required. A two dimensional mesh generation program, MESH2, was developed to meet this requirement. This mesh program generates a triangular finite element mesh for the axisymmetric orientation of the liquid. Asymmetric mesh arrangements were obtained by the technique discussed in Section 3.4.2.

The axisymmetric orientation of the liquid (Fig. 3-6) is bounded by the tank wall and liquid free surface. The tank wall is defined by the constraint surface equation. The free surface location of the liquid

can be determined from the tank geometry, fill volume and the acceleration vector direction. An iterative method to calculate the free surface location had previously been developed [Ref 1], and was available in a subroutine called FLUDCG. The MESH2 program used this subroutine to calculate the free surface location of the liquid in the tank.

Having analytically defined all the boundaries of the liquid, the problem is to divide the liquid in a uniform fashion. Due to the curved boundaries of the tank wall, this is difficult to accomplish in the tank rectangular coordinate system. The problem can be solved by using curvilinear coordinates to map square meshes in the ξ-η plane into quadralaterals with parabolic sides in the Y-Z plane. An example of this is shown in Figure 3-13.

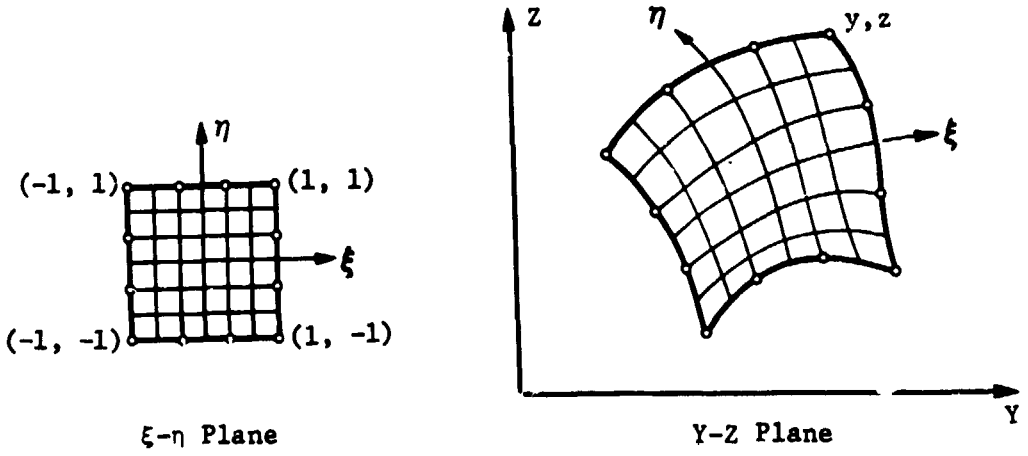

Figure 3-13. Curvilinear Mapping

This mapping indicates that for every point in the ξ-η plane, there is a corresponding point in the Y-Z plane. Therefore, the ξ-η plane can be divided uniformly to produce uniform divisions in the Y-Z plane. The resultant mesh in the Y-Z plane reflects the curved boundaries.

This method of mesh generation requires the definitions of the mapping relationships from the ξ-η plane to the Y-Z plane,

$$y = y(\xi,\eta) \tag{3-71a}$$

$$z = z(\xi,\eta) \tag{3-71b}$$

The MESH2 program employs a set of "serendipity" shape functions [Ref 13] derived from an eight-noded rectangular element in the ξ-η plane. In terms of shape functions, the mapping relationships become,

$$y(\xi,\eta) = \sum_{i=1}^{8} N_i \, yc_i \qquad (3\text{-}72a)$$

$$z(\xi,\eta) = \sum_{i}^{8} N_i \, zc_i \qquad (3\text{-}72b)$$

where

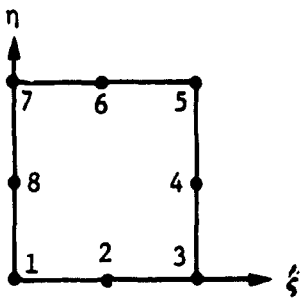

$$N_1 = +1.0\ (1 - \xi)(1 - \eta)(1 - 2\xi - 2\eta)$$
$$N_2 = +4.0\ (\xi)(1 - \xi)(1 - \eta)$$
$$N_3 = -1.0\ (\xi)(1 - \eta)(1 - 2\xi + 2\eta)$$
$$N_4 = +4.0\ (\xi)(\eta)(1 - \eta)$$
$$N_5 = -1.0\ (\xi)(\eta)(3 - 2\xi - 2\eta)$$
$$N_6 = +4.0\ (\xi)(1 - \eta)(\eta)$$
$$N_7 = -1.0\ (1 - \xi)(\eta)(1 + 2\xi - 2\eta)$$
$$N_8 = +4.0\ (1 - \xi)(\eta)(1 - \eta)$$

The (yc_i, zc_i) coordinates are eight points that define the boundary of the region that is being mapped by the ξ-η plane. The three points along any side are used to define the parabolic curve in the Y-Z plane used for that side. The mesh definition is obtained by defining the number of divisions along sides 1 and 2. The ξ-η plane is then divided into the specific number of divisions and the ξ-η coordinates are obtained. The ξ-η coordinates are then transformed, by using the shape functions, into the Y-Z plane [equation (3-72)].

Figure 3-14 shows two arrangements of the boundary nodes used to define two mesh orientations. In either case, the node point-side definition is,

Side 1 - Nodes 1,2,3

Side 2 - Nodes 3,4,5

Side 3 - Nodes 5,6,7

Side 4 - Nodes 7,8,1

After mapping, if the mesh boundary points do not match the boundary location as defined by the distorted ellipsoidal constraint surface (due to parabolic mapping), the boundary points are moved to match the constraint surface definition.

The triangular elements are formed by selecting the shortest diagonal in each square after mapping to the Y-Z plane. If a series of rectangular elements are created with equal diagonals, the direction of the diagonal is alternated from one element to the next.

Examples of the type I and type II mesh arrangements are shown for a 10% full tank in Figures 3-15 and 3-16, respectively. Both mesh types were evaluated in the correlation analysis.

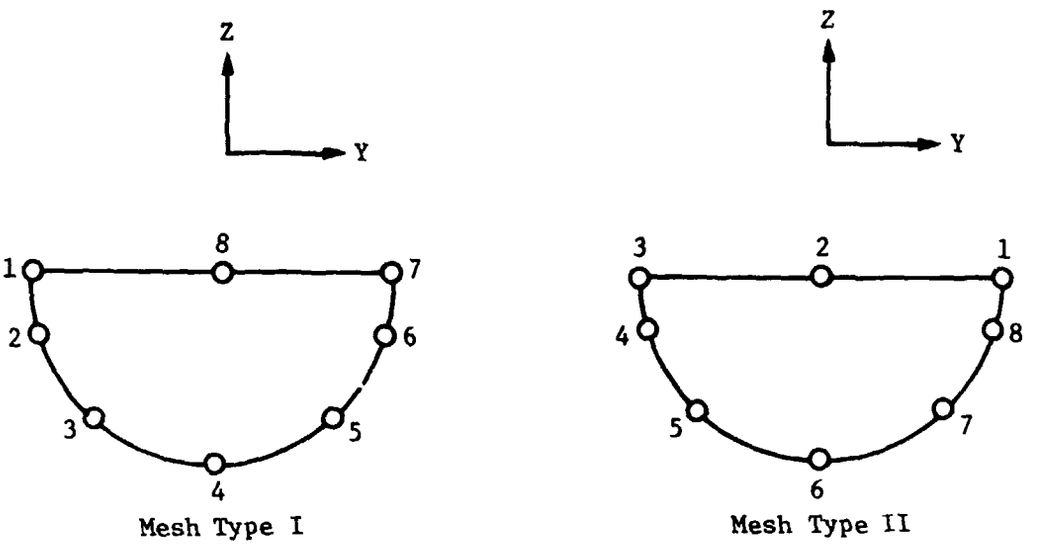

Figure 3-14. Boundary Node Arrangement for Mesh Generation

3.4.2 Liquid Initial Position

The mesh generation program considered only the axisymmetric orientation of the liquid. Initial positions of the liquid, other than the axisymmetric case were required for the correlation analysis. These asymmetric orientations were determined by an iterative scheme that minimized the potential energy of the liquid.

Figure 3-17 shows a sketch of the tank tilted with respect to the gravity vector. Hence, the axisymmetric orientation is not the equilibrium position. There is a delta potential energy (ΔPE) between the center of mass position of the axisymmetric orientation and the true equilibrium position. Minimizing this ΔPE yields an equilibrium state for the liquid in the tilted tank.

Calculation of the potential energy requires a reference datum. This datum will vary with the orientation of the tank with respect to the initial acceleration vector. This makes it difficult to calculate the potential energy of the liquid. An alternative approach is to calculate the kinetic energy of the liquid as it moves from the axisymmetric orientation to the equilibrium position. The kinetic energy peaks as minimum potential energy is achieved. Furthermore, if the liquid velocity is killed at the point at which the kinetic energy is a maximum, the liquid remains at rest, since it is at a minimum potential energy state.

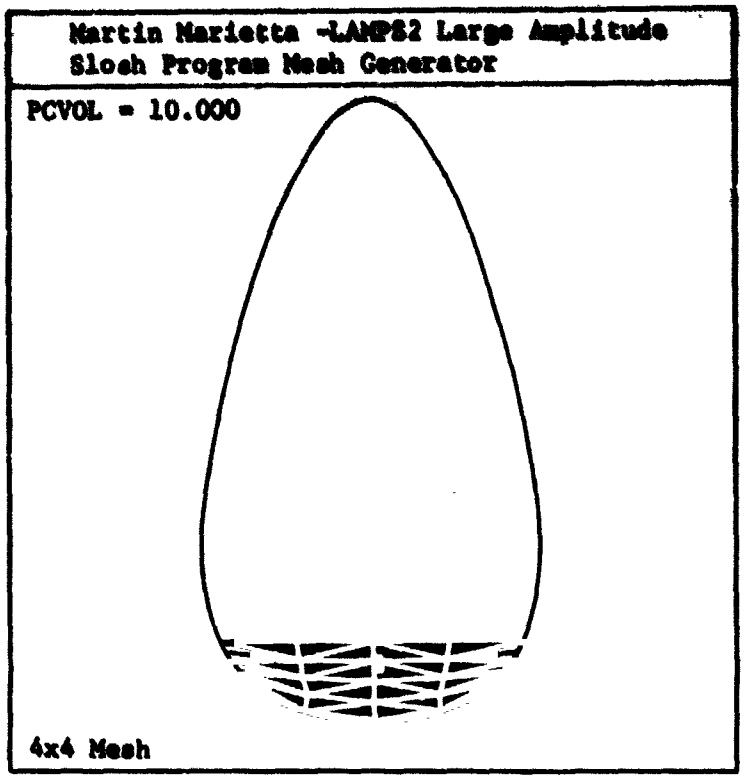

Figure 3-15. Mesh Type I Example

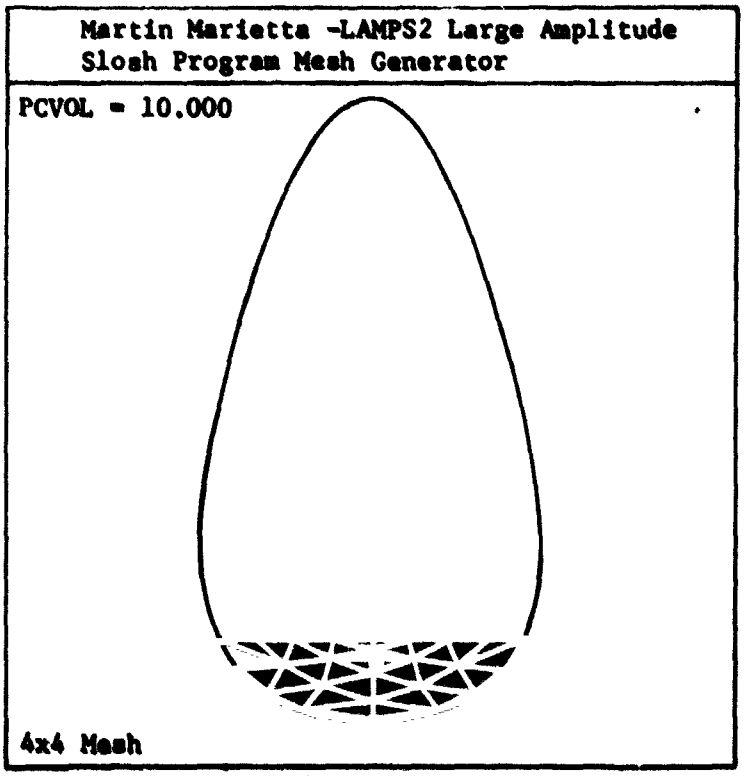

Figure 3-16. Mesh Type II Example

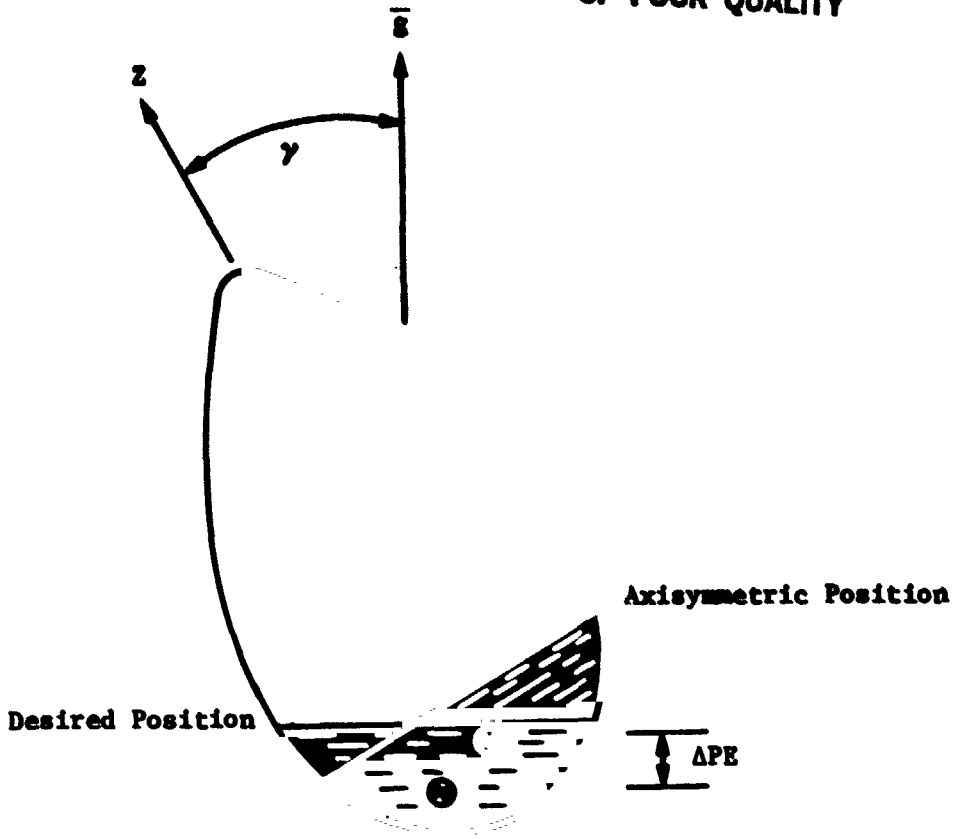

Figure 3-17. Asymmetric Liquid Orientation

The method by which the kinetic energy is determined relies on numerical integration of the equations of motion given the initial acceleration vector. The direction of the acceleration vector is defined by specifying a tilt angle of the tank (Y) with respect to the gravity vector. This is shown in Figure 3-17.

The kinetic energy time history produced by this technique is not continuous. Therefore, the point at which the slope of the kinetic energy time history is zero (a minimum or maximum) can not be determined exactly. The rate of change of KE can be expressed by a difference equation based on the current kinetic energy (KE_c) and the kinetic energy at the previous integration step (KE_ℓ).

$$\frac{dKE}{dt} \simeq \frac{KE_c - KE_\ell}{\Delta t} \qquad (3\text{-}73)$$

where: Δt is the integration time step.

The LAMPS2 program requires that this approximation of the slope of the kinetic energy time history be less than a small number, εKE, for convergence to an equilibrium state. The program facilitates convergence by killing the liquid velocity as the kinetic energy passes through a maximum. Figure 3-18 shows an example of this stratagem.

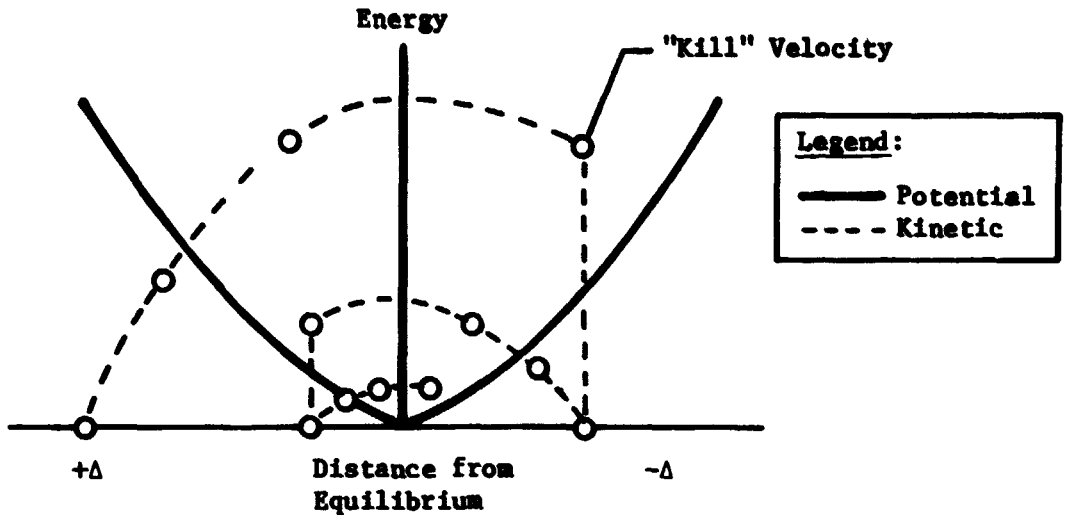

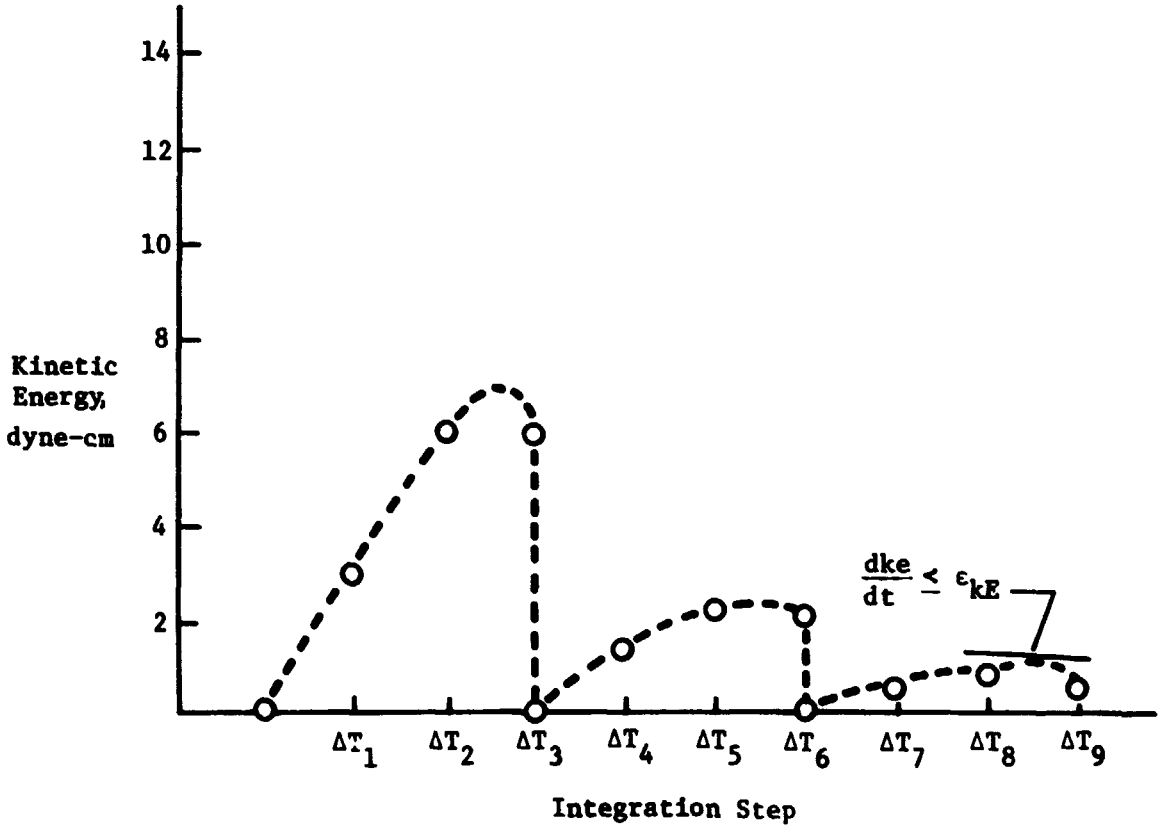

Figure 3-18.
A Stratagem for Liquid Position Initialization Based on Kinetic Energy

The top graph shows an energy diagram of the liquid as it approaches the equilibrium position. The lower graph depicts the kinetic energy time history.

An additional capability included in the convergence procedure is the ability to move the liquid to the desired tank tilt, in increments of the tilt angle. The angle of tilt is divided into NGAMMA segments and the liquid equilibrium positions are determined for each successive segment. This capability is useful for large angles of tank tilt ($\gamma > 20^{o}$).

3.4.3 Variable Integration Step Algorithm

The purpose of the variable step integration algorithm is to prevent tank wall penetration by a free surface or boundary node point. This penetration can result from too large an integration interval. This penetration can be prevented by reducing the magnitude of the integration step size. The integration interval required to prevent penetration, DTNEW, can be calculated by estimating the new positions of the nodes based on their current state definitions.

Referring to Figure 3-19, the estimated position, R_E, of a point may be obtained through the following kinematic relationship,

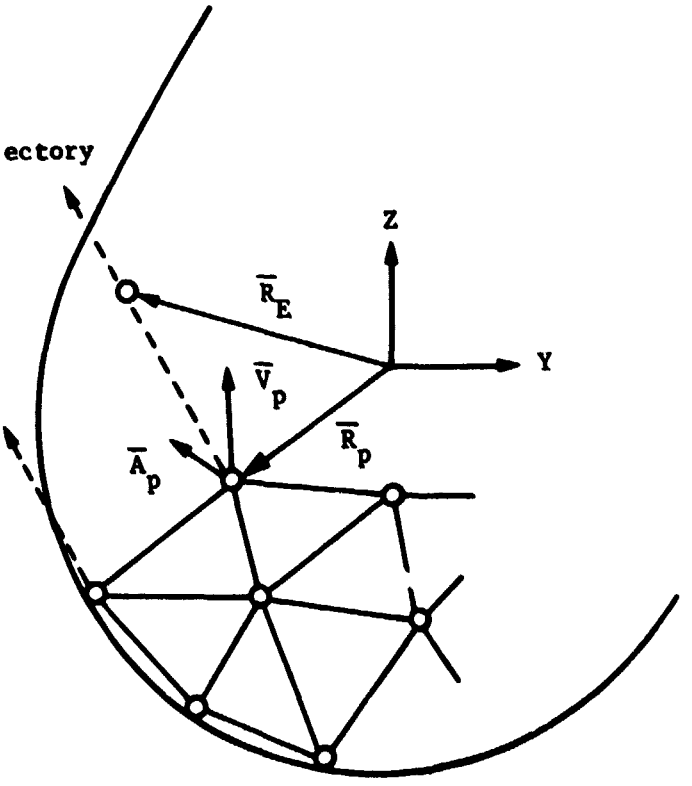

Figure 3-19. Estimation of Node Point Locations

$$\bar{R}_E = \bar{R}_p + \bar{V}_p \, DTNEW + 1/2 \, \bar{A}_p \, (DTNEW)^2 \qquad (3\text{-}74)$$

Where:

$\bar{R}_p$ = Current Position of Point p;

$\bar{V}_p$ = Current Velocity of Point p;

$\bar{A}_p$ = Current Acceleration of Point p.

The estimated position for a given value of Δt can be substituted into the constraint surface equation to evaluate wall penetration. The procedure used in the program starts the estimate with a minimum value of integration step, Δt_{min}. This minimum value is obtained by dividing the input DTMAX by an integer, N (N is currently set to 5 in the program). If the position estimate is inside the boundary, Δt is incremented such that,

$$\Delta t = (\Delta t_{min}) \, (INCR) \quad ; \; INCR = 1, 2, \ldots, N. \qquad (3\text{-}75)$$

The new value of Δt is substituted into equation (3-74) and boundary penetration is evaluated again. The largest fraction of DTMAX that does not cause wall penetration is the maximum integration step to be used for that node. All free surface and boundary nodes are evaluated in this manner and the minimum DTNEW of the set is selected as the next integration step size used in the solution of the equations of motion. This technique has proven very successful in preventing wall penetration.

3.5 CORRELATION OF THE LAMPS2 MODEL TO TEST DATA

A primary objective of this study was to develop a test-verified analytical model capable of simulating ET large amplitude slosh. Accomplishment of this objective required correlation of the Phase I and Phase II test data to the two-dimensional analytical model. Three criteria were selected to assess the accuracy of the simulation:

1) Correlation of the liquid motion character, with that observed in the high-speed movies (i.e., liquid position and free surface shape time history correlation to the test data);

2) Force/moment magnitude and phase correlation;

3) Correlation of the total impulse applied to the tank.

The first criterion provides a qualitative assessment of the overall liquid motion simulation. This criterion is evaluated by comparing the photographic images of the test data, at specific times, with the computer-generated graphics of the simulation.

The force/moment correlation (second criterion) provides a quantitative assessment of analysis accuracy in representing the tank/liquid interaction forces.

The third criterion provides a measure of model conservatism. The total impulse or double integral of the force and moment time histories indicates the degree to which the liquid motion will affect ET rigid body dynamics [Ref 4]. A total impulse of the simulated forces greater than the test-derived total impulse indicates the analysis is conservative in predicting ET response to liquid motion. The point mass model, previously discussed, has been shown to be overly conservative by this criterion [Ref 4].

Several model parameters were varied in the correlation study. These parameters include the finite element geometry, analytical representation of the baffles region, and the numerical integration step size. The finite element geometry is defined by the mesh type (I or II), mesh size (number of elements), and the mass matrix formulation (lumped or consistent). The analytical representation of the baffles region was evaluated by varying baffle height, spacing, and number of baffles represented. Analytical convergence to the test results is a function of the numerical integration step size. The solution sensitivity to this parameter was assessed by varying the integration step size for a given model geometry.

The analytical model was correlated with the Phase I drop tower test data and the Phase II, KC-135 test data.

Initial drop tower test/analytical correlations indicated an offset between the analytical predictions of the Y-axis force and test measurements. Figure 3-20 presents a comparison of the test and analytically derived forces for test 22. The drop tower test forces reflect the acceleration transient from the 1-g environment to the applied test accelerations. The test force initially approaches the analytical result, then trails off to a value less than the analytical data.

The force traces in Figure 3-20 consist of longitudinal and lateral components of the test forces resolved to the tank Y axis. Investigations of these components have indicated that the difference in the test and analytical force profile is a result of experimental error in the lateral force measurement. Figure 3-21 shows a copy of the strip chart measurements for test 22. The lateral force measurement (F_1) exhibits drift before drop capsule release and erratic behavior for the first 0.15 seconds of test time. Study of the longitudinal forces and photographed liquid motion indicates that the suspect lateral force behavior is not a function of the propellant dynamics. It is hypothesized the lateral force experimental errors are a result of the high-sensitivity setting of the lateral force transducer and test fixture construction.

Based on the above observations, the drop tower test data were adjusted to match the analytical data at a point after the transient event and before any significant propellant motion. This adjustment was accomplished by the following steps:

1) The values of analytical and test forces and moments were determined at t = 0.15 seconds;

2) These values were subtracted such that all forces and moments (test and analysis) were zero at t = 0.15 s to facilitate correlation of liquid motion induced forces;

3) All force correlations and impulse calculations were initiated at t = 0.15.

Analytical correlation with the drop tower data was adversely affected by the technique used to determine test accelerations. Drop tower accelerations were calculated from high speed movies as described in Reference 3. Consequently, in the drop tower test/analytical correlations, which follow, the analytically predicted liquid motion lags the test data slightly. However, analytical/test phasing correlation for the KC-135 tests was excellent. Accelerations were directly measured during KC-135 testing.

Analytical correlation to the KC-135 aircraft test data was initiated at the time the aircraft Z acceleration passed through +1 g [Ref 4]. In several instances, force transducer data channels were saturated for a period of time after the +1-g mark. In these instances, the correlation analysis was initiated after the data saturation period. No additional adjustments were required, since actual accelerations were measured during KC-135 testing and the use of strain gage load cells (and larger test forces) resulted in more accurate force measurements.

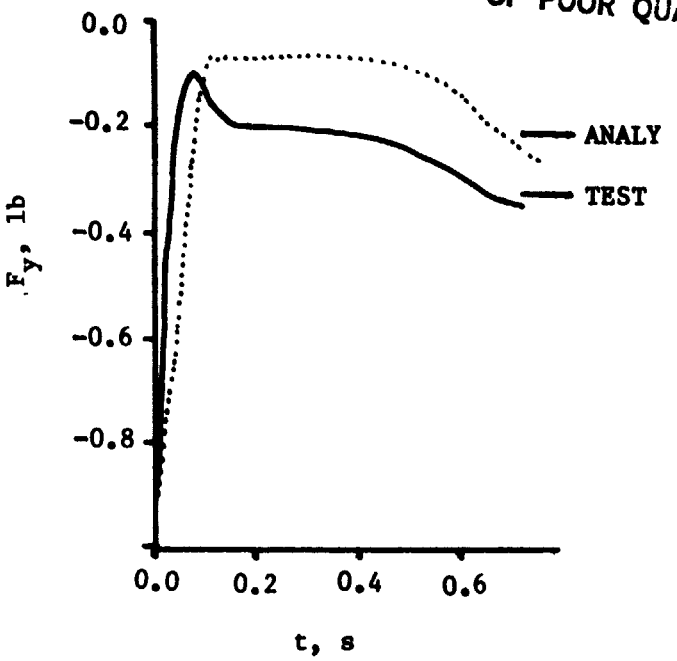

Figure 3-20. Test/Analytical Correlation: Tank Y-Axis Force, Drop Tower Test 22

3.5.1 Evaluation of Model Parameters

Two mesh arrangements were evaluated in the correlation analysis. Both lumped and consistent mass matrices were used in the two arrangements. Figure 3-22 shows a liquid motion profile comparison for the two mesh arrangements using a lumped mass matrix (drop tower test 21 conditions). The liquid motion comparisons for the consistent mass matrix are shown in Figure 3-23.

The lumped mass, mesh type I analysis produced the most uniform flow of the liquid. The second best liquid motion profile was produced by the type II, lumped mass formulation. The consistent mass formulation, which couples the inertial forces within the liquid, produced the poorest simulation of the liquid motion. Results of these four cases for drop tower test 21 conditions are shown in Figure 3-24. Note that good liquid motion correlation results in good force correlation.

It is postulated that the poor simulation quality for the consistent mass matrix is a result of the inertial coupling in the equations of motion. This inertial coupling appears to require a smaller integration step to achieve solution convergence. Since the computational costs for the consistent mass formulation exceeded those of the lumped mass formulation (for the same integration step size) and correlation was not improved, this method was not pursued further.

A numerical integration convergence study was performed using the lumped mass formulation. The liquid motion was simulated using the same mesh arrangement and size for various integration step sizes (DTMAX). Figure 3-25 shows the test/analytical correlations of the

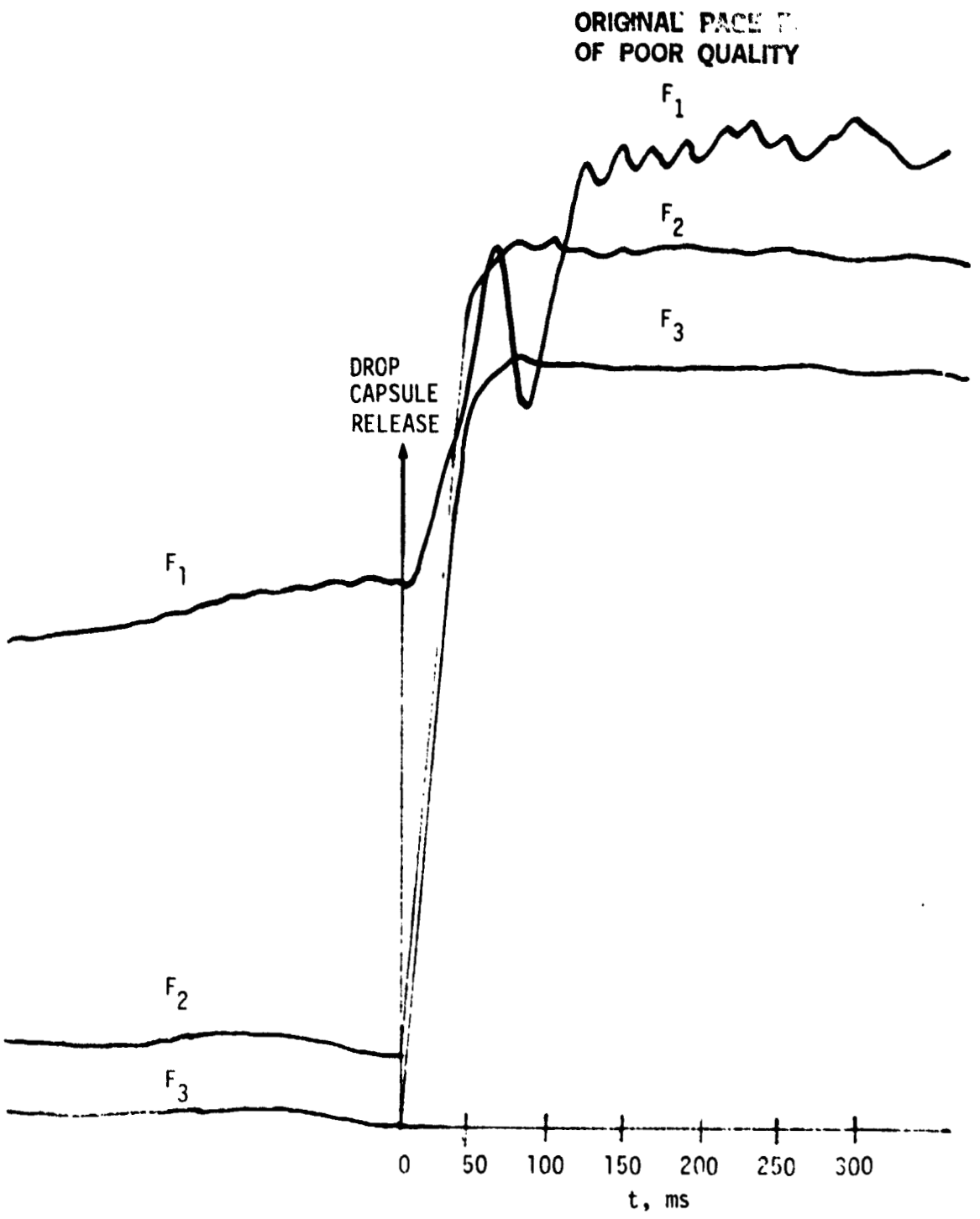

Figure 3-21. Strip Chart Data for Drop Tower Test 22

tank Z-axis force and total impulse for a KC-135 aircraft test condition. Three integration step sizes were evaluated in the correlation. As the integration step size was reduced, the magnitude of the analytical forces converged to the test data. Accompanying the magnitude reduction is a lengthening of the force duration, thus, the total impulse was not significantly affected. Furthermore, the liquid motion profiles produces for these integration step sizes were very similar.

The model was correlated to similar drop tower and KC-135 aircraft test data. This correlation produced additional validation of the test scaling approach (Chapter 2.0). The analytical model produced similar results for the 1/60th- and 1/10-scale tests. Figure 3-26 shows force and total impulse correlation to drop tower test 5 (10% fill) and KC-135 aircraft test 1.2.2 (10% fill). In both cases, the model correlates well to the test data. Liquid motion correlation to the test photographs is shown in Figure 3-27 for the drop tower test data and Figure 3-28 for the KC-135 aircraft test data. This correlation indicates the model should produce an accurate simulation of full-scale ET propellant dynmaics.

The effect of fill volume on the model was evaluated. The model was used to simulate fill volumes varying from 2% to 15%. The same size mesh and arrangement was used in all cases. Figure 3-29 shows the force and total impulse correlations for 5% and 15% fill volumes. Figure 3-29 presents the correlation for F_z, F_y and the moment (M_x) transferred to the scaled (1/60th scale) location of the external tank's CG. This allows for an assessment of the differences (test/analysis) as related to overall external tank dynamics. Reference 4 (chapter IV) used the same technique for evaluating slosh simulations for the first Shuttle flight (OFT-1). Figure 3-29 shows that the force magnitudes are in general, conservative. However, the integrated effects (double integrals) correlate very well with the test data.

Figure 3-30 and Figure 3-31 show test/analytical liquid motion comparisons for 2% and 15% fill volumes. The analyses do not correlate as well at the 15% fill volume. This indicates a finer mesh size should be used with higher fill volumes.

The baffled tank configurations were analyzed with the two-dimensional model. A multiple baffle approach, which varied analytical baffle height, was evaluated. The multiple baffle arrangement consisted of eight baffles represented by the superposition of a (1-cos) function with the distorted ellipse constraint surface. This approach resulted in entrapment of the finite elements in the baffle region and other numerical difficulties. The result was poor correlation of the model with the test data.

A single-baffle approach, which represented the baffle region as one baffle (central in region), was evaluated. The analytical height of this single baffle equaled the actual baffle height. The liquid motion correlation to a baffled KC-135 test is shown in Figure 3-32. The corresponding force and total impulse correlations for the tank Y-axis and Z-axis forces are shown in Figure 3-33. The analytical flow leads the

test data, but in general correlates well. This is the preferred approach to baffle representation at this time. More work needs to be done in this area.

In conclusion, the two-dimensional model has simulated accurately the liquid motion in scale models of the external tank. The degree of accuracy can be controlled by the choice of mesh size and numerical integration interval. The model produces conservative results that are more representative of the liquid motion dynamics than those produced by the single-point mass analog.

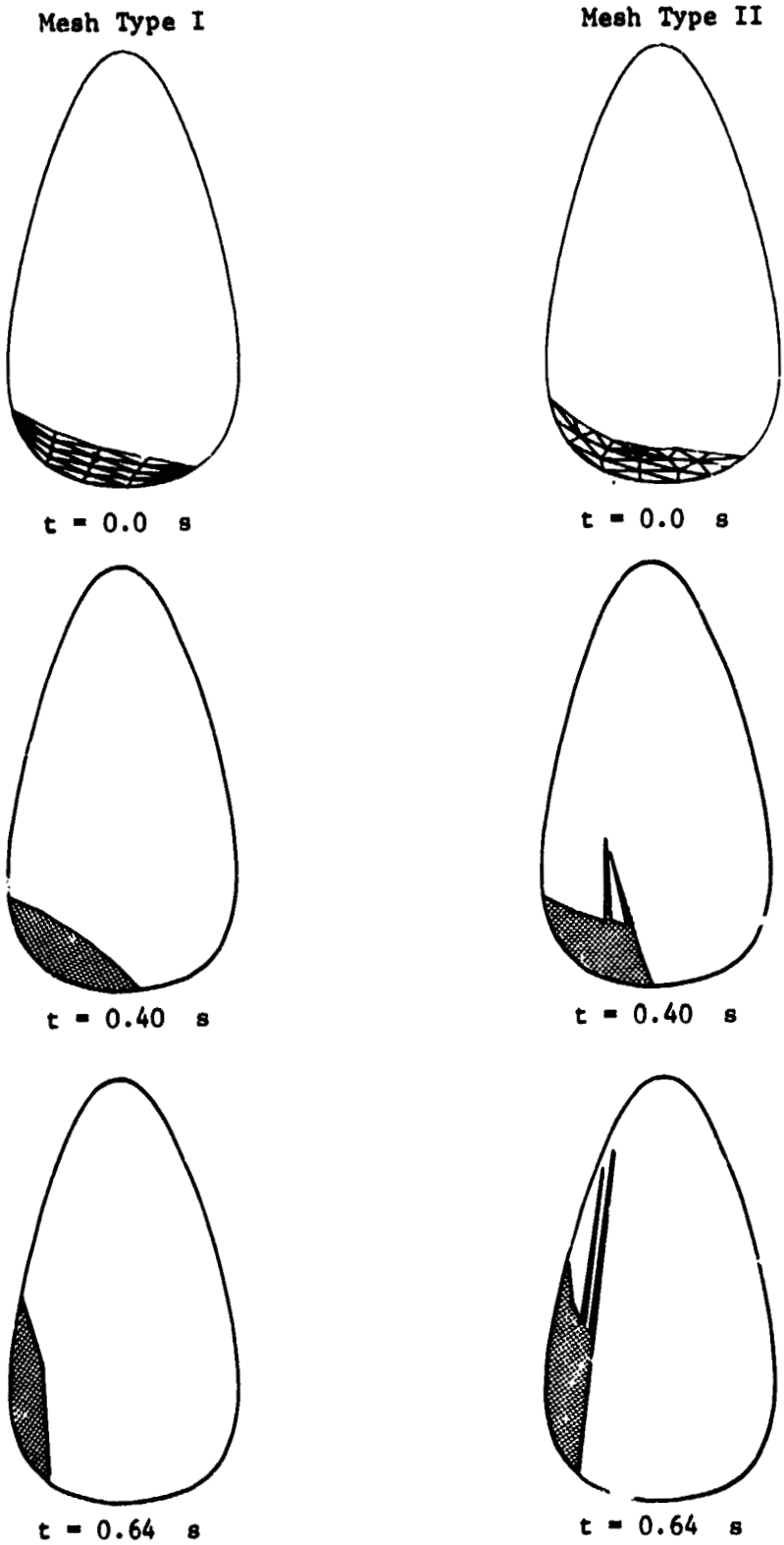

Figure 3-22. Mesh Evaluation: Lumped Mass Matrix; Motion Time History Comparison for Drop Tower Test 21 Conditions

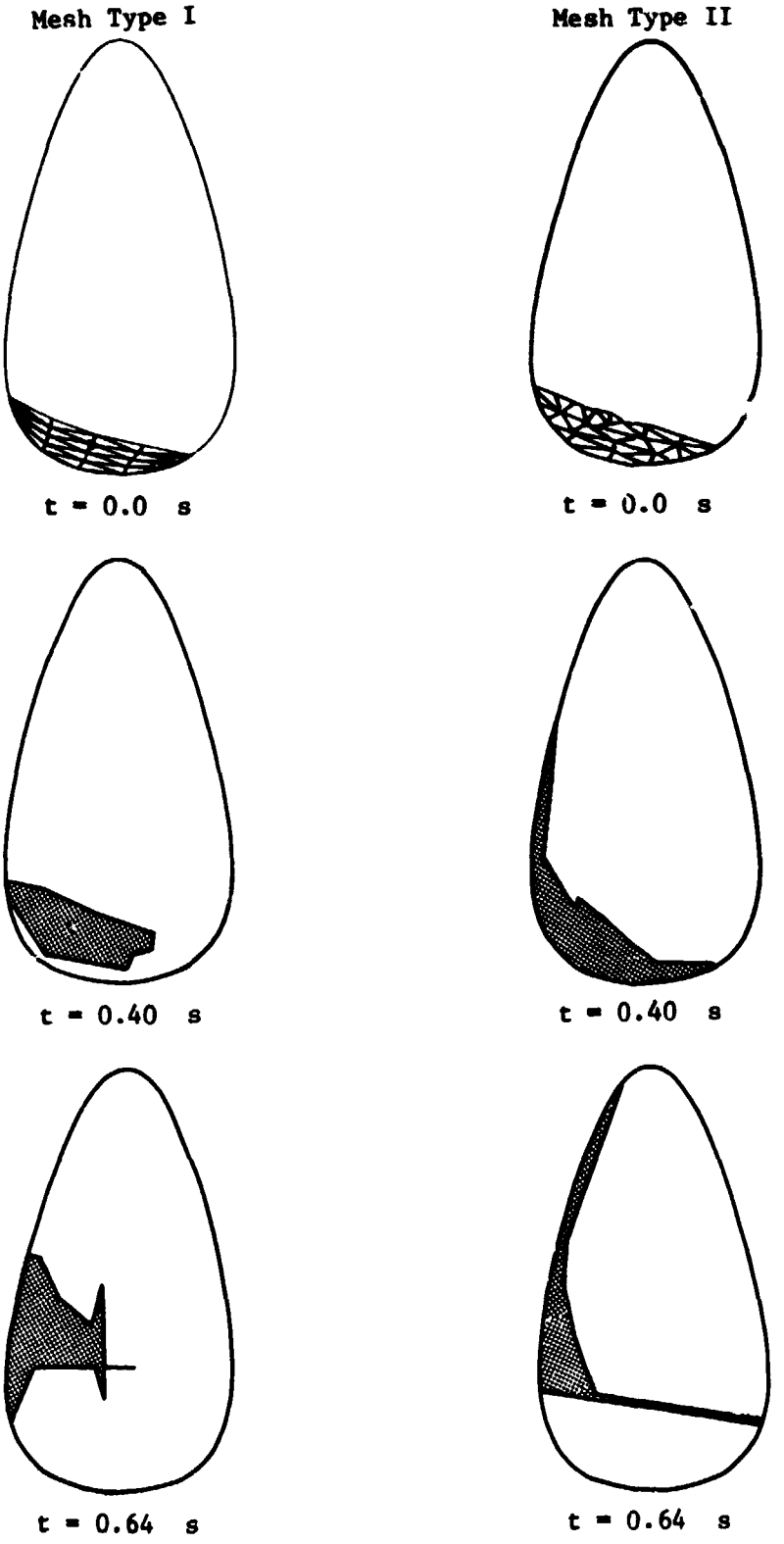

Figure 3-23. Mesh Evaluation: Consistent Mass Matrix; Motion Time History Comparison for Drop Tower Test 21 Conditions

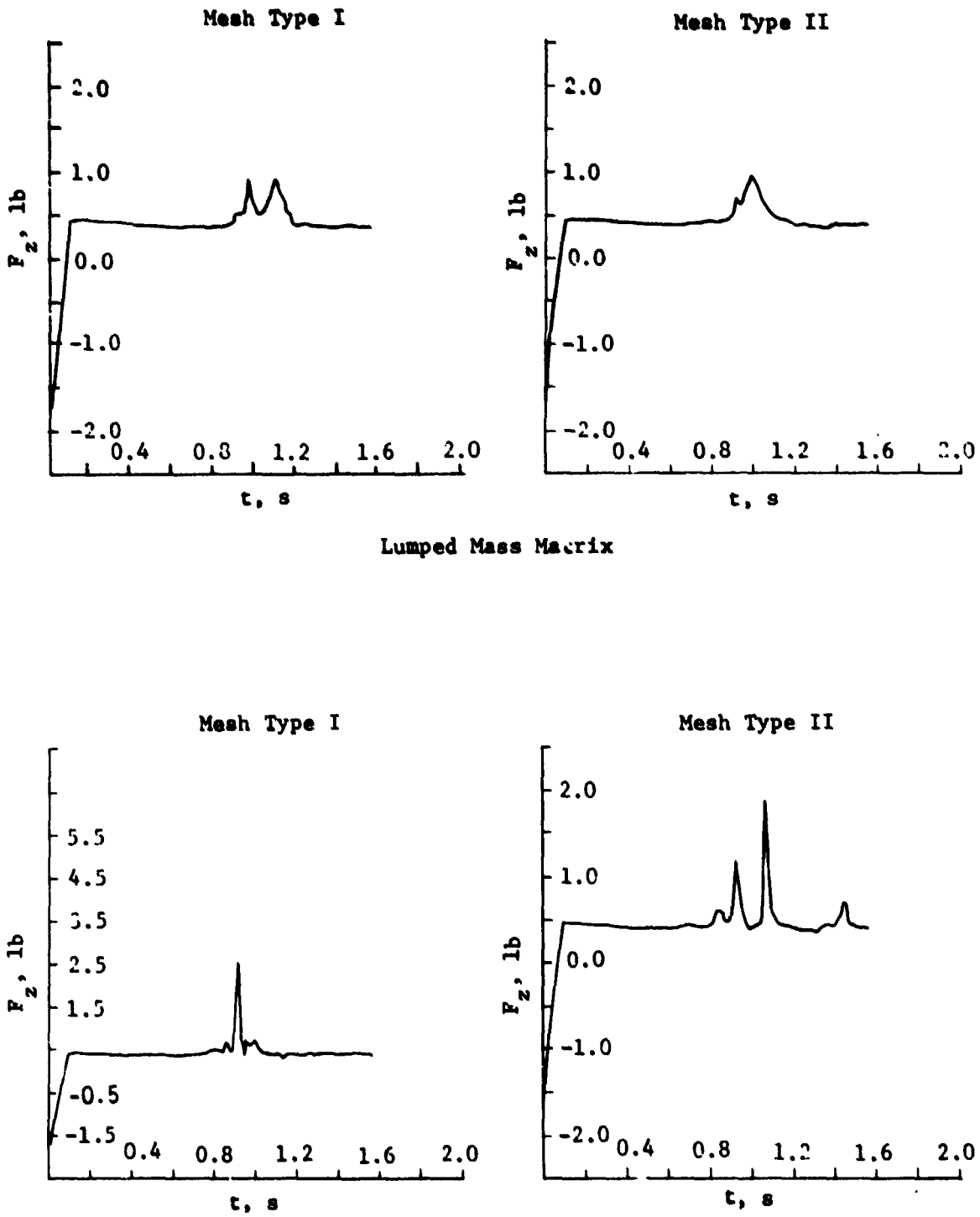

Figure 3-24. Mesh Evaluation: Lumped and Consistent Mass Matrices, Tank Z-Axis Force Comparison; Drop Tower Test 21 Conditions

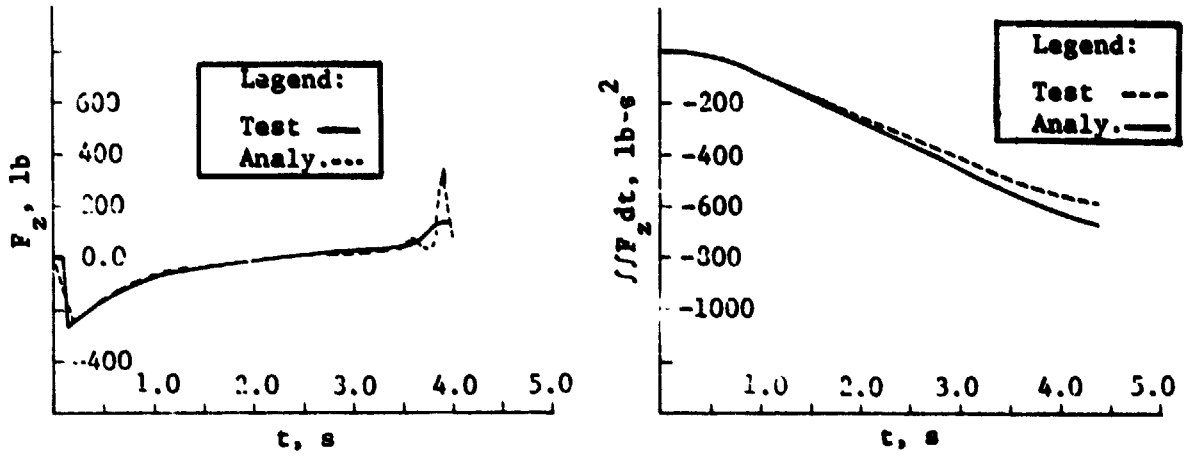

Integration Step = 0.10 s

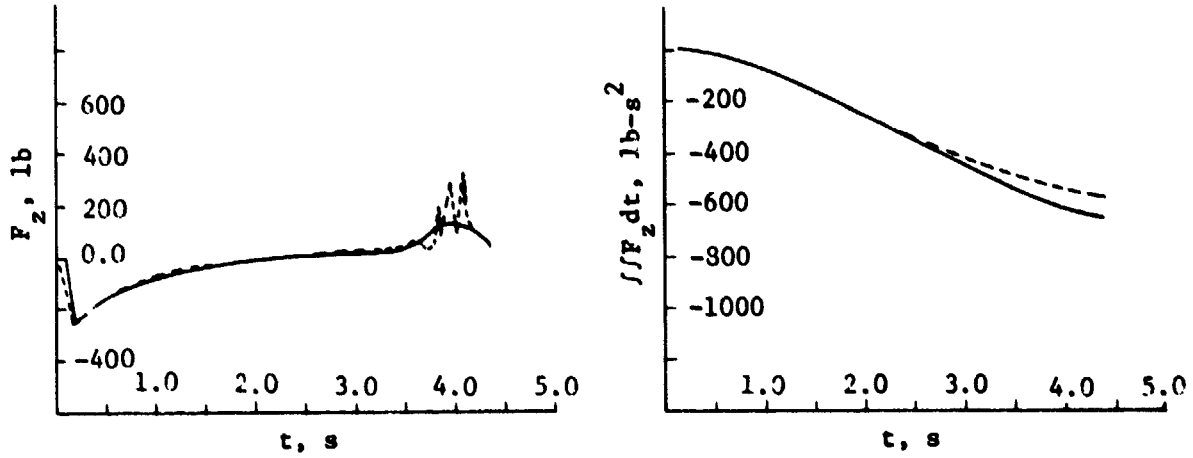

Integration Step = 0.05 s

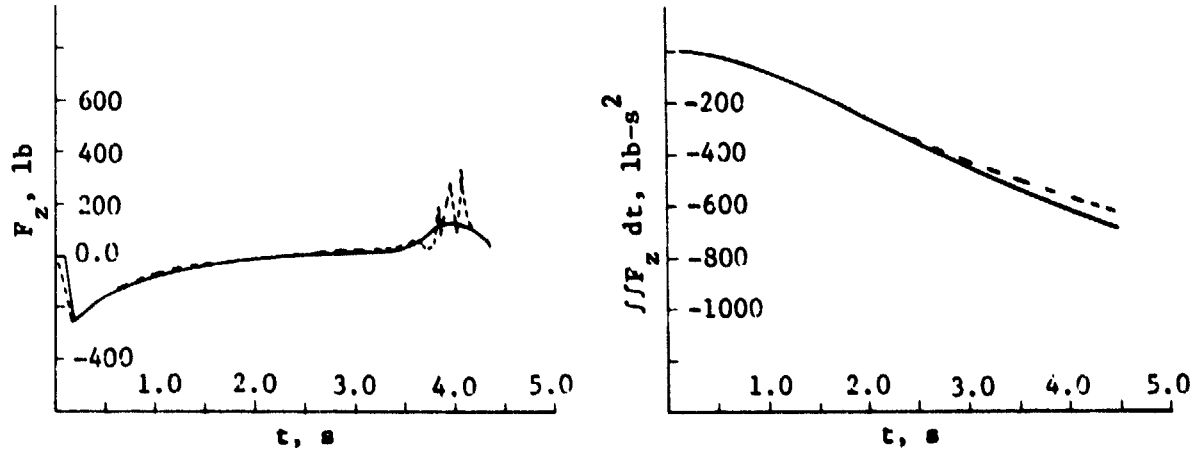

Integration Step = 0.025 s

Figure 3-25. Integration Step Size Evaluation: Tank 2-Axis Force and Total Impulse KC-135 Aircraft Test 1.2.2 Conditions

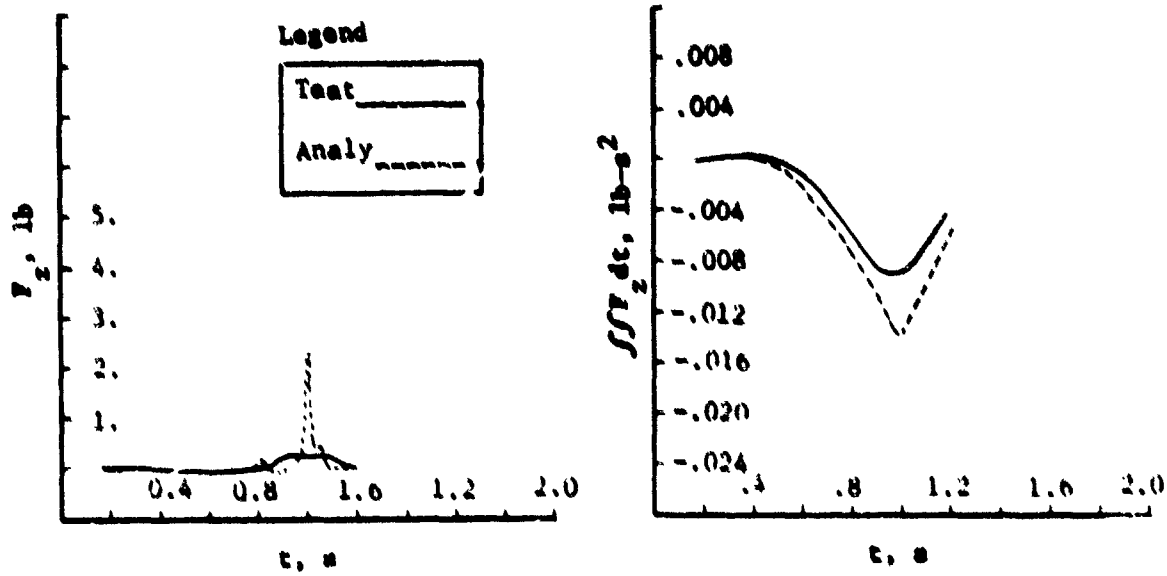

Drop Tower Test 5 (10% Fill)

*NOTE: Drop tower test/analytical correlations reflect data adjustment to zero force at t = 0.15s to facilitate correlation as discussed on page 3-38.

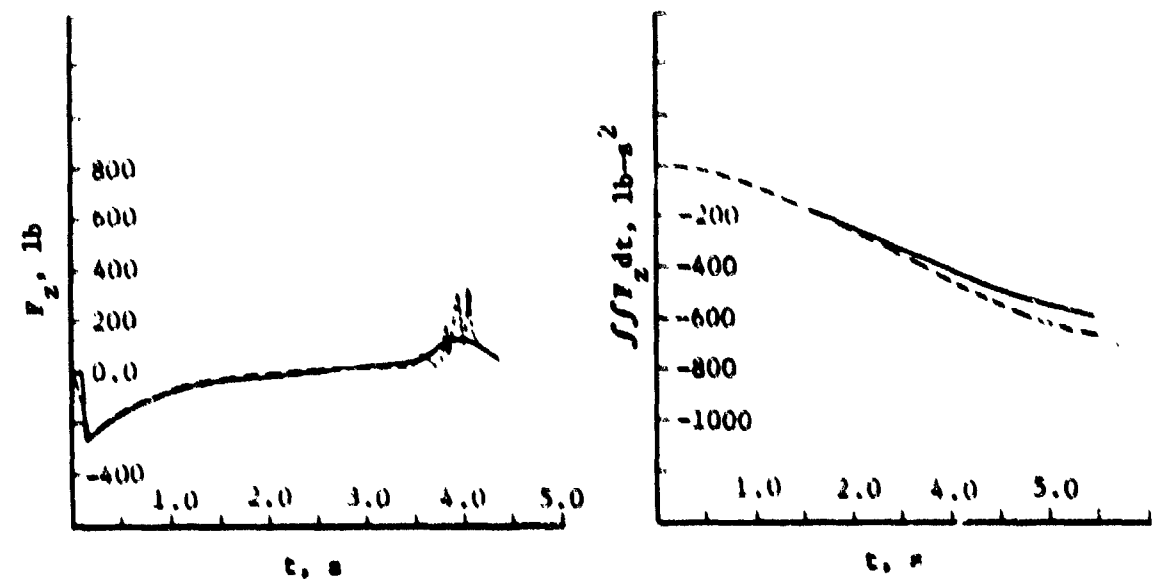

KC-135 Aircraft Test 1.2.2 (10% Fill)

Figure 3-26. Test/Analytical Comparisons for Drop Tower Test 5 and KC-135 Aircraft Test 1.2.2

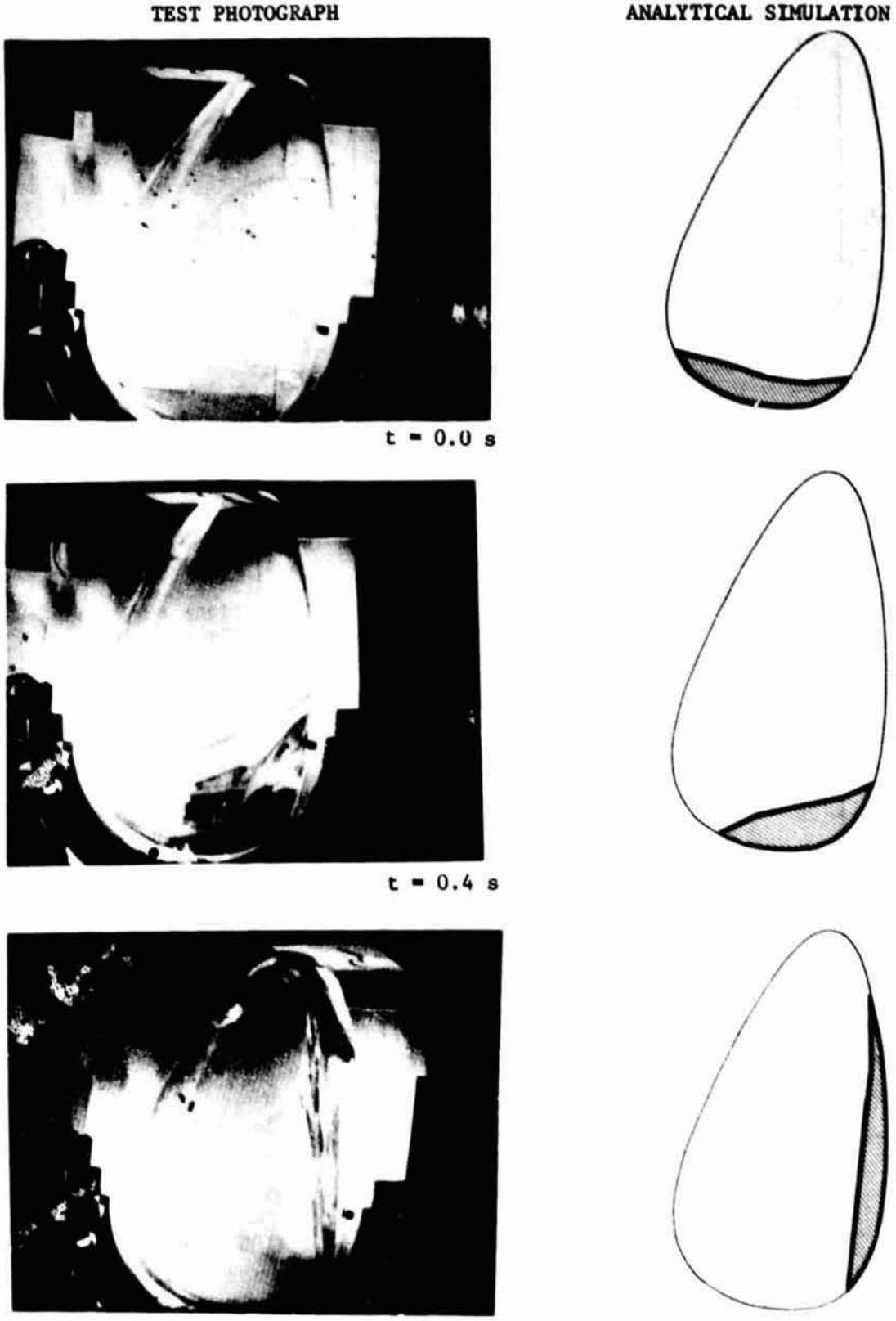

Figure 3-27. Test/Analytical Liquid Motion Comparison Drop Tower Test 5 (10% Fill)

TEST PHOTOGRAPH

ANALYTICAL SIMULATION

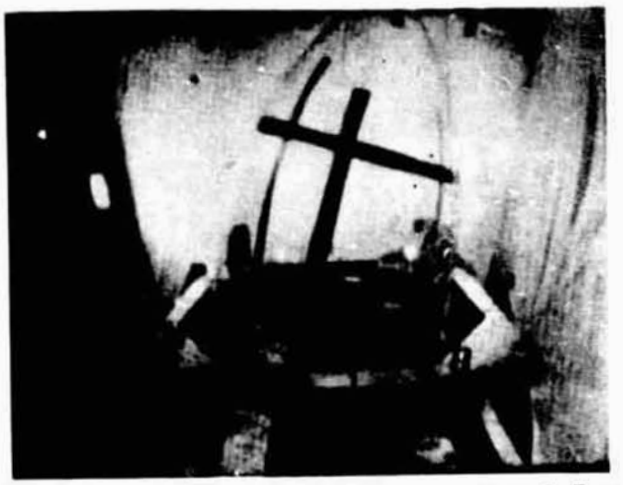

t = 2.7 s

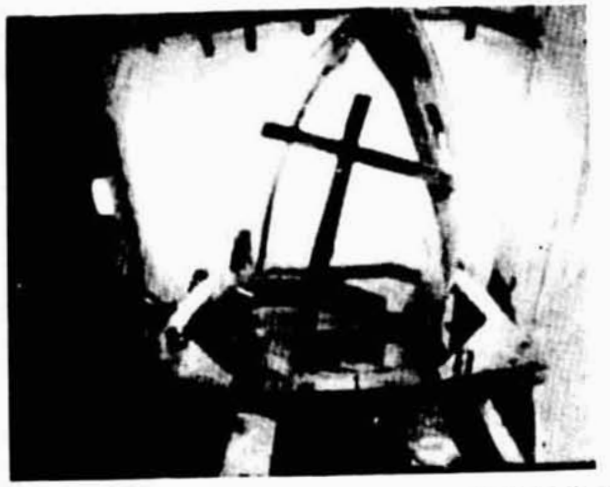

t = 3.8 s

Figure 3-28. Test/Analytical Liquid Motion Comparison KC-135 Aircraft Test 1.2.2 (10% Fill)

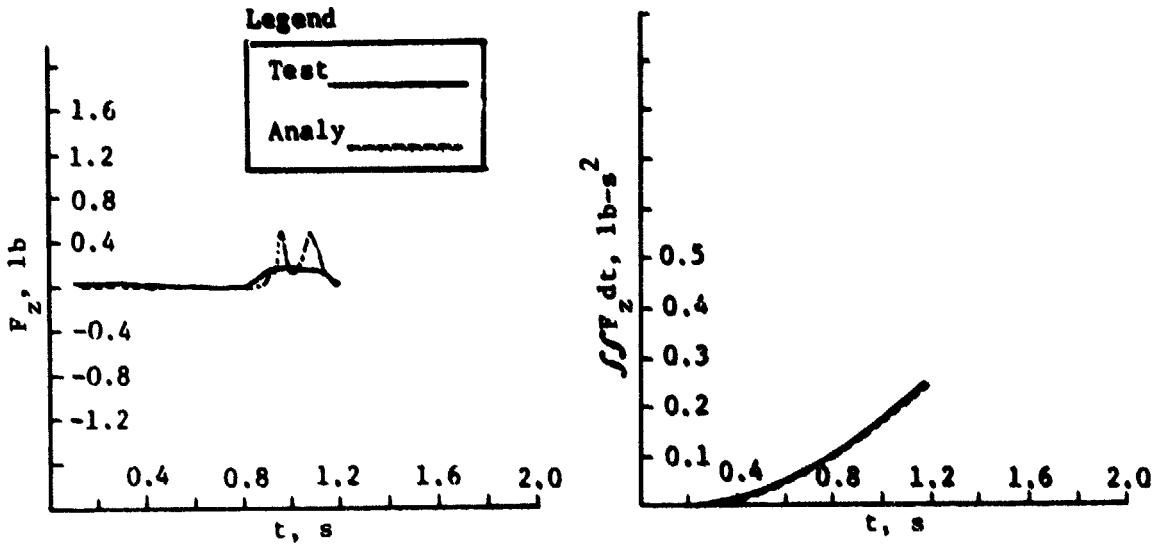

Drop Tower Test 21 (5% Fill)

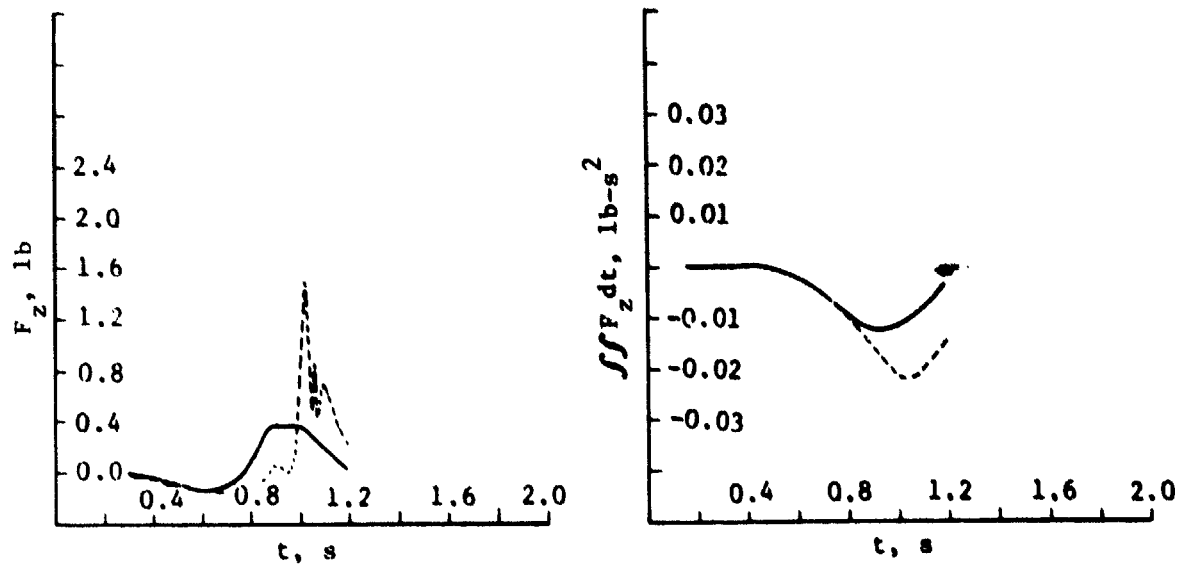

Drop Tower Test 22 (15% Fill)

Figure 3-29. Test/Analytical Comparisons for Drop Tower Tests 21 and 22

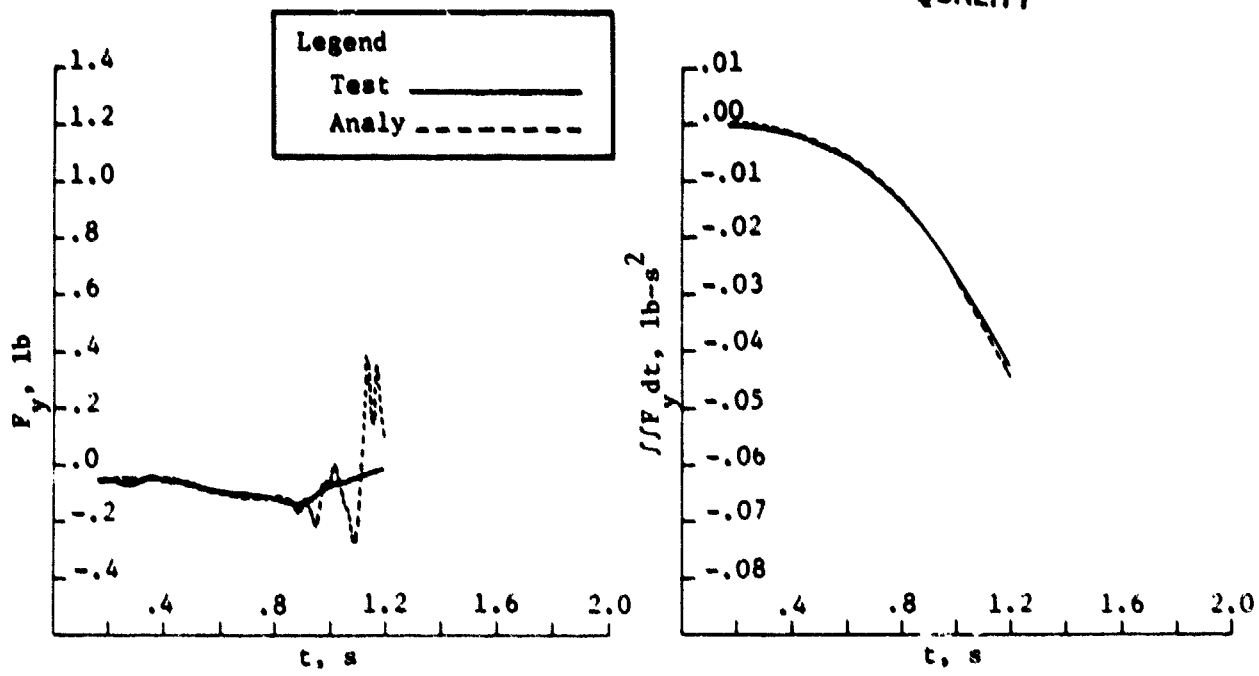

Drop Tower Test 21 (5% Fill)

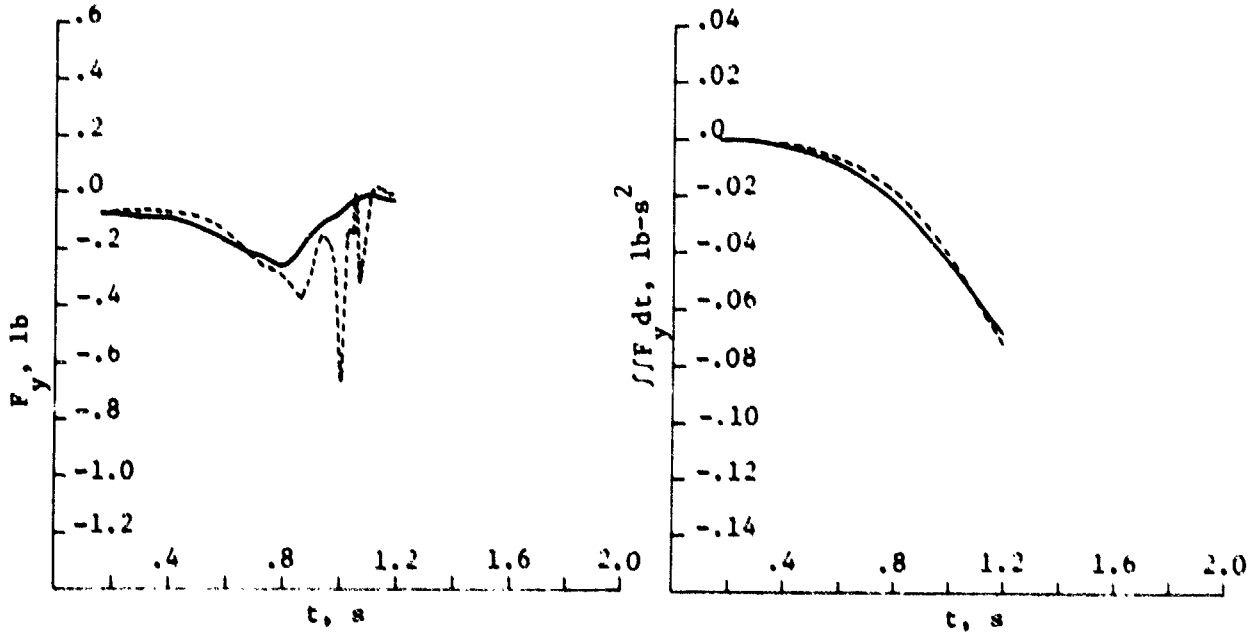

Drop Tower Test 22 (15% Fill)

Figure 3-29 (cont)

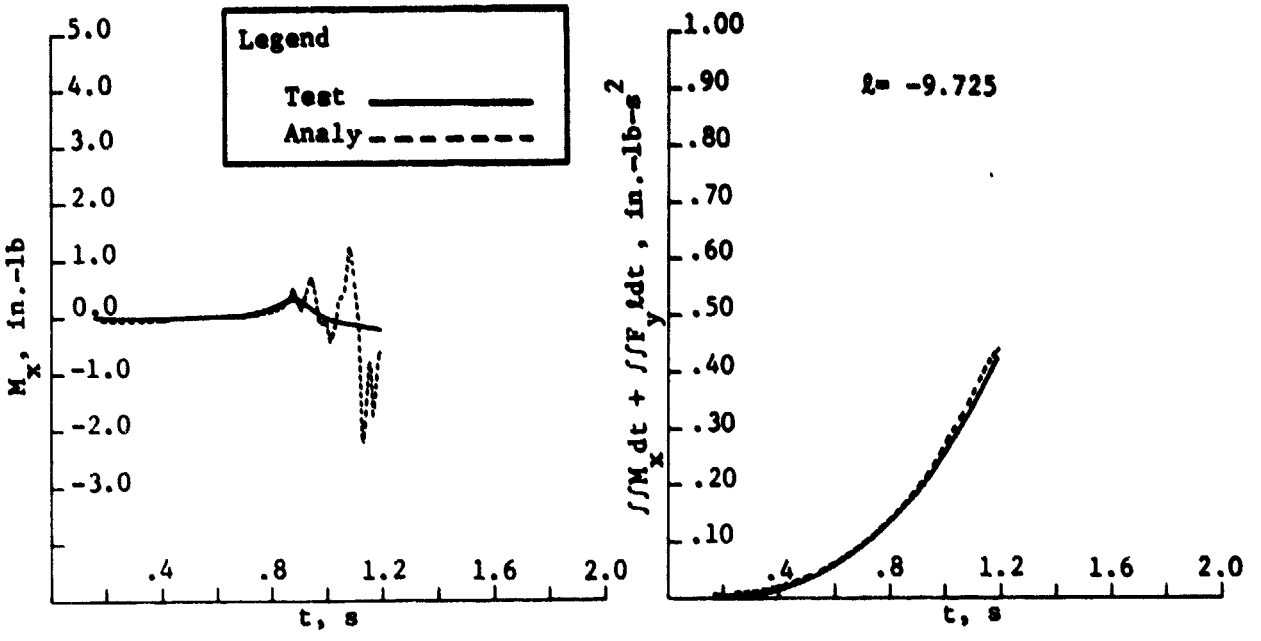

Drop Tower Test 21 (5% Fill)

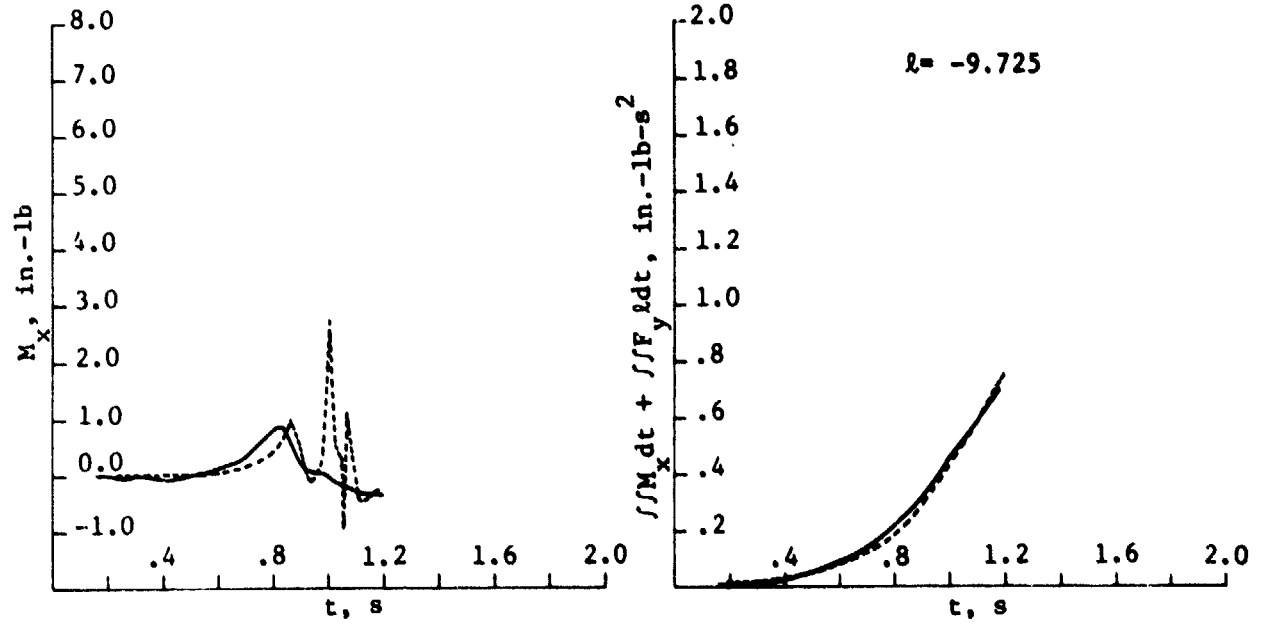

Drop Tower Test 22 (15% Fill)

Figure 3-29 (concl)

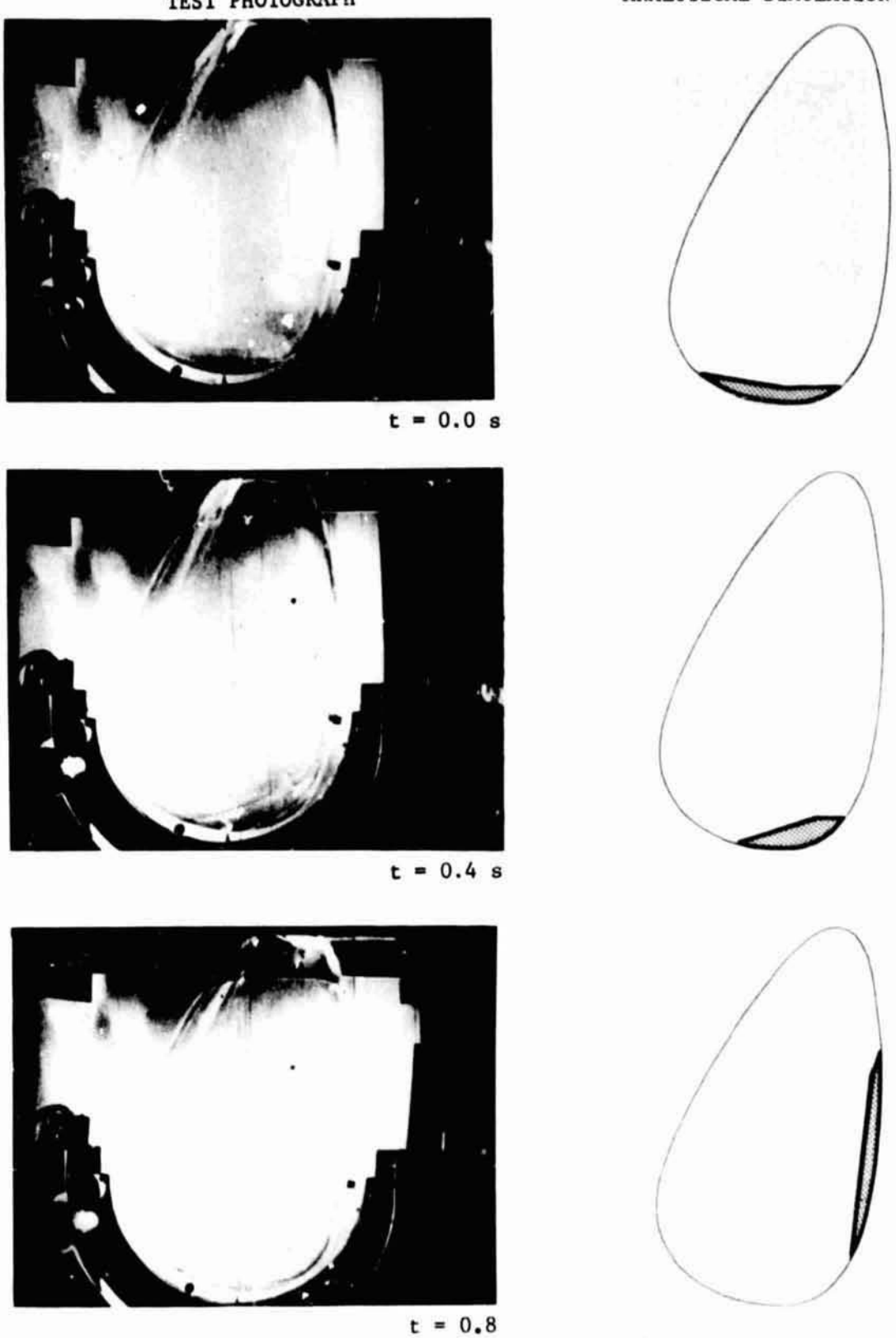

Figure 3-30. Test/Analytical Liquid Motion Comparison Drop Tower Test 9 (2% Fill)

TEST PHOTOGRAPH

ANALYTICAL SIMULATION

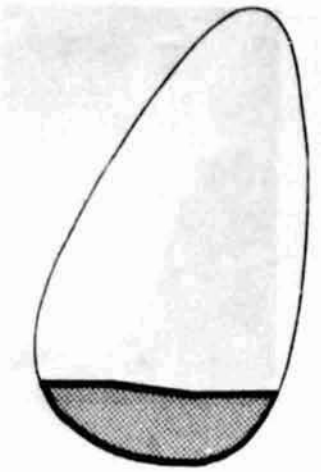

t = 0.0 s

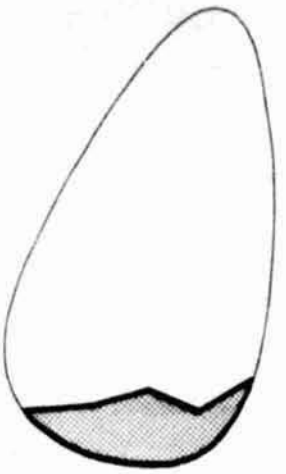

t = 0.4 s

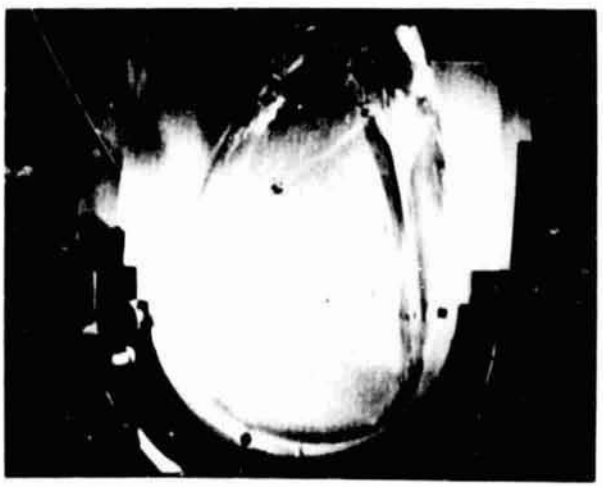

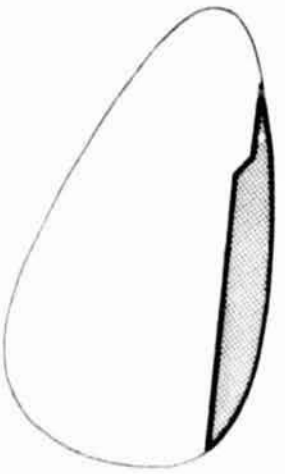

t = 0.3 s

Figure 3-31. Test/Analytical Liquid Motion Comparison Drop Tower Test 22 (15% Fill)

Test Photograph

Analytical Simulation

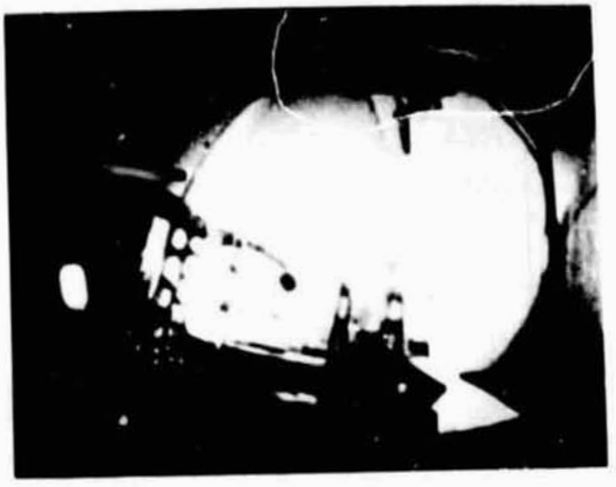

t = 3.9

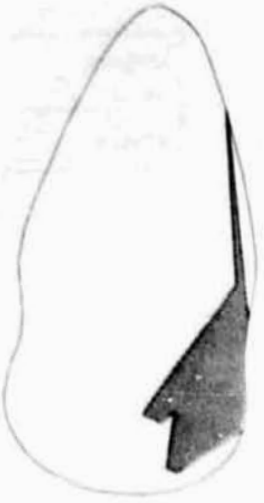

t = 3.8

t = 4.8

t = 4.79

Figure 3-32. Test/Analytical Liquid Motion Comparison KC-135 Aircraft Test 2.7.2 (Baffled, 10% Fill)

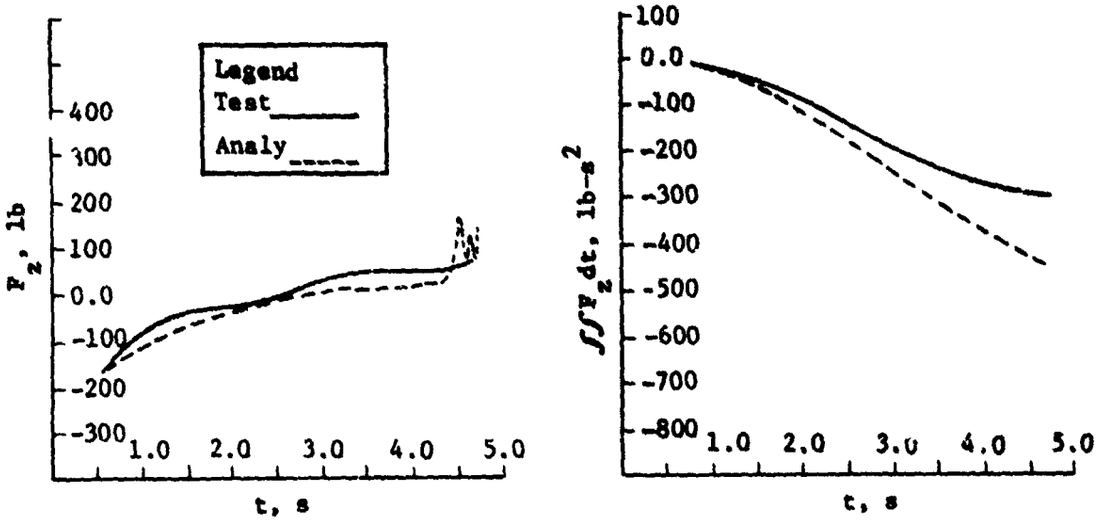

Tank Z-Axis Force

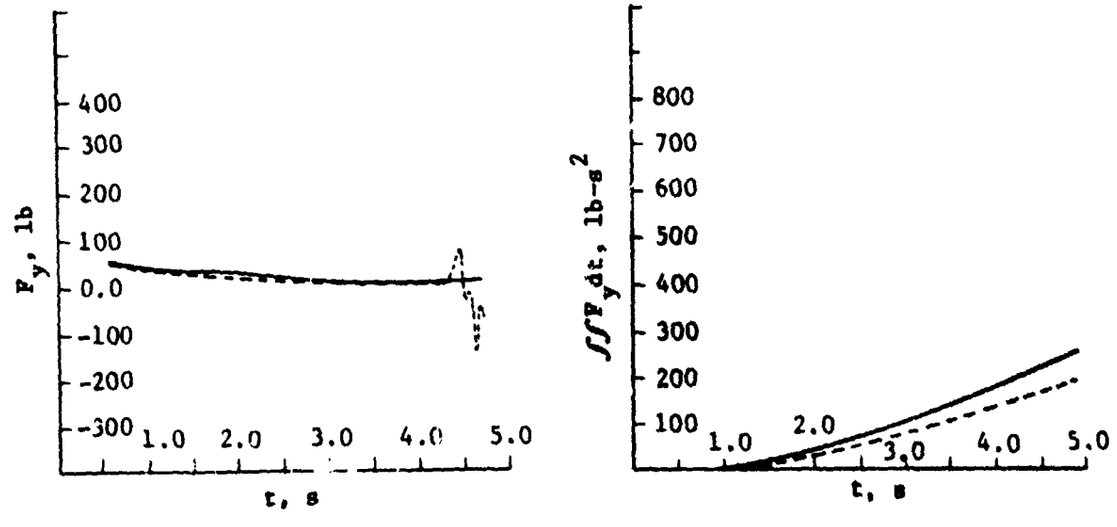

Tank Y-Axis Force

Figure 3-33. Test/Analytical Comparison for KC-135 Aircraft Test 2.7.2, Baffled

4.0 THREE-DIMENSIONAL FINITE ELEMENT MODEL (LAMPS3)

The analysis of the separation of the ET from the Orbiter during RTLS requires the solution of the general three-dimensional equations of motion for the propellant. Based on the correlation results for the two-dimensional model, a three-dimensional finite element model was formulated to analyze the propellant dynamics during RTLS. This model couples the ET rigid body dynamics with the propellent dynamics to provide a closed-loop analysis of the ET system. This chapter discusses the development of the equations of motion for this closed-loop system. The ET rigid body dynamics are developed first, followed by the equations that couple the propellent to the ET. The coupling equations section includes a discussion of the interaction forces between the liquid and tank. A three-dimensional finite element is derived to model the liquid incompressibility and viscous shear forces. The numerical techniques employed to solve the equations of motion and the correlation of the three-dimensional model are included in this chapter.

4.1 EXTERNAL TANK RIGID BODY DYNAMICS

The rigid body equation of motion for the ET were developed from Lagrange's Equations assuming the Lagrangian only consists of kinetic energy terms. These equations included generalized forces and nonholonomic constraints applied to the ET.

$$\frac{d}{dt}\left(\frac{\partial T}{\partial \dot{q}_k}\right) - \left(\frac{\partial T}{\partial q_k}\right) = \bar{Q}_k + b_{k\ell}\,\lambda_\ell \qquad 4\text{-}1$$

Six generalized coordinates were selected to describe the ET motion. These coordinates consist of three displacements of the ET center of mass and three Euler angles, which relate the ET body axes to the inertial axes. Therefore, the state vector for the ET rigid body is,

$$\begin{Bmatrix} q_1 \\ q_2 \\ q_3 \\ q_4 \\ q_5 \\ q_6 \end{Bmatrix} = \begin{Bmatrix} X \\ Y \\ Z \\ \psi \\ \theta \\ \phi \end{Bmatrix} \qquad 4\text{-}2$$

Figure 4-1 shows the ET center of mass relationship to the inertial frame. The center of mass is positioned by the vector R_c, and the orientation of the ET body axes with respect to the inertial frame is defined by the direction cosine matrix $[\gamma]$. The direction cosine matrix is a function of the Euler angles. Figure 4-2 delineates the Euler angle sequence employed in this analysis and the derivation of the $[\gamma]$ matrix.

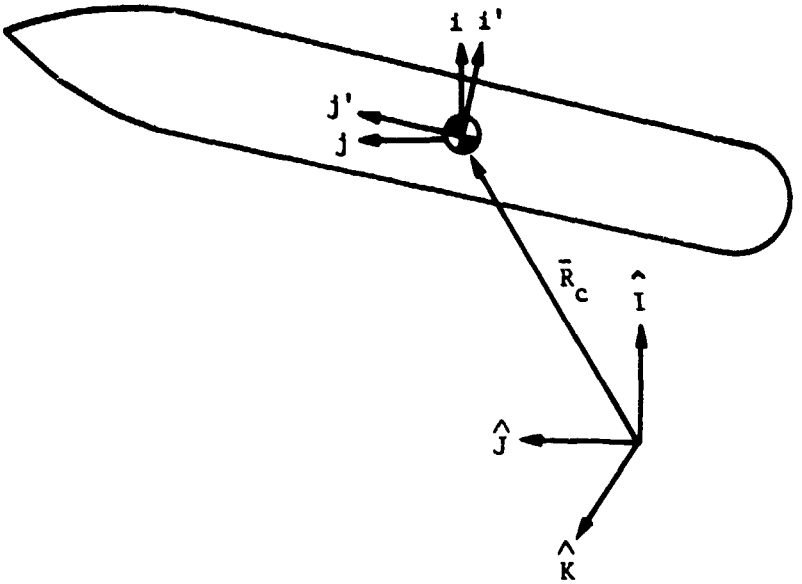

$$\bar{R}_c = X\hat{I} + Y\hat{J} + Z\hat{K} \tag{4-3}$$

$$\begin{pmatrix} i \\ j \\ k \end{pmatrix}' = |\gamma| \begin{pmatrix} \hat{I} \\ \hat{J} \\ \hat{K} \end{pmatrix} \tag{4-4}$$

where

$|\gamma| = f(\Psi, \Theta, \phi)$

Figure 4-1. ET Center of MASS Coordinate Definition

$$\begin{Bmatrix} i \\ j \\ k \end{Bmatrix}''' = \overset{[T\psi]}{\begin{bmatrix} C\psi^* & 0 & -S\psi \\ 0 & 1 & 0 \\ S\psi & 0 & C\psi \end{bmatrix}} \begin{Bmatrix} \hat{I} \\ \hat{J} \\ \hat{K} \end{Bmatrix} \qquad (4\text{-}5a)$$

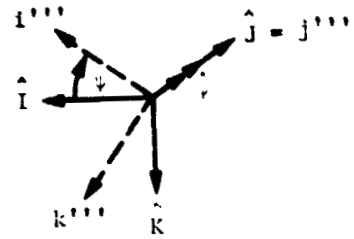

$$\begin{Bmatrix} i \\ j \\ k \end{Bmatrix}'' = \overset{[T\theta]}{\begin{bmatrix} C\theta & S\theta & 0 \\ -S\theta & C\theta & 0 \\ 0 & 0 & 1 \end{bmatrix}} \begin{Bmatrix} i \\ j \\ k \end{Bmatrix}''' \qquad (4\text{-}5b)$$

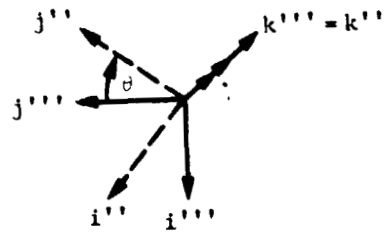

$$\begin{Bmatrix} i \\ j \\ k \end{Bmatrix}' = \overset{[T\phi]}{\begin{bmatrix} 1 & 0 & 0 \\ 0 & C\phi & S\phi \\ 0 & -S\phi & C\phi \end{bmatrix}} \begin{Bmatrix} i \\ j \\ k \end{Bmatrix}'' \qquad (4\text{-}5c)$$

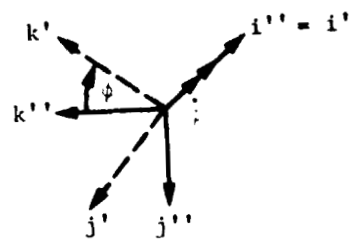

Combine 4-5a, b, and c

$$\begin{Bmatrix} i \\ j \\ k \end{Bmatrix}' = [T\phi]\,[T\theta]\,[T\psi] \begin{Bmatrix} \hat{I} \\ \hat{J} \\ \hat{K} \end{Bmatrix} = [\gamma] \begin{Bmatrix} \hat{I} \\ \hat{J} \\ \hat{K} \end{Bmatrix} \qquad (4\text{-}6)$$

where

$$[\gamma] = \begin{bmatrix} C\theta C\psi & S\theta & -C\theta S\psi \\ -C\phi S\theta C\psi + S\psi S\phi & C\phi C\theta & C\phi S\theta S\psi + S\phi C\psi \\ S\phi S\theta C\psi + S\psi C\phi & -S\phi C\theta & -S\phi S\theta S\psi + C\phi C\psi \end{bmatrix} \qquad (4\text{-}7)$$

*C = cosine, S = sine

Figure 4-2 Euler Angle Sequence

Having defined the state vector, the kinetic energy expression for the ET can be obtained. This expression consists of the translational kinetic energy of the center of mass plus the rotational kinetic energy about the center of mass.

$$T = 1/2 \{\dot{X}\ \dot{Y}\ \dot{Z}\}\ [M] \begin{Bmatrix} \dot{X} \\ \dot{Y} \\ \dot{Z} \end{Bmatrix} + 1/2 \{\omega_x\ \ \omega_y\ \ \omega_z\}\ [\tilde{I}] \begin{Bmatrix} \omega_x \\ \omega_y \\ \omega_z \end{Bmatrix} \qquad (4\text{-}8)$$

where

$\dot{X}$, $\dot{Y}$, $\dot{Z}$ = inertial velocities of ET center of mass

[M] = mass matrix of ET

ω_x, ω_y, ω_z = body axis instantaneous angular velocities (nonholonomic velocities)

$[\tilde{I}]$ = ET inertia matrix or tensor

The inertia tensor is defined as,

$$[\tilde{I}] = \begin{bmatrix} Ixx & -Ixy & -Ixz \\ -Iyx & Iyy & -Iyz \\ -Izx & -Izy & Izz \end{bmatrix} \qquad (4\text{-}8a)$$

where

$Ixx = \int_{\Psi} \rho(y^2+z^2)$

$Ixy = \int_{\Psi} \rho xy d\Psi$

ρ = mass density

All other terms of this inertia tensor can be obtained by cyclic permutation of the indexes x, y, z.

Substitution of the first term of the kinetic energy expression into equation (4-1) results in the equation of motion for the translation of the ET center of mass (neglecting constraint forces at this time).

$$\begin{bmatrix} M & & 0 \\ & M & \\ 0 & & M \end{bmatrix} \begin{Bmatrix} \ddot{X} \\ \ddot{Y} \\ \ddot{Z} \end{Bmatrix} = \begin{Bmatrix} Q_x \\ Q_y \\ Q_z \end{Bmatrix} \qquad (4\text{-}9)$$

The rotational kinetic energy of the ET must be written in terms of the Euler angle generalized coordinates. The instantaneous angular velocities can be expressed as projections of the Euler angle rates onto the body axes. Using Figure 4-2 to define these projections,

$$\begin{Bmatrix}\omega_x\\ \omega_y\\ \omega_z\end{Bmatrix} = \left[\begin{array}{c|c|c} S\theta & 0 & 1 \\ C\phi C\theta & S\phi & 0 \\ -C\theta S\phi & C\phi & 0 \end{array}\right] \begin{Bmatrix}\dot\psi\\ \dot\theta\\ \dot\phi\end{Bmatrix} = [\beta] \begin{Bmatrix}\dot\psi\\ \dot\theta\\ \dot\phi\end{Bmatrix} \tag{4-10}$$

Substitution of equation 4-10 into the second term of the kinetic energy expression yields,

$$T_2 = 1/2 \{\dot\psi\ \dot\theta\ \dot\phi\} [\beta]^T [I] [\beta] \begin{Bmatrix}\dot\psi\\ \dot\theta\\ \dot\phi\end{Bmatrix} \tag{4-11}$$

The partial derivatives of this kinetic expression with respect to the Euler angle generalized coodinates, q_j, (j = 4, 5, 6), results in,

$$\frac{\partial T_2}{\partial q_j} = 1/2 \{\dot\psi\ \dot\theta\ \dot\phi\} \left[\frac{\partial \beta}{\partial q_j}\right]^T [I] [\beta] \begin{Bmatrix}\dot\psi\\ \dot\theta\\ \dot\phi\end{Bmatrix} + 1/2 \{\dot\psi\ \dot\theta\ \dot\phi\} [\beta]^T [I] \left[\frac{\partial \beta}{\partial q_j}\right] \begin{Bmatrix}\dot\psi\\ \dot\theta\\ \dot\phi\end{Bmatrix} \tag{4-12}$$

The inertia tensor is a symmetric matrix, therefore

$$\frac{\partial T_2}{\partial q_j} = \{\dot\psi\ \dot\theta\ \dot\phi\} \left[\frac{\partial \beta}{\partial q_j}\right]^T [\tilde I] [\beta] \begin{Bmatrix}\dot\psi\\ \dot\theta\\ \dot\phi\end{Bmatrix} \tag{4-13}$$

Define a matrix, $[P_j]$, which contains the partial derivatives of the $[\beta]$ matrix with respect to each Euler angle coordinate.

$$[P_j] = \{\dot\psi\ \dot\theta\ \dot\phi\} \left[\frac{\partial \beta}{\partial q_j}\right]^T, \quad j = 4, 5, 6 \tag{4-14}$$

Assembling these matrices into $[P]$, the change in kinetic energy with respect to each Euler angle coordinate can be written as,

$$\begin{Bmatrix} \frac{\partial T_2}{\partial \dot\psi} \\ \frac{\partial T_2}{\partial \dot\theta} \\ \frac{\partial T_2}{\partial \dot\phi} \end{Bmatrix} = [P] [I] [\beta] \begin{Bmatrix}\dot\psi\\ \dot\theta\\ \dot\phi\end{Bmatrix} \tag{4-15}$$

The partials of the kinetic energy with respect to the generalized velocities of the Euler angles are,

$$\begin{Bmatrix} \frac{\partial T_2}{\partial \dot{\psi}} \\ \frac{\partial T_2}{\partial \dot{\theta}} \\ \frac{\partial T_2}{\partial \dot{\phi}} \end{Bmatrix} = [\beta]^T [\tilde{I}] [\beta] \begin{Bmatrix} \dot{\psi} \\ \dot{\theta} \\ \dot{\phi} \end{Bmatrix} \tag{4-16}$$

Substitution of equations (4-15) and (4-16) into equation (4-1) results in the homogenous equations of motion for ET rotation,

$$[\beta]^T [I] [\beta] \begin{Bmatrix} \ddot{\psi} \\ \ddot{\theta} \\ \ddot{\phi} \end{Bmatrix} + \left[[\dot{\beta}]^T [I] [\beta] + [\beta]^T [I] [\dot{\beta}] - [P] [I] [\beta] \right] \begin{Bmatrix} \dot{\psi} \\ \dot{\theta} \\ \dot{\phi} \end{Bmatrix} = \{0\} \tag{4-17}$$

where

$$[\dot{\beta}] = \begin{bmatrix} C\phi\dot{\theta} & 0 & 0 \\ -S\phi C\theta\dot{\phi} - C\phi S\theta\dot{\theta} & C\phi\dot{\phi} & 0 \\ C\phi C\theta\dot{\phi} \quad S\phi S\theta\dot{\theta} & -S\phi\dot{\phi} & 0 \end{bmatrix}$$

The transformations that relate the body axis forces and torques to the generalized forces, Q_k, can be obtained through the virtual power method. The virtual power of the impressed forces and of the body axis velocities is,

$$\delta\dot{W} = \{ \delta u \ \delta v \ \delta w \ \delta\omega_x \delta\omega_y \delta\omega_z \} \begin{Bmatrix} f_x \\ f_y \\ f_z \\ T_x \\ T_y \\ T_z \end{Bmatrix} \tag{4-18}$$

where

$\delta u, \delta v, \delta w$ = virtual velocities measured in the body axis system,

$\delta\omega_x, \delta\omega_y \ \delta\omega_z$ = virtual rotational rates,

f_x, f_y, f_z = forces measured in the body axis system,

T_x, T_y, T_z = torques measured in the body axis system.

The virtual power in terms of the generalized velocities and forces is,

$$\delta\dot{W} = \{\delta\dot{X}\ \delta\dot{Y}\ \delta\dot{Z}\ \delta\dot{\psi}\ \delta\dot{\theta}\ \delta\dot{\phi}\} \begin{Bmatrix} Q_1 \\ Q_1 \\ Q_2 \\ Q_3 \\ Q_4 \\ Q_5 \\ Q_6 \end{Bmatrix} \tag{4 19}$$

The body axis velocities are related to the generalized velocities through the [Y] and the [β] matrices,

thus,

$$\{u\ v\ w\} = \{\dot{X}\ \dot{Y}\ \dot{Z}\}\ [\gamma]^T \tag{4-20}$$

and

$$\{\omega_x\ \omega_y\ \omega_z\} = \{\dot{\psi}\ \dot{\theta}\ \dot{\phi}\}\ [\beta]^T \tag{4-21}$$

Substitution of equations (4-20) and (4-21) into equation (4-18) results in,

$$\delta W = \{\delta\dot{X}\ \delta\dot{Y}\ \delta\dot{Z}\ \delta\dot{\psi}\ \delta\dot{\theta}\ \delta\dot{\phi}\} \left[\begin{array}{c|c} \gamma^T & 0 \\ \hline 0 & \beta^T \end{array}\right] \begin{Bmatrix} f_x \\ f_y \\ f_y \\ T_x \\ T_y \\ T_z \end{Bmatrix} \tag{4-22}$$

Comparing equation (4-19) to equation (4-22) the expression for the generalized forces is obtained,

$$\begin{Bmatrix} Q_1 \\ Q_2 \\ Q_3 \\ Q_4 \\ Q_5 \\ Q_6 \end{Bmatrix} = \left[\begin{array}{c|c} \gamma^T & 0 \\ \hline 0 & \beta^T \end{array}\right] \begin{Bmatrix} f_x \\ f_y \\ f_z \\ T_x \\ T_y \\ T_z \end{Bmatrix} \qquad (4\text{-}23)$$

These generalized forces were incorporated into the right-hand side of equations (4-9) and (4-17) to complete the rigid body equations of motion for the ET.

4.2 PROPELLANT COUPLING TO ET EQUATIONS OF MOTION

The position of the i th liquid mass point can be specified by using the vector relationship shown in Figure 4-3. This states that the absolute motion of the liquid can be obtained from the sum of the LOX tank motion, plus the motion of the liquid relative to the LOX tank. The position coordinates of the liquid relative to the tank reference axis were selected as the generalized coordinates for the liquid. This selection of generalized coordinates results in coupling the ET rigid body dynamics to that of the liquid through the mass matrix of the system. This approach simplifies the expression for the interaction constraint forces between the liquid and tank. Thus, the state vector for the liquid and ET is,

$$\{q_{x1}, q_{y1}, q_{z1}, \ldots, q_{xn}, q_{yn}, q_{zn}, X, Y, Z, \psi, \theta, \phi\}$$

where

n = the number of node points used to represent the liquid.

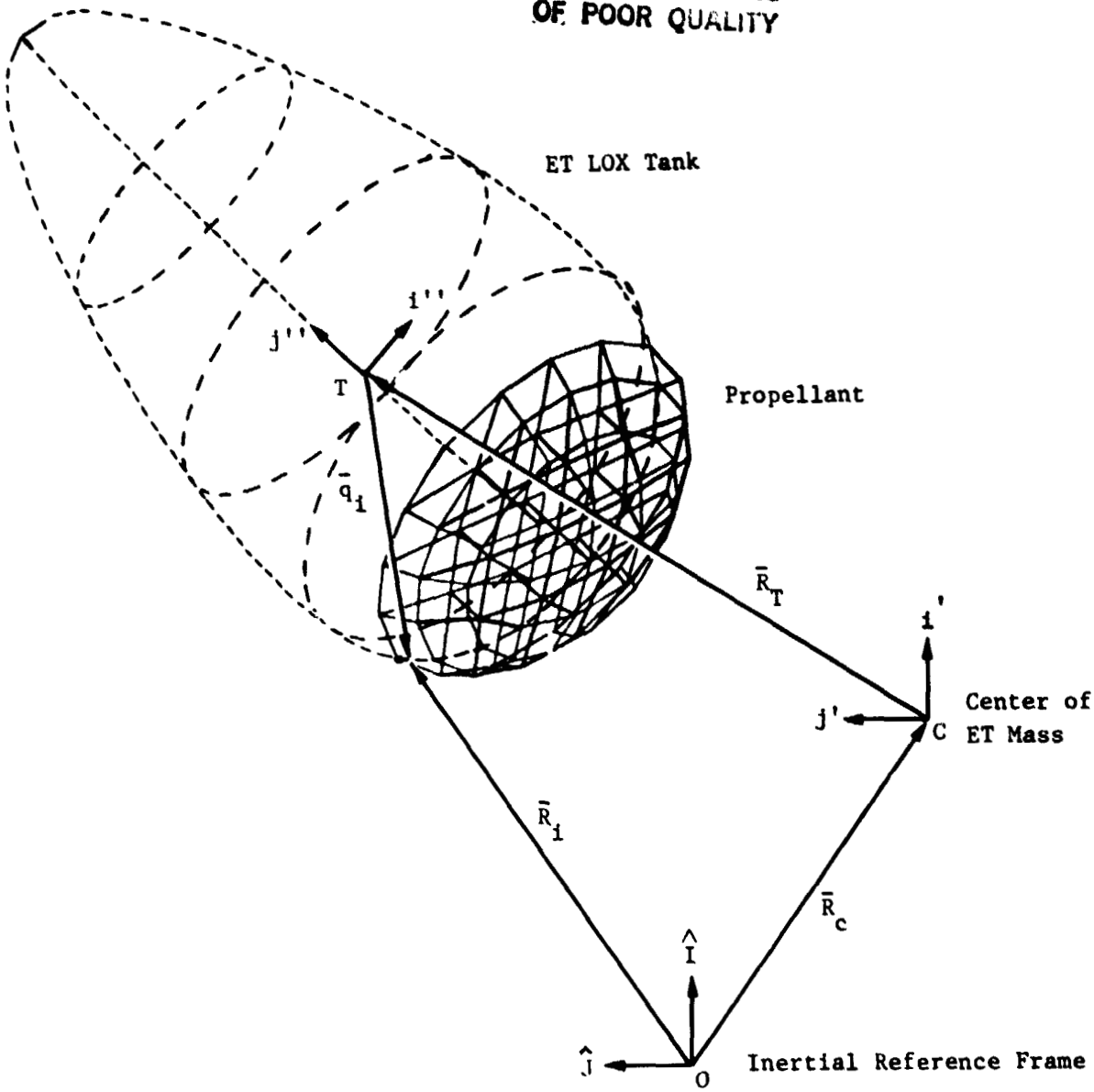

$$\bar{R}_i = \bar{R}_c + \bar{R}_T + \bar{q}_i \qquad (4\text{-}24)$$

$$R_c = X\,\hat{I} + Y\,\hat{J} + Z\,\hat{K}$$

Figure 4-3. Position of Liquid MASS in Inertial Space

The inertia coupling between the liquid and ET rigid body is derived from the principal of virtual work.

$$\int_{\Psi} \delta R_i (\rho \ddot{R}_i - f_i)\, d\Psi = 0 \qquad (4\text{-}25)$$

where δR_i = Virtual displacement of ith mass point

$\ddot{R}_i$ = Inertial acceleration of ith mass point

f_i = External forces on ith mass point

ρ = Mass density

Solution of equation (4-25) requires definition of δR_i and $\ddot{R}_i$. Using Figure 4-3, and assuming a rigid ET, the inertial velocity and acceleration of the ith liquid point are,

$$\dot{\bar{R}}_i = \dot{\bar{R}}_c + \bar{\omega} X \bar{R}_T + \bar{\omega} X \bar{q}_i + \dot{\bar{q}}_i \qquad (4\text{-}26)$$

and

$$\ddot{\bar{R}}_i = \ddot{\bar{R}}_c + \dot{\bar{\omega}} X \bar{R}_T + \bar{\omega} X (\bar{\omega} X \bar{R}_T) + \ddot{\bar{q}}_i + 2\bar{\omega} X \dot{\bar{q}}_i + \dot{\bar{\omega}} X \bar{q}_i + \bar{\omega} X (\bar{\omega} X \bar{q}_i) \qquad (4\text{-}27)$$

where $\{\bar{\omega}\} = \begin{Bmatrix} \omega_x \\ \omega_y \\ \omega_z \end{Bmatrix}$, equation (4-8).

The above expression assumed the same basis for all the vectors. In general, the tank coordinate system will not be alligned with the ET center of mass triad. Furthermore, the center of mass triad rotates with respect to inertial space. The $[\gamma]$ matrix, equation (4-6), relates the body axis triad to the inertial triad. The tank triad (T) can be related to the body axis triad (C) by,

$$\begin{Bmatrix} i \\ j \\ k \end{Bmatrix}'' = \left[T^{R}_{C}\right] \begin{Bmatrix} i \\ j \\ k \end{Bmatrix}' \qquad (4\text{-}28)$$

where

i", j", k" are the tank axes base vectors.

The $\bar{R}_T$ and $\bar{q}_i$ vectors can be defined in terms of their components,

$$\bar{R}_T = \lfloor i' \; j' \; k' \rfloor \begin{Bmatrix} r_x \\ r_y \\ r_z \end{Bmatrix}, \text{ body axis system} \qquad (4\text{-}29)$$

and

$$\bar{q}_i = \lfloor i'' \; j'' \; k'' \rfloor \begin{Bmatrix} q_x \\ q_y \\ q_z \end{Bmatrix}, \text{ tank axis system.} \qquad (4\text{-}30)$$

Combining these vectors, the total distance from the ET center of mass (empty) to the ith liquid point is,

$$\lfloor i' \; j' \; k' \rfloor \begin{Bmatrix} h_x \\ h_y \\ h_z \end{Bmatrix}_i = \lfloor i' \; j' \; k' \rfloor \left(\begin{Bmatrix} r_x \\ r_y \\ r_z \end{Bmatrix} + \begin{bmatrix} C^{R_T} \end{bmatrix} \begin{Bmatrix} q_x \\ q_y \\ q_z \end{Bmatrix}_i \right) \tag{4-31}$$

The angular velocity cross products (in terms of the body axis triad) can be rewritten in matrix form using this total distance vector. Hence,

$$\bar{\omega} X (\bar{R}_T + \bar{q}_i) = \lfloor i' \; j' \; k' \rfloor \; [r_s]_i \begin{Bmatrix} \omega_x \\ \omega_y \\ \omega_z \end{Bmatrix} \tag{4-32}$$

where $[r_s]_i = \begin{bmatrix} 0 & h_z & -h_y \\ -h_z & 0 & h_x \\ h_y & -h_x & 0 \end{bmatrix}_i$

Furthermore, the centripetal and coriolis accelerations can be written in a similar fashion,

$$\bar{\omega} X (\bar{\omega} X (\bar{R}_T + \bar{q}_i)) = \lfloor i' \; j' \; k' \rfloor [\Omega] \; [r_s]_i \begin{Bmatrix} \omega_x \\ \omega_y \\ \omega_z \end{Bmatrix} \tag{4-33}$$

and

$$2\bar{\omega} X \dot{\bar{q}}_i = 2 \lfloor i' \; j' \; k' \rfloor [\Omega] \left[{}_{C}R_T \right] \begin{Bmatrix} \dot{q}_x \\ \dot{q}_y \\ \dot{q}_z \end{Bmatrix}_i \tag{4-34}$$

where $[\Omega] = \begin{bmatrix} 0 & -\omega_z & \omega_y \\ \omega_z & 0 & -\omega_x \\ -\omega_y & \omega_x & 0 \end{bmatrix}$

The ET body axis angular velocities, ω, and angular accelerations, $\dot{\omega}$, can be written as functions of the state variables (ψ, θ, ϕ) and their time derivatives. Recalling equation (4-10),

$$\begin{Bmatrix} \omega_x \\ \omega_y \\ \omega_z \end{Bmatrix} = [\beta] \begin{Bmatrix} \dot{\psi} \\ \dot{\theta} \\ \dot{\phi} \end{Bmatrix} \tag{4-35}$$

Differentiating, the angular acceleration of the body triad is.

$$\begin{Bmatrix} \dot{\omega}_x \\ \dot{\omega}_y \\ \dot{\omega}_z \end{Bmatrix} = [\beta] \begin{Bmatrix} \ddot{\psi} \\ \ddot{\theta} \\ \ddot{\phi} \end{Bmatrix} + [\dot{\beta}] \begin{Bmatrix} \dot{\psi} \\ \dot{\theta} \\ \dot{\phi} \end{Bmatrix} \tag{4-36}$$

Substituting equations (4-28) thru (4-36) into equations (4-26) and (4-27) we obtain the inertial velocities and accelerations of the liquid in terms of the ET and liquid generalized coordinates.

$$\lfloor \hat{I}\ \hat{J}\ \hat{K} \rfloor \begin{Bmatrix} \dot{R}_x \\ \dot{R}_y \\ \dot{R}_z \end{Bmatrix}_i = \lfloor \hat{I}\ \hat{J}\ \hat{K} \rfloor \left[\begin{Bmatrix} \dot{X} \\ \dot{Y} \\ \dot{Z} \end{Bmatrix} + [\gamma]^T [{}_C R_T] \begin{Bmatrix} \dot{q}_x \\ \dot{q}_y \\ \dot{q}_z \end{Bmatrix}_i + [\gamma]^T [r_s]_i [\beta] \begin{Bmatrix} \dot{\psi} \\ \dot{\theta} \\ \dot{\phi} \end{Bmatrix} \right] \tag{4-37}$$

and

$$\lfloor \hat{I}\ \hat{J}\ \hat{K} \rfloor \begin{Bmatrix} \ddot{R}_x \\ \ddot{R}_y \\ \ddot{R}_z \end{Bmatrix}_i = \lfloor \hat{I}\ \hat{J}\ \hat{K} \rfloor \left[\begin{Bmatrix} \ddot{X} \\ \ddot{Y} \\ \ddot{Z} \end{Bmatrix} + [\gamma]^T [{}_C R_T] \begin{Bmatrix} \ddot{q}_x \\ \ddot{q}_y \\ \ddot{q}_z \end{Bmatrix}_i + 2[\gamma]^T [\Omega] [{}_C R_T] \begin{Bmatrix} \dot{q}_x \\ \dot{q}_y \\ \dot{q}_z \end{Bmatrix}_i \right] + \lfloor \hat{I}\ \hat{J}\ \hat{K} \rfloor \left[[\gamma]^T [\Omega] [r_s]_i [\beta] \begin{Bmatrix} \dot{\psi} \\ \dot{\theta} \\ \dot{\phi} \end{Bmatrix} + [\gamma]^T [r_s]_i [\dot{\beta}] \begin{Bmatrix} \dot{\psi} \\ \dot{\theta} \\ \dot{\phi} \end{Bmatrix} \right] + \lfloor \hat{I}\ \hat{J}\ \hat{K} \rfloor \left[[\gamma]^T [r_s]_i [\beta] \begin{Bmatrix} \ddot{\psi} \\ \ddot{\theta} \\ \ddot{\phi} \end{Bmatrix} \right] \tag{4-38}$$

The virtual displacements, δR_i, are related to the generalized coordinates through the kinematic relationships of equation (4-37)*. Thus,

$$\lfloor \hat{I}\ \hat{J}\ \hat{K} \rfloor \begin{Bmatrix} \delta R_x \\ \delta R_y \\ \delta R_z \end{Bmatrix}_i = \lfloor \hat{I}\ \hat{J}\ \hat{K} \rfloor \left[\begin{Bmatrix} \delta X \\ \delta Y \\ \delta Z \end{Bmatrix} + [\gamma]^T [{}_C R_T] \begin{Bmatrix} \delta q_x \\ \delta q_y \\ \delta q_z \end{Bmatrix} + [\gamma]^T [r_s]_i [\beta] \begin{Bmatrix} \delta\psi \\ \delta\theta \\ \delta\phi \end{Bmatrix} \right] \tag{4-39}$$

*See Appendix A, Virtual Power Concept

Having obtained expressions for the acceleration and virtual displacements of a point within the liquid, the virtual work expression can be evaluated to obtain the liquid-ET inertia coupling. The virtual work integral (eq. 4-25) is replaced with a summation over n liquid mass points representing the mass of the liquid volume. Furthermore, this summation can be separated into acceleration and velocity components of the generalized coordinates. Thus,

$$\sum_{i=1}^{n} \lfloor \delta\Xi_i \delta\chi \delta\alpha \rfloor \begin{bmatrix} [{}_T R_C][\gamma] \\ [I] \\ [\beta]^T [r_s]_i^T [\gamma] \end{bmatrix} [m_i] \left[[\gamma]^T [{}_C R_T] \;\vdots\; [I] \;\vdots\; [\gamma]^T [r_s]_i [\beta] \right] \begin{Bmatrix} \ddot{\Xi}_i \\ \ddot{\chi} \\ \ddot{\alpha} \end{Bmatrix}$$

$$+ \sum_{i=1}^{n} \lfloor \delta\Xi \delta\chi \delta\alpha \rfloor \begin{bmatrix} [{}_T R_C][\gamma] \\ [I] \\ [\beta]^T [r_s]_i^T [\gamma] \end{bmatrix} [m_i] \left[\begin{array}{c|c|c|c} 2[\gamma]^T [\Omega][{}_C R_T] & [0] & [\gamma]^T & \\ & & & \end{array} \right.$$

$$\left. \left[[\Omega][r_s]_i [\beta] + [r_s]_i [\dot{\beta}] \right] \right] \begin{Bmatrix} \ddot{\Xi}_i \\ \dot{\chi} \\ \dot{\alpha} \end{Bmatrix} \qquad (4\text{-}40)$$

where Ξ_i = q_x, q_y, q_z for the ith liquid mass

χ = X, Y, Z

α = ψ, θ, ϕ

$[m_i]$ = mass matrix for the ith liquid mass (3x3)

The coupled mass matrix is obtained by combining the first summation of equation (4-40) with the mass matrices defined in the ET rigid body equations (4-9) and (4-17). Thus,

$$[\overline{M}] = \left[\begin{array}{ccc|c|c} \ddot{\Xi}_1 & \ddot{\Xi}_2 & \ddot{\Xi}_n & \ddot{\chi} & \ddot{\alpha} \\ \hline [m_1] & & & [m_1][{}_T R_C][\gamma] & [m_1][{}_T R_C][r_s]_1[\beta] \\ & [m_2] & & [m_2][{}_T R_C][\gamma] & [m_2][{}_T R_C][r_s]_2[\beta] \\ & & \ddots & \vdots \;\vdots\; \vdots & \vdots \;\vdots\; \vdots \\ & & [m_n] & [m_n][{}_T R_C][\gamma] & [m_n][{}_T R_C][r_s]_n[\beta] \\ \hline & & & \sum_{i=1}^{n} [m_i] + [M] & \sum_{i=1}^{n} [m_i][\gamma]^T [r_s]_i [\beta] \\ \hline & & & & \sum_{i=1}^{n} [\beta]^T [r_s]_i^T [m_i][r_s]_i [\beta] \\ & & & & + [\beta]^T [\tilde{I}][\beta] \end{array}\right]$$

or in short,

$$[\bar{M}] = \begin{bmatrix} M_{\Xi\Xi} & M_{\Xi\chi} & M_{\Xi\alpha} \\ M_{\chi\Xi} & M_{\chi\chi} & M_{\chi\alpha} \\ M_{\alpha\Xi} & M_{\alpha\chi} & M_{\alpha\alpha} \end{bmatrix} \tag{4-41}$$

The second summation of equation (4-40) represents the liquid inertia forces which are a function of liquid and ET generalized velocities. These forces are treated as generalized forces applied to the right hand side of the equations of motion and are combined with the ET inertia forces which are a function of the ET generalized velocities (4-17). Thus, the coupled equations of motion (neglecting external and constraint forces) are,

$$\begin{bmatrix} M_{\Xi\Xi} & M_{\Xi\chi} & M_{\Xi\alpha} \\ M_{\chi\Xi} & M_{\chi\chi} & M_{\chi\alpha} \\ M_{\alpha\Xi} & M_{\alpha\chi} & M_{\alpha\alpha} \end{bmatrix} \begin{Bmatrix} \ddot{\Xi} \\ \ddot{\chi} \\ \ddot{\alpha} \end{Bmatrix} = - \begin{bmatrix} Q_{\Xi} \\ Q_{\chi} \\ Q_{\alpha} \end{bmatrix} \tag{4-42}$$

where,

$$[Q_{\Xi}] = \begin{bmatrix} 2[{}_{T}R_{C}][\Omega][{}_{C}R_{T}][m]_{1}\dot{\Xi}_{1} + [{}_{T}R_{C}]\left[[\Omega][r_{s}]_{1}[\beta] + [r_{s}]_{1}[\dot{\beta}]\right][m]_{1}\dot{\alpha} \\ \vdots \\ 2[{}_{T}R_{C}][\Omega][{}_{C}R_{T}][m]_{n}\dot{\Xi}_{n} + [{}_{T}R_{C}]\left[[\Omega][r_{s}]_{n}[\beta] + [r_{s}]_{n}[\dot{\beta}]\right][m]_{n}\dot{\alpha} \end{bmatrix}$$

$$[Q_{\chi}] = \left[[\gamma]^{T} \sum_{i=1}^{n} \left[2[\Omega][m]_{i}[{}_{C}R_{T}]\dot{\Xi}_{i} + \left[[\Omega][m]_{i}[r_{s}]_{i}[\beta] + [m]_{i}[r_{s}]_{i}[\dot{\beta}] \right]\dot{\alpha} \right] \right]$$

$$[Q_{\alpha}] = \begin{bmatrix} [\beta]^{T}\left[\sum_{i=1}^{n} [r_{s}]_{i}^{T}[m]_{i}\left[2[\Omega][{}_{C}R_{T}]\{\dot{\Xi}_{i}\} + [\Omega][r_{s}]_{i}[\beta]\{\dot{\alpha}\} + [r_{s}]_{i}[\dot{\beta}]\dot{\alpha} \right] \right] \\ + \left[[\dot{\beta}]^{T}[\tilde{I}][\beta] + [\beta]^{T}[\tilde{I}][\dot{\beta}] + [P][\tilde{I}][\beta] \right]\{\dot{\alpha}\} \end{bmatrix}$$

This completes the development of the inertia coupling between the liquid and ET rigid body dynamics.

4.3 SOLUTION OF THE COUPLED EQUATION OF MOTION

Before proceeding with the detailed derivations of the constraint and liquid shear forces, the general procedure for solving the coupled equation will be discussed. This discussion includes the development of the equations to conserve the momentum of the coupled system.

The generalized forces applied to the liquid and ET, as well as the constraint forces, can be added to equation (4-42).

$$\begin{bmatrix} M_{\Xi\Xi} & M_{\Xi\chi} & M_{\Xi\alpha} \\ M_{\chi\Xi} & M_{\chi\chi} & M_{\chi\alpha} \\ M_{\alpha\Xi} & M_{\alpha\chi} & M_{\alpha\alpha} \end{bmatrix} \begin{Bmatrix} \ddot{\Xi} \\ \ddot{\chi} \\ \ddot{\alpha} \end{Bmatrix} = - \begin{bmatrix} Q_{\Xi} \\ Q_{\chi} \\ Q_{\alpha} \end{bmatrix} + \begin{bmatrix} Q_{E\Xi} \\ Q_{E\chi} \\ Q_{F\alpha} \end{bmatrix} + \begin{bmatrix} b_{\Xi}^{T} \\ b_{\chi}^{T} \\ b_{\alpha}^{T} \end{bmatrix} \{\lambda\} \tag{4-43}$$

subject to,

$$\begin{bmatrix} b_\Xi & b_\chi & b_\alpha \end{bmatrix} \begin{Bmatrix} \ddot{\Xi} \\ \ddot{\chi} \\ \ddot{\alpha} \end{Bmatrix} + \begin{bmatrix} \dot{b}_\Xi & \dot{b}_\chi & \dot{b}_\alpha \end{bmatrix} \begin{Bmatrix} \dot{\Xi} \\ \dot{\chi} \\ \dot{\alpha} \end{Bmatrix} = \{0\} \tag{4-44}$$

where $[Q_{\Xi\Xi}]$, $[Q_{E\chi}]$, $[Q_{E\alpha}]$ = External and dissipative generalized forces applied to the liquid and ET.

The first step in the solution process requires that the momentum of the system be conserved in accordance with the constraints imposed upon the system. Analagous to the development presented in Chapter 3.0, the impulse-momentum expression for an inelastic impact can be written as,

$$\begin{bmatrix} M_{\Xi\Xi} & M_{\Xi\chi} & M_{\Xi\alpha} \\ M_{\chi\Xi} & M_{\chi\chi} & M_{\chi\alpha} \\ M_{\alpha\Xi} & M_{\alpha\chi} & M_{\alpha\alpha} \end{bmatrix} \begin{Bmatrix} \dot{\Xi}_+ \\ \dot{\chi}_+ \\ \dot{\alpha}_+ \end{Bmatrix} = \begin{bmatrix} M_{\Xi\Xi} & M_{\Xi\chi} & M_{\Xi\alpha} \\ M_{\chi\Xi} & M_{\chi\chi} & M_{\chi\alpha} \\ M_{\alpha\Xi} & M_{\alpha\chi} & M_{\alpha\alpha} \end{bmatrix} \begin{Bmatrix} \dot{\Xi}_- \\ \dot{\chi}_- \\ \dot{\alpha}_- \end{Bmatrix} + \begin{bmatrix} b_\Xi^T \\ b_\chi^T \\ b_\alpha^T \end{bmatrix} \{f\} \tag{4-45}$$

where (-) subscript denotes velocities before contact and (+) subscript denotes the velocities after impact. The impulsive force at impact is represented by {f}. Furthermore, after the liquid node point has contacted the wall,

$$\begin{bmatrix} b_\Xi & b_\chi & b_\alpha \end{bmatrix} \begin{Bmatrix} \dot{\Xi} \\ \dot{\chi} \\ \dot{\alpha} \end{Bmatrix} = \{0\} \tag{4-46}$$

A two step solution process, which required inversion of the system mass matrix, was employed in Chapter 3.0. The system mass matrix is now highly coupled and contains a large number of non-zero terms. Therefore, an alternative solution procedure is employed. Equation (4-46) is appended to equation (4-45) and the impulse forces {f} are placed on the left hand side. Thus,

$$\begin{vmatrix} M_{\Xi\Xi} & M_{\Xi\chi} & M_{\Xi\alpha} & b_\Xi^T \\ M_{\chi\Xi} & M_{\chi\chi} & M_{\chi\alpha} & b_\chi^T \\ M_{\alpha\Xi} & M_{\alpha\chi} & M_{\alpha\alpha} & b_\alpha^T \\ b_\Xi & b_\chi & b_\alpha & (\varepsilon-1) \end{vmatrix} \begin{Bmatrix} \dot{\Xi}_+ \\ \dot{\chi}_+ \\ \dot{\alpha}_+ \\ -f \end{Bmatrix} = \begin{vmatrix} M_{\Xi\Xi} & M_{\Xi\chi} & M_{\Xi\alpha} & 0 \\ M_{\chi\Xi} & M_{\chi\chi} & M_{\chi\alpha} & 0 \\ M_{\alpha\Xi} & M_{\alpha\chi} & M_{\alpha\alpha} & 0 \\ 0 & 0 & 0 & 0 \end{vmatrix} \begin{Bmatrix} \dot{\Xi}_- \\ \dot{\chi}_- \\ \dot{\alpha}_- \end{Bmatrix} \tag{4-47}$$

The "plus" velocity states are obtained by solving these algebraic equations with a Gaussian elimination and backward substitution procedure. The (ε-1) diagonal terms permit decomposition when a constraint becomes zero (ε=0).

Having obtained the generalized velocities of the liquid and ET after the liquid impacts the wall, the velocity dependent forces can be evaluated and the coupled equations of motion solved. Equations (4-43) and (4-44) are cast into a format similar to equation (4-47).

$$\begin{bmatrix} M_{\Xi\Xi} & M_{\Xi\chi} & M_{\Xi\alpha} & b_{\Xi}^T \\ M_{\chi\Xi} & M_{\chi\chi} & M_{\chi\alpha} & b_{\chi}^T \\ M_{\alpha\Xi} & M_{\alpha\chi} & M_{\alpha\alpha} & b_{\alpha}^T \\ b_{\Xi} & b_{\chi} & b_{\alpha} & (\varepsilon-1) \end{bmatrix} \begin{Bmatrix} \ddot{\Xi} \\ \ddot{\chi} \\ \ddot{\alpha} \\ -\lambda \end{Bmatrix} = -\begin{Bmatrix} Q_{\Xi} \\ Q_{\chi} \\ Q_{\alpha} \\ 0 \end{Bmatrix} + \begin{Bmatrix} Q_{E\Xi} \\ Q_{E\chi} \\ Q_{E\alpha} \\ 0 \end{Bmatrix} - \begin{bmatrix} 0 & 0 & 0 \\ 0 & 0 & 0 \\ 0 & 0 & 0 \\ b_{\Xi} & b_{\chi} & b_{\alpha} \end{bmatrix} \begin{Bmatrix} \dot{\Xi} \\ \dot{\chi} \\ \dot{\alpha} \end{Bmatrix} \quad (4\text{-}48)$$

Note, the left hand side coefficient matrix has remained the same, therefore, the state solution only requires evaluation of the right hand side and a new back substitution.

The constraint forces between the liquid and tank will be shown in section 4.4 to be only functions of the liquid generalized coordinates.

Therefore, $[b_{\chi}]$ and $[b_{\alpha}]$ are null matrices. This simplifies the expression for the velocity change after impact (equation 4-47) and the constraint force expression (equation 4-48). Note, however, the impact of the liquid onto the tank wall still affects the ET velocities through the inertial coupling terms. Likewise, the constraint forces, λ, reflect the ET generalized forces and momentum through the inertial coupling. This coupling provides closed-loop feedback between the liquid and ET dynamics.

4.4 THREE-DIMENSIONAL IMPERMEABILITY CONSTRAINTS

The liquid at the ET wall is constrained to move tangent to the wall. The previous section stated that the auxiliary equation, (equation

4-39), which defines these constraint conditions, did not directly involve the ET velocities. This section will develop these constraint expressions and define the analytical representation of the constraint surface.

Consider two points separated a distance of Δ, one point on the tank boundary the companion point interior to the boundary. Define the boundary point as point A and the interior point as a liquid mass point, point B. Referring to Figure 4-4, the absolute positions and velocities of both points can be obtained.

$$\bar{R}_a = \bar{R}_c + \bar{R}_T + \bar{q}_a \qquad (4\text{-}49a)$$

$$\bar{R}_b = \bar{R}_c + \bar{R}_T + \bar{q}_b \qquad (4\text{-}49b)$$

and

$$\dot{\bar{R}}_a = \dot{\bar{R}}_c + \dot{\bar{R}}_T + \bar{\omega} \times \bar{R}_T + \dot{\bar{q}}_a + \bar{\omega} \times \bar{q}_a \qquad (4\text{-}50a)$$

$$\dot{\bar{R}}_b = \dot{\bar{R}}_c + \dot{\bar{R}}_T + \bar{\omega} \times \bar{R}_T + \dot{\bar{q}}_b + \bar{\omega} \times \bar{q}_b \qquad (4\text{-}50b)$$

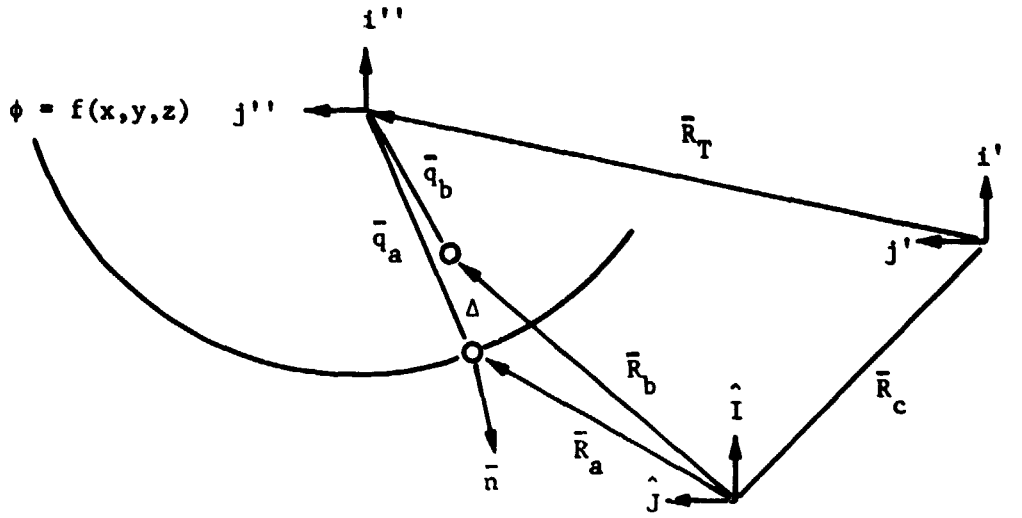

Figure 4-4. Definition of Three-Dimensional Tank Boundary Constraint

The velocity of point B, the liquid mass point, relative to wall is $\dot{\Delta}$ or,

$$\dot{\Delta} = \dot{\bar{R}}_b - \dot{\bar{R}}_a = \dot{\bar{q}}_b + \bar{\omega} \times \bar{q}_b - (\dot{\bar{q}}_a + \bar{\omega} \times \bar{q}_a) \tag{4-51}$$

The tank is rigid, therefore, the velocity of point A is zero, relative to the tank axis. Furthermore, the constraint condition is imposed when $\bar{q}_a = \bar{q}_b$. These conditions simplify equation (4-51). Hence,

$$\dot{\Delta} = \dot{\bar{q}}_b \tag{4-52}$$

The impermeability constraint requires that the velocity of the liquid normal to the constraint surface be zero. This can be expressed as,

$$\bar{n} \cdot \dot{\bar{q}}_b = 0 \tag{4-53}$$

where

$\bar{n}$ = the outward normal vector to the constraint surface

The normal vector is defined as the gradient of the constraint surface, ϕ, evaluated at the location of the liquid mass point. Thus,

$$\bar{n} = \nabla\phi = \frac{\partial\phi}{\partial x}\bigg|_{x,y,z} i'' + \frac{\partial\phi}{\partial y}\bigg|_{x,y,z} j'' + \frac{\partial\phi}{\partial z}\bigg|_{x,y,z} k'' \tag{4-54}$$

The time derivative of the constraint equation, (4-53), is required for the solution of the equations of motion. Therefore,

$$\frac{d}{dt}(\nabla\phi\cdot\dot{\bar{q}}_b) = \dot{\nabla}\phi\cdot\dot{\bar{q}}_b + (\bar{\omega}X\nabla\phi)\cdot\dot{\bar{q}}_b + \nabla\phi\cdot\ddot{\bar{q}}_b + \nabla\phi\cdot(\bar{\omega}X\dot{\bar{q}}_b) = 0 \tag{4-55}$$

From vector algebra, the following relationships are evident,

$$\nabla\phi\cdot(\bar{\omega}\ X\ \dot{\bar{q}}_b) = (\nabla\phi\ X\ \bar{\omega})\cdot\dot{\bar{q}}_b \tag{4-56a}$$

and

$$\nabla\phi X\bar{\omega} = -\bar{\omega}X\nabla\phi \tag{4-56b}$$

Thus, equation (4-55) simplifies to,

$$\dot{\nabla}\phi\cdot\dot{\bar{q}}_b + \nabla\phi\cdot\ddot{\bar{q}}_b = 0 \tag{4-57}$$

This expression is equivalent to equation (4-39) and shows that the auxiliary equations are not functions of the velocities of the ET.

The ET tank is axisymmetric. Therefore, the definitions of the constraint surface and [b] matrices follow that of the two-dimensional development; this is also true for the baffles region of the constraint surface. Therefore,

$$\phi = \left(\frac{x}{b_0}\right)^2 + \left(\frac{y}{b_0}\right)^2 + \left(\frac{z}{a_0 - a_1 z}\right)^2 - 1 = 0 \tag{4-58}$$

and referring to Figure 3-8, the baffles region ϕ is,

$$\phi = \left(\frac{x}{b_0}\right)^2 + \left(\frac{y}{b_0}\right)^2 - 1 + \frac{2\eta}{b_0}\left[1 - \left(\frac{z}{a_0 - a_1 z}\right)^2\right]^{1/2} - \left(\frac{\eta}{b_0}\right)^2 = 0 \tag{4-59}$$

where x, y, z are measured in the tank reference frame. The [b] matrices for the bare and baffles regions are,

$$[b]_j \{\dot{\xi}\}_j = \left[\frac{2x_j}{b_0^2} \;\middle|\; \frac{2y_j}{b_0^2} \;\middle|\; \frac{2a_0 z_j}{\left(a_0 - a_1 z_j\right)^3}\right] \begin{Bmatrix} \dot{x}_j \\ \dot{y}_j \\ \dot{z}_j \end{Bmatrix} = \{0\} \tag{4-60}$$

and

$$[b]_j \{\dot{\xi}\}_j = \left[\frac{2x_j}{b_0^2} \;\middle|\; \frac{2y_j}{b_0^2} \;\middle|\; -\frac{\partial a}{\partial z} + \frac{\eta}{b_0}\left[\frac{\partial a}{\partial z} a^{-1/2} - \frac{2}{b_0}\frac{\partial \eta}{\partial z}\right]\right.$$

$$\left. + \frac{2}{b_0}\frac{\partial \eta}{\partial z} a^{1/2}\right] \begin{Bmatrix} \dot{x}_j \\ \dot{y}_j \\ \dot{z}_j \end{Bmatrix} \tag{4-61}$$

where

x_j, y_j, z_j = = the coordinates of the i th liquid mass point

$\dot{x}_j, \dot{y}_j, \dot{z}_j$ = = the velocity components of the i th liquid mass point

$$\alpha = 1 - \left(\frac{z_j}{a_0 - a_1 z_j}\right)^2$$

$$\frac{\partial \alpha}{\partial z} = - \frac{2a_0 z_j}{(a_0 - a_1 z_j)^3}$$

$$\frac{\partial \eta}{\partial z} = \frac{\pi h}{\ell} \sin\left(\frac{2\pi\xi}{\ell}\right)$$

The time derivatives of the [b] matrices are,

$$[\dot{b}]_j \{\dot{\xi}\}_j = \left[\frac{2}{b_0^2} \dot{x}_j \;\middle|\; \frac{2}{b_0^2} \dot{y}_j \;\middle|\; \frac{2a_0 + 4a_0 a_1 z_j}{(a_0 - a_1 z_j)^4} \dot{z}_j\right] \begin{Bmatrix} \dot{x}_j \\ \dot{y}_j \\ \dot{z}_j \end{Bmatrix} \tag{4-62}$$

and

$$[\dot{b}]_j \{\dot{\xi}\}_j = \left[\frac{2}{b_0^2} \dot{x}_j \;\middle|\; \frac{2}{b_0^2} \dot{y}_j \;\middle|\; \bar{k} \dot{z}_j\right] \begin{Bmatrix} \dot{x}_j \\ \dot{y}_j \\ \dot{z}_j \end{Bmatrix} \tag{4-63}$$

where

$\bar{k}$ is defined as the z_j velocity coefficient in equation (3-35), Chapter 3.0.

4.5 THREE-DIMENSIONAL INCOMPRESSIBILITY CONSTRAINT

The three-dimensional liquid incompressibility was modeled with a solid parallelepiped element. This element (also used to define viscous shear forces) maintained an average incompressibility within its volume; the volume of any fraction of the element could vary, but the element as a whole maintained constant volume. This averaging technique was accomplished by dividing the parallelepiped into two unique arrangements of tetrahedra as shown in Figure 4-5. The volume of each arrangement (consisting of five tetrahedra) equals the volume of the parallelepiped. The parallelepiped volume was defined as one-half the sum of the ten tetrahedra volumes. The incompressibility constraint coefficients, [b], for a given parallelepiped, are formed for each of the two unique tetrahedra arrangements. The constituents of the two [b] matrices are then averaged, term by term, to arrive at the final incompressibility constraint matrix for that parallelepiped element.

The incompressibility constraint coefficients for each tetrahedron are derived by requiring the volume of the tetrahedron to remain constant The tetrahedron volume can be written as a scalar triple product. Referring to Figure 4-6, the volume for a tetrahedron with the local element node numbering ℓ , m, n, o, can be written as,

$$\forall = 1/6\ A\cdot(B \times C) = \text{Constant} \tag{4-64}$$

The rate of change of the tetrahedron volume must equal zero. Therefore, $\frac{d}{dt} =$

$$\begin{aligned}\frac{d\forall}{dt} = {} & \dot{A}_1(B_2C_3 - B_3C_2) + A_1(\dot{B}_2C_3 - \dot{B}_3C_2) + A_1(B_2\dot{C}_3 - B_3\dot{C}_2) \\ & + \dot{A}_2(B_3C_1 - B_1C_3) + A_2(\dot{B}_3C_1 - \dot{B}_1C_3) + A_2(B_3\dot{C}_1 - B_1\dot{C}_3) \\ & + \dot{A}_3(B_1C_2 - B_2C_1) + A_3(\dot{B}_1C_2 - \dot{B}_2C_1) + A_3(B_1\dot{C}_2 - B_2\dot{C}_1) = 0\end{aligned} \tag{4-65}$$

Collecting the terms of equation (4-65) by the node point velocities of the tetrahedron, the components of the [b] matrix for that particular tetrahedron are formed.

Node ℓ Components

$$[(B_3C_2 - B_2C_3) - (A_3C_2 - A_2C_3) - (A_2B_3 - A_3B_2)]\dot{x}_\ell \tag{4-66a}$$

$$[(B_2C_3 - B_3C_1) - (A_1C_3 - A_3C_1) - (A_3B_1 - A_1B_3)]\dot{y}_\ell \tag{4-66b}$$

$$[(B_2C_1 - B_1C_2) - (A_2C_1 - A_1C_2) - (A_1B_2 - A_2B_1)]\dot{z}_\ell \tag{4-66c}$$

Node m Components

$$[A_3C_2 - A_2C_3]\dot{x}_m \tag{4-67a}$$

$$[A_1C_3 - A_3C_1]\dot{y}_m \tag{4-67b}$$

$$[A_2C_1 - A_1C_2]\dot{z}_m \tag{4-67c}$$

Node n Components

$$[A_2B_3 - A_3B_2]\dot{x}_n \tag{4-68a}$$

$$[A_3B_1 - A_1B_3]\dot{y}_n \tag{4-68b}$$

$$[A_1B_2 - A_2B_1]\dot{z}_n \tag{4-68c}$$

Node o Components

$$[B_2C_3 - B_3C_2]\dot{x}_o \tag{4-69a}$$

$$[B_3C_1 - B_1C_3]\dot{y}_o \tag{4-69b}$$

$$[B_1C_2 - B_2C_1]\dot{z}_o \tag{4-69c}$$

The components of each tetrahedron (for the two arrangements) were assembled to form two global [b] matrices for the parallelepiped element. This assembly used the node point numbering key indicated below each parallelepiped in Figure 4-5. The two global [b] matrices were averaged, term by term, to form the incompressibility constraint coefficients for a given parallelepiped element. The parallelepiped [b] matrices were assembled to form the incompressibility constraint matrix for the liquid.

The time derivative of the constraint matrix is required in the definition of the auxiliary equation (4-39). These time derivatives were derived using an averaging technique similar to that used in deriving the [b] matrix. Using equations (4-66) thru (4-69), the components of the [b] matrix for a particular tetrahedron are,

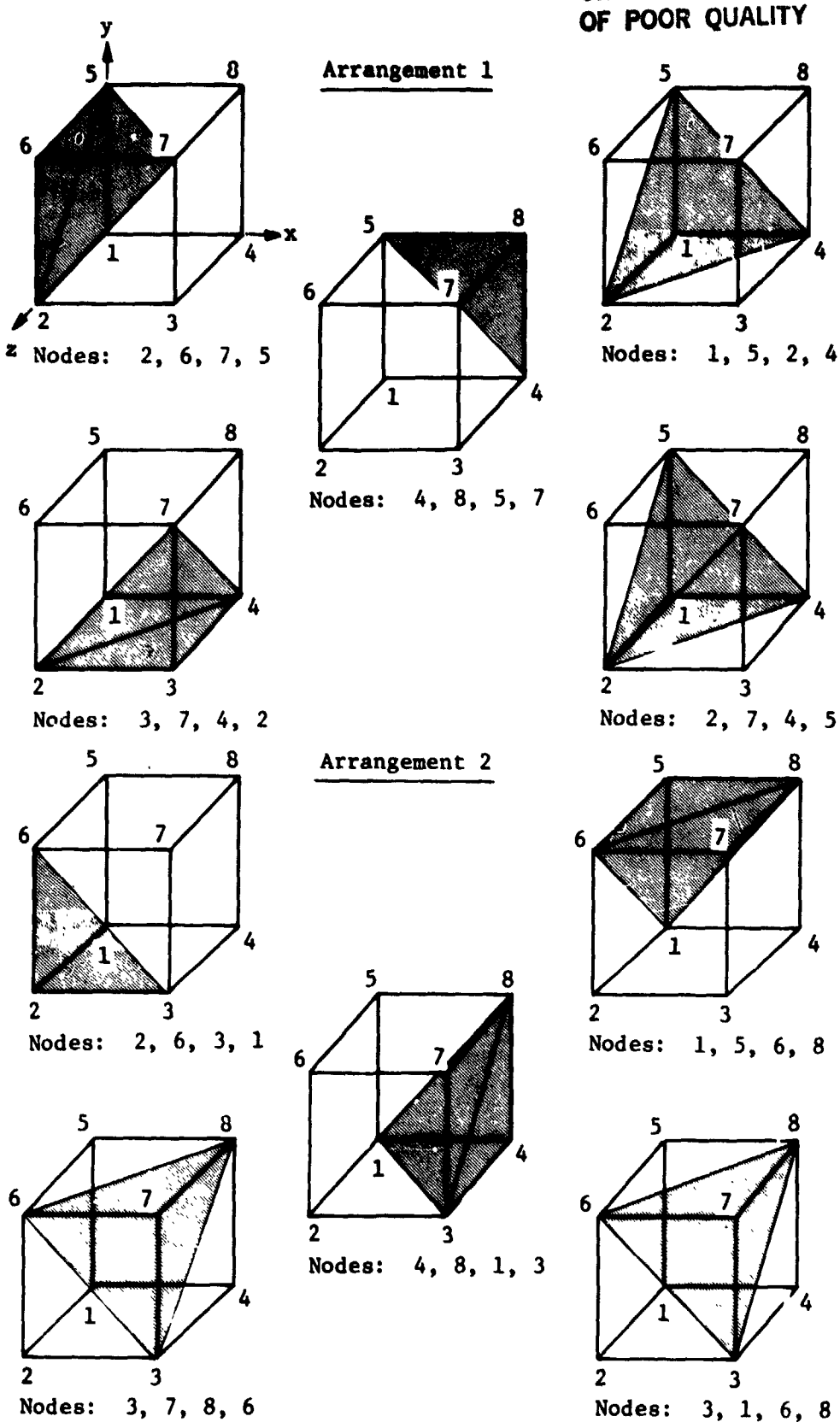

Figure 4-5. Tetrahedron Definition of Parallelepiped Element

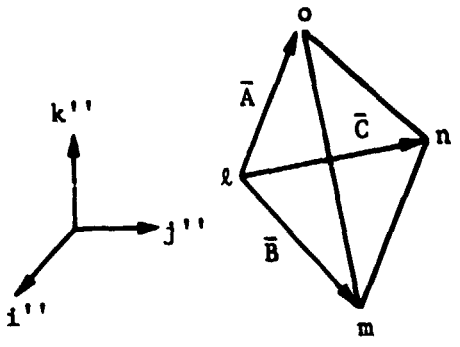

$$\bar{A} = (x_o - x_\ell)i'' + (y_o - y_\ell)j'' + (z_o - z_\ell)k''$$
$$= A_1 i'' + A_2 j'' + A_3 k''$$
$$\bar{B} = (x_m - x_\ell)i'' + (y_m - y_\ell)j'' + (z_m - z_\ell)k''$$
$$= B_1 i'' + B_2 j'' + B_3 k''$$
$$\bar{C} = (x_n - x_\ell)i'' + (y_n - y_\ell)j'' + (z_n - z_\ell)k''$$
$$= C_1 i'' + C_2 j'' + C_3 k''$$

Figure 4-6. Tetrahedron Vector Definition

Node ℓ Components

$$[-\dot{B}_2C_3 + \dot{B}_3C_2 - B_2\dot{C}_3 + B_3\dot{C}_2 - \dot{A}_3C_2 + A_2C_3 - A_3\dot{C}_2 + A_2\dot{C}_3 - \dot{A}_2B_3 + \dot{A}_3B_2 - A_2\dot{B}_3 + A_3\dot{B}_2]\dot{x}_\ell \quad (4\text{-}70a)$$

$$[-\dot{B}_3C_1 + \dot{B}_1C_3 - B_3\dot{C}_1 + B_1\dot{C}_3 - \dot{A}_1C_3 + \dot{A}_3C_1 - A_1\dot{C}_3 + A_3\dot{C}_1 - \dot{A}_3B_1 + \dot{A}_1B_3 - A_3\dot{B}_1 + A_1\dot{B}_3]\dot{y}_\ell \quad (4\text{-}70b)$$

$$[-\dot{B}_1C_2 + \dot{B}_2C_1 - B_1\dot{C}_2 + B_2\dot{C}_1 - \dot{A}_2C_1 + \dot{A}_1C_2 - A_2\dot{C}_1 + A_1\dot{C}_2 - \dot{A}_1B_2 + \dot{A}_2B_1 - A_1\dot{B}_2 + A_2\dot{B}_1]\dot{z}_\ell \quad (4\text{-}70c)$$

Node m Components

$$[\dot{A}_3C_2 - \dot{A}_2C_3 + A_3\dot{C}_2 - A_2\dot{C}_3]\dot{x}_m \quad (4\text{-}71a)$$

$$[\dot{A}_1C_3 - \dot{A}_3C_1 + A_1\dot{C}_3 - A_3\dot{C}_1]\dot{y}_m \quad (4\text{-}71b)$$

$$[\dot{A}_2C_1 - \dot{A}_1C_2 + A_2\dot{C}_1 - A_1\dot{C}_2]\dot{z}_m \quad (4\text{-}71c)$$

Node n Components

$$[\dot{A}_2B_3 - \dot{A}_3B_2 + A_2\dot{B}_3 - A_3\dot{B}_2]\dot{x}_n \quad (4\text{-}72a)$$

$$[\dot{A}_3B_1 - \dot{A}_1B_3 + A_3\dot{B}_1 - A_1\dot{B}_3]\dot{y}_n \quad (4\text{-}72b)$$

$$[\dot{A}_1B_2 - \dot{A}_2B_1 + A_1\dot{B}_2 - A_2\dot{B}_1]\dot{z}_n \quad (4\text{-}72c)$$

Node o Components

$$[\dot{B}_2C_3 - \dot{B}_3C_2 + B_2\dot{C}_3 - B_3\dot{C}_2]\dot{x}_o \quad (4\text{-}73a)$$

$$[\dot{B}_3C_1 - \dot{B}_1C_3 + B_3\dot{C}_1 - B_1\dot{C}_3]\dot{y}_o \qquad (4\text{-}73b)$$

$$[\dot{B}_1C_2 - \dot{B}_2C_1 + B_1\dot{C}_2 - B_2\dot{C}_1]\dot{z}_o \qquad (4\text{-}73c)$$

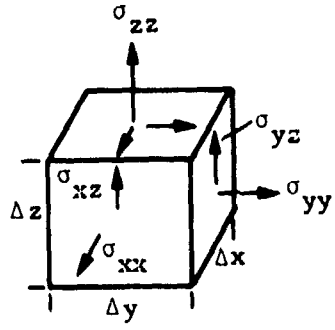

$$\sigma_{ii} = \begin{Bmatrix} \sigma_{xx} \\ \sigma_{xy} \\ \sigma_{xz} \\ \sigma_{yy} \\ \sigma_{yx} \\ \sigma_{yz} \\ \sigma_{zz} \\ \sigma_{zx} \\ \sigma_{zy} \end{Bmatrix}$$

where $\sigma_{ij} = \sigma_{ji}$ due to symmetry

Figure 4-7. Definition of Stress Tensor for Liquid

These components were averaged and assembled to form the incompressibility constraint matrix [$\dot{b}$] for the liquid.

4.6 DERIVATION OF THE LIQUID SHEAR FORCES IN THREE DIMENSIONS

A three-dimensional parallelepiped finite element was used to represent the shear forces within the liquid. This element was derived from the liquid stress-strain rate relationships using a variational mechanics approach.

Consider the stresses on a differential volume of size Δx, Δy, Δz (Figure 4-7). Furthermore, assume the stress field results from liquid resistance to strain rate (deviatoric stresses) and the mean pressure on the differential volume.

The stress-strain rate relationships for a viscous liquid have been derived [Ref 15]. Hence, the stresses on the differential volume can be expressed in terms of the strain rates as,

$$\sigma_{xx} = -P - \frac{2}{3}\mu(\theta) + 2\mu\frac{\partial u}{\partial x} \qquad (4\text{-}75a)$$

$$\sigma_{yy} = -P - \frac{2}{3}\mu(\theta) + 2\mu\frac{\partial v}{\partial y} \qquad (4\text{-}75b)$$

$$\sigma_{zz} = -P - \frac{2}{3}\mu\,(\theta) + 2\mu\frac{\partial w}{\partial z} \tag{4-75c}$$

$$\sigma_{xy} = \sigma_{yx} = \mu\left(\frac{\partial v}{\partial x} + \frac{\partial u}{\partial y}\right) \tag{4-75d}$$

$$\sigma_{xz} = \sigma_{zx} = \mu\left(\frac{\partial w}{\partial x} + \frac{\partial u}{\partial z}\right) \tag{4-75e}$$

$$\sigma_{yz} = \sigma_{zy} = \mu\left(\frac{\partial w}{\partial y} + \frac{\partial v}{\partial z}\right) \tag{4-75f}$$

where

u, v, w = the velocities of the liquid in the tank x, y, z directions,

m = coefficient of viscosity,

P = mean pressure.

$$\theta = \frac{\partial u}{\partial x} + \frac{\partial v}{\partial z} + \frac{\partial w}{\partial z}$$

The velocity-strain rate expressions can be written using tensor notation.

$$\varepsilon_{ij} = \frac{1}{2}\left(\frac{\partial u_i}{\partial x_j} + \frac{\partial u_j}{\partial x_i}\right) \tag{4-76}$$

Furthermore, the liquid has been assumed incompressible. Hence,

$$\frac{\partial u}{\partial x} + \frac{\partial v}{\partial y} + \frac{\partial w}{\partial z} = 0 \tag{4-77}$$

Using equation (4-76) and the incompressibility statement, equation (4-77), the stress-strain rate relationships can be written in, tensor notation,

$$\sigma_{ij} = -P\,\delta_{ij} + 2\mu\,\varepsilon_{ij} \tag{4-78}$$

where

δ_{ij} = Knonecker Delta $\begin{cases} i \neq j & \delta = 0 \\ i = j & \delta = 1 \end{cases}$

Defining the deviatoric stress as,

$$\sigma_{ij}' = 2\mu\, \varepsilon_{ij} \tag{4-79}$$

the functional of the work done by the liquid stresses can be written as,

$$J = \frac{1}{2}\int_{Ve} \sigma_{ij}'\, \varepsilon_{ij}\, dVe + \frac{1}{2}\int_{Ve} -(P\delta_{ij})\, \varepsilon_{ij}\, dVe \tag{4-80}$$

The variation of this functional is,

$$\delta J = \frac{1}{2}\int_{Ve} \delta\sigma_{ij}'\, \varepsilon_{ij}\, dVe + \frac{1}{2}\int_{Ve} \sigma_{ij}'\delta\varepsilon_{ij} dVe - \frac{1}{2}\int_{Ve} \delta P\, \delta_{ij}\, \varepsilon_{ij} dVe - \frac{1}{2}\int_{Ve} P\delta_{ij}\, \delta\varepsilon_{ij}\, dVe \tag{4-81}$$

Since only incompressible liquids are being considered,

$$\varepsilon_{ii} = 0 \tag{4-82}$$

and

$$\delta\varepsilon_{ii} = 0 \tag{4-83}$$

Thus, the variation of the work integral simplifies to,

$$\delta J = \frac{1}{2}\int_{Ve} \delta\sigma_{ij}'\varepsilon_{ij} dVe + \frac{1}{2}\int_{Ve} \sigma_{ij}'\, \delta\varepsilon_{ij} dVe \tag{4-84}$$

Using equation (4-79), the variation of the deviatoric stress can be expressed as a function of the strain rate variations, further simplifying equation (4-84).

$$\delta J = \int_{Ve} 2\mu\delta\varepsilon_{ij}\varepsilon_{ij} dVe \tag{4-85}$$

This integral can be written in matrix form as,

$$\delta J = 2\mu\int_{Ve} [\delta\varepsilon_{xx}\ \delta\varepsilon_{xy}\ \delta\varepsilon_{xz}\ \delta\varepsilon_{yy}\ \delta\varepsilon_{yx}\ \delta\varepsilon_{yz}\ \delta\varepsilon_{zz}\ \delta\varepsilon_{zx}\ \delta\varepsilon_{zy}] \begin{bmatrix} \varepsilon_{xx} \\ \varepsilon_{xy} \\ \varepsilon_{xz} \\ \varepsilon_{yy} \\ \varepsilon_{yx} \\ \varepsilon_{yz} \\ \varepsilon_{zz} \\ \varepsilon_{zx} \\ \varepsilon_{zy} \end{bmatrix} dVe \tag{4-86}$$

The liquid strain rates can be expressed in terms of the liquid velocities thru the velocity-strain rate relationships (equation 4-76). Furthermore, the velocity field within a finite element region can be approximated by the nodal point velocities of the finite element. Likewise, the strain rate components can also be approximated by the nodal point velocities. Using a tetrahedron finite element with four node points, the velocity field and, hence, the strain rate components within the element, can be expressed as,

$$u_j = [N_1 \; N_2 \; N_3 \; N_4] \begin{Bmatrix} \dot{q}_1 \\ \dot{q}_2 \\ \dot{q}_3 \\ \dot{q}_4 \end{Bmatrix} \tag{4-87}$$

and

$$\frac{\partial u_j}{\partial x_j} = \begin{bmatrix} \frac{\partial N_1}{\partial x_j} & \frac{\partial N_2}{\partial x_j} & \frac{\partial N_3}{\partial x_j} & \frac{\partial N_4}{\partial x_j} \end{bmatrix} \begin{Bmatrix} \dot{q}_1 \\ \dot{q}_2 \\ \dot{q}_3 \\ \dot{q}_4 \end{Bmatrix} \tag{4-88}$$

where

N_1, N_2, N_3, N_4 = the element shape function associated with each node point;

$\dot{q}_1, \dot{q}_2, \dot{q}_3, \dot{q}_4$ = nodal point velocities. ($\dot{q}_1 = \dot{x}_1, \dot{y}_1, \dot{z}_1$)

Substitution of the strain rate components into the velocity-strain rate relationships (equation 4-76) yields,

$$\begin{Bmatrix} \varepsilon_{xx} \\ \varepsilon_{xy} \\ \varepsilon_{xz} \\ \varepsilon_{yy} \\ \varepsilon_{yx} \\ \varepsilon_{yz} \\ \varepsilon_{zz} \\ \varepsilon_{zx} \\ \varepsilon_{zy} \end{Bmatrix} = [\partial N_1 \quad \partial N_2 \quad \partial N_3 \quad \partial N_4] \begin{Bmatrix} \dot{q}_1 \\ \dot{q}_2 \\ \dot{q}_3 \\ \dot{q}_4 \end{Bmatrix} = [\partial \bar{N}] \; \{\dot{q}\} \tag{4-89}$$

$$[\partial N_1]\ \{\dot{q}_1\} = \begin{bmatrix} \frac{\partial N_1}{\partial x} & 0 & 0 \\ \frac{1}{2}\frac{\partial N_1}{\partial y} & \frac{1}{2}\frac{\partial N_1}{\partial x} & 0 \\ \frac{1}{2}\frac{\partial N_1}{\partial z} & 0 & \frac{1}{2}\frac{\partial N_1}{\partial x} \\ 0 & \frac{\partial N_1}{\partial y} & 0 \\ \frac{1}{2}\frac{\partial N_1}{\partial y} & \frac{1}{2}\frac{\partial N_1}{\partial x} & 0 \\ 0 & \frac{1}{2}\frac{\partial N_1}{\partial z} & \frac{1}{2}\frac{\partial N_1}{\partial y} \\ 0 & 0 & \frac{\partial N_1}{\partial z} \\ \frac{1}{2}\frac{\partial N_1}{\partial z} & 0 & \frac{1}{2}\frac{\partial N_1}{\partial x} \\ 0 & \frac{1}{2}\frac{\partial N_1}{\partial z} & \frac{1}{2}\frac{\partial N_1}{\partial y} \end{bmatrix} \begin{Bmatrix} \dot{x}_1 \\ \dot{y}_1 \\ \dot{z}_1 \end{Bmatrix} \qquad (4\text{-}90)$$

The variation of the strain rates can be replaced by the variation of the nodal point velocities. Therefore, substituting equation (4-89) into equation (4-86) yields,

$$\delta J = 2\mu \int_{Ve} \{\delta\dot{q}\}^T\ [\partial\bar{N}]^T\ [\partial\bar{N}]\ \{\dot{q}\}\ dVe \qquad (4\text{-}91)$$

The nodal point viscous forces, F_v, for a tetrahedron can be shown from the above expression to be,

$$\begin{Bmatrix} Fv_1 \\ Fv_2 \\ Fv_3 \\ Fv_4 \end{Bmatrix} = [D_e] \begin{Bmatrix} \dot{q}_1 \\ \dot{q}_2 \\ \dot{q}_3 \\ \dot{q}_4 \end{Bmatrix} \qquad (4\text{-}92)$$

where

$$[D_e] = 2\mu \int_{Ve} [\partial\bar{N}]^T\ [\partial\bar{N}]\ dVe$$

4.6.1 Tetrahedron Shape Function Definition

The specific form of the partial derivatives and the averaging of the dissipative forces within the parallelepiped element must be determined. The shape function used in the partial derivatives must be at

least first order approximation functions. A linear approximation to the displacement field is,

$$h_j = \alpha_1 + x\alpha_2 + y\alpha_3 + z\alpha_4 = [C]\begin{Bmatrix}\alpha_1\\ \alpha_2\\ \alpha_3\\ \alpha_4\end{Bmatrix} \tag{4-93}$$

where

h_j = displacements within the tetrahedron

α_i = coefficients of the interpolation polynomial

A local coordinate system originating at the centroid of the tetrahedron can be developed. The nodal point displacements can then be written using the linear approximation function and the local nodal point coordinates.

$$\begin{Bmatrix}h_1\\ h_2\\ h_3\\ h_4\end{Bmatrix} = \begin{bmatrix}1 & \bar{x}_1 & \bar{y}_1 & \bar{z}_1\\ 1 & \bar{x}_2 & \bar{y}_2 & \bar{z}_2\\ 1 & \bar{x}_3 & \bar{y}_3 & \bar{z}_3\\ 1 & \bar{x}_4 & \bar{y}_4 & \bar{z}_4\end{bmatrix}\begin{Bmatrix}\alpha_1\\ \alpha_2\\ \alpha_3\\ \alpha_4\end{Bmatrix} = [A]\begin{Bmatrix}\alpha_1\\ \alpha_2\\ \alpha_3\\ \alpha_4\end{Bmatrix} \tag{4-94}$$

where

h_i = displacements of the i th tetrahedron node point

($h_i = x_i, y_i, z_i$: $i = 1, 2, 3, 4$);

$\bar{x}_i, \bar{y}_i, \bar{z}_i$ = local coordinates of the i th node point of the tetrahedron.

Solving equation (4-94) for $\{\alpha\}$, and substituting into equation (4-93) the element shape functions are obtained,

$$h_j = [C]\,[A]^{-1}\begin{Bmatrix}h_1\\ h_2\\ h_3\\ h_4\end{Bmatrix} = [N_1 \quad N_2 \quad N_3 \quad N_4]\begin{Bmatrix}hj_1\\ hj_2\\ hj_3\\ hj_4\end{Bmatrix} \tag{4-95}$$

where

hj_i = deflection in the j th direction at node 1, etc;

*

$N_1 = a_1 + b_1x + c_1y + d_1z$

$N_2 = a_2 + b_2x + c_2y + d_2z$

$N_3 = a_3 + b_3x + c_3y + d_3z$

$N_4 = a_4 + b_4x + c_4y + d_4z$

*These shape functions are equivalent to volume coordinates for a tetrahedron. Further discussion of volume coordinates can be found in Reference [13].

The partial derivatives of the shape functions, used in equation (4-92), can be written as,

$$\left.\begin{aligned} \frac{\partial N_i}{\partial x} &= b_i \\ \frac{\partial N_i}{\partial y} &= c_i \\ \frac{\partial N_i}{\partial z} &= d_i \end{aligned}\right\} \quad i = 1, 2, 3, 4 \qquad \begin{aligned} &(4\text{-}96a) \\ &(4\text{-}96b) \\ &(4\text{-}96c) \end{aligned}$$

These partial derivatives are constants that can be placed outside the integral of equation (4-92). The volume of the tetrahedron is obtained through equation (4-64). The nodal point forces for a parallelepiped were determined by averaging the tetrahedron nodal point forces for the ten tetrahedra of each parallelepiped (Figure 4-5). These forces form the generalized forces Q_f applied to the liquid (equation 4-38).

4.6.2 Viscous Formulation Checkout

The viscous force formulation was checked by calculating the forces that result from shearing a unit cube of liquid. Referring to Figure 4-8a, the shear stress and resulting shear forces can be expressed as,

$$\tau = F/A = \mu \frac{du}{dy} \qquad (4\text{-}97a)$$

or

$$F = A\mu \frac{du}{dy} \qquad (4\text{-}97b)$$

The magnitude of the force on the cube for a unit velocity and unit surface area equals the viscosity, μ. The forces on the cube produced by the viscous force subroutine are shown in Figure 4-8b. The sum of the nodal forces in the X direction equals μ, verifying the formulation section 4.6.1.

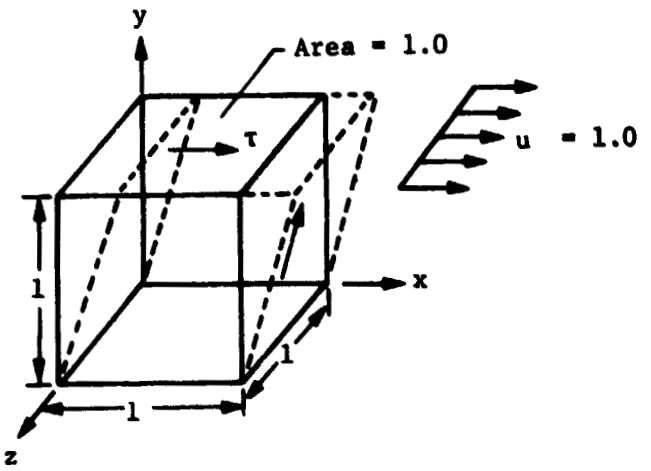

Figure 4-8a. Shear Stress on Unit Cube

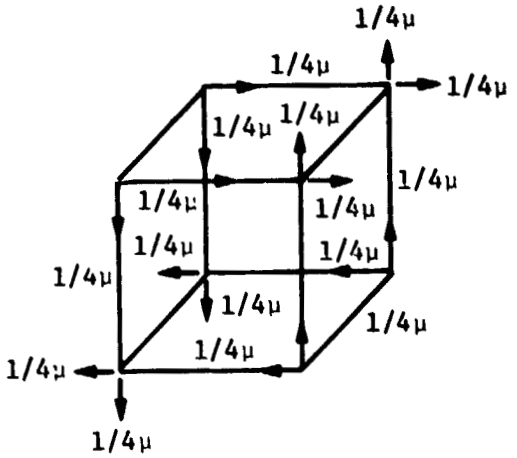

Figure 4-8b. Force Results from Subroutine VISCOUS

Figure 4-8. Viscous Force Formulation Validation

4.7 COMPUTER PROGRAM IMPLEMENTATION

Numerical techniques similar to those used in the two-dimensional model were required to transform the equation of motion into a workable computer program. The methods used in initial liquid positioning and numerical integration step size estimation, parallel those used in the two-dimensional model. The mesh generation used a three-dimensional mapping function, which is discussed in the subsequent paragraphs. In addition, specialized program logic, used to reduce computational costs, will be discussed.

4.7.1 Parallelepiped Finite Element Mesh Generator (CUBIT Program)

The liquid volume is divided into parallelepiped finite elements for the LAMPS3 model. The liquid volume is bounded by the tank wall and free surface. The tank boundary was analytically defined as a distorted ellipsoid function, ϕ. The FLUDCG subroutine [Ref 1] was again used to obtain an approximation of the free surface geometry. The CUBIT program considers only axisymmetric orientations of the liquid. Asymmetric mesh arrangements were obtained by the techniques discussed in Section 3.4.2.

Curvilinear coordinates were used to map cubic meshes from the ξ-η-ν space into a volume in rectangular coordinate space. This volume has eight faces, each having parabolic curvature. This mapping concept is shown schematically in Figure 4-9.

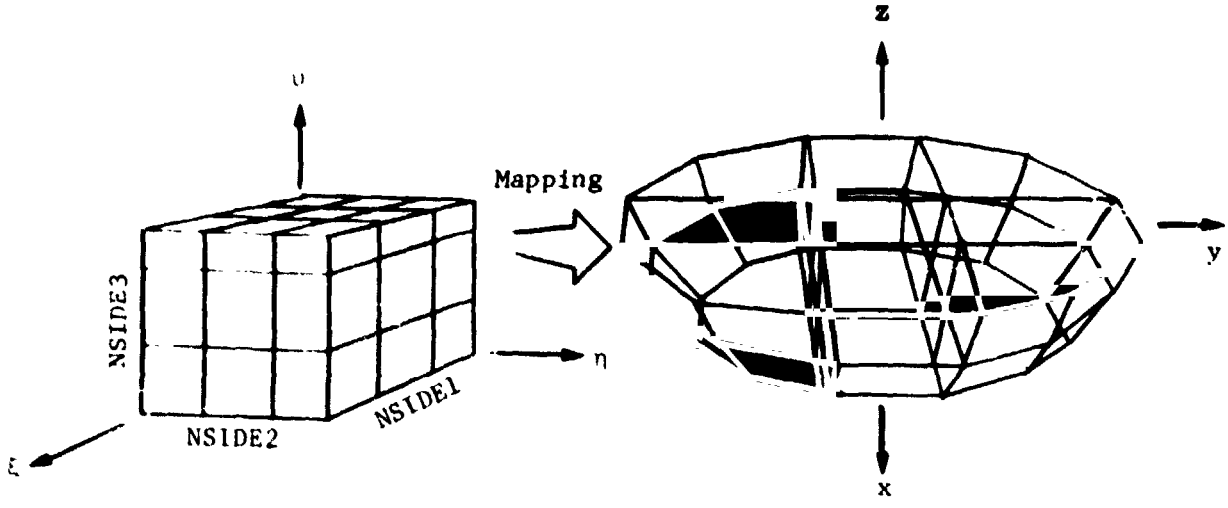

Figure 4-9. Three-Dimensional Curvilinear Mapping

Mapping is achieved through a set of "serendipity" shape functions [Ref 13] derived from a 26-noded cube. The cube has nine node points

defining each face. This allows each face to be described as a quadric surface. In terms of these shape functions, the mapping relationships can be written as,

$$X(\xi, \eta, \nu) = \sum_{i=1}^{26} N_i \, Xc_i \qquad (4\text{-}98a)$$

$$Y(\xi, \eta, \nu) = \sum_{i=1}^{26} N_i \, Yc_i \qquad (4\text{-}98b)$$

$$Z(\xi, \eta, \nu) = \sum_{i=1}^{26} N_i \, Zc_i \qquad (4\text{-}98c)$$

where

$$N_1 = (1-\nu)(1-\xi)(1-\eta) - 1/2[N_2+N_8+N_9] - 1/4[N_{21}+N_{22}+N_{25}]$$

$$N_2 = 4\,(1-\nu)(1-\xi)(1-\eta) - 1/2[N_{21}+N_{22}]$$

$$N_3 = (1-\nu)(1-\eta)(\xi) - 1/2[N_2+N_4+N_{10}] - 1/4[N_{21}+N_{22}+N_{23}]$$

$$N_4 = 4\,(1-\nu)(1-\eta)(\xi)(\eta) - 1/2[N_{21}+N_{23}]$$

$$N_5 = (1-\nu)(\xi)(\eta) - 1/2[N_4+N_6+N_{11}] - 1/4[N_{21}+N_{23}+N_{24}]$$

$$N_6 = 4\,(1-\nu)(1-\xi)(\xi)(\eta) - 1/2[N_{21}+N_{24}]$$

$$N_7 = (1-\nu)(1-\xi)(\eta) - 1/2[N_6+N_8+N_{12}] - 1/4[N_{21}+N_{24}+N_{25}]$$

$$N_8 = 4\,(1-\nu)(1-\xi)(1-\eta)(\eta) - 1/2[N_{21}+N_{25}]$$

$$N_9 = 4\,(1-\xi)(1-\eta)(1-\nu)(\nu) - 1/2[N_{22}+N_{25}]$$

$$N_{10} = 4\,(1-\nu)(1-\eta)(\nu)(\xi) - 1/2[N_{22}+N_{23}]$$

$$N_{11} = 4\,(1-\nu)(\eta)(\xi)(\eta) - 1/2[N_{23}+N_{24}]$$

$$N_{12} = 4\,(1-\nu)(1-\xi)(\nu)(\eta) - 1/2[N_{24}+N_{25}]$$

$$N_{13} = (\nu)(1-\xi)(1-\eta) - 1/2[N_9+N_{14}+N_{20}] - 1/4[N_{22}+N_{25}+N_{26}]$$

$$N_{14} = 4\ (1-\xi)(1-\eta)(\nu)(\xi) - 1/2[N_{22}+N_{26}]$$

$$N_{15} = (\nu)(\xi)(1-\eta) - 1/2[N_{10}+N_{14}+N_{16}] - 1/4[N_{22}+N_{23}+N_{26}]$$

$$N_{16} = 4\ (1-\eta)(\nu)(\xi)(\eta) - 1/2[N_{23}+N_{26}]$$

$$N_{17} = (\nu)(\xi)(\eta) - 1/2[N_{11}+N_{16}+N_{18}] - 1/4[N_{23}+N_{24}+N_{26}]$$

$$N_{18} = 4\ (1-\xi)(\nu)(\eta)(\xi) - 1/2[N_{24}+N_{26}]$$

$$N_{19} = (\nu)(1-\xi)(\eta) - 1/2[N_{12}+N_{18}+N_{20}] - 1/4[N_{24}+N_{25}+N_{26}]$$

$$N_{20} = 4\ (1-\eta)(1-\xi)(\nu)(\eta) - 1/2[N_{25}+N_{26}]$$

$$N_{21} = 16\ (1-\nu)(1-\eta)(1-\xi)(\eta)(\xi)$$

$$N_{22} = 16\ (1-\nu)(1-\xi)(1-\eta)(\xi)(\nu)$$

$$N_{23} = 16\ (1-\eta)(1-\nu)(\xi)(\eta)(\nu)$$

$$N_{24} = 16\ (1-\xi)(1-\nu)(\nu)(\eta)(\xi)$$

$$N_{25} = 16\ (1-\eta)(1-\xi)(1-\nu)(\eta)(\nu)$$

$$N_{26} = 16\ (1-\eta)(1-\xi)(\eta)(\nu)(\xi)$$

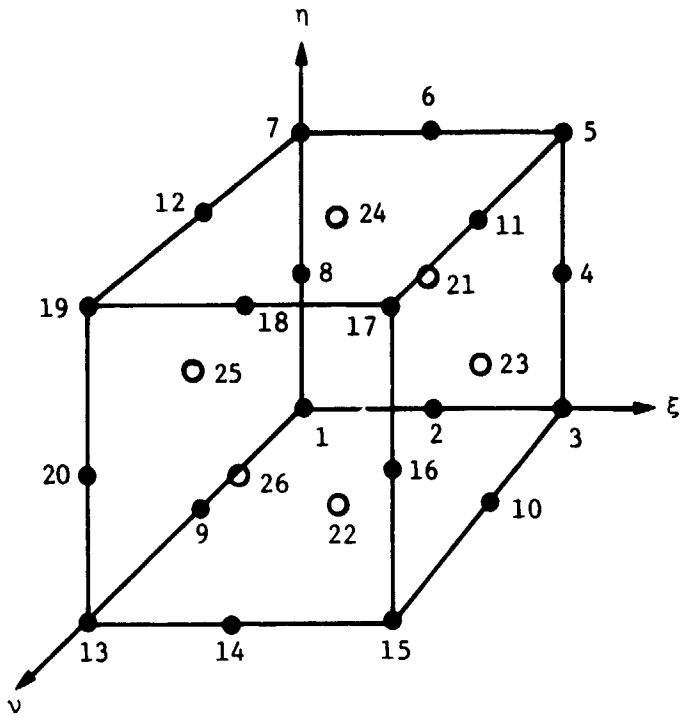

O = face center node point

Mesh definition is obtained by defining the number of divisions along sides 1, 2 and 3. The ξ-η-ν space is then divided into the specific number of divisions, and the ξ-η-ν coordinates are obtained. These coordinates are then transformed, by the shape functions, into x-y-z rectangular coordinate space. After mapping, if the mesh boundary points do not match the tank surface as defined by the distorted ellipsoid constraint surface (due to parabolic mapping), the boundary points are adjusted so that they lay on the constraint surface.

4.7.2 "B-MATRIX" Programing Logic

Several specialized subroutines were developed to minimize the computational costs of the LAMPS3 program code. These routines reduced the number of operations on zero-value elements in the constraint matrices, [b] and [b]. Subroutine logic was based upon storage and manipulation of only the terms within the bandwidth of a given row of the [b] matrix. These routines are:

Operation	Description	Subroutine
[A] = [B] {V}	Multiplication of Matrix and Vector	BXV

$[A] = [B]^T\{V\}$	Multiplication of Matrix Transpose and Vector	BTXV
$[A] = [C]^{-1}\{V\}$	Decomposition by Gauss Elimination and Forward-Backward Substitution	SKY

4.8 TEST CORRELATION TO LAMPS3 MODEL

A limited correlation analysis was performed with the three-dimensional model. The model was correlated to the KC-135 aircraft test data. The three axes of test measured accelerations were applied to the model, providing three-dimensional force and moment time histories. The force and total impulse correlation results for KC-135 Test 1.2.2 are shown in Figure 4-10. The analytical Z-axis force and total impulse resemble the test data. A similar result is obtained for the Y-axis force and total impulse. The analytical X-axis force time histories also looked reasonable, based on X acceleration time histories. However, since X-axis forces were not measured, no correlation is presented for this axis. The analysis employed a 2x2x2 mesh (8 elements, 24 node points).

The results of Figure 4-10 can be compared to those of Figure 3-26, the two-dimensional analytical correlations to the KC-135 test 1.2.2 data. The two-dimensional model employed a finer mesh, containing 32 elements. Even though the correlation in Figure 4-10 (with the coarse 8 element mesh) is good, the correlation can be improved by using a finer mesh.

The three-dimensional model produces results similar to the LAMPS2 model at reduced computational costs (due to special programming techniques, Section 4.7). Additional correlation analyses using various integration steps and mesh sizes could be used to further optimize the model. However, based on the correlation performed, the LAMPS3 model is a notable improvement over the two-dimensional LAMPS2 formulation.

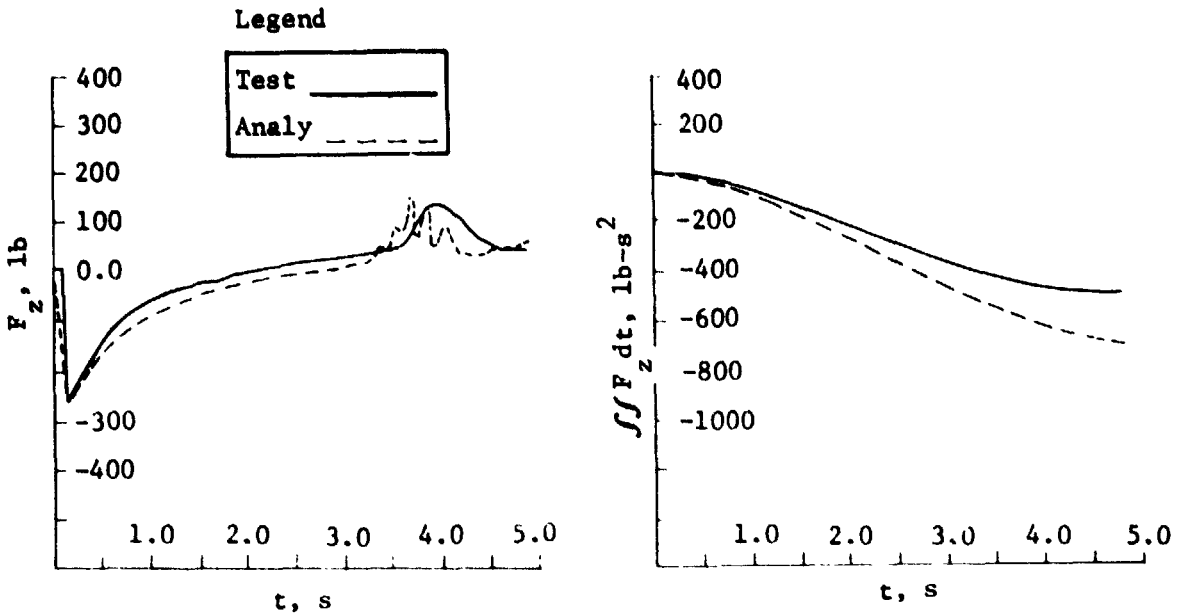

Tank Z-Axis Force

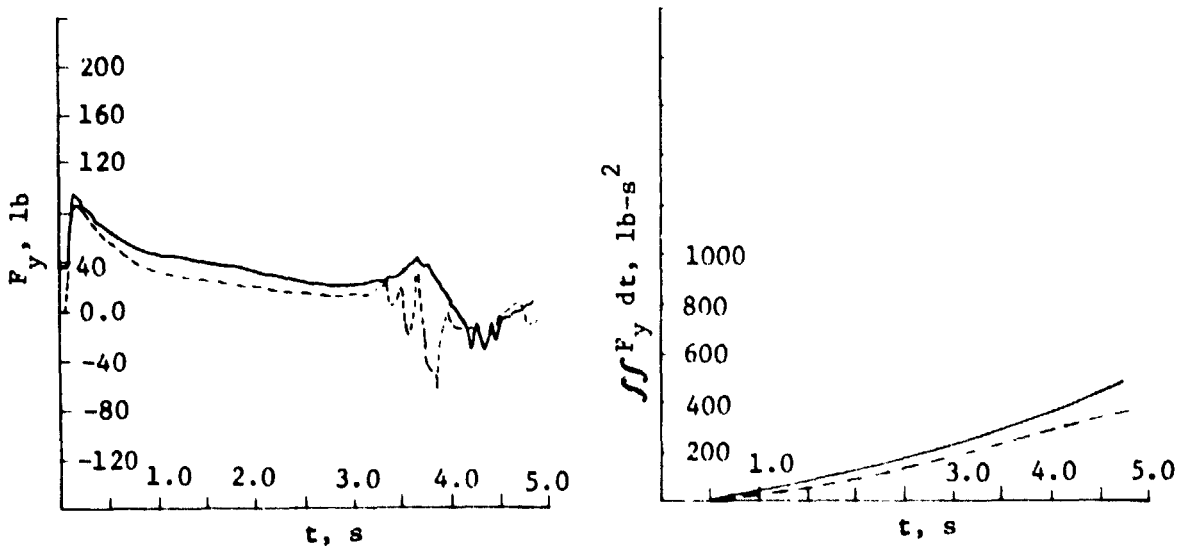

Tank Y-Axis Force

Figure 4-10. LAMPS3 Test/Analytical Comparison KC-135 Aircraft Test 1.2.2

5.0 CONCLUSIONS AND RECOMMENDATIONS

The test data obtained in the Phase I and Phase II test programs have greatly contributed to the understanding of low-g propellant reorientation during orbiter/ET RTLS separation. Evaluation and comparison of the drop tower and KC-135 data has resulted in the following conclusions regarding scaling and the influence of various parameters on reorientation.

1) The external tanks' slosh and antivortex baffles have a significant effect on reorientation character and forces. The baffles create flow turbulence, which dissipates energy and reduces reorientation forces.

2) Variation in tank fill volume, in general, has little effect on reorientation character (in the range of 1% to 25% volume). However, with baffles installed, the antivortex baffle causes small fill volumes (1% to 2%) to travel inside to the tank, instead of along the tank wall.

3) In the range of Bond and Reynolds numbers expected during RTLS, and simulated during testing, liquid viscosity does not have a significant influence on the character of bulk liquid reorientation.

4) The liquid motion observed during drop tower and KC-135 testing is representative of that expected during RTLS separation. Froude number scaling, when $BO \geq 10$ and $Re \geq 50$, is valid.

The multiple mass, finite element models (LAMPS2, LAMPS3) developed during Phase III of the study, are a significant improvement over the single-point mass model currently used in the SVDS program. Correlation between the LAMPS2/LAMPS3 models and test data has resulted in the following observations and conclusions.

1) The lumped mass formulation is recommended. Simulation results using a lumped mass matrix, correlate better to test data, and computational costs are significantly reduced over runs using a consistent mass matrix.

2) Correlation of the models to both drop tower and KC-135 data provides additional validation of the model scaling concept, i.e., the analytical models are based on the premise that Froude number scaling is valid.

3) Force correlation is improved by reducing the integration interval (dt) and by using a "fine," finite element mesh. However, an ultrafine mesh is not required to achieve satisfactory impulse and total impulse correlation. A 4x4 mesh has been found adequate, for the LAMPS2 model, for both drop tower and KC-135 simulations. This same mesh should be adequate for full-scale ET simulation.

4) Higher fill volumes require a finer mesh to achieve good correlation to test data. Volumes ≥15% will require a mesh finer than the 4x4 mesh recommended above.

5) The three-dimensional LAMPS3 model more accurately represents the actual liquid mass distribution in the tank.

6) Analytical simulations of the baffled tank do not correlate exceedingly well to baffled test data. The best correlation has been achieved using only a single baffle in the analytical model. When simulating the entire baffled region, the liquid gets "trapped" and numerical difficulties occur. Neglecting the baffles, for actual RTLS simulations, will result in conservative reorientation forces and is recommended at this time.

Overall, the objectives of this study have been accomplished. However, additional work is needed to refine the analytical tools that have been developed. In addition, application of the models to other intact aborts should be considered. The following are recommendations for additional study.

1) Testing (drop tower, KC-135) should be conducted for higher fill volumes to obtain data for anticipated intact aborts.

2) Applicability of the LAMPS2/LAMPS3 models in simulating higher fill volume aborts should be studied. Correlation to test data should be used in this assessment.

3) Additional work needs to be done in the area of baffled tank simulation.

4) Initialization of the liquid position should be modified. The technique discussed in Chapters 3.0 and 4.0 has some numerical difficulties. Mapping directly to the asymmetric initial liquid orientation should be investigated.

5) Surface tension force effects should be incorporated into the models in order to allow simulation of the low Bond number regime.

6.0 REFERENCES

1. Berry, Robert L., and Tegart, James R.: Experimental Study of Transient Liquid Motion in Orbiting Spacecraft, Interim Report. NASA CR-144003, February 1975.

2. Berry, Robert L., and Tegart, James R.: Experimental Study of Transient Liquid Motion in Orbiting Spacecraft, Final Report. NASA CR-144213, February 1976.

3. Berry, Robert L., and Tegart, James R.: Analysis and Test for Space Shuttle Propellant Dynamics (1/60th-Scale Model Test Results). MCR-78-523. (Contract NAS9-15302), March 1978.

4. Berry, Robert L.; Tegart, James R.; and Demchak, Leonard J.: Analysis and Test for Space Shuttle Propellant Dynamics (1/10th-Scale Model Test Results). 2 vols. MCR-79-560. (Contract NAS9-15302), May 1979.

5. Tegart, James R.: Zero-G Aircraft Test Plan. ZGTP-001 (Contract NAS9-15302), June 1978.

6. Williams, Robert K.: Test Procedure for External Tank Fluid Motion Test. NASA TTA-T-2P635, 17 July 1978.

7. McCarthy, J. F., Jr.: Zero-G Propulsion Problems. Jet, Rocket, Nuclear, Ion, and Electric Propulsion: Theory and Design. Edited by W.H.T. Loh. Springer-Verlag, New York, 1968.

8. West, R. C., ed.: Handbook of Chemistry and Physics. 53rd ed. The Chemical Rubber Company, Cleveland, Ohio, 1972.

9. Jasper, J. J.: The Surface Tension of Pure Liquid Compounds. Journal of Physical and Chemical Reference Data, Vol I, No. 4, 1972.

10. E. I. du Pont de Nemours & Co.: FC-114B2, Dibromotetra-fluoroethane. Freon Technical Bulletin, B-4B. Wilmington, Delaware.

11. Coney, T. A.: Surface Tension Viscosity and Density Measurements of Two Fluorocarbon Solvents. NASA TMX-1862, NASA Lewis Research Center, Cleveland, Ohio, August 1969.

12. Stephens, D. G.: Experimental Investigations of Liquid Impact in a Model Propellant Tank. NASA-TND-2913, NASA Langley Research Center, Hampton, Virginia, October 1965.

13. Zienkiewicz, O. C.: The Finite Element Method. McGraw-Hill Book Company, Maiden Head, Berkshire, England. 3rd ed. Copyright 1977.

14. Bowman, T. E.: Response of the Free Surface of a Cylindrically Contained Liquid to Off-Axis Accelerations. Proceedings of the 1966 Heat Transfer and Fluid Mechanics Institute, Stanford University Press, 1966.

15. Lamb, Horace, Sir: Hydrodynamics. 6th ed. Dover Publications. New York, 1932.

APPENDIX A--VIRTUAL POWER CONCEPT

The virtual power concept is a convenient way to apply the principle of virtual work to mechanics problems. This appendix discusses the concepts of the virtual power method. This documentation is an excerpt from the "Skylab Docking Maneuver Simulation Mathematical Model Report (Final)," ED-2002 1395, 1971, authored by Carl Bodley and Colton Park.

The concept of a virtual displacement and the principle of virtual work provide very effective tools in the analysis of a mechanical system. The utility of the principle of virtual work is mainly due to being able to eliminate the action of the inner forces necessary to maintain prescribed kinematical conditions. For example, a deformable structure may be analyzed for stress and strain by prescribing certain possible modes of deformation. These modes are a finite number of kinematical conditions with which the virtual displacements of the system must comply. Because the virtual displacements are in harmony with the given kinematical conditions, the action of the inner forces may be eliminated. The number of equations, equal to the number of modes of deformation (or degrees of freedom assumed), is smaller than the number of particles contained in the system.

The principle of virtual work is a variational principle that allows a given mechanical system to be analyzed without considering the infinity of particles and the infinity of inner forces acting between them. The transformation that relates the rectangular coordinates of the system's particles (X_i, Y_i, Z_i) to the generalized coordinates $(q_1, q_2, \ldots, q_n)$ is used to transform the virtual work expression that is in terms of the δX_i, δY_i, δZ_i and the resultant particle forces;

That is

$$\delta W = \sum_{i=1}^{N} \bar{F}_i \cdot \delta \bar{r}_i \qquad \text{(A-1)}$$

is transformed to

$$\delta W = \sum_{j=1}^{n} Q_j \, \delta q_j. \qquad \text{(A-2)}$$

The analytical form of the generalized forces, Q_j, is obtained through this transformation. The transformation that relates the particles' rectangular coordinates to the generalized coordinates is in essence, the prescribed kinematical conditions of constraint:

$$\bar{r}_i = \bar{r}_i \left(q_1, q_2, \ldots, q_n; t\right), \qquad i = 1, 2, \ldots N. \tag{A-3}$$

The virtual displacements $\delta \bar{r}_i$ may be expressed as

$$\delta \bar{r}_i = \sum_{k=1}^{n} \frac{\delta \bar{r}_i}{\delta q_k} \delta q_k, \tag{A-4}$$

thus, from (A-1)

$$\delta W = \sum_{i=1}^{N} \bar{F}_i \cdot \sum_{k=1}^{n} \frac{\partial \bar{r}_i}{\partial q_k} \delta q_k$$

$$= \sum_{k=1}^{n} \left(\sum_{i=1}^{N} \bar{F}_i \cdot \frac{\partial \bar{r}_i}{\partial q_k} \right) \delta q_k \tag{A-5}$$

and it follows that

$$Q_k = \sum_{i=1}^{N} \bar{F}_i \cdot \frac{\partial \bar{r}_i}{\partial q k}. \tag{A-6}$$

Equation (A-6) shows the transformation relating the particle forces to the generalized forces. By the principle of virtual work, only those F_i that are impressed forces contribute to δW, and therefore, to Q_k. If the system is a flexible solid, some of the F_i may be considered to be resultant stresses acting on virtual strains that are consistent with (equation A-4); the system has the capacity for storing

tential energy (U). Q_k may be considered to be composed of contributions from all the conservative impressed forces and from the position-dependent (or conservative) forces,

$$Q_k = \sum_{i=1}^{L} \bar{F}_i \cdot \frac{\partial \bar{r}_i}{\partial q_k} - \sum_{i=1}^{N} (\nabla U)_i \cdot \frac{\partial \bar{r}_i}{\partial q_k}, \tag{A-7}$$

where L is the total of the unconservative impressed forces. In defining the explicit form of the Q_k it is necessary to form the derivatives $(\partial \bar{r}_i)/(\partial \bar{q}_k)$. Given the explicit form of the kinematical conditions, such as (equation A-3), one needs only to differentiate to express the required derivatives. However, often in practice the form of the transformation (equation A-3) is only implied and the derivatives are difficult to obtain. It is generally possible to easily express the particle velocities and the time (t), simply by writing well known kinematical expressions that comply with (equation A-3);

$$\dot{\bar{r}}_i = \dot{\bar{r}}_i \left(q_1, q_2, \ldots, q_n; \dot{q}_1, \dot{q}_2, \ldots, \dot{q}_n; t \right) \tag{A-8}$$

also

$$\dot{\bar{r}}_i = \sum_{j=1}^{n} \frac{\partial \bar{r}_i}{\partial q_j} \dot{q}_j + \frac{\partial \bar{r}_i}{\partial t}. \tag{A-9}$$

The derivatives being sought appear in (equation A-9); the accomplishment has been to express r_i in a simple "kinematical fashion" and equate the result to that given by (equation A-9) obtaining explicit expressions for $(\delta \bar{r}_i)/(\delta \bar{q}_i)$ without needing to differentiate (equation A-3) or without even needing to know the explicit form of A-3. Since the second term on the right of (equation A-9) does not enter into the comparison, it only needs to be recognized.

Virtual velocity can now be defined. The virtual velocity concept is analogous to that of virtual displacements, in that the $\dot{q}_k$ can be imagined to assume arbitrary values independent of time. Particle velocities take on values consistent with the conditions

$$\dot{\bar{r}}_i^* = \sum_{k=1}^{n} \frac{\partial \bar{r}_i}{\partial q_k} \dot{q}_k^*. \tag{A-10}$$

The difference between (equation A-9 and equation A-10) is the term $(\partial \bar{r}_i)/(\partial t)$, which vanishes since "time is held constant" while impressing arbitrary values of $\dot{q}_k^*$, similar to expressing virtual displacements. Thus, the virtual velocity of the i^{th} particle is defined to be that which satisfies (equation A-10) for arbitrary values of the <u>independent</u> $\dot{q}_k^*$. The superscript $(^*)$ is used to distinguish between virtual velocities and real velocities.

$\bar{r}_i^*$ may be expressed from simple well known kinematical relationships and these results compared with (equation A-10) to obtain the explicit form of the derivatives $(\partial \bar{r}_i)/(\partial q_k)$, again without needing to know the explicit form of (equation A-3).

In conjunction with virtual velocity, virtual power, $\delta \dot{W}$, is conceived to be analogous to virtual work. It is an expression involving virtual velocities rather than virtual displacements:

$$\delta \dot{W} = \sum_{i=1}^{N} \bar{F}_i \cdot \dot{\bar{r}}_i^* .$$

$$= \sum_{k=1}^{n} \left(\sum_{i=1}^{N} \bar{F}_i \cdot \frac{\partial \bar{r}_i}{\partial q_k} \right) \dot{q}_k^* \qquad \text{(A-11)}$$

$$= \sum_{k=1}^{n} Q_k \, \dot{q}_k^* . \qquad \text{(A-12)}$$

The virtual power has served the exact same purpose that virtual work does, namely to provide the explicit form of the generalized forces.

APPENDIX B--USER GUIDE FOR LAMPS2 PROGRAM

This appendix provides user information for the two-dimensional model (LAMPS2) and its mesh generator (MESH2).

The MESH2 program is a stand-alone program, which generates the finite element mesh geometry based on user input data. The mesh data are written on a disk file, which LAMPS2 accesses directly. Figure B-1 shows the use and interaction of the two programs.

The tank constraint surface, ϕ, is developed (automatically) based on input tank geometry. Any axisymmetric tank geometry can be simulated by the LAMPS2 program, from a cylinder to a sphere. Figure B-2 shows example geometry information input to the programs (MESH2, LAMPS2).

Figure B-3 shows the overlay structure of the LAMPS2 program and the computer core requirements for a CDC CYBER computer. Table B-1 defines the input parameters for program MESH2. Table B-2 shows sample input data for MESH2. Table B-3 defines the input parameters for program LAMPS2. Table B-4 shows sample input data for LAMPS2.

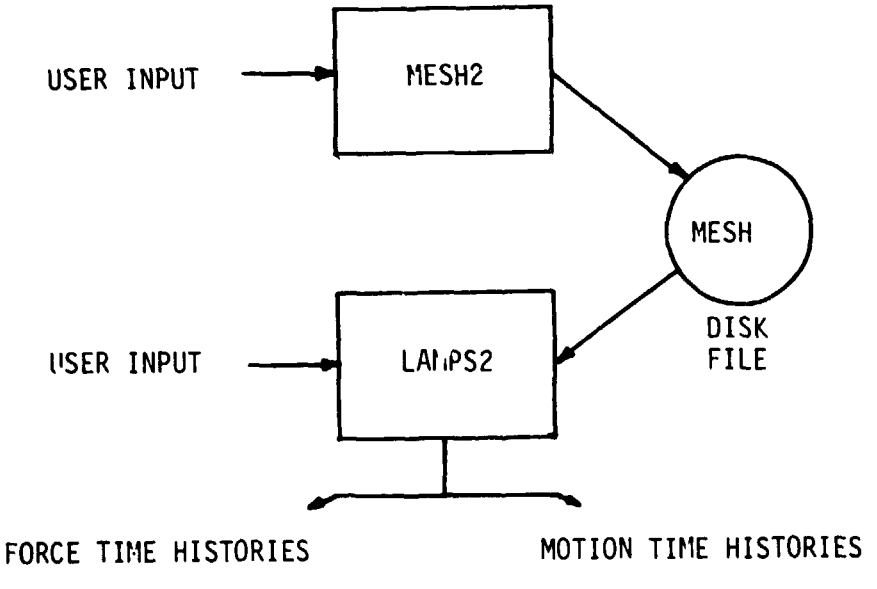

Figure B-1. Two-Dimensional Model Program Interaction

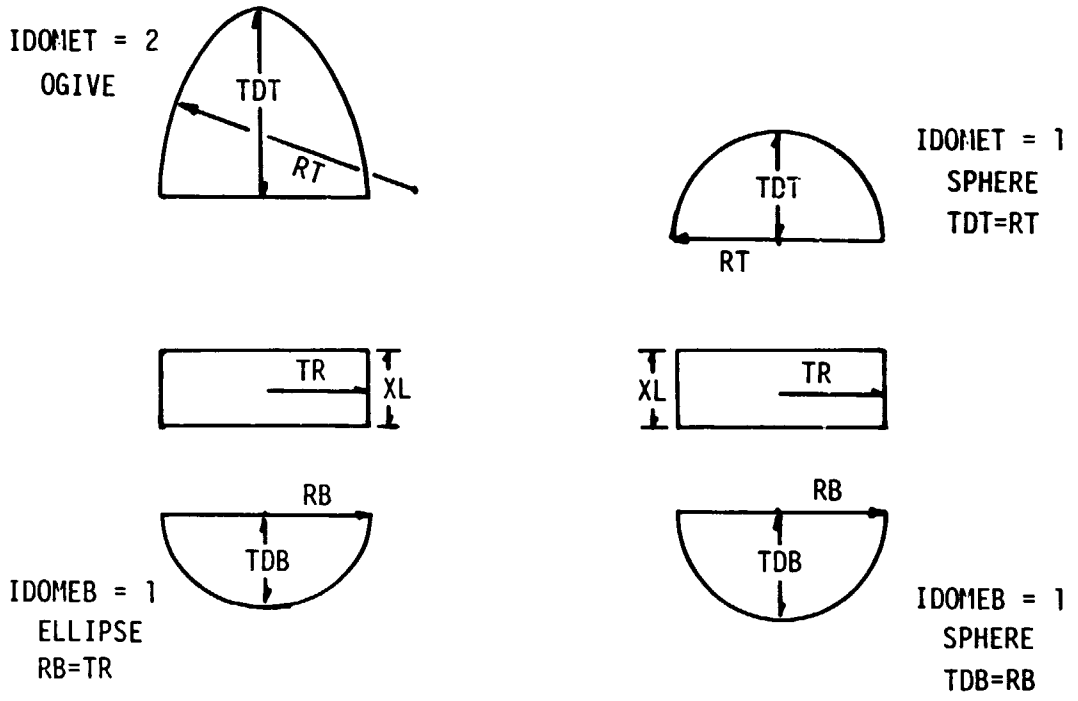

IDOMET	= 1, top dome is ellipsoidal or spherical 2, top dome is ogive
RT	= radius of ellipse or ogive
TDT	= height of upper dome
IDOMEB	= 1, bottom dome is ellipsoidal or spherical 2, botton dome is ogive
RB	= radius of ellipse or ogive
TDB	= height of lower dome
XL	= length of tank cylindrical section
TR	= tank radius

Figure B-2. Tank Constraint Surface Geometry Definition

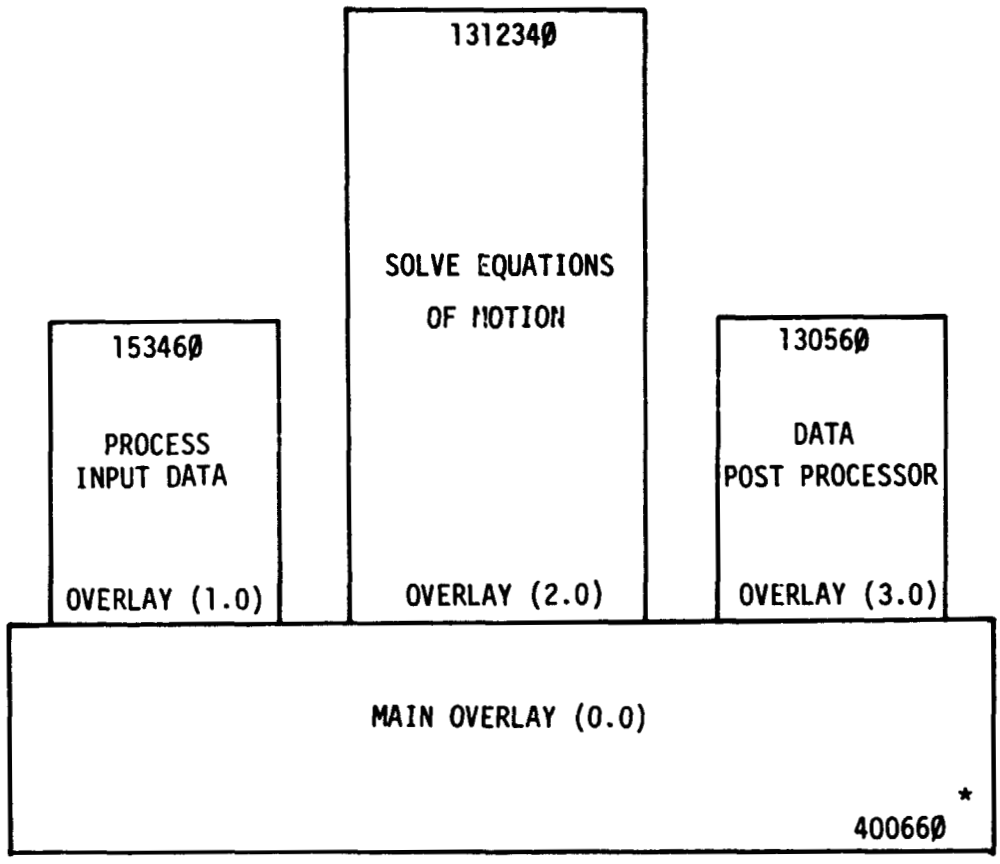

* OCTAL NUMBER

CORE REQUIREMENTS FOR CDC CYBER COMPUTER

Figure B-3. LAMPS2 Program Overlay Structure

```
**********************************************************************
   L A M P S 2   M E S H   G E N E R A T O R   P R O G R A M
        PROGRAM FORMS FINITE ELEMENT MESH FOR LAMPS2
        DEVELOPED BY  : R.L. BERRY AND L.J DEMCHAK
                        FOR NAS9-15302
                        LAST REVISION APRIL 1980
**********************************************************************

          TANK  VARIABLES EXPECTED.
    ------------------------------------------------
 FOR THE TOP DOME:
IDOMET = 1, TOP ELLIPSOIDAL OR SPHERICAL DOME
       = 2, TOP OGIVE DOME
RT     = RADIUS OF ELLIPSE OR OGIVE
TDT    = HEIGHT OF ELLIPSE OR OGIVE (TRUNCATED HGT OF OGIVE)
 FOR THE BOTTOM DOME:
IDOMEB = 1, BOTTOM ELLIPSOIDAL OR SPHERICAL DOME
       = 2, BOTTOM OGIVE DOME
RB     = RADIUS OF ELLIPSE OR OGIVE
TDB    = HEIGHT OF ELLIPSE OR OGIVE (TRUNCATED HGT OF OGIVE)
XL     = LENGTH OF PROPELLANT TANK CYLINDRICAL SECTION.
         (L UNITS)
TR     = TANK RADIUS. (L UNITS)

          FLUID POSITION AND GRID VARIABLES EXPECTED
    ------------------------------------------------------
THETAX = ORIENTATION OF TANK (DEG), IF .NE. 0 ITERATE TO
         POSITION DEFINED
NSIDE1 = NUMBER OF DIVISIONS OF SIDE 1 OF FLUID GRID,
         IF NSIDE1 .LE. 0 READ IN PREVIOUSLY FORMED GRID DATA
NSIDE2 = NUMBER OF DIVISIONS OF SIDE 2 OF FLUID GRID
 NMESH = 1, SIDE1,SIDE2,SIDE3 ON BOUNDARY, SIDE4 ON
         FREE SURFACE
 NMESH = 2, SIDE1,SIDE4 ON BOUNDARY, SIDE2,SIDE3 ON
         FREE SURFACE

           MESH GENERATION CAPABILITY
    ------------------------------------------------
      THE PROGRAM IS CURRENTLY SET UP FOR A MAXIMUM
      GENERATION OF 81 NODE POINTS.  THIS IS EQUATED
      AS FOLLOWS:  NUMNP = (NSIDE1 + 1) X (NSIDE2 + 1)
      **NOTE** THE LAMPS2 PROGRAM HAS ITS OWN CRITERIA
      FOR THE MAXIMUM NUMBER OF NODE POINTS.  THIS IS
      CURRENTLY SET AT NUMNP = 49 FOR COST SAVINGS.

          FLUID PARAMETERS EXPECTED
    ---------- ---------------------------------------
  FDEN = MASS DENSITY OF FLUID
 PCVOL = PERCENT TANK FILL.LE.100.
 AMTOT = ACTUAL LIQUID MASS

           PLOT TITLE INFORMATION EXPECTED
    ------------------------------------------------
  PTIT = ALPHA-NUMERIC PLOT TITLE (4A10)
```

Table B-1. Program MESH2 Input Parameter Definition

BAFFLE(S) PARAMETERS EXPECTED

NBAFF= 0,NO BAFFLES ADDITIONAL INPUT NOT REQUIRED
= 1,ONE BAFFLE SET BAFFZL=BAFFZU, INPUT BAFCON
= N,N NUMBER OF BAFFLES ,BAFCON OVERRIDDEN
BAFFZL= LOWER BAFFLE LOCATION
BAFFZU= UPPER BAFFLE LOCATION
BAFHGT= EFFECTIVE HEIGHT OF BAFFLE
BAFCON= EFFECTIVE WIDTH OF BAFFLE

Table B-1. (concl)

```
MESHGN      S.W.WIRTH
MESH GENERATION FOR CASE 19----5 % FILL;MESH TYPE 1, 5X7
ONE BAFFLE IS UTILIZED FOR THE FULL BAFFLE DISTANCE
MESH/MASS PRG 5X7 MESH VERSION
P$INPUT
 XL=1.31,
 TR=2.75,
 RT=10.16,
 TDT=6.46,
 IDOMET=2,
 RB=2.75,
 TDB=2.06,
 THETAX=0.0,
 PCVOL=5.,
 IDOMEB=1,
 FDEN=2.0213E-4,
 AMTOT=1.5666E-03,
 NSIDE1=5,
 NSIDE2=7,
 NMESH=1,
 NBAFF=1,
 BAFFZL=1.00,
 BAFFZU=1.00,
 BAFHGT=0.5,
 BAFCON=3.5,
 $
STOP
```

Table B-2. Sample Input Data for Program MESH2

```
**********************************************************************
          L A M P S 2  P R O G R A M
  LARGE AMLPITUDE 2 DIMENSIONAL SLOSH ANALYSIS PROGRAM
  DEVELOPED BY : R.L. BERRY AND L.J. DEMCHAK
  FOR NAS9-15302
  LAST REVISION MAY 1980
**********************************************************************

TAPE1 RESERVED FOR FORCE TIME HISTORY STORAGE
TAPE2 RESERVED FOR INPUT OF EXTERNALLY GENERATED MESH DATA OR
      RESTART
TAPE3 RESERVED FOR LIQUID MOTION TIME HISTORY STORAGE
TAPE4 RESERVED FOR RESTART DATA OUTPUT

        TANK  VARIABLES EXPECTED.
    ------------------------------------------------
 IDOMET = 1, TOP ELLIPSOIDAL OR SPHERICAL DOME
        = 2, TOP OGIVE DOME
 RT     = RADIUS OF ELLIPSE OR JGIVE
 TDT    = HEIGHT OF ELLIPSE OR OGIVE (TRUNCATED HGT OF OGIVE)
 IDOMEB = 1, BOTTOM ELLIPSOIDAL OR SPHERICAL DOME
 IDOMEB = 2, BOTTOM OGIVE DOME
 RB     = RADIUS OF ELLIPSE OR OGIVE
 TDB    = HEIGHT OF ELLIPSE OR OGIVE (TRUNCATED HGT OF OGIVE)
 XL     = LENGTH OF PROPELLANT TANK CYLINDRICAL SECTION.
          (L UNITS)
 TR     = TANK RADIUS. (L UNITS)

        FLUID POSITION AND GRID VARIABLES EXPECTED
    ------------------------------------------------------
 THETAX = ORIENTATION OF TANK (DEG), IF .NE. 0 ITERATE TO
          POSITION DEFINED
 NTHETA = NUMBER OF INCREMENTS OF THETA TO ACHIEVE
          CONVERGENCE
 CONVKE = CHANGE IN KINETIC ENERGY FOR POSITION CONVERGENCE
 CONVDT = INTERGRATION STEP SIZE FOR INITIAL POSITION
          CONVERGENCE
     G1 = ACCELERATION MAGNITUDE FOR INITIAL POSITION
          CONVERGENCE
 NITERP = NUMBER OF ITERATIONS TO ESTABLISH FLUID INITIAL
          POSITON, THETAX .NE. 0.  FOR ITH THETA INCREMENT

        FLUID PARAMETERS EXPECTED
    ------------------------------------------------
   FDEN = MASS DENSITY OF FLUID
   XMUC = FLUID VISCOSITY (CENTIPOISE) , IF .LE. 0 NO VISCOUS
          FORCES
  FGLUE = GLUE FACTOR FOR FLUID TO REMAIN ON WALL,
          RECOMMEND 1.0
```

Table B-3. Program LAMPS2 Input Parameter Definition

```
 PCVOL = PERCENT TANK FILL.LE.100.
 AMTOT = ACTUAL LIQUID MASS

       INTERGRATION AND PRINT/PLOT FLAGS EXPECTED
   ------------------------------------------------
    DT = MAXIMUM DELTA TIME INCREMENT
    TF = END TIME OF SIMULATION
 NPRNT = PRINT COUNTER, PRINT EVERY NPRNT TIME
 NPLOT = PLOT COUNTER, PLOT EVERY NPLOT TIME
IFSAVE = SAVE STATE ,ETC. TO JUMP START LATER (TAPE4)
IFJUMP = RESTART PROGRAM FORM PREVIOUS RUN
         (SEE SUBROUTINE JUMPRD FOR INPUT REQUIREMENTS)

          PLOT TITLE INFORMATION EXPECTED
   ------------------------------------------------
  PTIT = ALPHA-NUMERIC PLOT TITLE (4A10)

          BAFFLE(S) PARAMETERS EXPECTED
   ------------------------------------------------
  NBAFF= 0,NO BAFFLES ADDITIONAL INPUT NOT REQUIRED
       = 1,ONE BAFFLE, SET BAFFZL=BAFFZU, INPUT BAFCON
       = N,N NUMBER OF BAFFLES, BAFCON OVERRIDDEN
 BAFFZL= LOWER BAFFLE LOCATION
 BAFFZU= UPPER BAFFLE LOCATION
 BAFHGT= EFFECTIVE HEIGHT OF BAFFLE
 BAFCON= EFFECTIVE WIDTH OF BAFFLE

          ACCELERATION DATA EXPECTED
   - - - - - - - - - - - - - - - - - - - - - - - - - -

 ACCEL   = TABLE OF TANK ACCELERATIONS:
           COL 1- TIME, COL 2- AY, COL 3- AZ

          MESH DATA EXPECTED
   - - - - - - - - - - - - - - - - - - - - - - - - - -

 TABLES DEFINING FINITE ELEMENT MESH FROM PROGRAM MESH2 ON FILE 2
```

Table B-3. (cont)

```
LAMPS2    S.W.WIRTH
TEST 19 CASE 1 LAMPS RUN
5 % FILL WITH ONE BAFFLE
TEST 19 CASE1--5% FILL LAMPS RUN.
P$INPUT
 XL=1.31,
 TR=2.75,
 RT=10.16,
 TDT=6.46,
 IDOMET=2,
 RB=2.75,
 TDB=2.06,
 THETAX=13.0,
 PCVOL=5.,
 IDOMEB=1,
 FDEN=2.0213E-04,
 XMUC=1.0,
 SMASS=4.751E-03,
 AMTOT=1.5666E-03,
 ZCGS=-35.9045,
 YCGS=12.7403,
 DT=0.02,
 TF=1.00,
 FGLUE=1.0,
 NPRNT=4,
 NPLOT=4,
 NITERP=40,
 NBAFF=1,
 BAFFZL=1.0,
 BAFFZU=1.0,
 BAFHGT=0.5,
 BAFCON=3.5,
 G1=190.0,
 CONVKE=5.0E-04,
 CONVDT=0.025,
 $
ACCEL     3     3
     1    1       0.0          12.7403          386.07
     2    1       0.07         12.7403          -35.1320
     3    1       1.6          12.7403          -35.1320
0000000000
YZCORD    0     2MESHGN
NTYPE     0     2MESHGN
NP        0     2MESHGN
NLINE     0     2MESHGN
AMASS     0     2MESHGN
AREA      0     2MESHGN
HGT       0     2MESHGN
STOP
```

TIME AY AZ

DATA FROM PROGRAM MESH2

Table B-4. Sample Input Data for Program LAMPS2

APPENDIX C--USER GUIDE FOR LAMPS3 PROGRAM

This appendix provides user information for the three-dimensional model (LAMPS3) and its mesh generator (CUBIT).

The CUBIT program is a stand-alone program, which generates the finite element mesh geometry based on user input data. The mesh data are written on a disk file, which LAMPS3 accesses directly. Figure C-1 shows the use and interaction of the two programs.

The tank constraint surface, ϕ, is developed (automatically) based on input tank geometry. Any axisymmetric tank geometry can be simulated by the LAMPS3 program, from a cylinder to a sphere. The tank geometry information required is identical to that for the two-dimensional model (see Figure B-2).

Figure C-2 shows the overlay structure of the LAMPS3 program and the computer core requirements for a CDC CYBER computer. Table C-1 defines the input parameters for program CUBIT. Table C-2 shows sample input data for CUBIT. Table C-3 defines the input parameters for program LAMPS3. Table C-4 shows sample input data for LAMPS3.

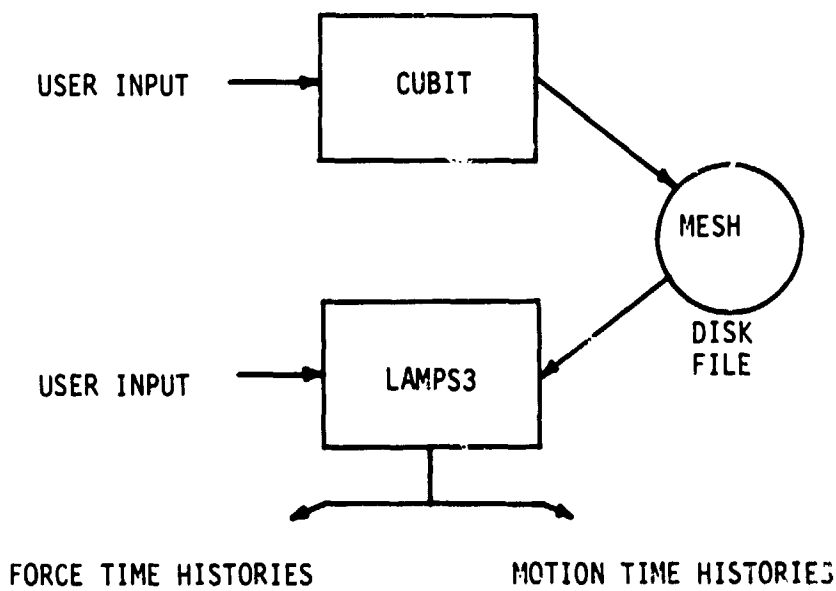

Figure C-1. Three-Dimensional Model Program Interaction

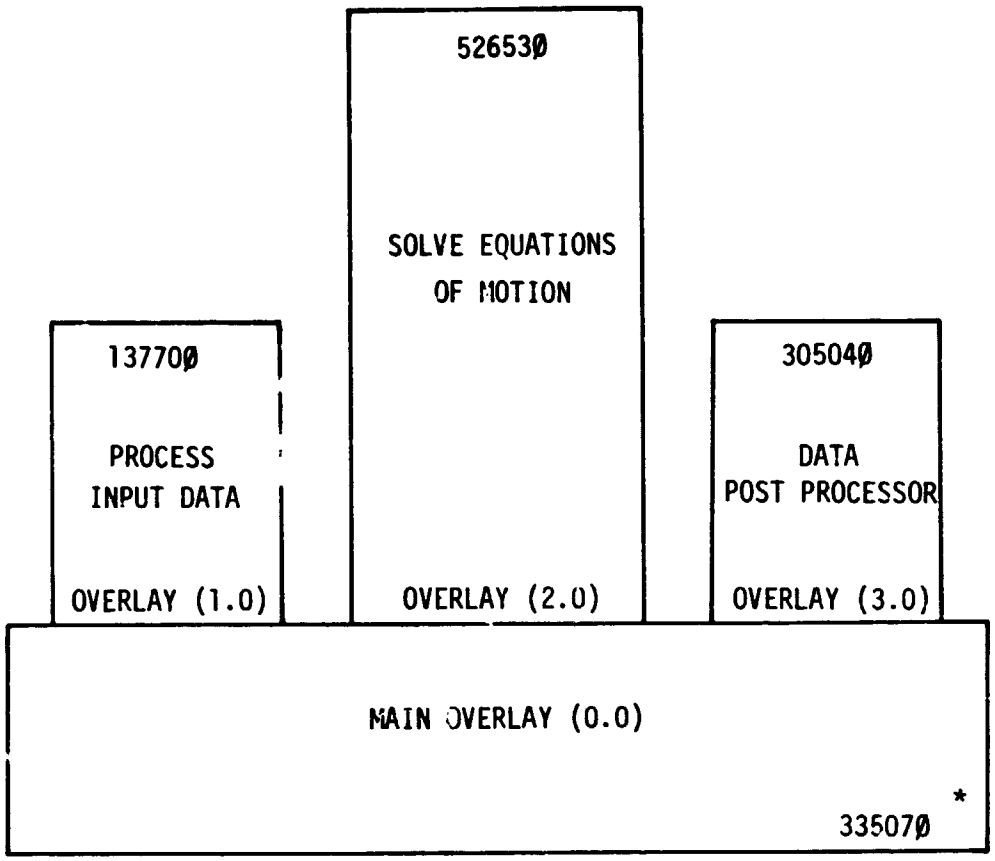

* OCTAL NUMBER
CORE REQUIREMENTS FOR CDC CYBER COMPUTER

Figure C-2. LAMPS3 Program Overlay Structure

```
**************************************************************
   C U B I T   M E S H   G E N E R A T O R   P R O G R A M
      PROGRAM FORMS FINITE ELEMENT MESH FOR LAMPS3
      DEVELOPED BY : R.L. BERRY, L.J DEMCHAK, A. COVINGTON
                     FOR NAS9-15302
                     LAST REVISION SEPT 1980
**************************************************************

           TANK  VARIABLES EXPECTED.
    -------------- --------------------------------
 IDOMET = 1, TOP ELLIPSOIDAL OR SPHERICAL DOME
        = 2, TOP OGIVE DOME
 RT     = RADIUS OF ELLIPSE OR OGIVE
 TDT    = HEIGHT OF ELLIPSE OR OGIVE (TRUNCATED HGT OF OGIVE)
 IDOMEB = 1, BOTTOM ELLIPSOIDAL OR SPHERICAL DOME
 IDOMEB = 2, BOTTOM OGIVE DOME
 RB     = RADIUS OF ELLIPSE OR OGIVE
 TDB    = HEIGHT OF ELLIPSE OR OGIVE (TRUNCATED HGT OF OGIVE)
 XL     = LENGTH OF PROPELLANT TANK CYLINDRICAL SECTION.
          (L UNITS)
 TR     = TANK RADIUS. (L UNITS)

                 GRID VARIABLES EXPECTED
    ---------------------------------------------------
 NSIDE1 = NUMBER OF DIVISIONS ON X AXIS (TOP SURFACE)
 NSIDE2 = NUMBER OF DIVISIONS ON Y AXIS (TOP SURFACE)
 NSIDE3 = NUMBER OF DIVISIONS ON Z AXIS (DEPTH OF TANK)

              FLUID PARAMETERS EXPECTED
    ---------------------------------------------------
  FDEN = MASS DENSITY OF FLUID
 PCVOL = PERCENT TANK FILL.LE.100.
 AMTOT = ACTUAL LIQUID MASS

           PLOT INFORMATION EXPECTED
    ---------------------------------------------------
  PTIT = ALPHA-NUMERIC PLOT TITLE (8A10)
   IFJ = 1, PLOT NODE NUMBERS
   NVW = 1, PLOT FULL TETRAHEDRA ELEMENTS
       = 2, PLOT ONLY CUBES
  IFPT = PRODUCE DIAGNOSTIC PRINT OUTPUT
 IFCORN= INPUT OPTION FOR GENERAL MESH GENERATION,
         REQUIRES ADDITIONAL INPUT OF "CORNER" NODES BY
         CALL READ (3 TIMES)
```

Table C-1. Program CUBIT Input Parameter Definition

```
        BAFFLE(S) PARAMETERS EXPECTED
 ------------------------------------------------
 NBAFF= 0,NO BAFFLES ADDITIONAL INPUT NOT REQUIRED
      = 1,ONE BAFFLE SET BAFFZL=BAFFZU, INPUT BAFCON
      = N,N NUMBER OF BAFFLES ,BAFCON OVERRIDDEN
BAFFZL= LOWER BAFFLE LOCATION
BAFFZU= UPPER BAFFLE LOCATION
BAFHGT= EFFECTIVE HEIGHT OF BAFFLE
BAFCON= EFFECTIVE WIDTH OF BAFFLE
```

Table C-1. (concl)

```
MESH3D      S.W.WIRTH
MESH GENERATION FOR 3D MODEL -10 % FILL; 1 BAFFLE
2X2X2 MESH TYPE FOR P4LMP3B
3DMESH FOR 10% FILL; 2X2X2; 1 BAFFLE
P$INPUT
 XL=1.31,
 TR=2.75,
 RT=10.16,
 TDT=6.46,
 IDOMET=2,
 RB=2.75,
 TDB=2.06,
 PCVOL=10.,
 IDOMEB=1,
 FDEN=2.0213E-4,
 AMTOT=3.1212E-03,
 NSIDE1=2,
 NSIDE2=2,
 NSIDE3=2,
 NBAFF=1,
 IFCORN=0,
 IFPT=0,
 NVW=2,
 BAFFZL=1.00,
 BAFFZU=1.00,
 BAFHGT=0.5,
 BAFCON=3.5,
 $
STOP
```

Table C-2. Sample Input Data for Program CUBIT

```
**************************************************************
            L A M P S 3  P R O G R A M
     LARGE AMLPITUDE 3 DIMENSIONAL SLOSH ANALYSIS PROGRAM
     DEVELOPED BY : R.L. BERRY AND L.J. DEMCHAK
                    FOR NAS9-15302
               LAST REVISION DEC 20 1980
**************************************************************

TAPE1 RESERVED FOR FORCE TIME HISTORY STORAGE
TAPE2 RESERVED FOR INPUT OF EXTERNALLY GENERATED MESH DATA
                  OR RESTART
TAPE3 RESERVED FOR LIQUID MOTION TIME HISTORY STORAGE
TAPE4 RESERVED FOR RESTART DATA OUTPUT

           TANK  VARIABLES EXPECTED.
    ------------------------------------------------
 IDOMET = 1, TOP ELLIPSOIDAL OR SPHERICAL DOME
        = 2, TOP OGIVE DOME
 RT     = RADIUS OF ELLIPSE OR OGIVE
 TDT    = HEIGHT OF ELLIPSE OR OGIVE (TRUNCATED HGT OF OGIVE)
 IDOMEB = 1, BOTTOM ELLIPSOIDAL OR SPHERICAL DOME
 IDOMEB = 2, BOTTOM OGIVE DOME
 RB     = RADIUS OF ELLIPSE OR OGIVE
 TDB    = HEIGHT OF ELLIPSE OR OGIVE (TRUNCATED HGT OF OGIVE)
 XL     = LENGTH OF PROPELLANT TANK CYLINDRICAL SECTION.
          (L UNITS)
 TR     = TANK RADIUS. (L UNITS)

           FLUID POSITION AND GRID VARIABLES EXPECTED
    ------------------------------------------------------
 THETAX = ORIENTATION OF TANK (DEG), IF .NE. 0 ITERATE TO
          POSITION
 NTHETA = NUMBER OF INCREMENTS OF THETA TO ACHIEVE
          CONVERGENCE
 CONVKE = CHANGE IN KINETIC ENERGY FOR POSITION
          CONVERGENCE
 CONVDT = INTERGRATION STEP SIZE FOR INITIAL POSITION
          CONVERGENCE
     G1 = ACCELERATION MAGNITUDE FOR INITIAL POSITION
          CONVERGENCE
 NITERP = NUMBER OF ITERATIONS TO ESTABLISH FLUID INITIAL
          POSITION, THETAX .NE. 0 FOR ITH THETA INCREMENT
          THETAX .NE. 0.  FOR ITH THETA INCREMENT

           FLUID PARAMETERS EXPECTED
    ------------------------------------------------
   XMUC = FLUID VISCOSITY (CENTIPOISE) , IF .LE. 0
          NO VISCOUS FORCES
```

Table C-3. Program LAMPS3 Input Parameter Definition

```
 FGLUE = GLUE FACTOR FOR FLUID TO REMAIN ON WALL
         RECOMMEND 1.0
 AMTOT = ACTUAL LIQUID MASS

         INTERGRATION AND PRINT/PLOT FLAGS EXPECTED
   ------------------------------------------------
 DTMAX = MAXIMUM DELTA TIME INCREMENT
    TF = END TIME OF SIMULATION
 NPRT  = PRINT COUNTER, PRINT EVERY NPRT TIME
IFPLT  = DIAGONSTI     FOR PLOT ROUTINES
IFSAVE = SAVE STATE ,ETC. TO JUMP START LATER (TAPE4)
IFJUMP = RESTART PROGRAM FORM PREVIOUS RUN
         (SEE SUBROUTINE JUMPRD FOR INPUT REQUIREMENTS)
NCHECK = 1, MINIMUM OUTPUT (DEFAULT VALUE)
       = 2, ST`TE OUTPUT/ B BD ETC...
       = 3, ALL OUTPUT, BRING WHEEL BARREL

          PLOT TITLE INFORMATION EXPECTED
   ------------------------------------------------
  PTIT = ALPHA-NUMERIC PLOT TITLE (4A10)
 NPLOT = PLOT COUNTER, PLOT EVERY NPLOT TIME
NSIDE1 = NUMBER OF DIVISION ALONG X AXIS
NSIDE2 = NUMBER OF DIVISION ALONG Y AXIS
NSIDE3 = NUMBER OF DIVISION ALONG Z AXIS
IPLOPT = 0, FREE SURFACE PLOT OPTION
IPLOPT = 1, BRICK PLOT OPTION

          BAFFLE(S) PARAMETERS EXPECTED
   ------------------------------------------------
  NBAFF= 0,NO BAFFLES ADDITIONAL INPUT NOT REQUIRED
       = 1,ONE BAFFLE, SET BAFFZL=BAFFZU, INPUT BAFCON
       = N,N NUMBER OF BAFFLES, BAFCON OVERRIDDEN
 BAFFZL= LOWER BAFFLE LOCATION
 BAFFZU= UPPER BAFFLE LOCATION
 BAFHGT= EFFECTIVE HEIGHT OF BAFFLE
 BAFCON= EFFECTIVE WIDTH OF BAFFLE

          ACCELERATION DATA EXPECTED
   - - - - - - - - - - - - - - - - - - - - - - - - - -
 ACCEL  = TABLE OF TANK ACCELERATIONS:
          COL 1- TIME, COL 2- AX, COL 3- AY, COL 4- AZ

          MESH DATA EXPECTED
   - - - - - - - - - - - - - - - - - - - - - - - - - -
 TABLES DEFINING FINITE ELEMENT MESH FROM PROGRAM CUBIT ON FILE 2
```

Table C-3. (concl)

```
LAMPS3    S.W.WIRTH
P4LMP3B RUN FOR 10% FILL 1 BAFFLE
2X2X2 MESH--VISCOUS SUBROUTINE INCLUDED,DT=.005
LAMPS 3D FOR 10% FILL; 1 BAFF;DT=.005
P$INPUT
 XL=1.31,
 TR=2.75,
 RT=10.16,
 TDT=6.46,
 IDOMET=2,
 RB=2.75,
 TDB=2.06,
 THETAX=13.0,
 IPLOPT=1,
 IDOMEB=1,
 IFPLT=0,
 XMUC=0.75,
 SMASS=5.77387E-03,
 AMTOT=3.1212E-03,
 ZOFF=35.9425,
 NTHETA=1,
 DTMAX=0.005,
 TF=1.10,
 FGLUE=1.0,
 NPRT=4,
 NPLOT=4,
 NITERP=40,
 IFAPP=1,
 NBAFF=1,
 BAFFZL=1.0,
 BAFFZU=1.0,
 BAFHGT=0.5,
 BAFCON=3.5,
 G1=190.0,
 CONVKE=1.0E-04,
 CONVDT=0.005,
 IFSAVE=0,
 IFJUMP=0,
 NSIDE1=2,
 NSIDE2=2,
 NSIDE3=2,
```

Table C-4. Sample Input Data for Program LAMPS3

```
                                TIME          AX          AY          AZ
$                                 ↓           ↓           ↓           ↓
ACCEL     3     4
    1     1       0.0         0.0          0.0        386.07
    2     1       0.07        0.0         11.582      -34.94
    3     1       2.0         0.0         11.582      -34.94
0000000000
XYZCOR    0    -2MESH3D
NTYPE     0    -2MESH3D
NP        0    -2MESH3D
MEND      0    -2MESH3D      DATA FROM PROGRAM CUBIT
IDIAG     0    -2MESH3D
AMASS     0    -2MESH3D
ELVOL     0    -2MESH3D
STOP
```

Table C-4. (concl)